Detection and Imaging studies with fast neutrons using D-D/D-T Neutron Generators

By

Saroj Bishnoi

PHYS01201104013

Bhabha Atomic Research Centre, Trombay, Mumbai.

A thesis submitted to the

Board of Studies in Physical Sciences

In partial fulfillment of requirements

For the Degree of

DOCTOR OF PHILOSOPHY

of

HOMI BHABHA NATIONAL INSTITUTE

March, 2019

Homi Bhabha National Institute
Recommendations of the Viva Voce Board

As members of Viva Voce Board, we certify that we have read the dissertation prepared by "**Saroj Bishnoi**" entitled "**Detection and imaging studies with fast neutrons using D-D/D-T neutron generators**" and recommend that it may be accepted as fulfilling the thesis requirement for the award of Degree of Doctor of Philosophy.

Chairman- Dr D. C. Biswas
Bhabha Atomic Research Centre, Trombay, Mumbai-400085, India
Biswas 1/3/2019 **Date:**

Guide- Dr Alok Saxena
Bhabha Atomic Research Centre, Trombay, Mumbai-400085, India
Alok Saxena 1/3/2019 **Date:**

Co-Guide- Dr Amar Sinha
Bhabha Atomic Research Centre, Trombay, Mumbai-400085, India
Amar Sinha 1/3/2019 **Date:**

Examiner- Prof. Surjit Mukherjee
The M. S. University of Baroda, Vadodara-390002, India
1/3/2019 **Date:**

Examiner- Prof. Marco Cinausero
Legnaro National Laboratories (LNL), INFN Italy
1/3/2019 **Date:**

Member- Dr P. K. Pujari
Bhabha Atomic Research Centre, Trombay, Mumbai-400085, India
1/3/2019 **Date:**

Member- Dr L. M. Pant
Bhabha Atomic Research Centre, Trombay, Mumbai-400085, India
1/3/2019 **Date:**

Final approval and acceptance of this dissertation is contingent upon the candidate's submission of the final copies of the dissertation to HBNI.
I hereby certify that I have read this dissertation prepared under my direction and recommend that it may be accepted as fulfilling the dissertation requirement.

Guide- Alok Saxena

Date: 1/3/2019 **Place: Mumbai**

DECLARATION

I, *Saroj Bishnoi*, hereby declare that the investigation presented in the thesis has been carried out by me. The work is original and has not been submitted earlier as a whole or part for a degree/diploma at this or any other Institution/University.

Saroj Bishnoi

STATEMENT BY AUTHOR

This dissertation has been submitted in partial fulfillment of requirements for an advanced degree at Homi Bhabha National Institute (HBNI) and is deposited in the Library to be made available to borrowers under rules of the HBNI.

Brief quotations from this dissertation are allowable without special permission, provided that accurate acknowledgement of source is made. Requests for permission for extended quotation from or reproduction of this manuscript in whole or in part may be granted by the Competent Authority of HBNI when in his or her judgement the proposed use of the material is in the interests of scholarship. In all other instances, however, permission must be obtained from the author.

Saroj Bishnoi

Saroj Bishnoi

List of publications

International Journals

Related to Thesis :

1. **S. Bishnoi**, R. G. Thomas, Arnab Sarkar, P. S. Sarkar, Amar Sinha, Alok Saxena, S. C. Gadkari. "Modeling of tagged neutron method for explosive detection using GEANT4" *Nuclear Inst. and Methods in Physics Research* A, 923 **(2019)** 26

2. **S. Bishnoi**, P. S. Sarkar, R. G. Thomas, T. Patel, M. Pal, P. S. Adhikari, A. Sinha, A. Saxena, S. C. Gadkari. "Preliminary Experimentation of Fast Neutron Radiography with D-T Neutron Generator at BARC." *Journal of Nondestructive Evaluation.* 38:13 **(2019**)

3. **S. Bishnoi**, P. S. Sarkar, Mayank Shukla, Nirmal Ray, Tarun Patel, Yogesh Kashyap, T. and Amar Sinha."High spatial resolution fiber based miniature detector for neutron flux mapping in a subcritical assembly and neutron generator." *Journal of Neutron Research. pp.169-175* ***(2017)*** *DOI: 10.3233/JNR-170045*.

4. **S. Bishnoi**, R. G. Thomas, P. S. Sarkar, V. M. Datar and A. Sinha."Simulation study of Fast Neutron Radiography using GEANT4." *Journal of Instrumentation*. 10 **(2015)** P02002 doi:10.1088/1748-0221/10/02/P02002

5. **S. Bishnoi**, P. S. Sarkar, T. Patel, P. S. Adhikari and Amar Sinha. Feasibility study of prompt gamma neutron activation analysis (PGNAA) of explosives simulants and bulk material using DD/DT neutron generator. *AIP Conf. Proc.* 1524 **(2013)** 275.

6. **S. Bishnoi**, T. Patel, Jilju R, R. G. Thomas, P. S. Sarkar, A. Sinha, A. Saxena. "Tagged neutron (D-T) based system development for CNO elements detection in bulk material," Under Preparation

7. **S. Bishnoi**, R. G. Thomas, P. S. Sarkar, T. Patel, G. Mishra, Ajay Kumar, Amar Sinha, Alok Saxena, S. C. Gadkari. "Neutron efficiency and n-γ response study of 5" liquid scintillator detector". Under Preparation

Conferences

1. Modeling of Gamma Response of BGO using GEANT4. **Saroj Bishnoi**, R. G. Thomas, P. S. Sarkar, A. Saxena, S. C. Gadkari. *Proc. of the DAE Symp. on Nucl. Phys.* 63 **(2018)** 1074

2. Fast Neutron Radiography with D-T Neutron Generator. **S. Bishnoi**, P.S. Sarkar, R. G. Thomas, T. Patel, S. C. Gadkari. *NDT.net issue, Vol.22 No.06**(June 2017)** ISSN 1435-4934.*

3. Neutron Tagging Experimentation for Explosive Detection. **S. Bishnoi**, P. S. Sarkar, T. Patel, Jilju Ratheesh, Payal Singhai, P. S. Adhikari and A. Sinha *Proc. of the DAE Symp. on Nucl. Phys.* 59 (**2014)** 846-847

4. Online Monitoring of Fast Neutron (DT/DD) at Purnima Neutron Generator. **S. Bishnoi**, T. Patel, M. Shukla , P. S. Adhikari and A. Sinha. *Proc. of the DAE Symp. on Nucl. Phys.* 57 **(2012)** 880-881.

5. Source characterization of Purnima Neutron Generator (PNG). **Saroj Bishnoi**, T. Patel, Ram K. Paul, P. S. Sarkar, P. S. Adhikari and Amar Sinha. *Proc. of the DAE Symp. on Nucl. Phys.* 56 **(2011)** 1102-1103.

Other Publications:

1. Amar Sinha , Tushar Roy, Yogesh Kashyap, Nirmal Ray, Mayank Shukla, Tarun Patel, Shefali Bajpai, P. S. Sarkar, **Saroj Bishnoi**., "Experimental subcritical facility driven by D-D/D-T neutron generator at BARC, India." *Nuclear Inst. and Methods in Physics Research B 350 (2015) 6670.*

2. Amar Sinha, Tushar Roy, Yogesh Kashyap, Nirmal Ray, Mayank Shukla, Tarun Patel, Shefali Bajpai, P.S. Sarkar,**S. Bishnoi**, P. S. Adhikari. "BRAHMMA: A compact experimental accelerator driven subcritical. "*Annals of Nuclear Energy 75 (2015) 590594*

3. H. Naik, S. V. Surayanarayana, **S. Bishnoi**, T. Patel, A. Sinha, A. Goswami. "Neutron induced reaction cross-section of ^{232}Th and ^{238}U at the neutron energies of 2.45 and 14.8 MeV."*Journal of Radioanalytical and Nuclear Chemistry 303(3) 2497-2504 (2015) DOI: 10.1007/s10967-014-3812-8*.

4. P. M. Prajapati, S. Mukherjee, H. Naik, A. Goswami, S. V. Suryanarayana, S. C. Sharma, B. S. Shivashankar, V. K. Mulik, K. C. Jagdeesan, S. V. Thakre, **S. Bisnoi**, T. Patel, K. K. Rasheed and S. Ganesan."Measurement of Neutron-Induced Reaction Cross Sections in Zirconium Isotopes at Thermal, 2.45 MeV and 9.85 MeV Energies." *Nuclear Science and Engineering*,171 (2012),7884.

Dedicated to my parents

Smt. Ramshawari Devi and *Sh. M. L. Bishnoi*

Acknowledgements

It is a great pleasure to express deep sense of gratitude and sincere thanks to my research guide **Prof. Alok Saxena**, Ex-Head NPD and Co-Guide **Prof. Amar Sinha,** HBNI for their valuable guidance, motivation, scientific discussions and encouragements throughout the course of my Ph.D. work. My confidence in attacking problems comes from the training I received from them.

I wish to express my gratitude to **Dr. S. C. Gadkari**, Head TPD for his wholehearted encouragement and support, without whom it would have been difficult to carry out the work. I am thankful to Doctoral Committee Chairman **Dr. D. C. Biswas** and Committee members **Dr. P. K. Pujari**, **Dr. L. M. Pant** for their constructive suggestions, insightful comments and questions. I am also thankful to **Dr. B. K. Nayak**, Dean HBNI, Physical Science for his constant encouragement and valuable suggestions.

It gives me immense pleasure to express my gratitude to **Dr. Renju Thomas,** NPD for his wholehearted encouragement and great support. His wide knowledge and logical way of thinking and reasoning on scientific problems helped me immensely during the course of work. I am especially thankful to **Dr. P. S. Sarkar,** TPD, who has been an integral part of all the works presented in this thesis.

I am thankful to Dr Arnab Sarkar, FCD for his technical support and help. I also wish to express heart filled thanks to all my colleagues from TPD for providing constructive suggestions throughout this work.

I wish to express heartful gratitude to my parents, brother and sisters for a lifetime support and encouragement. Without them I would have never had such great opportunities to learn and grow. The person whom I owe the largest acknowledgement is Mr Amit, my husband and best friend. Along with him parents-in-laws share the credit for constantly sustaining me with courage and perseverance. I am extremely thankful to my lovely son aditya, for his love and delightful smile which is a great source of energy in my life.

Last but not least, I would like to thank God almighty, teachers, all my friends and everyone, whose contributions were important for the successful realization of this thesis, but I could not mention them personally.

Synopsis

Neutron interrogations techniques for elemental detection and imaging applications [1] are important tools in Non Destructive Evaluation and have been applied in valuable fields such as inspection of aircraft corrosion, inspection of explosive devices for space technology, inspection of vehicle for illicit material detection at various entry points and so on. Based on physical properties, X-rays have limited penetration power in certain materials (high Z) and weak contrast for materials made out of light elements (hydrogen (H), carbon (C), nitrogen (N) and oxygen (O)). Both limitations are most evident if relevant structures are composed of light elements while the surrounding structures are thick or made of heavy materials (metals or compounds). An example is scanning of the large transport vehicles such as sea/air cargo, truck etc [2, 3]. Neutron interaction, on the other hand, has weak dependency on atomic number of the material and can provide elemental information as well as high contrast images of low-Z elements encapsulated by massive shielding and therefore are considered a complementary tool to X-ray in such cases. Within neutron based imaging or low Z elemental detection techniques, fast neutrons ($\sim$MeV) play a particular role when large objects of dense material consisting of low and high-Z materials have to be probed. Detection of low Z elements especially C, H, O, N are of interest because these are major elemental composition of most of the threat/illicit material including chemical explosive, narcotic, chemical weapons which present serious security threats to any nation. In this direction, during last few decades the development of neutron interrogation techniques such as fast neutron analysis, Fast Neutron Radiography, Pulsed Fast Neutron Analysis and associated particle imaging have been focussed on detection and imaging of low Z elements in bulk. However, at present neutron interrogation systems for these applications are still either at R&D level or at field testing and only few of them are installed at site and in use. Under the scope of neutron imaging / interrogation techniques for detection and imaging of low Z

elements, this thesis work has been carried out and summary of the work is described here.

At present, X-ray based commercial imaging systems have been in use to interrogate large number of objects for various types of threat materials and contrabands. X-ray based these systems have high throughput and are ideally suited for detection of metallic objects with distinctive/unique shapes and sizes such as Firearms and Ammunitions. At the best, these systems provide only gross information about the elemental contents of the inspected item (low Z vs. high Z discrimination) and have limitation on material specificity. Unfortunately, most of the current potential threats such as narcotics and explosives [4] do not have unique or specific discernible shapes and these systems fail to differentiate them from benign.

On the contrary, neutron based systems offer the possibility of identifying these elements irrespective of their structure or shape. Neutron interaction with material generates gamma lines specific to the elements present in it [5]. The exploitation of these elemental signatures represent a promising solution in detecting threat materials such as explosives, chemical weapons, narcotics [6] and distinguish with other benign materials. Most commonly used explosives (TNT, RDX, C-4, etc.) are composed primarily of the chemical elements H, C, N and O, although many innocuous materials are also primarily composed of these same elements. However, these elements are found in each material with very different elemental ratios and their concentrations [7, 8]. It is thus possible to identify and differentiate threat material from benign, for example, TNT from paraffin. In narcotics, the C/O ratio is nearly or at least a factor of two larger than the innocuous materials. It have been shown that explosives can be differentiated by utilization of both the C/O ratio and the C/N ratio. Thus , the problem of identifying explosives (or other threat materials) is reduced to the problem of elemental detection in bulk via neutron probe. The distinctive ratios of these elements can be obtained with neutron interrogations, through a variety of signatures, including neutron induced characteristic

gamma rays or attenuated transmission neutrons.

Neutron interrogation techniques present a number of advantages for elemental characterization. The use of neutron induced reactions for non-destructive elemental analysis in bulk is well established and documented [9]. These phenomena are not strongly affected by the shape of the material, rendering the disguising of explosives ineffective. Neutron interrogation systems for threat detection [10, 11], are mostly based on neutron induced gamma-ray spectroscopy. Neutrons interact with bulk to excite the constituent element nuclei, which then de-excite with the emission of energetic prompt gamma rays specific to the nucleus. These gamma rays have energies in the range of 1 to 11 MeV and are detected using suitable gamma ray detectors. Then, the spectrum is analysed to determine the contents of the bulk and the detection of threat is achieved by determining the elemental ratios (C/N, N/O, C/O etc) from the intensity of the characteristic gamma-ray [12, 13].

Furthermore, neutron being highly penetrating, their intensity is not diminished signicantly by the thickness of commonly utilized transport containers and also as the emitted characteristic gamma rays are of very high energy, they can come out after penetrating large volumes at ease. These basic features set the essentiality of neutron induced non-intrusive (the interrogation can take place from a distance of several centimetres) and non-destructive (because of no need to physically examine the bulk) technique for threat material detection.

Nuclear Techniques for Threat Detection

During the last two decades, great strides were made in research & development for construction and deployment of neutron based techniques for explosive and other contraband detection. Only a few of these techniques; Thermal Neutron Analysis (TNA), Fast Neutron Analysis (FNA), Pulsed Fast Neutron Analysis (PFNA), associated particle imaging (API) and fast neutron radiography (FNR) has shown potential towards a practical and efficient inspection

system [15]. This section deals with brief description of each technique starting with its technical name, the characteristics of the incident probing radiation used, the main nuclear reaction responsible for the elemental signals of interest, the detected radiation, possible sources for the probing radiation, the primary and secondary signatures and their capabilities.

Generally, neutron interrogation systems are based on Prompt Gamma Neutron Activation Analysis (PGNAA). The prompt gammas are neutron induced discrete gamma lines resulting either from thermal (n, γ) neutron capture or neutron inelastic scattering (n, n'γ) occurring with fast neutrons. These two types of reactions are generally complementary. Thermal neutron capture reaction is basis of the TNA and detects the emitted prompt gamma rays from the nucleus. Analysis of emitted gamma rays helps in identifying nitrogen, chlorine certain elements, present in explosives (for instance, trinitrotoluene (TNT) - $C_7H_5N_3O_6$ or pentaerythritol tetra nitrate (PETN)-$C_5H_8N_4O_{12}$) or narcotics [16]. However, TNA based devices have limited capability to detect oxygen or carbon. This restriction results in the high rate of false alarms from nitrogen, present in other benign materials such as urea, melamine etc. Even though TNA systems are in use for small air baggage inspection it is not implementable for large containers from the fact that thermal neutrons do not have sufficient penetration power to probe an entire container deep inside.

FNA and PFNA techniques uses fast neutrons ($\sim$ MeV) as probe beam and detection of neutron induced prompt-rays emitted by the decay of specific levels populated via (n, n/γ) neutron inelastic scattering or other fast neutron induced reactions with the nuclei in the interrogated sample. Using spectral analysis software, the elemental ratios of carbon, nitrogen and oxygen, contained in common explosive materials can be established. This enables real time identication of the explosive material by comparison with reference data. FNA is typically performed with an accelerator based D-T neutron generator providing 14.1 MeV neutrons emitted in 4 pi direction [17]. The major drawback associated with FNA is the large background. Fast neutrons, can interact

with surrounding materials or within the gamma ray detectors and distort the gamma ray signals coming from the interrogated bulk. To improve the signal-to-noise ratio, source neutrons as well as detector should be shielded effectively. The shielding will make system bulky and as a result system footprint will be large. On the other hand, PFNA employs pulsed neutrons generated by an accelerator source in short bursts of 1-2 ns in width for Time spectrum analysis to provide imaging information and reduced background. The main challenges in developing PFNA into a practical system is a tedious process of constructing a practical, collimated, pulsed energetic neutron beam that makes the operation safe and operationally acceptable and cost effective [18] . Infact, this technology is still in development stage and recently Brown et al. [19] has reported a cargo inspection system based on PFNA.

During the last two decades, signicant efforts have been put in using tagged neutron beams from neutron generators in order to improve the signal to noise ratio and 3D mapping of materials in the inspected bulk. This is achieved routinely with D-T neutron generator (NG) by using the Associated Particle Imaging also known as APT-Associated Particle Technique or Tagged Neutron Method. API is tagging the primary D-T neutron by associated alpha particles, that are produced through deuterium-tritium D(T, n) α fusion reaction [20]. In this reaction, neutron and associated alpha particle emits in almost back to back direction. The alpha particles are detected by a position sensitive charge particle detector and it determines the direction of the alpha particle and thus the direction of the outgoing neutron. Gamma rays are produced when this tagged neutron undergoes inelastic scattering or other reactions in the materials placed in neutron beam path defined by the solid angle of the alpha detector. They are detected by fast gamma-ray scintillation detectors in coincidence with the alpha particle (α-γ coincidence time spectrum), allowing the construction of time travel by neutron before interaction. This coincidence time spectrum allows determining the position of the neutron interaction point as the speed of 14.1 MeV neutrons approximately 5 cm/ns and gamma travel speed

is 30 cm/ns respectively. Using the α-γ coincidence time spectrum mechanism one can go inspecting a large volume in rectangular slabs placed perpendicular to the neutron beam path direction. Since, only coincident events are recorded, the scattered neutrons as well as background gamma signal are reduced and hence it provides high signal to noise ratio over other conventional neutron interrogation techniques. The interaction point location of the fast-neutron induced gamma rays is inferred from the neutron direction and the coincidence time spectrum. After that analysis of the gamma-ray spectrum associated to a given volume of interest provides information about the chemical elements located in it. Thus it appears as a 3D imaging non-destructive technique and named as associated particle imaging [21, 22].

Among these gamma-spectroscopy based neutron interrogation methods, most powerful one at present is API and it has been demonstrated for material detection in different environments such as unexploded ordnance (UXO), buried landmine, cargo scanning etc. One of the most successful implementation of an API system for cargo inspection was EURITRACK project [23]. It is a fixed type portal system which has been implemented at Croatian sea port.

Another neutron interrogation technique of importance using fast neutrons is fast neutron radiography. This technique mainly focuses on the transmitted neutrons through the object. The source neutrons pass through the bulk and based on the interaction probabilities with different type of materials and their thicknesses, a 2D image of the inspected objects is generated in the imaging detector. Consider a case of illegal transportation of hidden threat materials (which are mainly low Z (C, O, N, H, Cl etc)), masked by thick shielding materials such as of lead or depleted uranium (high Z), to shield them from X-rays and Gammas. In addition Cd and/or Boron can be used for neutron shielding to avoid detection with thermal neutron probe. In such cases, fast (MeV) neutron radiography has shown promising results [24].

The defence of depth principle in scanning of large containers or cargos is as follows. Initially they are scanned by X-ray / γ-ray based imaging systems.

If there is some suspicion is generated from the image and its contents in invoice, the container is opened and manually checked. This takes a lot of man hour and scanning throughput decreases. There can be two scenarios. Firstly, the image is too dark because of probe beam attenuation, in this case X-ray / γ-ray, possibly due to presence of thick high Z materials and secondly, the image is too light due to very little attenuation possibly because of low Z materials. To circumvent this problem, specific location of the suspicious container can be imaged with fast neutrons using FNR technique and finally if required API based interrogation technique can be implemented to characterize its contents as either containing any threat materials or benign.

Based upon the above mentioned facts, this research work focussed on the studies related to development of neutron interrogation imaging techniques, API and FNR, for imaging and identification of materials composed of light elements. Study of API technique has been aimed at detection of light elements (C, H, N, O) based on PGNAA and reconstruction of interaction location inside the interrogated object. On the other hand, FNR was studied in context of imaging low Z materials encapsulated by thick high Z materials using DT neutron generator. To perform API, initial developmental studies pertaining to PGNAA have been carried out for completeness, in the sense, to address the detection methodologies of a large set of elements for which API alone cannot be used. During the course of these studies, work related to D-D/D-T neutron source [25] characterization and real time monitoring through special miniature fibre detector and charge particle detector. In addition to this, study on neutron-gamma response of liquid scintillator detector has also been carried out for fast neutron spectrum measurement. These are of importance for both API and FNR.

Brief account of work done

The thesis work has been focussed on studies and implementation of FNR and API neutron interrogation techniques for imaging and detection of low Z material in bulk using indigenously designed DD/DT NG at BARC. In a nutshell, the studies carried out are the following:

The work begins with the feasibility experimental study of PGNAA, performed for detection of characteristic neutron induced gamma signature of H, C, N, O and Cl elements from various benign bulk samples of melamine, urea, salt and graphite. Emphasis was placed on two approaches; (1) detection of inelastic prompt gammas from C, O and N with FNA and (2) detection of capture prompt gamma 10.8 MeV from nitrogen using TNA technique. TNA was performed via moderating the D-D neutron and gamma signatures of hydrogen (2.22 MeV), nitrogen (10.83 MeV) and chlorine (6.61 MeV) were detected successfully with good signal to noise ratio. TNA has shown limitations for C and O elements detection as they are threshold reactions. In order to detect O and C, which are necessary for threat material identification, FNA method was explored with DT neutrons. Gamma signatures of C (4.43 MeV), O (6.13 MeV) and N (5.11 MeV) were detected successfully with FNA. TNA and FNA in combination could provide the fingerprints of the elements H, C, O, N and Cl in bulk. In the present experiment the main difficulty faced was the high gamma background due to neutron interactions with surroundings. This leads to reduction in signal-to noise ratio. To address this issue, tagged neutron based API technique was adopted and employed using D-T neutron generator.

As a first step, API technique was modelled and various aspects of API technique for material identification and 3D image reconstruction of the interrogated object were simulated using Monte Carlo based GEANT4 [26]. An array of BGO detectors for gamma detection and position sensitive detector for alpha detection was used in the simulation. The BGO detector was cho-

sen because of its high efficiency for high-energy gamma-ray detection and the reason that it is less sensitive to the neutron activation and capture than the other commonly used scintillation detectors (NaI and CsI etc). The physical response of BGO was incoporated in the simulation via comparing with its experimental response to mono-energetic gamma (0.511 MeV-4.43 MeV). The various parameters studied through these simulations are as follows: response of BGO detector to pure chemical elements (C, N, O, Al, Fe), response towards complex samples including threat (simulated-RDX, TNT, AN) and benign materials (Urea, Melamine), determination of elemental fractions by fitting sample spectra with linear combination of reference spectra of pure elements, detection of hidden threat surrounded with organic or iron matrix and reconstruction of 2D/3D images to find location of interrogated object inside a container. Towards implementing API technique, a laboratory based system was developed using indigenously designed D-T neutron Generator and was characterised. D-T neutrons were tagged via a position sensitive (64 pixel) YAP:Ce detector, installed inside NG tube for alpha detection. The choice of the YAP:Ce scintillator detector is motivated by their low cost, high count-rate capability, radiation hardness and good time resolution. In experiment, at present only one BGO gamma detector has been used and placed in a particular geometry with respect to the sample under investigation. VME based Front end electronics for data acquisition of 16 BGO and 64 alpha detectors was installed and tested successfully. An algorithm was developed for data acquisition, processing and analysis.

A number of experiments for detection of C, N and O signals from bulk samples (graphite, water, melamine and simulant of RDX) in various configurations have been carried out. Firstly, investigations were carried out with pure elements for individual spectra. In the second step pure elements were placed in combinations at different locations and through α-γ coincidence time spectrum method their energy spectra as well as positions could be established. In the third step, complex samples melamine and simulant of explosive (RDX,

C4) were investigated and spectra analysed. API system has demonstrated the detection capability of C, O and N elements from bulk of $\sim$ 3-5 kg within 15-20 minutes time with improved signal to noise compare to that in FNA. The experimental spectra of RDX simulant (3.6 kg) prepared from the mixture of benign materials (melamine ($C_3H_6N_6$), polyethylene ($(CH_2)_n$), sand (SiO_2) and graphite (C)) was compared with simulated spectra of RDX ($C_3H_6N_6O_6$). The comparison has shown overall satisfactory match in terms of possible gamma lines detected and their relative intensity with respect to carbon peak (4.43 MeV) intensity.

The next section describes the fast neutron radiography studies performed using DTNG. This work finds applications in the area of attenuation based imaging of low Z materials shielded by thick layers of high Z or hybrid (combination of low and high Z) materials. Prior to actual experimentation, FNR was modelled in GEANT4 and its potential as well as limitations were studied. Various configurations of different sample were simulated, analysed and images were constructed [27]. Based on the simulation a configuration of HDPe masked with thick layer of Lead was chosen for experimental studies. Most of the reported FNR experimental work, have used either high yield sources (yield $\geq 10^{10}$ n s^{-1}) [24] or large exposure time of 30-60 minutes. In this work we have studied and implemented the FNR using D-T NG of $\sim 2\times10^9$ yield and beam size (focal spot) of 20 mm. Since, the focal spot play important role in image quality, hence to reduce the focal spot from 20 mm to 10 mm size, simulation studies on the design of suitable collimator were carried out to achieve a respectable flux at the sample position, minimizing scatter contribution from collimator materials and maintain moderate L/D for such low yield NG. Based on these simulations, a metallic collimator of mild steel was designed and coupled with neutron imaging system comprising of Electron Multiplying CCD camera (EMCCD) in combination with a thick plastic scintillator. The sample configurations of step wedge, holes in step wedge and low Z masked with thick shield of lead were imaged and analysed.

During the course of these studies on fast neutron imaging techniques, work related to source neutron detection and characterisation were also carried out. These are of prime importance towards realization of actual neutron interrogation API and FNR based systems. The aim was to develop characterization devices for our D-D/D-T NG which would cater to source parameters such as real time monitoring of source yield and spectrum. Associated particle based real time neutron monitoring device has been developed using silicon charged detector. Miniature size ($\sim$1 mm) neutron (thermal/fast) detectors (TND/FND) have been developed for real time monitoring of thermal/ fast neutrons. TND and FND comprises of Li_6F (ZnS:Ag) and $^{232}ThO_2$ (ZnS:Ag) respectively. The sensitivity of TND and FND was found out to be $\sim 3.3\times 10^{-4}$ and 3.6×10^{-6} cps for one neutron per cm^{-2} field (unit neutron flux) respectively [28]. FND has been successfully used for DT neutron, a profile around the DT neutron source. While TND was developed as first step towards development of FND because large capture cross section of thermal neutron convertor material provides high probability of success comparatively and related issues could be taken care while developing FND. TND was characterised and its performance was evaluated in experimental accelerator driven subcritical system coupled with DTNG via thermal neutron profile measurement at various locations. For spectrum measurement of fast neutrons from DT/DD or around the API or FNR system, an organic liquid scintillator detector of $5''\times 5''$ was characterised. The parameters evaluated were gamma-neutron response measurement and extraction of response function via GEANT4 based simulation study. The efficiency was evaluated using extracted response function and it was verified with neutron spectrum measurement of ^{252}Cf source.

Organization of thesis

The thesis is organized as follows:

In chapter 1, we discuss the various existing different neutron based tech-

niques for low Z material detection particularly for threat material detection application. The current status of the detection system based on different methods is reviewed in brief and a basis is set for the study we carry out in further chapters. An outline of the thesis is provided.

Chapter 2 describes D-D/D-T NG neutron source used in thesis work and its yield characterisation. Different neutron detctors developed for real time neutron monitoring are presented. It includes associated particle based neutron monitor, miniature fiber based neutron detectors and characterisation of an organic liquid scintillator for fast neutron spectrum measurement.

Chapter 3, presents study of FNR performed for imaging of low Z material masked with thick layer of high Z material. First section of this chapter describes the Monte Carlo simulation study on FNR performed for capability and limitations of the FNR technique. Various simulated congurations of sample geometry and constructed images are detailed. Second part of this chapter presents the implementation of FNR with inhouse developed Neutron Generator and experimental studies on various sample configurations.

In Chapter 4, we describe the PGNAA based experimental study carried out for detection of C, H, N, O and Cl elemental signature in bulk of benign materials. It presents the experimental results and signal to noise ratio evaluated for different elements.

Chapter 5, discusses the modelling of API technique and presents the simulated physical response of BGO for gamma, a reference data set of gamma spectra generated for pure elements, spectrum decomposition methodology, analysis of sample (explosive and benign) spectra and matrix effect study for hidden explosive detection. It also describes the reconstruction of neutron interaction locations providing 3D mapping of the interrogated object under interrogation.

Chapter 6, describes the development of API based system and experimental studies carried out with the system. The major components of the system including position sensitive alpha detector, gamma detector,VME based Front-

end electronics and software tools developed for data acquisition, processing, analysis are described in detail. System characterisations with experimental measurements of systems time resolution, tagged neutron beam profile are presented here. Experimental results of pure element spectra, complex sample (benign and explosive simulants) spectra and spectra of different objects placed at different location in line at a certain distance identified through α-γ coincidence time spectrum and comparison with simulated one are discussed.

Thesis work is summarized and concluded in Chapter7. The discussion on future work is also provided here.

References

1. D.Hannum, J.Parmeter, Survey of Commercially Available Explosives Detection Technologies and Equipment, (1998).

2. George Zentai, IEEE Int. Workshop on Imaging Systems and Techniques IST (2008).

3. R.R. Eilbert and K.D. Krug, Proc. of SPIE 1824, 127143 (1992).

4. R. Lanza, Proc. an IAEA Technical Meeting: combined devices for humanitarian demining and explosives detection, Padova, 13-17 (2006).

5. Alexander P. B. et al.,Material Analysis Using Characteristic γ-Rays Induced by neutrons.

6. Gozani T, Int. topical meeting on nucl research applications and utilization of accelerators, Vienna, Austria, 48 (2009) .

7. Andy Bufer, Rad. Phy. and Chem. 71, 853-861 (2004).

8. Bufer A, Tickner, J Radiat Meas 45, 1186-1192 (2010).

9. A.M. Hassan, Proc. 7th Conf. Nucl. Particle Phys.(2009).

10. Gozani T, Strellis D, Nucl Inst Meth Phys Res B 261,311(2007).

11. T. IGUCHI et al , 16 WCNDT (2004) .

12. J. C. Overlay, J Appi. Radiat. Isot., Vol. 36, No. 3, pp.185-191(1985).

13. B.Perot et al. J Appi. Radiat. Isot. 66,421-434 (2008).
15. Tsahi Gozani, A Review of neutron based non-intrusive inspection techs.
16. John E. McFee et al, Proc. of SPIE Vol. 8357 V-2.
17. Tsahi Gozani, Nucl. Inst. Meth. in Phys Res A 353, 635-640 (1994).
18. Tsahi Gozani, Nucl. Instrum. Meth. in Phys Res B 99 743-747 (1995).
19. D.R Brown and T. Gozani, Nucl. Inst. Meth. B 99,753 (1995).
20. V. Valkovic et al, Nucl. Instr. and Meth. 76, 29-34 (1969).
21. M. Gierlik, Nucl. Inst. Meth in Phys Res A 834, 1623 (2016).
22. V.Valkovic et al., SPIE Proc. SPIE-2007, vol. 6540, pp. 654013.1-12.
23. B. Perot et al., Nucl. Inst. Meth. in Phys Res B 261, 295298 (2007).
24. J.Hall et al., UCRLCONF-230835, 2007.
25. Tarun Patel et al, BARC News Letter,Special Issue 2013
26. Agostinelli S. et al., Nucl. Inst. Meth. A 506, 250-303(2003).
27. S. Bishnoi et al, JINST 2014, doi:10.1088/1748-0221/10/02/P02002.
28. S. Bishnoi et al., Journal of Neutron Research, pp.169-175 (2017).

List of Acronyms

NG - Neutron Generator

D-D - Deuterium-Deuterium

D-T - Deuterium-Tritium

API -Associated Particle Imaging

PGNAA- Prompt Gamma Neutron Activation Analysis

TNA-Thermal Neutorn analysis

FNA - Fast Neutron Analysis

FNR - Fast Neutron Radiography

HDPe - High Density Polyethylene

EMCCD - Electron Multiplying Charge Coupled Device

YAP:Ce - Cerium doped Yttrium Aluminum Perovskite

BGO-Bismuth Germanate

SNR-Signal-to-noise ratio

Contents

List of Figures

List of Tables

CHAPTER 1

Background of the Study

1.1 Introduction

The aim of this thesis was to study some of the neutron based techniques towards design and development of neutron interrogation systems for imaging and detection of low Z materials in bulk using D-D/D-T neutron generator developed at BARC. The primary objective was to assess two imaging techniques. The Associated Particle Imaging (API), based on neutron in–gamma out approach for detection of lighter elements (hydrogen (H), carbon (C), nitrogen (N) and oxygen (O)) in bulk and fast neutron radiography (FNR), for direct imaging of low Z, masked with thick and high Z material. Low Z materials, specially if composed of C, H, N, O elements are of interest because most of the threat materials including chemical explosive, narcotics, chemical weapons primarily composed of these elements in common. Thus detection and imaging of such low Z materials is on prime importance towards security application as threat material detection in cargo and large containers. Both the imaging techniques are based on fast neutrons and suitable for such large object inspection. Fast neutrons, generated from neutron generators based on D-D/D-T fusion reactions are being considered as interrogating radiations in this thesis work. Accelerator based D-D/D-T neutron generators provide high yield suitable for FNR and electronic control of neutron emission which reduces the shielding requirement in idle condition. API utilizes the kinematics of fusion reactions which allows tagging of outgoing neutrons using the associated particles and highly penetrating power of fast neutron allows inspection of densely packed large containers such as sea cargo.

The thesis work comprises of study and implementation of neutron interrogation API and FNR imaging techniques using D-D/D-T Neutron Generator

for detection and imaging of low Z in bulk. The work is presented in the subsequent seven chapters.

1.1.1 Statement of Problem

The ability to effectively detect low Z objects (threat material i.e explosives) hidden in large container is one of the great technical challenges of national security that generally involves measurements in heavily shielded, challenging environments, for example entry ports with a requirement for few minute scan per container [1]. Effective methods of inspection of all sizes objects from luggage to shipping containers and from postal parcels to trucks is a vital component of any national security right from aviation to the control of land / sea ports at entry points [2]. At present the major approaches adopted for inspection and interrogation of such bulk objects include physical search, chemical identification, X-ray/gamma-ray imaging and neutron interrogation [3–5].

Physical search involves visual recognition of threat by trained personnel / sniffer dogs and are ineffective because of huge time consideration as well as they can be hidden to make it appear as an innocuous material. Chemical identification analysis detects explosives by analysing residues from surfaces, but fails when well-packaged [6]. X-ray based systems involve irradiation of a target item with X-rays, usually followed by image created on a detector system by X-rays that are either transmitted or backscattered by the inspected item. Standard (transmission) X-ray systems have been in use for quite a long time, but more in the role to detect threat items such as weapons, sharp objetcs and clues to explosive device such a trigger device containing metallic part rather than the explosive itself. Backscatter systems together with the standard absorption measurement provide information which can help in separating the effects of density and effective atomic number (Z_{eff}, in other words average atomic number). Dual energy X-ray systems yield material discrimination through comparison of the attenuation of X-ray beams at two energies and applying suitable algorithms. In Computed Tomography, cross-sectional images or slices through an object are reconstructed numerically from X-ray projections at various angles around the object. These cross-sectional images

can be stacked together to produce a three dimensional image. Z_{eff} can also calculated and materials with similar Z number as explosives can be identified [7, 8].

Over the years, immense progress has been made in the fields of X-ray / gamma ray based threat detection systems as evidenced by the ubiquitous presence of traditional X-ray machines, sub-millimeter scanners [4] and backscatter imaging devices [5] at airports, seaports, and other critical locations. They have high throughput and are ideally suited for detection of metallic objects with distinctive shapes and sizes. These systems provide at the best only gross information about the elemental content of the inspected item (low Z vs. high Z discrimination) and have the limitation of material specificity. Unfortunately, these systems are not reliable when searching for organic-based explosives or illicit materials because most of the current threats do not possess specific discernible shapes and these systems fail to differentiate such low density materials [4] from benign. Additionally, dense heavy materials can be used to shield the X-rays, obscuring the view within the objects being investigated. Hence inspection by X-ray and gamma ray imaging is not a viable solution since they lose specificity, low mass attenuation coefficients for low Z and high mass attenuation coefficient for high Z materials and require alternative methods.

Neutron based nuclear techniques (also named as neutron interrogation), can address these issues and offers the high penetration power with possibility of measuring the elemental density of most elements in materials independent from their particular size or shape.The exploitation of elemental signatures represents a promising solution towards detecting illicit materials such as explosives, chemical weapons, narcotics [9, 10]. The neutron based systems achieve this feat, mainly through the production of characteristic elemental prompt gamma rays by the nuclear reactions, primarily (n, γ) with thermal neutrons and (n,n,γ) with fast neutrons (also called as prompt gamma neutron activation analysis- PGNAA). Furthermore, neutron being highly penetrating, their intensity is not diminished significantly by the thickness of commonly utilized transport containers and also as the emitted characteristic gamma rays are of very high energy ($\sim$MeV), they can come out after penetrating large

volumes at ease. These basic features set the essentials of neutron induced non-intrusive (the interrogation can take place from a distance of several centimetres) and non-destructive (because of no need to physically examine the bulk) technique for threat material detection. While imaging is not a feature commonly associated with neutron based nuclear techniques, it is essential to the ability to distinguish with high selectivity, threat material from the overwhelming majority of benign substances surrounding it [11].

During the last few decades, great strides were made in research, development and partial deployment of neutron based techniques for explosive and other contraband detection. This chapter reviews the current status with respect to the use of neutron-based technologies for elemental analysis and imaging of materials in particular for the detection of hidden explosives and illicit drugs in bulk form.

The chapter begins adressing the problem through discussion on properties of various substances that make them detectable by neutron based techniques, principles behind neutron interrogations followed by different types of neutron sources, alpha-gamma detector requirement and related information. Then an overview of different existing neutron based nuclear techniques each with their merits-demerits and imaging capability for application of large objects (cargo containers or trucks) is discussed. After that, a description on literature survey followed by scope of thesis work in brief and finally an outline of the thesis is provided.

1.1.2 Characteristics of Threat

In order to detect threat material it is important to understand their characteristics. Various characteristics can be used for explosive detection [11]: such as density, geometry and elemental composition. *Geometry*: Usually, explosive devices consist of two main components: detonating system and an explosive agent. The detonators are made of metallic components with an initiating explosive. The presence of a metallic detonator and associated wires can be detected using shape based image analysis. *Material density:* Explosive material is more dense than most organic material but not as dense as metals. *El-*

emental composition: is one of the major parameter exploited by neutron based techniques. Most of the hidden threats like explosives, narcotics and chemical weapons, consist mainly of carbon, oxygen and nitrogen light elements as the majority organic materials. Threat materials have unique elemental compositions which are generally different from other benign materials. For example, chemical explosives are rich in oxygen than most common benign materials. Likewise, they are rich in nitrogen, but they have a relatively low concentration of carbon and hydrogen. The chemical composition of some of the threat materials are shown in figure (1.1).

The threat material can be discriminated among different materials using relative elemental ratios such as O/C and N/C and, in some other cases (as i.e. for chemical warfare agents), on the quantitative determination of elements like Cl, P, S, As, etc [5, 12].Chlorine based boosters are also sometimes added to enhance the destructive capabilities of explosives due to the instability of chlorine-oxygen chemical chains. The high fraction of oxygen and nitrogen, along with the use of chlorine boosters, provides major key signatures for any detection method [13]Figure (1.2) shows the discrimination of threat materials based on elemental contents of oxygen and nitrogen present in explosive.

1.1.3 The Need for Imaging

In addition to composition information, it is also desirable for a detection technique to be able to have imaging capabilities. With imaging one obtains geometry and localization information that can be of great help. If the measurement is localized, the determined elemental densities will represent the material composition at that specific volume element (voxel) and not an average over a larger volume. The latter may dilute the information and the unique composition of the concealed substance will be lost, resulting in a failure to detect. Since contraband is rarely the only contents of an inspected container (luggage, car, truck or a cargo container), the ability to measure locally C, O, N, etc., inside it is essential. However, explosives and narcotics, unless they are formed in thin sheets, typically exist in bulk and their detection does not require a very high spatial resolution. In this regard voxel resolution typically of

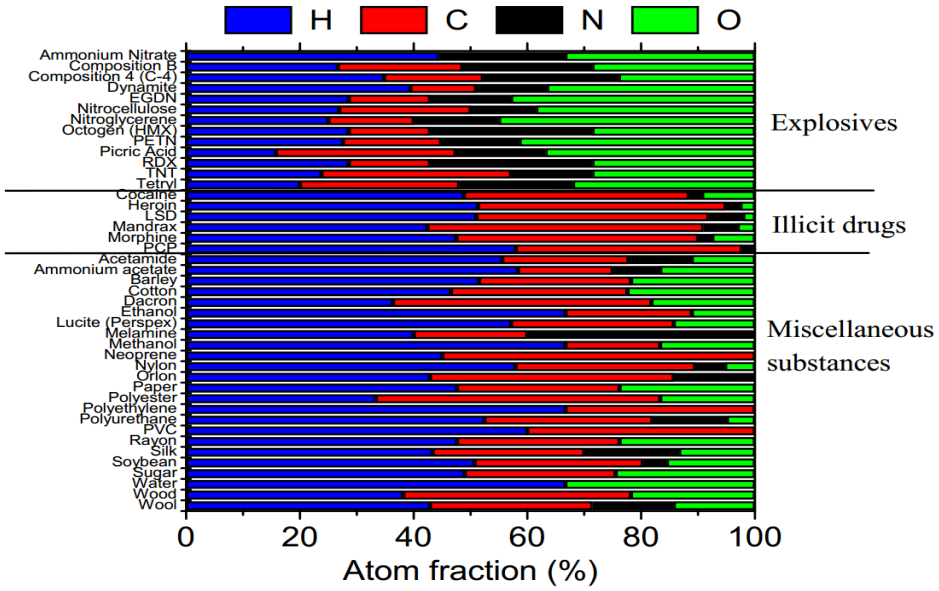

Figure 1.1: Chemical composition of CHNO elements which contitutes a selection of explosives, illicit drugs and miscellaneous everyday materials.

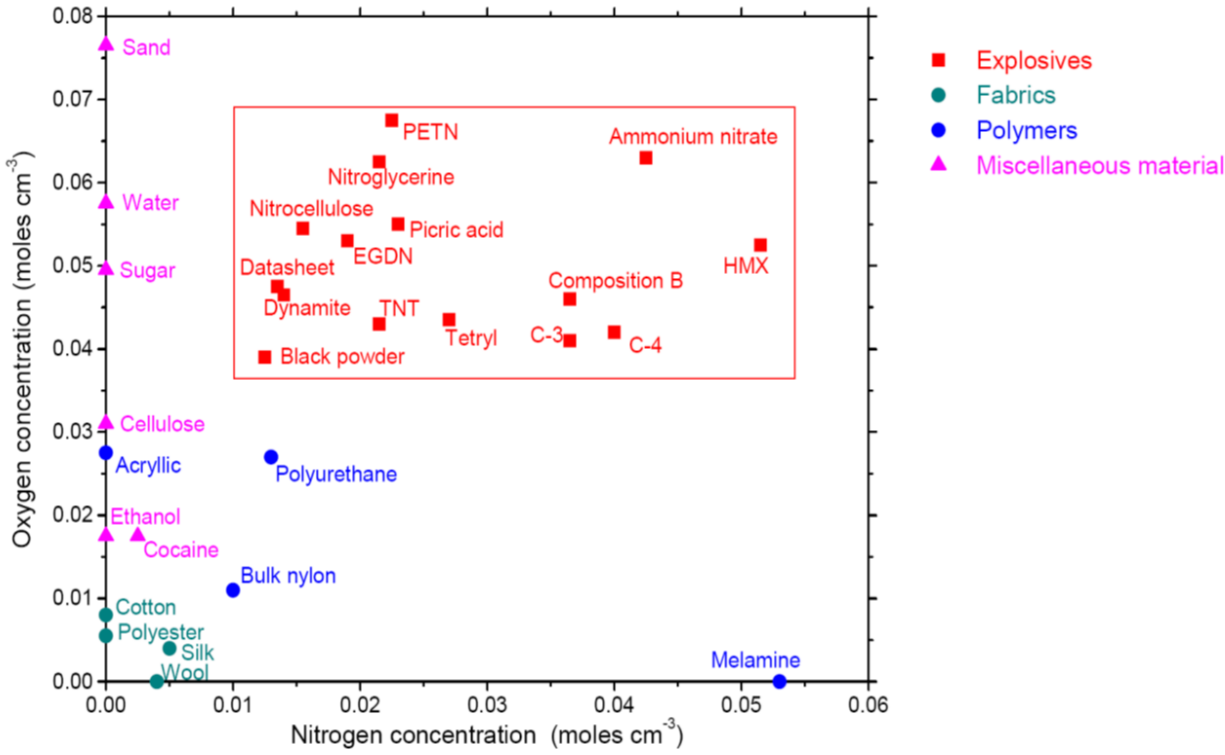

Figure 1.2: Identification of some explosives and benign materials based on nitrogen and oxygen fraction.

the order of few cm's $\sim$ 10-20 cm^3 is good enough for first-hand information.

1.1.4 Basic of Neutron Interrogation

Neutron interrogation systems, operate either through the principle of neutron induced gamma-ray spectroscopy (neutron in - gamma out) or based on transmitted neutrons /scattered neutrons (neutron in -neutron out). In neutron-induced gamma-ray spectroscopy approach, a neutron source irradiates a target to excite nuclei, which then de-excite with the emission of an energetic gamma-ray specific to the nucleus in the 1 MeV to 11 MeV range [14]. Primarily, neutrons undergo either capture (n,γ) or inelastic neutron scattering (n,n$\prime$ γ). Capture reactions have no threshold and thermal neutrons have high capture probabilty in compare to high energy neutrons. While inelastic neutron scattering is important for threshold reactions and requires neutrons of energy higher then that of reaction threshold. The gamma rays produced in these reactions are (known as prompt or delayed based on the time of emission) detected by an array of gamma-ray detectors and creates a spectrum containing peaks that correspond to the energy of the gamma-rays. The analysis of peaks provides isotopic content of the investigated volume and intensity of the γ-rays peak indicates the relative amount of material present. It is therefore in principle possible to calculate the elemental ratios, how much of each element is present with respect to the others in order to determine the type of substance under analysis.

The elemental densities of hydrogen, chlorine and nitrogen are measured by the prompt gamma emitted via thermal neutron capture (n,γ) process (for detail see1.2.1). Chlorine signal forms the basis for the detection of hydro chlorinated cocaine and heroin. Nitrogen signature detection forms the basis of detection of nitrogen rich explosives. More specific detection of these contraband is achieved by measuring their elemental constituents oxygen, carbon, nitrogen. These elements are detected by their characteristic prompt gamma-rays emitted when fast neutrons are inelastically scattered by the nuclei of the elements as detailed in section 1.2.2.

Other type of neutron interrogation systems are based on transmitted or

scattered neutrons, where the source neutrons pass through the interrogated object and detected by detector system. Based on the interaction probabilities of source neutrons with various elemental contents of inspected material, it is possible to deduce the objects images hidden inside large container. In such cases the gross information on elemental contents of the interrogated object is provided by based on attenuation or via transmitted neutron measurement

1.1.5 Neutron Sources

Common features in most of the neutron interrogation techniques for material identifications are the neutron source and detectors that identify the particles of interest whether those are gamma rays, scattered neutrons or transmitted. Neutron source play an important role in neutron interrogation, exploiting different neutron based interaction mechanisms. Depending on the chemical elements that one wishes to detect or measure, one might have to use neutrons of different energies (thermal or fast). The compact neutron sources, which can either be a radioisotopic (^{252}Cf, alpha-Be) sources or an accelerator based neutron sources such as neutron generator are in common use for neutron interrogation system. ^{252} Cf is a radioactive material with a half-life of about 2.6 years, which has neutron energy spectrum with most probable energy of 0.8 MeV and average energy of 2.1 MeV. Other type of radioisotopic sources are composed of two nuclides; one alpha-emitting and another that absorbs the emitted alpha particle and then emits a neutron. It includes plutonium-beryllium (PuBe), americium-beryllium (AmBe), americium-lithium (AmLi) etc. The neutron energy spectra of such sources are quite broad due to the variability of the alpha particle energy and dependent on the alpha source [15]

All of these types of neutron sources are easy to use and require no equipment other than shielding. The associated major drawback is that they are constantly decaying and there is no way to turn them off. Therefore, when the neutron source is unshielded, it presents a constant hazard to nearby personnel, even when it is not being used. Furthermore, the radioactive material can expose unknowing individuals to a constant radiation dose if it is lost or stolen. The sources themselves present possible risks for terrorism when coupled with

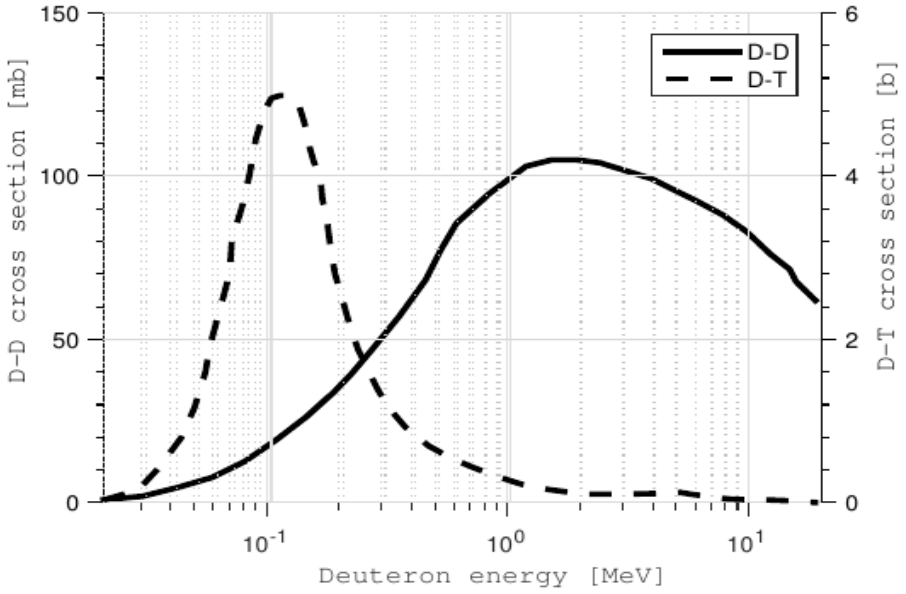

Figure 1.3: Total reaction cross-sections for D-D and D-T fusion at different deuteron beam energies (taken from [16]).

conventional explosives to create radiological dispersive devices.

Accelerator based neutron generators are a viable alternative that enable reactions that lead to the creation of neutrons. They allow for neutron emission as per requirement, can be turned off and thus are easier to transport and have high neutron fluxes [17, 18]. Deuterium-Tritium neutron generator is one example of such generator. When a D-T generator is turned on, deuterium ions ((d^+) are accelerated to a tritium target. The deuterium and tritium undergo a fusion reaction T(d,n)α to form an alpha particle (^{4}He) and a neutron whose average initial energy is $\sim$ 14.1 MeV [16]. The T(d, n)4 He reaction cross section in the 0-10 MeV deuteron energy range is presented in Figure 1.3. The maximum cross section is at deuteron beam energy of about 110 keV and then it decreases with further increase in the deuteron energy. Thus, in order to maximize the neutron flux, it is reasonable to use a deuteron beam of few hundreds of $\sim$ KeV. In D-T NG case, since the incident particle energy is small compared with the Q-value of the reaction (Q = 17.6 MeV), all produced neutrons have roughly the same energy and are emitted nearly back-to-back with respect to the associated α particles in the laboratory system. A deuterium-deuterium (D-D) neutron generator works in the same way, except

in this case deuterium ions are accelerated towards a deuterium target. When the two particles go through a fusion reaction, the product is ^{3}H and a neutron with an average energy of about 2.5 MeV. In Deuterium-Tritium reaction, yield is roughly 100 times higher than the Deuterium-Deuterium reaction. In both cases, if the generator is off, the deuterium is not directed towards the target (tritium or deuterium) and no neutrons are created. This makes it ideal choice for interrogation applications and reduces the risk of accidental exposure. Several compact D-T and D-D generators have been designed and being used specifically for active neutron interrogation applications [19].

These different sources are with their advantages and disadvantages. It is up to the system designer to decide which best suits his or her needs. A brief discussion of D-D/D-T Neutron generator used as neutron source in this thesis work is described in the next section.

D-D/D-T Neutron Generator

An indigenously built neutron generator [20] [21] operating in D-D/D-T mode at Purnima Lab, Bhabha Atomic Research Center (BARC) is known with the name of "PURNIMA Neutron Generator Facility ". A picture of this facility is shown in Figure 1.4. It is a 300 kV DC electrostatic deuteron accelerator based on Cockroft and Walton type multiplier. This facility incoporates RF ion source, RF ion source has advantage of its high mono-atomic ratio (about 70 - 90%) [16, 22]. Mono-atomic ions are preferred because they carry the full beam energy, whereas diatomic or triatomic ions have lower energy per nucleon, resulting in a lower fusion cross section per ion. The deuterium gas is supplied to ion source through a gas inlet and its flow is controlled by a motorised needle valve which is connected with deuterium gas cylinder. The plasma is produce using capacitor coupled 100 MHz, 200 W RF power. The D^+ ions are produced and extracted from ion source by applying extraction voltage which is focused by 30 kV DC electrostatic Einzel lens, accelerated and bombarded on the target. The target is maintained at ground potential. The deuteron ions impinge on titanium-tritium (TiT) or titanium-deuterium (TiD) targets (with copper backing), providing 14.1 MeV or 2.45 MeV neutrons via

Figure 1.4: Purnima Neutron Genarator

Table 1.1: Main parameters of the neutron generator.

Deuteron energy		0 – 300 KeV
Beam current		1-1000μA
Mode of operation Pulse repetition frequency	Pulse and continuous	10 μs to continuous 1 Hz to 1 kHz
Spot size		20 mm
D-D mode	Maximum neutron yield Neutron energy	3×10^{7} n/s 2.45 MeV
D-T mode	Maximum neutron yield Neutron energy	1×10^{10} n/s 14.1 MeV

T(d, n) ^{4}He or D(d, n) ^{3}He fusion reactions respectively.

The operating parameters of neutron generator are controlled and monitored through a computer based centralized system from the control room. Target holder accommodates 40 mm diameter tritium or deuterium target. Target is created by adsorption of tritium (or deuterium) in titanium layer. The titanium layer is deposited on a copper backing plate of 0.5 mm thick or less. Target is continuously cooled by a closed loop chilled water system. The accelerator is maintained at a vacuum of typical 1x10^{-6} mbar during operation, with vacuum system of a turbo molecular pump and a rotary pump. Different beam diagnostics components: ion beam steerer for beam alignment, beam profile monitor for beam profile, Faraday cup for current measurement are

placed in beam path to analyse beam.

The accurate monitoring of neutron yield of NG is important to know the number of neutrons incident on the sample. The detection of fast neutron is itself a challenging task and high background counting rate in the detectors, due to high gamma field associated with neutron source or caused by neutrons scattered from walls and from other surrounding materials in the experimental room makes it more complicated. Characterisation of the NG and its neutron yield measurement with different detectors developed is described in detail at chapter 2.

1.1.6 Choice of alpha and gamma detectors

Other then the neutron source, charge particle detector and gamma detectors are major components for study and development of any neutron based interrogation system. A brief discussion on choice of alpha and gamma detector related to the thesis work is described in the next section.

Alpha Particle Detector

Detection of the charged particle associated with D-D/D-T neutron emission from a NG can be used for neutron yield measurement of the NG. The key point in detection of charged particle associated with D-T (or D-D) neutron is the choice of charge (α or proton etc)particle detector. It is also important to note that some of the neutron interrogation imaging techniques for example API based system developement require a position sensitive alpha detector embedded inside DTNG. The important required characteristics of such detector are capability for high count rate with good time resolution, mechanical robustness and resistance to the radiation damage induced by neutrons and charged particles. In particular, it must have minimum outgassing and it should survive prolonged radiation exposure.

Semiconductor detectors are indeed characterized by good energy resolution, good stability, excellent efficiency and timing characteristics. But the prolonged exposure to neutrons and charged particles creates rapid performance

deterioration due to radiation damage in them. In typical surface barrier silicon detectors serious changes appear to take place for an irradiation of about 10^{12} fast neutron cm^{-2} or 10^9 α particle cm^{-2} respectively [23].

Several scintillators of different types have been investigated in the past for use in neutron generators for alpha charged particle detection. These were Silver-activated Zinc Sulfide (ZnS:Ag), Gallium-doped Zinc Oxide (ZnO:Ga), plastic scintillators and Yttrium aluminium perovskite activated by cerium (YAP:Ce) etc.

ZnS(Ag) is one of the oldest inorganic scintillator which has very high scintillation efficiency compare to that of NaI(Tl). It is polycrystalline in nature and available only as a polycrystalline powder. It makes its use limited to thin screens. Thickness greater than about 25 mg/cm^2 become unusable because of the opacity of the multi-crystalline layer to its own luminescence light [15].

ZnO(Ga) scintillator coatings are characterized by a decay time of about 1.5 ns, scintillation light peak at 390 nm [15] and light yield up to $\sim$ 3300 photons per MeV of deposited energy [24, 25] ZnO(Ga) absorbs its emitted light so that coating thickness and uniformity may be very critical. However, ZnO:Ga has been considered and utilized as a phosphor coating for alpha detection in NG in some cases [26, 27].

Plastic scintillators are very fast light decay time nearly 2 ns and are available in a large variety of different sizes and shapes. But in this case attention has to be given to the self absorption of the scintillation light.

YAP:Ce ($YAlO_3$:Ce), is of a special interest in various applications. The YAP:Ce exhibits several characteristics that are very well suited for our intended application such as fast response, high light output, non-hygroscopic, radiation hardness, excellent mechanical and chemical properties. YAP:Ce is characterized by high light output of 40% relative to NaI(Tl), a short decay time constant of 25 ns and a moderate efficiency for gamma-ray detection (density of 5.37 g/cm^3 and atomic number of yttrium Z = 39). These properties of YAP:Ce and the fact that its emission spectrum peak at 370 nm matches with the sensitivity of typical photomultiplier's suggest potential applications of YAP:Ce in γ-ray spectroscopy, nuclear medicine etc. It is important to note

Scintillator data table

	NaI:Tl	CsI:Tl	CaF_2:Eu	BaF_2	YAG:Ce	YAP:Ce	GSO:Ce	BGO
Physical								
Density [g/cm^3]	3.67	4.51	3.18	4.89	4.57	5.37	6.71	7.13
Hardness [Mho]	2	2	4	3	8.5	8.6	5.7	5
Index of refraction	1.85	1.78	1.44	1.5/1.58	1.82	1.95	1.85	2.15
Crystal Structure	Cubic	Cubic	Cubic	Cubic	Cubic	Rhombic	Monoclinic	Cubic
Melting point [C]	651	621	1360	1280	1970	1875	1950	1050
Hygroscopic	Yes	Slightly	No	Slightly	No	No	No	No
Linear Coef. of Thermal expansion [$10^{-5}/K$]	4.75	5	1.95	1.84	8–9	4–11	4–12	7
Cleavage	Yes	No	Yes	Yes	No	No	Yes	No
Chemical formula	NaI	CsI	CaF_2	BaF_2	$Y_3Al_5O_{12}$	$YAlO_3$	Gd_2SiO_5	$Bi_4(GeO_4)_3$
Luminescence								
Integrated Light Output [%NaI:Tl]	100	45	50	20/2	15	40	20–25	15–20
Wavelength of Max. Emission [nm]	415	550	435	325/220	550	370	440	480
Decay constant [ns]	230	900	940	630/0.6	70	25	30–60	300
Afterglow [% at 6 ms]	0.5–5	< 2	< 0.3	–	< 0.005	< 0.005	< 0.005	< 0.005
Radiation length [cm]	2.9	1.86	3.05	2.03	3.5	2.7	1.38	1.1
Photon yield at 300 K [10^3 Ph/MeV]	38	52	23	10	8	10	8–10	2–3

Figure 1.5: Properties of different detectors (taken from [28])

that, the energy resolution of YAP:Ce is comparable to that of NaI(T1) and CsI(T1) with a photo-diode. The measurements of light yield of YAP:Ce as compared with NaI(Tl) has been reported in a work of [28]. The studied crystals had 25 mm diameter and 1 mm thickness. The time distributions of the light emitted from YAP:Ce crystals for γ-rays and α particles are discussed in the work [29]. A very intense fast component with a decay time constant of 26.7$\pm$0.12 ns and an intensity of 89$\pm$2 %, followed by a slow component with the decay time constant of 140$\pm$10 ns were measured for gamma ray. The light emission due to α particles show a fast component of 24.8$\pm$0.12 ns with the intensity of 85$\pm$2 % and the slow component with the decay time constant of 100$\pm$5 ns. Also some energy spectra measured with YAP:Ce crystals showed that the energy resolution value is 16.1% and 5.7% at E_γ = 59.6 and 661.7 keV respectively. The basic physical and chemical properties of YAP:Ce are presented in Figure (1.5).

Gamma Detector

The choice of gamma ray detectors is one of the important component for neutron based system to be effective. The gamma ray detectors must be suitable

for operation in mixed radiation fields where both neutrons and gamma rays are present. The detector material must have a high Z value to effectively detect characteristic photons with energies up to ∼11 MeV. The detection material/medium must also provide the energy resolution that allows resolving peaks of interest.

The requirement of the high energy detection with high detection efficiency narrows the search for this application to a suitable crystal to large and widely affordable species as NaI(Tl) (Thallium doped sodium iodide) or BGO (bismuth germanate, formula - $Bi_4Ge_3O_{12}$). Even the latest lanthanide-halide scintillator based detectors such as lanthanum-chloride ($LaCl_3$(Ce)) and lanthanum-bromide ($LaBr_3$(Ce)) detectors offer far better properties, particularly when the energy resolution is concerned [30, 31]. For example, the energy resolution of at E_γ= 662 keV is of less than 3% [32]. However, they still cannot be grown inexpensively to large sizes and the high cost of these detectors (nearly 17-18 times for a high quality NaI(Tl) of similar size [15] limits their wider usage.

NaI and BGO detectors are inorganic scintillator class of detectors. The detection process in the inorganic scintillator starts when an incident γ-ray interacts with the crystal material, exciting the atoms to higher energy states. The atoms de-excite through the emission of optical photons. The photon strikes the surface of a photosensitive surface, usually of a photomultiplier tube, releasing less than one electron per photon (depending on the quantum efficiency of the PMT) via the photoelectric effect. These photo electrons are accelerated and multiplied until a pulse is formed whose voltage is proportional to the number of scintillation events and therefore the energy of the incoming gamma-ray [15]

NaI is the industry standard scintillation detector for the detection of gamma-rays of the order of 1 MeV or higher energy. The detection efficiency is relatively good because of the density of NaI (3.67g/cc) and the presence of the high Z element iodine (Z = 53). The NaI(Tl) scintillator material has the light yield 38 photons/keV, 1/e decay time 250 ns and typical resolution of 50 keV is reasonably good for resolving lines separated by at least 100 keV. The timing resolution is excellent and allows the detector to be operated at high rates on

the order of 100 to 200 kHz. The detector is usually operated at room temperature but may require a temperature-controlled environment to avoid gain drift in the photomultiplier tube with a loss in energy resolution [15] .

BGO is a strong competitor to NaI. The BGO scintillator has the light yield 8-10 photons/keV and 1/e decay time 300 ns. Due to the high atomic number of bismuth (Z_{Bi} = 83) and high density (7.13 g/cc) of crystal, the BGO scintillator is very effective for detection of high energy photons. Its energy resolution is lower than NaI(Tl) resolution, 10% FWHM versus 7% FWHM at 662KeV [33]. BGO demonstrates excellent behaviour under neutron irradiation without delayed decay issues as compared to NaI.

The superior efficiency of the BGO detectors has to be weighed against their inferior resolution and their higher price than that of the NaI detectors. Since the price of the BGO detectors strongly depends on the crystals size.

The BGO of size 3 inch x 3 inch was opted for our work in view of providing trade-off between detection performances and compactness of its integration in the API system. Hence the choice of BGO was dictated by their high efficiency to photon quanta and small dimensions, which allows one to minimize the dimensions and weight of the shielding, which protects crystals from direct flux of neutrons from the target of the neutron generator. Table 1.5 presents the comparison of different inorganic scintillator detectors.

1.2 Overview of Neutron Interrogation Techniques

A number of neutron based techniques have been proposed and researched depending upon kind of material to inspect in search of hidden threat in bulk [5, 34–36] each with their unique advantages and disadvantages. The some of them are briefed here, although this is by no means a complete list, it represents systems and techniques that have been studied or utilized in the past 10 years.

1.2.1 Thermal Neutron Analysis (TNA)

TNA is based on detection of characteristic gamma-rays generated by ^{14} N nuclei on thermal neutrons capture. Common nitrogen based explosive materials

have nitrogen in a quantity ($\sim$ about 17-38 $\%$ by weight) [7, 37] much larger than in common benign materials [38]. The nitrogen signature is given by the detection of 10.83 MeV prompt γ-ray emitted in the de-excitation of the populated ^{15}N compound nucleus. The energy of this γ-ray is higher than other γ-rays produced in the neutron irradiation of common materials, so that it can be easily identified in the high energy region of the spectrum. The neutron sources used in a TNA system are either a radioactive isotope such as ^{252}Cf or by an electronic neutron generator.

TNA based systems are most suitable and applicable to explosive and drug detection in small packages and luggage. TNA is probably the simplest one among various neutron based techniques. In fact the TNA based Explosive Detection System inspected more than a million passenger bags at different airports [39]. However, TNA devices have limited capability to detect oxygen or carbon, this restriction results in the high rate of false alarms from nitrogen present in other benign materials such as urea, melamine. Also TNA systems are not suitable for large container inspection due to the fact that thermal neutrons do not have sufficient penetration to probe an entire container.

1.2.2 Fast Neutron Analysis (FNA)

FNA technique is an improvement over TNA using high energy neutrons. It exploits the inelastic scatter of fast neutrons with nitrogen, oxygen and carbon nuclei to detect their characteristic γ-rays. The neutron energy threshold for carbon (4.44 MeV γ-rays) is about 5 MeV and 7 MeV for oxygen (6.13, 3.84 MeV). Nitrogen can also produce high energy (1.63, 2.3 and 5.1 MeV) γ-rays as a result of inelastic scattering [40]. By comparing the relative numbers of detected characteristic γ-rays and if they are detected in ratios similar to conventional explosives, an alarm is raised to examine the package more thoroughly. The DTNG based 14.1 MeV neutrons are generally used [41] in FNA.

FNA provides the additional information about concentration of oxygen and carbon over TNA method, which can be used to eliminate some of the false alarms associated with TNA [42]. At the same time the high penetration power of fast neutron makes FNA useful tool for inspection of large container

without much attenuation in neutron flux.

Though the attenuation of the probing neutrons is improved in the FNA technique over TNA, the imaging capabilities such as obtaining spatial distribution are still very poor. Other major drawback to this method is the large background noise associated with FNA . One way to limit the background is to use pulsed beam of fast neutron and detect the gamma signals in synchronization or an alternative approach is the use of associated particle imaging, which is more advanced and sophisticated method with imaging capability (spatial distribution) of elemental distribution present in interrogated object.

1.2.3 Pulsed Fast Neutron Analysis (PFNA)

PFNA technique employs pulse fast neutron and nanosecond Time-of-Flight (TOF) technique to obtain the spatial distribution of the signal. The TOF is achieved by using very narrow, about 1 ns pulses of mono-energetic neutrons with a frequency of 5 to 10 MHz. The TOF technique can be used to determine the location of the detected material. The nature of the material is provided by gamma spectroscopy analysis. The main advantage of using PFNA is that it unambiguously determines the elemental composition of investigated volume and the spatial location of these elemental concentrations. The main challenges in developing PFNA into a practical system is the tedious process of constructing a practical, collimated, pulsed energetic neutron beam that makes the operation safe and operationally acceptable as well as cost effective [43]. This technology is still at research stage. Recently Brown et al[44] described a cargo inspection system based on PFNA.

1.2.4 Associated Particle Imaging (API)

API is based upon the physics and kinematics of fusion reaction ^{2}H(^{3}H,n)α in D-T neutron generator [45]. In the D-T reaction, deuterium and tritium collide to produce a neutron (14.1 MeV) and an associated alpha particle (3.5 MeV) [46] at $\sim$ 180 degree apart. Alpha particles can be detected with a position sensitive detector measuring their time of generation and emission direction

relative to the source. This in turn measures the emission time and direction of outgoing of the accompanying neutron, hence tag the outgoing neutron. This information is used to gate the gamma detectors to enhance the signal to background ratio and this can lead to a significant reduction in background signal (called as electronic collimation). Tagged neutrons on interaction with material under test produces γ-rays signatures unique to the elements present in the interrogated material. These γ-rays are detected in coincident within a short time after the alpha particle emission. The γ-ray's energy and their time of arrival (relative to the alphas emission time) is recorded along with the x and y coordinates of the alpha. The velocities of the 14.1 MeV neutron ($\sim$5.12 cm/ns) and the resulting γ-ray (30 cm/ns) are both known constants. So the arrival time of the gamma can be translated into the distance travelled by the neutron before interaction with the object material. This is therefore again a Time-of-Flight technique. As the neutrons direction is also known, 3D spatial information of targets can in principle be provided, without the need for scanning. The nature of the elements in the test volume being analysed is again provided by γ-ray spectroscopy.

At present, API is the advanced and most powerful neutron interrogation technique compared to the above mentioned techniques and it has been demonstrated mostly for threat material detection in different environments as discussed under literature survey.

1.2.5 Neutron Transmission/Fast Neutron Radiography (FNR)

Neutron interrogation techniques based on another approach of neutron in–neutron out have also been explored for material detection and imaging as briefly discussed in this section. Neutron out refers to either elastically scattered source neutrons or unattenuated transmission neutrons.

Neutron attenuation/transmission depends upon neutron energy and the materials they are passing through. The transmission data through a target (objects) reveals unique information about the elemental detail. Using a ^{252}Cf source, it is possible to search for nitrogen and oxygen in the target. As both of these elements have neutron absorption resonances and the energy spectrum

of the transmitted neutrons will show a decrease at these resonance energies compared to a sample that contained no nitrogen or hydrogen [47]. Also, looking at the ratio of fast neutron transmission to gamma ray transmission can help provide an idea as to the type of material in an inspected volume such as air cargo container [48]. This method allows the materials density determination as well as their class of composition (organic, glass, ceramic or metal). Recent advances in fast neutron radiography have shown promise [49–51]. By combining neutron and gamma ray transmission, fast neutron/gamma ray radiography can determine the average composition of an unknown target material. This can be accomplished either using separate compact D-D or D-T sources for the neutrons and a ^{60}Co source for gamma rays or a high energy accelerator [52]. Alternatively, a variable-energy, quasi-monoenergetic neutron source can be employed to interrogate the target through fast neutron resonance radiography and can differentiate the hydrogen, carbon, nitrogen, and oxygen present in the target. This requires relatively complicated accelerators and implementation [53].

1.3 Literature review

Extensive discussion and review of the individual problems addressed in this thesis is included in their respective chapters. However, for completeness, historical development and realization towards fast neutron based FNR and API techniques for imaging and detection of low Z elements as C, N and O is presented here.

Imaging with neutrons particularly using thermal (or epithermal) neutrons has been widely explored and successfully applied for numerous scientific and technical pursuits [54, 55]. In the early seventies, several experiments were performed to evaluate the usefulness of fast neutron imaging in nondestructive examination of bulky objects [56, 57]. The initial results were quite promising, but at that time it had the limited use because of two reasons, namely (a) unavailability of high intensity fast neutron sources and (b) lack of sensitive imaging systems for FNR, including digital recording & processing of images.

The potential effectiveness of this imaging technique depends on the development of high intensity fast neutron source and suitable imaging detectors. Over the years, with extensive research and development both these obstacles have been overcome to a great extent.

In the literature one can find the detailed information about electrostatic accelerators based NG capable of producing 10^{11}-10^{13} of 14 MeV/2.45 MeV neutrons per second [58, 59] and compact neutron sources of plasma-focus type, capable of producing over 10^{14} of 14 MeV neutrons per second [60, 61]. .

There has also been continuous progress in the research towards production of efficient scintillators and different types of fast neutron imaging detectors [62, 63] along with new methods of digital imaging and image processing. Several applications of fast neutron imaging have been investigated over the years. One of the important applications was for nuclear stockpile stewardship by Los Alamos Neutron Science Centre (LANSCE) and Ohio University Accelerator Laboratory (OHUL) of USA [64]. Various test samples such as step wedges fabricated from lead, Lucite, mock high explosive, aluminum, beryllium, graphite, brass, polyethylene, and stainless steel were imaged and it was shown to be a powerful imaging technique complementing x-rays for nuclear warhead and related. Imaging of fractured ceramic and polyethylene test object shielded by 2.54 centimeters of depleted uranium has been reported by this group to reveal the potential of FNR. The imaging detector was comprised of 2k$\times$2k cooled CCD camera system in combination with a plastic scintillator and a turning mirror. FNR has also been demonstrated to be of immense help for national security towards detection of heavily shielded explosives [65] or contraband [13]. The researcher's from Japan has explored the fast neutron imaging application for qualification of ageing based deterioration of the large-scale concrete structures [66, 67] successfully. Ageing and deteriorated social infrastructures including bridges, tunnels and elevated roads etc mostly made of concrete and steel are becoming increasingly serious problems throughout the world. It has also been used as a tool for imaging of thick cultural heritage objects complementing conventional X-ray techniques [68] or for industrial applications like looking into glued wooden boards [69].

Other than the accelerator based fast neutrons, there has been renewed interest in the use of reactor source for fast neutron imaging. A dedicated fast neutron imaging beam line NECTOR has been developed at FRM II research reactor [70]. Fast Neutron Radiography tests at the YAYOI reactor and at beam line on the 10 MW research reactor of the Budapest Neutron Center [71, 72] imaging have proved the reactor as potential source for fast neutron imaging. It was used non-intrusive, non-contact method for investigating industrial processes in heavy enclosures under potentially harsh conditions such as two-phase flows in nuclear fuel bundles [73–76].

Detection of fast neutron itself a challenging task. Lack of efficient fast neutron detector, offers relatively poor spatial resolution and also results usually in long exposure times to enable reasonable image quality. Furthermore, high detection efficiency is also desired and the development of efficient imaging screens for fast neutrons is of high importance. The increased interest in FNR prompted development of efficient fast neutron imaging detectors. The use of novel highly sensitive photo-luminescent imaging plates in combination with threshold activation detectors as converter screens in transfer imaging technique were proposed and used by various researchers such as Rant, Mikerov and co-workers [77–79]. In this direction, Seki et al.[66] has developed a pixel-type fast neutron scintillator detector with semiconductor photon sensor for transmission imaging of bulk and identified a steel bar, a void hole, and water with 300-mm-thick concrete blocks via a RIKEN Accelerator-driven compact Neutron Source (RANS) [80]. Makowska et al. (2017) [81] provided a detail overview of fast neutron imaging detector and scintillator developments while focusing on quantifying the performance of Polypropylene(PP)/ZnS type commercially available scintillator screens produced by RC Tritec AG [82]. On the other side, such promising applications of fast neutron imaging have opened the area of research in development of very high intensity fast neutron sources suitable to imaging. A high-brightness, quasi-monoenergetic neutron source of 10^{10-11} n/s/sr with energies set at 7 MeV or 10 MeV for fast neutron-based imaging has been developed at Lawrence Livermore National Laboratory [83].

On the other side, such promising applications of fast neutron imaging has opened the area of research in developement of very high intensity fast neutron sources suitable to imaging. A high-brightness, quasi-monoenergetic neutron source of 10^{10-11} n/s/sr with energies set at 7 MeV or 10 MeV for fast neutron-based imaging has been developed at [83] Lawrence Livermore National Laboratory (LLNL) is developed . This could provided fast neutron images of submm spatial resolution of good contrast images of low Z enclosed with thick layer of high Z with in exposure time of 10-15 minutes.

Transmission based FNR provides image of low Z materials when encapsulated by thick high Z materials or combination of high and low Z materials, the exact nature of the investigated low Z material remains unknown. FNR actually serves the first hand information regarding the investigated object's Z number range; low or high with respect to the shielding materials. The information regarding the exact nature of the object, that is, its chemical composition can be found out by nuclear imaging techniques which solely depends upon the detection of emitted gamma signatures by neutron interrogation. Among the various nuclear interrogation techniques discussed above API is one of the most important candidate. The idea is to use fast neutrons generated through D-T reaction to interact with object under investigation and detect the neutron induced γ-rays in coincidence of associated alpha particles. The analysis of the detected gamma signal provides the exact nature of the object and through α-γ coincidence time spectrum along with detected alpha particle, the location of the detected materials can be localized. This provides the so called 3D imaging of the object within a volume (detail at section 1.2.4).

The concept of coincidence measurement of D-T neutron and its associated alpha charged particle was purposed in 1969 Valkovic et al [45]. Using the concept of coincidence measurement of alpha and D-T neutron induced gamma, the API technique has been offered quite long ago [26, 46, 84]. However, the lack of advanced technology of neutron generators, fast response detectors and fast data acquisition prevented its widespread use. Early work on API in the 1990's were limited to nuclear and chemical treaty verification measurements [85, 86]. The major component of the API based study is D-T

neutron generator with built-in position-sensitive alpha detector which allows one to know precisely which area (or volume) is investigating and suppress the background clutter thereby enhancing the SNR. Reports from Argonne National Laboratory suggests research and development on the use of Associated Particle Neutron Generator technology for arms control treaty verification and non-proliferation applications. The initial results have indicated that this technology has significant potential for non-destructively detecting elemental compositions inside large volumes. Further, studies were carried out on improving the instrumentation towards improving the data quality [87–89]. It was focused mostly on performing inelastic-scatter prompt-gamma neutron activation analysis using API-NG for detecting and locating high explosives, narcotics and special nuclear material for hold-up assay applications [27].

Though various experiments were carried out with fixed type D-T neutron generators, the advancement of technology in developing small associated-particle detector embedded sealed-tube neutron generator has shown potential towards transferring this technique out of the laboratory for field applications. This lately opened up various novel applications of API in different environments ranging from buried landmine, unexploded ordnance (UXO) [90], cargo scanning SENNA [91], EURITRACK [92] and under water threat detection UNCOSS [93]. A proof of concept study was performed for non-destructive identification of unexploded ordnance using API concept by Sudeep Mitra et al [90] at Brookhaven National Laboratory, USA. The system consists of a portable NG with inbuilt ZnO(Ga) alpha detector and a 12.7 $\times$ 12.7 cm diameter NaI(Tl) detector. A large scanning system using 14 MeV tagged neutron was developed and its capability for landmine detection has been demonstrated at Italy [94] by Lunardon and co-workers. The focus was on the post-war demining activities in mine-affected countries. A concept of using an array of Parallel Plate Avalanche Counters for alpha detection and 10 BaF_2 scintillator detectors for coincident gamma-rays was purposed.

Applied Science & Technology Center, Russia [91] has developed a small portable device 'SENNA' capable of finding small amounts (as low as hundreds of grams) of explosives concealed among large amount of material within

a minute. SENNA uses a portable neutron generator developed by VNIIA, Moscow, Russia, with built in nine-segment semiconductor detector of associated α-particles and two BGO γ-rays detectors of dimensions 6.3 cm $\times$ 6.3 cm. Thus, API method has been rapidly progressing and investigated for a number of applications for more than four decades. In the last two decades, the focus on API was towards detection of explosives and illicit materials in cargo, parcels and airline baggages. API based EURITRACK inspection system is one of the most successful project undertaken for sea cargo inspection. It has been designed to perform non-destructive assay of suspect region inside cargo container identified by X-ray scanner operating in a seaport. It is a fixed type inspection system implemented at Croatian sea port [95]. In EURITRACK system, 8$\times$8 matrix of YAP(Ce) scintillators coupled with Hamamatsu H8500 multi-anode PMT designed for alpha particle detection and three separate detector arrays made of large volume NaI(Tl) scintillators are positioned around the container (top, transmission and reflection) to detect the γ-rays produced in fast neutron induced reaction [96]. The read-out and data processing of all detectors in time and energy measurements was performed with VME based front-end electronics using high density VME modules and cards [97] interfaced with a PC. This mehodology allows constructing a compact front-end with an option for ease of expansion in case of increase in the number of γ-ray detectors.

The application has been also extended for underwater threat detection. During wartime and the activities such as training and munitions testing, dumping and accidents, terrorist activities have generated significant munitions contamination in the coastal and inland waters. The most common military explosives are characterized by major C, N, O elemental signatures and their ratios. It makes API based system suitable for such threat materials detection. An underwater system 'UNCOSS' (UNderwater COastal Sea Surveyor) developed by scientists at a European Union research project aimed at improving security near Europes key maritime infrastructures and along sea routes [98–101]. Under this project a compact neutron sensor developed and tested with the most recent and performing detector technology as well as a new numerical

electronics, speed data acquisition and processing system specifically developed for UNCOSS. A dedicated Remotely Operated Vehicle has been entirely designed and manufactured to carry the neutron generator with gamma sensor onto the UXO (Unexploded Ordnance) of interest lying on the seafloor [98]. The UNCOSS underwater neutron inspection system was finally operated in a field demonstration in the vicinity of Punat Seaport, Krk Island, Croatia, showing its capability to distinguish explosive surrogates from sediments in metallic objects lying on the seafloor in 10 min measurements.

Other than threat material detection, the tagged neutron based API techniques has also been utilized for the search of diamonds by detection of excess carbon at a particular point of the kimberlite sample by Alexakhin and co-workers [102]. Large penetrability of fast neutrons makes it possible to examine appreciably large samples of kimberlite. Thus, rock pieces containing large-size diamonds can be identified before the crushing stage. API has also been utilized in the fundamental and applied research of fast neutron induced nuclear reactions [103]. A feasibility study of in vivo 14MeV neutron activation analysis with API methodology performed by R. Garrett and S. Mitra [104] has proved the potential of API for measuring the body composition of humans or farm animals in vivo. S. Mitra et al [105] [106] has investigated the whole body measurement of C, N and O and based on the results obtained from irradiating a 41.4 kg meat phantom, it was suggested that an API instrument comprising of a small NG and four Nal(Tl) gamma ray detectors of 15 cm $\times$ 15 cm $\times$ 45 cm can be assembled to determine in vivo protein, fat and water with precisions of 4.1, 5.4 and 1.2%, respectively, within a 15 min scan. The radiation dose ($\sim$0.03 mSv) would be almost one-tenth of the dose from existing facilities.

The combinational use of FNR and API based fast neutron technique in providing first-hand and conclusive information regarding the suspected objects is no doubt the best that can be achieved for research, non-destructive testing, security and strategic applications.

1.4 Scope of thesis work

The thesis work has focussed on novel approach of FNR and API neutron interrogation techniques for detection and imaging of low Z materials (composed of C,H,N,O) in bulk through use of a D-T neutron generator.

Under the scope of thesis work, study and implementation of FNR and API neutron imaging techniques and system development with indigenously developed D-D/D-T neutron generator at BARC was performed. At first simulation approach was adopted in order to reduce the experimental efforts needed in developing experimental complex system. FNR was modelled with 14.1 MeV neutron using GEANT4 [107, 108] and different samples ranging from low Z, metallic and high Z materials were simulated for their radiographic images.It has provided insight deep understanding of the potentials and limitations of the FNR especially for imaging of composite structure made up of both low and high Z materials. Next to implement the FNR and to image the large robust sample containing mixed low-Z/high-Z materials, an experimental FNR set-up was designed and coupled with D-T neutron generator of $\sim 2{\times}10^9$ n/s strength. Imaging with such moderate source intensity was an challenge. The reasonable contrast images of various test specimens have proven the high transmission of FNR through thick and high density objects and has demonstrated the capability of the FNR system for imaging of robust sample. Detail description of D-T NG and fast neutron imaging work has been provided in the Chapter 2 and the Chapter 3 respectively.

Eventhough FNR has shown a promising result for imaging of large and complex sample but has lack of elemental informations. For elemental detection, feasibility study of PGNAA was performed with conventional techniques TNA and FNA, a wide range of light elements (C, H, O, N, Cl, Fe) were detected using D-D/D-T NG as described in Chapter 4. The SNR obtained was quite low and to improve it, tagged neutron based API technique was investigated. To facilitate the design and construction of a prototype API based system, the technique was simulated in Geant4. This has provided the groundwork for analysis of gamma-ray spectra utilizing detectors elemental

responses measured with tagged (14.1 MeV) neutron for material identification and image reconstruction of objects location under inspection. It is presented in Chapter 5. Further work was extended by implementing the API technique and system development. It was realised with a laboratory based inhouse developed D-T NG and a system was designed, characterised and experiments were performed. The laboratory experiments have been successfully performed to demonstrate the efficacy of the API system for C,N,O elemental analysis of pure and complex sample (benign and explosive simulants) spectra with improved SNR as reported inChapter 6. While this work is not intended to demonstrate actual cargo scanning, we show a proof-of-concept of imaging and elemental characterization using inhouse developed D-T NG, a novel system which is promising for development into a fully engineered scanning system for field deployment.

1.5 Outline of the Thesis

Chapter II, describes the characterisation of D-D/D-T NG. It presents the neutron source strength measurement with foil activation and neutron detection devices developed for real time D-D/D-T neutron monitoring. This includes APT based neutron monitor, fiber based miniature neutron detectors and characterisation of a liquid scintillator detector for fast neutron spectrum measurement.

Chapter III, presents the simulation and experimental study of FNR carried out using DT neutron. Various configurations modelled to image low to high Z material and experimental study performed and demonstrated for imaging of low Z material, masked with thick and high Z material are described.

Chapter IV, describes the experimental feasibility study of PGNAA for elemental detection in bulk. TNA and FNA methods were implemented to investigate a wide range of elemental signatures (H, N, Cl, C, N and Fe) in bulk from benign materials.

Chapter V, describe the modelling of API technique incorporating physical response of BGO detector. It includes study of pure elemental response spec-

tra, complex sample spectra analysis, 3D image reconstruction of the interrogated object and methodology of material identification (benign or threat).

Chapter VI, describes the implementation and realisation of API with in-house developed laboratory based DTNG. It includes API based experimental system development, optimization and characterisation of the system's parameters and various experiments performed with benign and explosive simulants. The major components of the systems discussed are 64 pixel YAP:Ce alpha detector, BGO gamma detector, VME based Front-End-Electronics and software tools developed for data acquisition and analysis. The comparison with simulated results of few samples are also presented.

The thesis is concluded in chapter VII. Main conclusions of the thesis are summarized here and a discussion on future work is given.

CHAPTER 2

Characterization of D-D/D-T Neutron Generator

The neutron source is an important part of the thesis work and the detail knowledge of neutron source parameters such as source strength, stability and dose are necessary for study of imaging techniques and optimised design of FNR/API based experimental system. This chapter describes the high yield D-D/D-T Neutron Generator used for the thesis work, its source strength characterization and the detection tools developed for real time neutron (D-D/D-T) emission rate measurement. The standard foil activation method was used for absolute neutron yield measurement of NG. Two different detectors were developed to monitor neutron yield in real time (1) silicon based charged particle detector and (2) optical fiber based miniature neutron detector. These tools were used as monitoring device throughout the thesis work. In addition to that it also presents, characterisation of a liquid scintillator detector with the purpose of fast neutron spectrum measurement around NG for future work.

2.1 Neutron Generator

As a part of this research work, a series of experiments were planned for detection and imaging of materials in bulk using Neutron Generator. An Open-End Accelerator based fixed type NG's found to be more suitable then compact sealed tube NG for this. Fixed type NG can provides high neutron yield with target replacement option and target can be tritium or deuterium as per requirement. However these NG occupies larger footprint then compact sealed NG. Commercially available compact neutron generators would be preferred for field deployable system, which in general is second stage after benchmarking of the developed system's performance at Laboratory scale. A laboratory

based fixed type D-D/D-T Neutron Generator, BARC was used [20] [21]for the thesis work. Details of the NG has been provided at introduction Chapter under the section 1.1.5. It is housed inside Purnima Hall of dimension 7.5 m$\times$7.5 m$\times$ 7.5 m and concrete wall thickness of 30 cm on three sides. The concrete wall between accelerator hall and control room is 1.5 meter. This facility has been made full fledged operational during 2010-2011 and being utilized for various departmental projects. Though NG have advanced features of pulsed mode operation, however we have used only countinuous mode of operation. In countinuous mode it can produce 14.1 MeV neutrons with tritium target (DT Mode) or 2.45 MeV neutrons with Deuterium target (DD Mode) [Eq. 2.1-2.2].

$$^{3}H +^{2} H =^{4} He +^{1} n, Q = 17.6MeV, En = 14.1MeV \tag{2.1}$$

$$^{2}H +^{2} H =^{3} He +^{1} n, Q = 3.3MeV, En = 2.45MeV \tag{2.2}$$

Neutron source strength (or say Neutron emission rate), of NG is a crucial parameter for any experiment and an important parameter for characterization of neutron generators and experimental data analysis. Thus before using this Neutron Generator for experimental study of FNR or PGNAA, we have focused on its neutron source strength measurement. Detection of fast neutron is comparatively difficult in comparison to that of thermal neutron detection. Different methods were employed for fast ($\sim$ MeV) neutron measurement in offline as well in real time neutron monitoring with the assumption of isotropic and monoenergetic neutron source.

2.2 Neutron emission rate: Offline Measurement

At first offline neutron yield measurements with standard foil activation technique [15, 109, 110] has been performed. The principle of neutron activation technique is provided at Appendix A. Procedure followed in this method is straightforward [15]: a foil is irradiated with neutron source for a pre-defined time followed by measurement of neutron induced γ-ray activities by means of a suitable detector such as HPGe or NaI(TI). The activation foil material should

possess certain properties: a suitable half-life, an energy threshold, easily detectable activation products and usable cross section for the selected reaction. The advantage of this method is of small size foil, insensitive to gamma radiation, low cost and free from radiation damage problems.

2.2.1 D-T neutron yield measurement

Copper (Cu), Aluminum (Al) and Fluorine (F) materials were selected to measure the DT neutron yield. The reactions chosen were ^{27}Al(n,p)^{27}Mg, ^{63}Cu(n, 2n)^{62}Cu and ^{19}F(n,2n)^{18} F because of their higher threshold energies (3.25 MeV, 11.03 MeV and 12 MeV respectively), well known measured cross section [111] and half-life of reaction products is in order of few minutes. Standard foils of Al (dia = 5 mm, thick=1-1.5 mm), Cu (dia=15 mm, thick = 0.5-0.8 mm) and Teflon (dia=5 mm, thick=1-2 mm) were used for yield measurement and four sets of experiments were carried out. Two sets were carried out using Al, Cu and Teflon foils and rest two were carried out using only Al and Cu foils. The foils were placed parallel to each other. One of the foil set was placed at a distance (x) of 15 cm from target at 0 degree angle with respect to D^+ beam direction. The foils were irradiated and induced activity was measured using a calibrated p-type HPGe gamma spectrometry system (Appendix A). The neutron flux (n cm^{-2} sec^{-1}) was calculated using equation (2.3).

$$\Phi = \frac{C_p A \lambda}{N_A m \sigma a_i I_\gamma \eta \Omega (1 - e^{-\lambda t_1}) e^{-\lambda t_2} (1 - e^{-\lambda t_3})} \tag{2.3}$$

Where, Φ=neutron flux (n sec^{-1}cm^{-2}), λ decay constant(sec^{-1}), A(gm) the atomic mass number, C_p the net counts (area) under photo peak of characteristic gamma lines at 843.7 keV, 511 keV and 511 keV of Al, Cu and F respectively, (where 511 keV is coming from positron annihilation in the β^+ decay of ^{62}Cu and ^{18}F and 843.7 keV is coming from the de-exitation of an excited states of ^{27}Al populated after β^- decay of ^{27}Mg), N_a is avogadro number [112], m(gm) the mass of foil, a_i the isotopic abundance, η the photo-peak efficiency, I_y gamma abundance, σ the reaction cross section, t_1, t_2 and t_3 are irradiation, cooling and counting time respectively. Assuming uniform emission of neutrons in 4pi from a point

Table 2.1: Experimental Parameters for DT neutron flux measurement

Exp	HV	I	t1	x
Set	(kV)	(uA)	(min)	(cm)
Set1	182	120	10	15
Set2	100	104	12	15
Set3	81.5	95	15	15
Set4	60	71	25	15

Table 2.2: Experimentally measured DT neutron Source strength

Exp Set	Source strength measured with foil activation (n sec^{-1})			Neutron Dose
No	$^{27}Al(n,p)^{27}Mg$	$^{63}Cu(n,2n)^{62}Cu$	$^{19}F(n,2n)^{18}F$	(mSv/hr)
1	$1.2(\pm0.06)\times10^{10}$	$1.1(\pm0.04)\times10^{10}$	$1.08(\pm0.06)\times10^{10}$	44±1.8
2	$2.84(\pm0.20)\times10^{9}$	$2.87(\pm0.13)\times10^{9}$	-	12.54±0.77
3	$1.05(\pm0.09)\times10^{9}$	$1.0(\pm0.06)\times10^{9}$	$1.06(\pm0.08)\times10^{9}$	4.25±0.36
4	$4.0(\pm0.39)\times10^{8}$	$4.8(\pm0.37)\times10^{8}$	-	2.05±0.2

source the neutron emission rate (n sec^{-1}) was evaluated from flux (ϕ) via multiplying it with 4pix^2. The experiment was repeated with remaining three sets of foil at different accelerating HV and D^+ion current operating parameters of NG to measure maximum yield. The experimental parameters are listed in table (2.1) and respective measured neutron emission rate of DT neutron are summarized in table (2.2). The maximum measured neutron yield was $\sim 1\times10^{10}$ n/sec.

Neutron dose data are also very important in view of shielding requirement and precautions to prevent personnel radiation exposure. The time integrated neutron dose was measured for each experimental set, using BF_3 Neutron rem monitor (model No BDKN-03, ATOMTEX) [113] placed below the neutron target at 80 cm distance ($\sim$ at angle of 90 degree with respect to target position). The recorded neutron dose rates at different neutron yield are given in last column of Table (2.2) with measurement (statistical) uncertainty.

2.2.2 D-D neutron yield measurement

For D-D neutron emission rate measurement tritium target was replaced with deuterium target and activation method was used similar way as explained

above. The activation was carried out with indium foil using the reaction ^{115}In(n,n')^{115m}In. This reaction has a threshold energy of 0.33 MeV, cross section 0.33 barn, half-life of induced activity 4.49h, isotopic abundance of ^{115}In in natural indium(95.7%) and characteristic gamma ray(336 keV). D-D neutron yield measured was $\sim$ 3x10^7.

2.3 Real Time D-D/D-T neutron monitoring

In accelerator based neutron generator the neutron emission rate is critically dependent on its operating parameters mainly on accelerating voltage, D^+ beam current, focusing voltage and target (tritium or deuterium) strength condition which tends to produce considerable drift in output neutron emission rate during operation. Though the foil activation method is the standard primary method for absolute flux measurement, it is an offline technique, time consuming and provides average flux over the exposure time. Thus any change in neutron emission rate with time during experiments cannot be recorded using this method. Hence a real time neutron (D-D/D-T) monitor is necessary.

The conventionally used neutron detectors for high energy neutron ($\sim$ MeV) detection are proton recoil based detectors such as plastic or liquid scintillator. These detectors are sensitive to gamma as well as their output gets affected from scattered neutrons. For these reasons the detector outputs are error prone and depend upon the surrounding materials around the NG. To overcome these problems we have used two different methods (1) An indirect way of D-D/D-T neutron monitoring using associated particle based neutron detector(APND) and (2) an optical fiber based miniature neutron detectors.

2.3.1 Associated Particle based Neutron Detector

It is based on detection of charged particle associated with D-D/D-T neutron emission in NG. The neutron output of NG is determined by collecting the charge particle associated with neutrons emission [Eq. 2.1-2.2] in a small solid angle. The neutron monitor based on associate particle technique was devel-

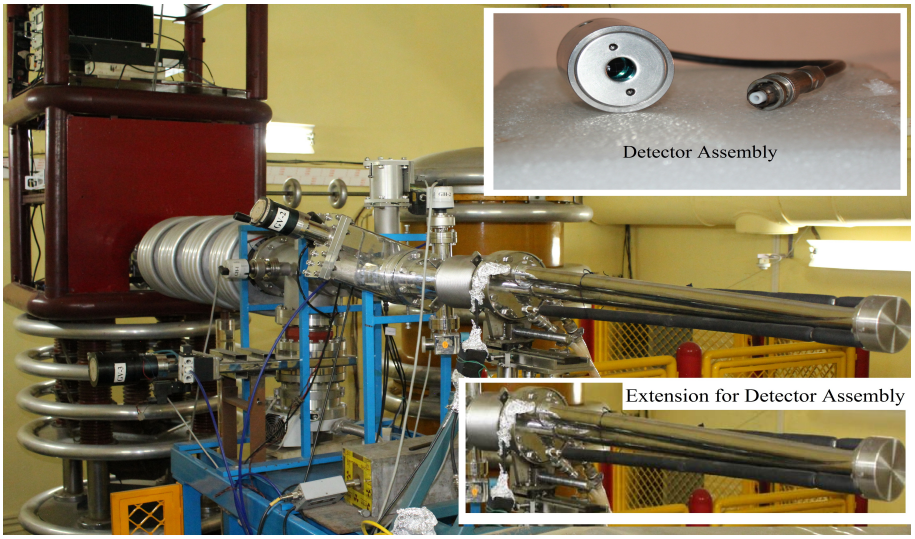

Figure 2.1: (a)NG with extension of associated particle based neutron detector, (insight) Detector assembly placed inside NG

oped using a passivated ion implanted planar silicon detector of 10×10 mm^2 active area and 300 μm depletion width. Silicon detector mounted on printed circuit board (PCB) and fixed inside a stainless steel (SS) cylindrical collimator of 10 mm diameter. This was further reduced to 5 mm diameter by placing an additional aperture in front of the detector. It was covered with a 0.5 μm mylar foil in order to stop the backscattered deuterons. The detector assembly was installed inside the NG's tube on a movable holder as shown in Figure 2.1. In this configuration the detector was nearly at 4 degree w.r.t d+ beam direction.

The detector was biased at +25 Volt and the output signal was processed using a charge-sensitive preamplifier, shaping amplifier and MCA or Counter. The pulse height spectra of charged particles asscociated with D-T/D-D neutron emission recorded on MCA (4k) is shown in figure(2.2 and 2.4). In D-T reaction, alpha charge particle were counted and the accumulated alpha counts during the irradiation period were normalized with time and solid angle, then integrated over 4pi to determine the total neutron yield. On the other hand in case of D-D mode there are two reaction channel takes place within the deuterium target with equal probability:

D + D = ^{3}H (1.01 MeV) + p (3.02 MeV) ———- (2a)

D + D = ^{3}He (0.82 MeV) + n (2.45 MeV) ———- (2b)

The spectrum of charged particles from both reactions (2) are collected and the

peak area under ^{3}He or proton peak is measured for D-D neutron yield [1].

2.3.1.1 Performance of APND

Detector performance was tested with D-T mode and initially the detector was placed at a distance of 16 cm from the target to acquire alpha particle spectrum at different D-T neutron yields. The dead time observed at MCA was nearly 50% to 70% due to high count rate with increase of neutron yield from 10^8 to 10^{10}. For minimization of detector dead time, the detector was moved away from target to a distance of 30 cm and 69 cm. The 69 cm distance was optimised, where monitor has measured sufficient counts for neutron yield of 5x10^8 to 10^{10} and dead time reduced to 10-16%. The spectra acquired at the distances of 16 cm, 30 cm and 69 cm are shown in figure 2.2 for neutron yield of $\sim 10^9$. The alpha particle peak is clearly observed (at 750 channel) far from low noise signals. The total counts collected under alpha peak was calibrated with the known neutron yield measured via Cu foil activation (sec2.2) at the same time. The plot of count rate versus neutron strength is shown in figure 2.3, where the linear response of the detector can be observed with increasing neutron source strength 5 $\times 10^8$ –10^{10}. Hence the system can be used as online neutron monitor for this range. For the case of D-D mode, the measured yield was nearly three order less then that of D-T, thus the detector system was moved near the target (deuterium) at 21 cm. The spectra acquired at D-D neutron yield of 10^6 and at 10^7 are shown in figure (2.4). The three peaks corresponds to three charge particles ^{3}He (= 0.82 MeV), ^{3}H (=1.01 MeV) and p (=3.02 MeV) are well resolved and distinguishable. Hence the system can be used for online D-D neutron monitoring and it was calibrated for D-D neutron yield of 3×10^7 n/sec. The ^{3}He based counting system has the possibility of error due to closely lying noise signals and nearby triton peak. In such cases, the proton which has a well defined clean peak due to its high energy of $\sim$3 MeV, can be used as an alternative for D-D neutron yield measurement [114].

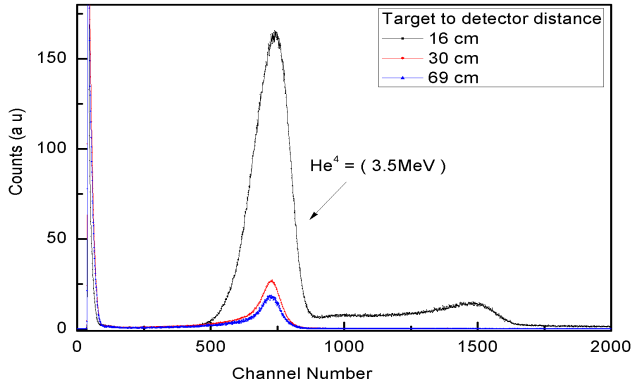

Figure 2.2: Spectrum of charge particles in D-T mode

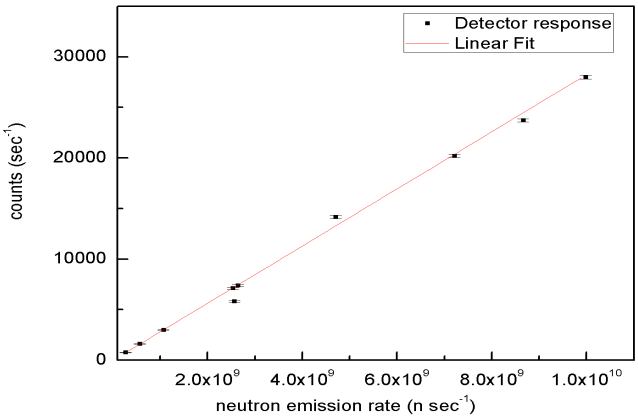

Figure 2.3: Plot of counts versus D-T neutron yield.

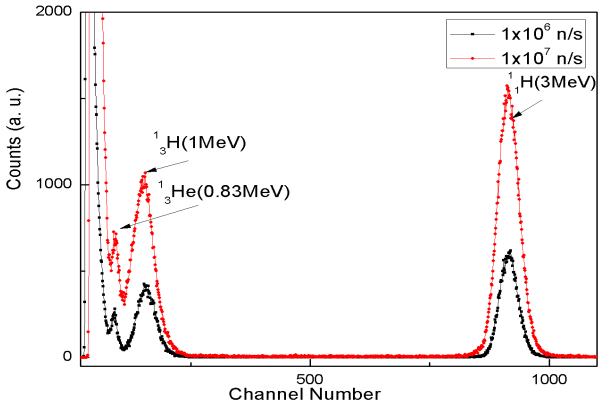

Figure 2.4: Spectrum of charge particles in D-D mode

2.3.2 Fiber based miniature neutron detector

The APND has shown promising performance for real time neutron yield measurement of NG and was used as neutron monitor for PGNAA experiments [Ch4]. However, semiconductor based APND is susceptible to the radiation hardness, particularly with exposure to high energy DT neutrons. Hence, over the years there has been degradation in the detector performance and we have to replace it with fresh one. In this respect we have looked for another possibility to have scinitillator based detector for real time DT neutron monitoring.

2.3.2.1 Detector design

As mentioned above (section 2.3) the scintillator based detectors are sensitive to the gamma radiation, thus to minimize the gamma sensitivity, dimension of the detector was decided to be as small as possible. Keeping this in mind we have developed a miniature size ($\sim$ mm) fiber based detector .This detector utilizes fast neutron converter-scintillator (ThO_2 :ZnS(Ag)) coupled to the tip of a plastic optical fiber at one end with the other end coupled to a photomultiplier tube. The neutron (D-T) interaction with neutron converter (^{232}Th) nuclei produces charged particle which interacts with scintillator (ZnS(Ag)), resulting in visible light. This light is guided to PMT through the long optical fiber and corresponding electronic signals generated are processed with associated electronics such as amplifier, discriminator and counter.

Developing this type of fast neutron detector (FND) is a challenging task, because the interaction probability (n,f) of D-T neutron with ^{232}Th, ($\sim$ 0.350 barn) is very low and smaller size of the detector would further reduce its sensitivity. Thus, to have confidence in developing such detectors for fast neutron, we have first developed a thermal neutron detector (TND) using Li_6F converter materials mixed with (ZnS(Ag)). It has high thermal neutron cross section of $\sim$ 940 barn (^{6}Li(n,α)) [15], which ensures high probability of successfull development of miniature detectors.

The TND detector was designed by depositing a uniform layer of Li_6F+ZnS material (thickness$\backsim$ 300um) on an aluminum disk of 3 mm diameter and 1

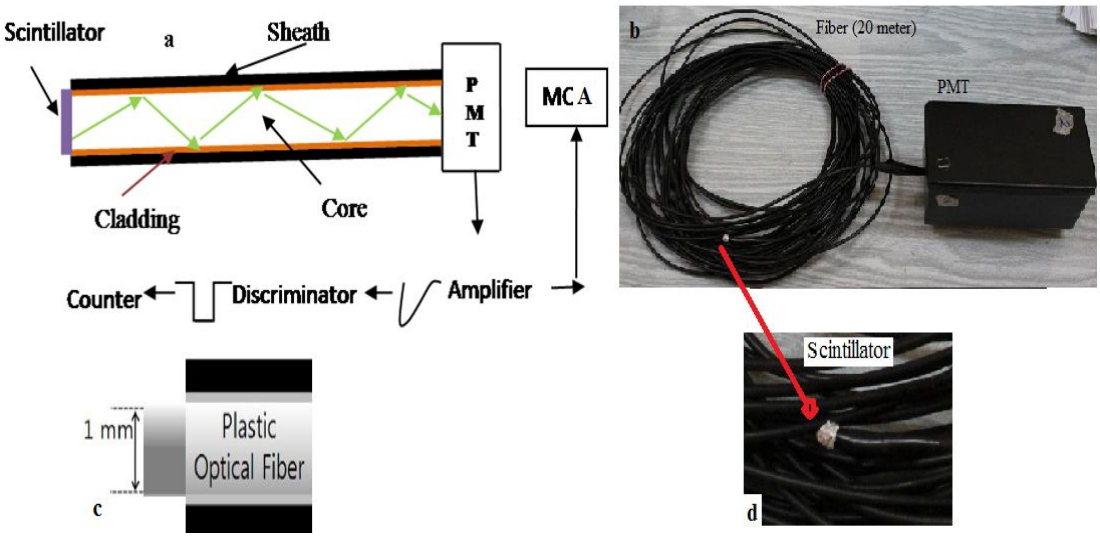

Figure 2.5: (a) Schematic of fiber based detector and allied electronics (b) Photograph of the detector assembly (c,d) Zoom view of scintillator tip

mm thick. The neutron converter and scintillator material was mixed in equal proportions. This disk was carefully glued on the tip of a plastic optical (1mm) fiber using optical glue. The other end of the fiber (20 meter long) was coupled to a low noise PMT. A thin aluminum cap was placed over scintillator for light shielding and reflection. FND was developed with same methodology with ThO_2:ZnS(Ag) in place of Li_6F:ZnS(Ag). Figure (2.5) shows the schematic and photograph of the detector.

Sensitivity Measurement of TND

For thermal neutron sensitivity measurement of TND, a thermal neutron assembly was set up using HDPE surrounded by graphite on all sides. Pu-Be (500mCi) neutron source was placed at the centre of the assembly. The radiation shielding of assembly was provided using borated polyethylene and cadmium. Measurement of thermal neutron flux at the center of the assembly was carried out using the gold (Au) foil activation method [12]. The signal counts were also recorded by placing the tip of the TND at the same location as the foil. A typical neutron signal observed on an oscilloscope is shown in Figure (2.6). The sensitivity was calculated taking the ratio of detector count rate (cps) to the measured flux (n cm^{-2} sec^{-1}) via activation method. It was

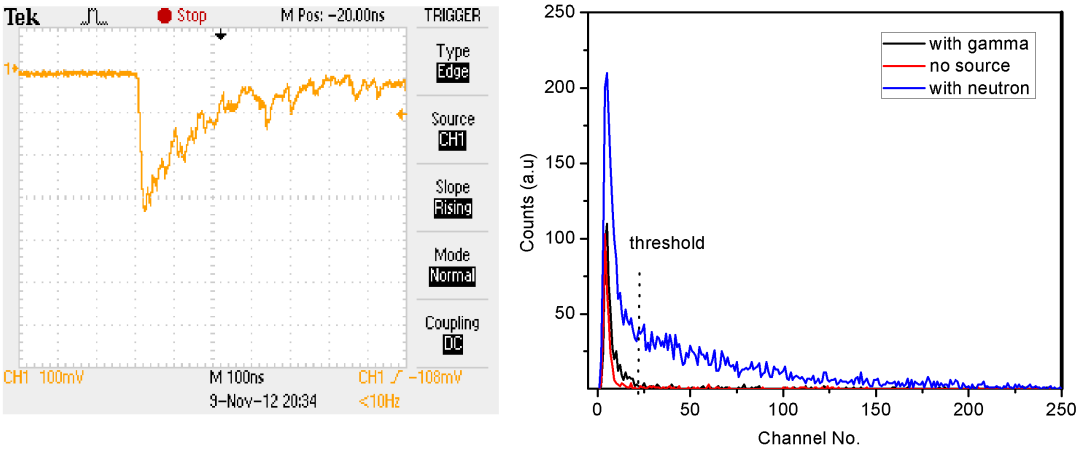

Figure 2.6: (Left)Neutron signal of TND observed on an oscilloscope (right)Pulse height spectra of gamma(black), neutron(blue) and background (black) with TND

found to be 3×10^{-4}cps per unit neutron flux. Unit neutron flux corresponds to neutron field of one neutron per unit area per second. The gamma sensitivity of TND was tested using a 33 mCi gamma source of ^{137}Cs kept at $\sim$1 cm from the tip. The count rate observed was nearly background (3-5 cps) level indicating very low gamma sensitivity which is due to the small thickness ($\sim$300μm) of the detector.

2.3.2.2 Performance of TND

The performance of the TND was investigated with an experimental subcritical reactor system [115]. This system has experimental channels ($\sim$ 7-10 mm size) in radial direction (perpendicular to the fuel rod length) and axial direction (parallel to fuel rod length). The detail about the subcritical reactor system can be found at reference [116]. TND was used for thermal neutron flux profile measurement in radial and axial directions in the subcritical assembly.

Radial profile measurement

A thermal neutron distribution profile in radial direction was measured in one of the radial experimental channel (EC6). Thermal neutron fluxes were measured at every 1 cm to match the pitch (48 mm) of fuel rod inside the assembly. The experimental data were plotted against scanned positions as shown in Figure (2.7). From the result, it was observed that variation in flux at different

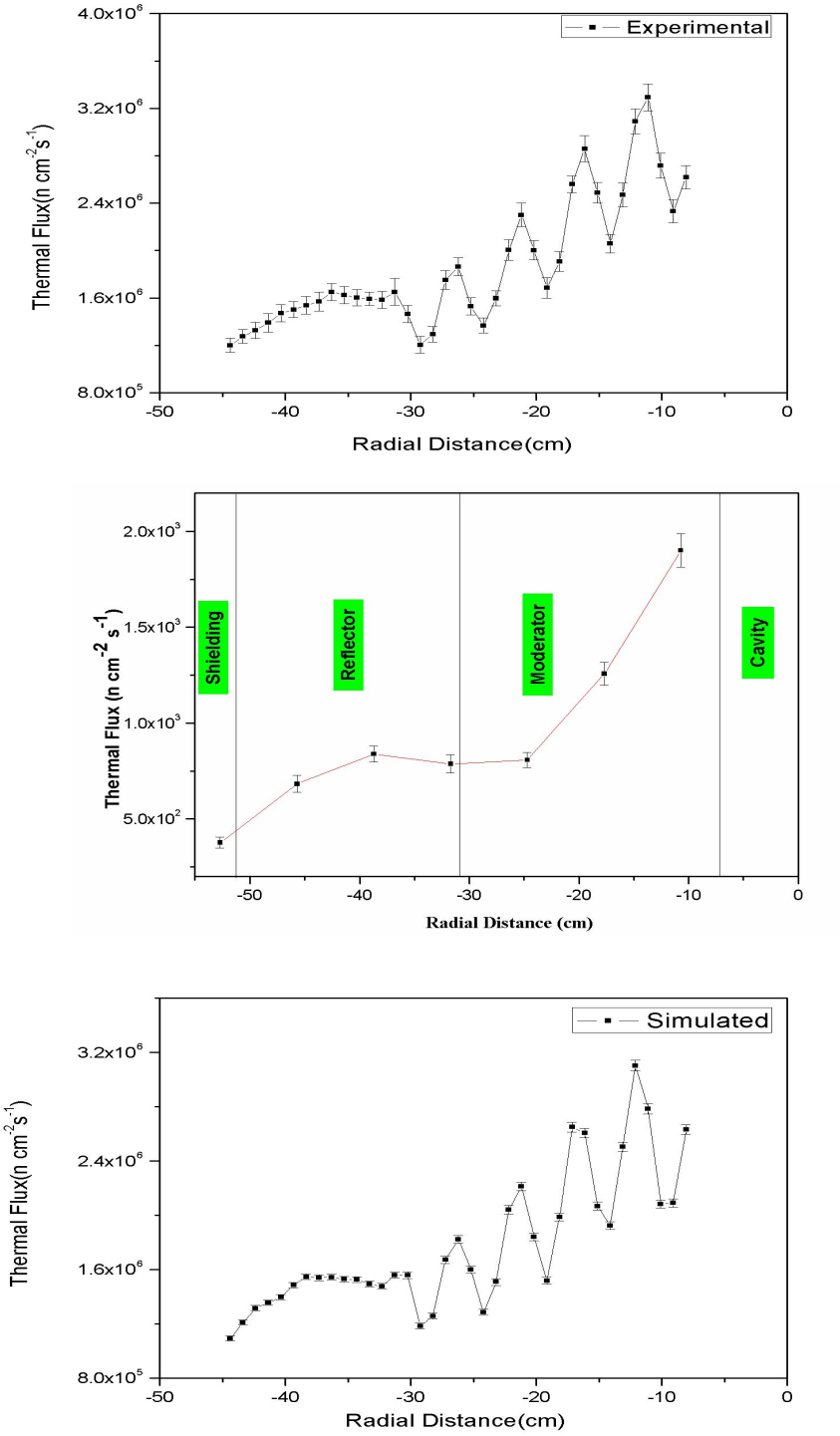

Figure 2.7: Radial thermal neutron flux distribution profile in subcritical assembly measured with (top) TND (middle) ^{3}He detector (taken from [117]) (bottom) Simulated.

scanned position follows the periodic fuel lattice distribution. Also the peak intensity decreases as we go away from the neutron source cavity as expected. The results were compared with previously measured ^{3}He results (taken from [117]) as shown in Figure (2.7) (middle). Such variation of the flux at fuel pin position in radial direction could not be observed with the ^{3}He detector, because of its larger active length (70 mm). Further, the results were also reconfirmed with simulated data as shown in Figure (2.7). Such observations were possible only because of miniature size of developed TND thus providing high spatial resolution.

Axial profile measurement

In similar fashion, a thermal neutron flux distribution profiling across the axial direction was measured. The whole length along the axial direction was scanned every 5 cm. The experimental data were plotted against scanned positions as shown in Figure (2.8). The results were compared with results of previously measured data using a ^{3}He detector. It was observed that axial profiles from both the detectors were of similar nature and the peak position of flux was at the center of the assembly. Peak flux at the center was expected due to the fact that source neutrons (D-T/D-D) were emitted in the middle of the cavity which was along the central axis of the assembly. The flux range across the axial/radial position measured was (0.1 - 2)$\times 10^6$n/cm^2/sec.

In the above flux profile measurement the observation for each data position was carried out ten times and averaged over it. The estimated error bars in the data was around 3.5%.

The difference in the absolute value of flux measured with two different detectors (Figure (2.7-2.8) is because, the thermal flux inside assembly was reduced from high to low range ($\sim$ two orders less) for measurement with ^{3}He by operating DTNG at lower source strength. Since the ^{3}He detector used was of higher sensitivity, suitable for flux range of 4×10^2-4×10^5 n cm^{-2}sec^{-1} (see the reference [117]) and only relative shape of flux profile was compared not the absolute flux itself for TND performance.

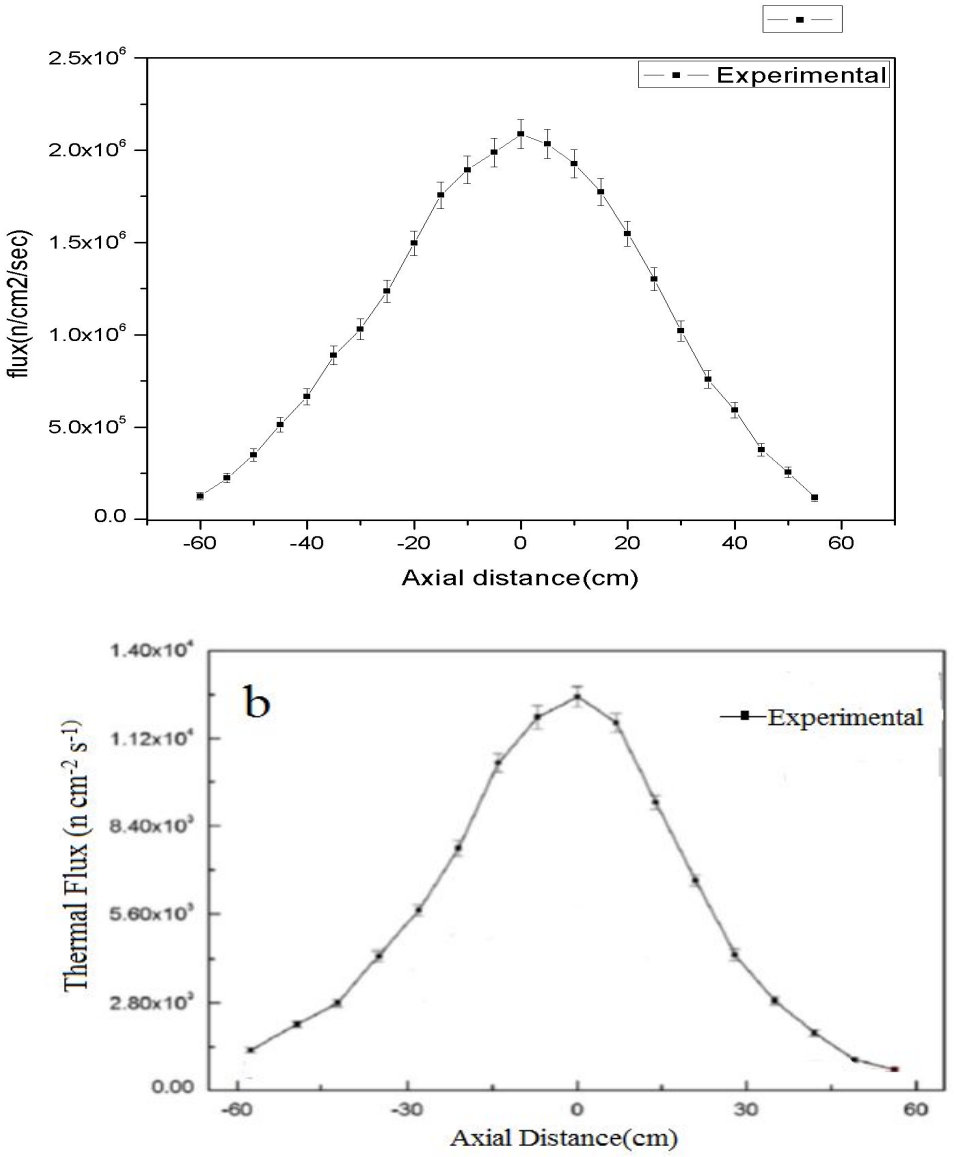

Figure 2.8: Axial thermal neutron flux distribution profile in subcritical assembly measured with (top) TND (bottom) ^{3}He detector (taken from [117]).

2.3.2.3 Performance of Fast Neutron Detector (FND)

Sensitivity Measurement of FND

Sensitivity of the FND for fast neutron was tested in neutron field of D-T neutron generator. The neutron sensitivity of FND in fast neutron (D-T) range was expected to be much smaller than TND in the thermal range. That is due to low fission cross-section [^{232}Th (n, f)] at high energy (14MeV) neutron. Thus, DT neutron flux measurements were restricted in location near the target of DT NG, where the fast flux is higher and significant statistical counts could be obtained. This fast flux measurement was carried out with 10^{10} n sec^{-1} D-T neutron yield, which was calibrated with foil activation technique using the reaction ^{63}Cu (n,2n) ^{62}Cu for the absolute value calculation of fast neutron flux. The detection sensitivity of the detector was found to be 3.6×10^{-6} cps per unit neutron flux of D-T neutrons. The gamma sensitivity of this detector was also tested in a similar method as done for TND and its gamma sensitivity was found to be almost negligible. The count rate observed was nearly same as background (8-10 cps) level indicating very low gamma sensitivity which is due to the small thickness of the detector.

D-T neutron distribution profile measurement

The distribution of fast neutrons (14 MeV) across the source target of the D-T neutron generator was measured using FND. The scanned step size was about 2 cm. The measured fast neutron distribution profile is shown in Figure (2.9)(a). As expected, the measured maximum flux is at the target location and it decreases as we move away from the target. In order to use FND for pulsed neutron application its response was also observed with the neutron beam in ON /OFF condition. Figure (2.9)(b) shows the FND response with respect to neutron beam ON/OFF condition. This detector has been used for online monitoring of neutron source yield of the D-T neutron generator for neutron yield more then 10^{9}n sec^{-1}.

Despite of its low sensitivity, FND was of importance for real time monitoring of DT neutron particularly for FNR experiments, which was executed with

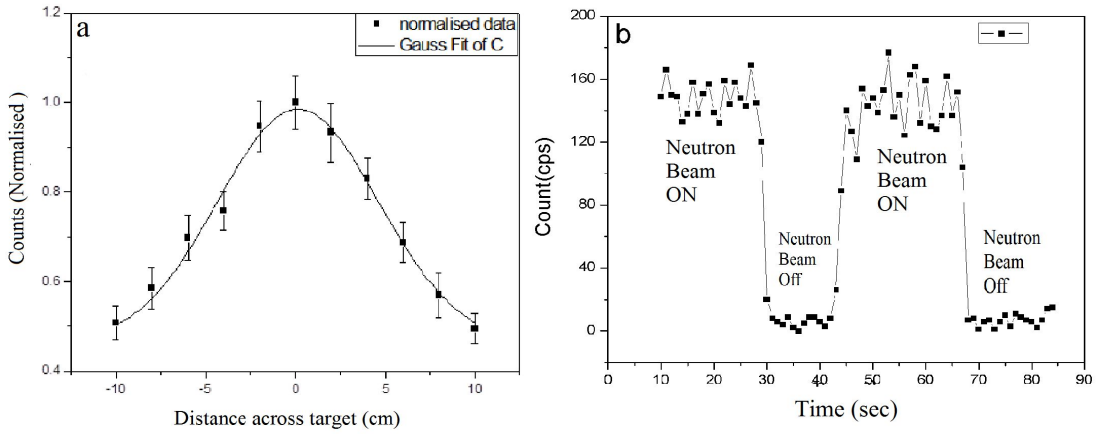

Figure 2.9: (a) Neutron distribution profile across DT target measured using FND and (b) FND response for DT neutron beam ON and OFF conditions.

DTNG at neutron yield of $\sim$ 2x10^9 n sec^{-1}.

2.4 Fast neutron Spectrum Measurement

During the experimental study of API and FNR, it was realized that the gamma detectors (in case of API) and CCD camera (in case of FNR) get exposure to unwanted scattered neutrons causing radiation damage to these as well as an increase in noise in the data and image. To protect them from scattered neutrons, they need to be shielded. The knowledge of scattered neutron energy spectrum at the detector/camera position is important for the design of an effective and compact shielding structure. Organic liquid scintillator based neutron detector has been proven to be one of the most suitable choices for this application and we have employed a liquid scintillator detector for this purpose because of their fast time response, high detection efficiency and excellent neutron-gamma discrimination.

At first it was characterized and the response of a 5″ x 5″ (EJ-301) detector has been investigated using ^{137}Cs, ^{22}Na gamma sources as well as 2.45 MeV and 14.1 MeV mono energetic neutron sources. The Monte-Carlo simulations using GEANT4 have been carried out to fit the experimental pulse-height distributions for all the cases to obtain the light output function. Using the extracted light output function, the neutron detection efficiencies were deter-

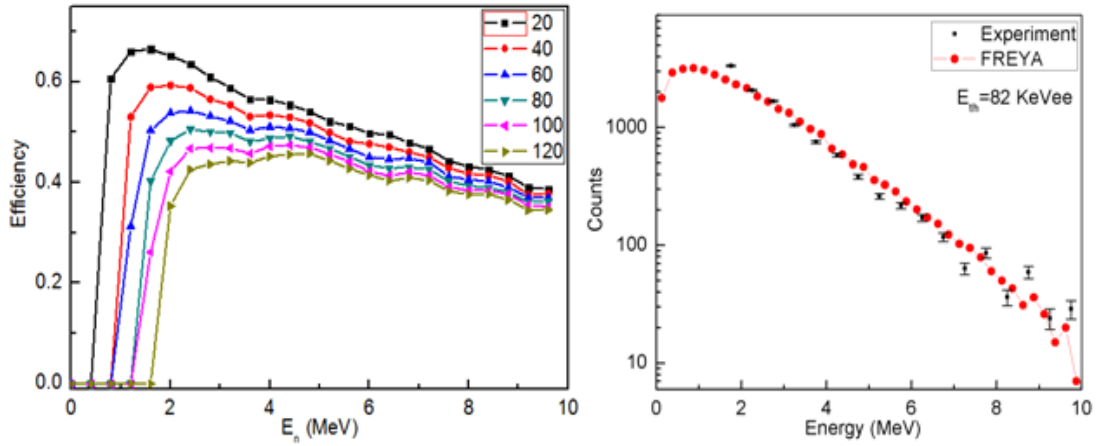

Figure 2.10: Geant4 simulated efficiency curve at different energy threshold (keVee- electron energy equivalent) (right) Comparison of efficiency corrected measured (black) and theoretical (red) neutron spectra of ^{252}Cf.

mined at different thresholds as shown in Figure 2.10. The evaluated efficiency was applied to experimentally obtained neutron spectrum of ^{252}Cf via a Time-of-Flight technique to obtain the energy spectrum. The efficiency corrected neutron energy spectrum of ^{252}Cf is found to be in good agreement (Figure 2.10) with the existing data in the literature .

Morever, the neutron spectrums measurement around API or FNR experimental set up could not be performed during the course of this thesis work and will be used in near future, hence the detector characterization work has been described in Appendix B.

2.5 Conclusions

In this chapter, we have presented the neutron yield measurement of D-D/D-T NG and development of devices for real time neutron monitoring. The maximum neutron yield of D-D/D-T NG measured with foil activation method was 1×10^{10} of D-T and 3×10^{7} of D-D neutron. Two different types of neutron detectors were developed for real time neutron monitoring. The associated particle based neutron detector has shown promising performance for real time monitoring of D-T neutron emission rate in the range of $\sim10^{8}$- 10^{10} n/sec. It has also been shown to be useful for monitoring of D-D neutron at yield $\sim 10^{7}$ n/sec,

but at a position more close to target in compared to that of D-T mode.

However, this silicon based neutron detector is susceptible to the radiation damage, particularly due to long exposure to D-T neutron. To overcome this, fiber based miniature neutron detector with ThO_2:ZnS(Ag) was developed and sensitivity obtained was 3.6×10^{-6} cps per neutron flux of D-T neutrons. Due to its less sensitivity it can be used efficiently for higher neutron yield D-T NG of $\sim10^8$ n sec^{-1} and more.

Future work in this direction will be on development of associated particle based neutron detector with scintillator such as YAP:Ce or ZnO(Ga) which have better radiation hardness in comparison to semiconductor based detectors. Also the sensitivity of fiber based detectors, can be further improved using optical fibers doped with a wavelength shifter.

CHAPTER 3

Fast Neutron Radiography with D-T neutron

Imaging with fast neutron (∼2-20 MeV) is relatively advanced technique that offers unique advantages over conventional X-ray and thermal neutron imaging. Particularly because of the following reasons: in fast energy range the macroscopic neutron interaction cross sections are in general low and do not exhibit significant element-to-element variation. This makes fast neutron imaging a promising inspection modality for many practical problems especially for inspection of large samples containing mixed low-Z/high-Z materials.

3.1 Introduction

Neutron radiography is an efficient non-destructive investigation tool for a number of tasks not possible by conventional X-ray or gamma radiography [52, 118–121]. The neutrons offers unique advantages over the x-rays are their ability to image light elements and neutron can penetrates heavy elements such as tungsten, tantalum, lead etc. It allows the imaging of materials with neutron in complex sample environments. This is because neutron and x-ray/gamma radiation interacts with matter differently. X-ray attenuation coefficient for different materials increases with increasing atomic number (Z). Whereas for neutrons it does not show any regular pattern as a function of atomic number. Figure 3.1 [taken from [122]] compares the mass attenuation coefficient of thermal neutrons, X-rays (60KeV and 100 keV typical energies used in imaging) and gamma (1MeV) clearly demonstrates the complementarity of neutron and X-ray/gamma imaging for a broad range of materials.

For instance, some of light elements such as H, B, Li, have a neutron attenuation coefficient which is two-three order higher than for element of moderate

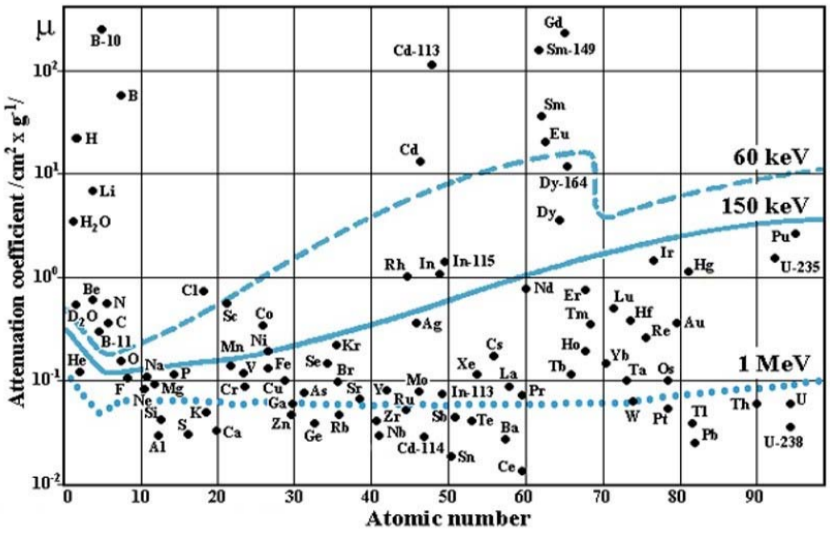

Figure 3.1: Attenuation coefficient (loarithemic scale) of elements for neutrons (separate dots), for 1MeV gamma-ray (dotted line), for 150 keV X-ray (solid line) and for 60 keV X-ray (dashed line) [taken from [122]].

Z such as Al, Fe, Si [123]. On the other hand X-Rays/Gamma radiation is absorbed to a great extent by heavy elements whereas as it penetrates light material without significant loss in intensity. Neutrons can also distinguish between different isotopes of the same element. This makes neutron radiography an important tool in many fundamental research applications and in the field of non-destructive techniques. In principle neutrons of all energies can be used for radiography it is thermal (∼meV) and epithermal (∼keV) neutron based radiography that is more widely used.

However, thermal neutron/epithermal imaging is not always effective in imaging of materials such as plastics, lubricants and chemical explosives when these materials are shielded by thick layers of light elements material (HDPe, Boron etc) or masked with dense and high-Z (Cd, Lead, Gd) material. An example of this is the inspection of airline luggage or cargo containers. This is because most of these objects contain a large amount of hydrogenous materials including plastics and thermal neutrons are essentially unusable as they are so attenuated by such an environment.

In such cases fast neutron imaging offers unique advantages over conventional X-ray and thermal neutron imaging, due to their greater penetrating power (that is lower attenuation) through high-Z materials and compared to

X-rays, their much stronger interaction (that is, higher attenuation) in low-Z materials [124, 125]. This makes them a unique tool for non-destructive inspection of large-scale objects and products containing light and heavy elements simultaneously.

But the major challenge in using it is to find a sufficiently intense source of fast neutrons. Effectively used fast neutron sources are i) isotope based and ii) accelerator based. The latter ones are preferred over the former on account of their high yield, electronic switching control and no shielding requirement in idle condition. Accelerator based D-D/D-T neutron generators are available with moderate source intensity in portable size and could be used for FNR purposes. Some of the investigated applications are worth mentioning such as nuclear stockpile stewardship [64] using 10 MeV neutrons, national security applications to detect heavily shielded explosives or contraband [126] and fast-neutron radiography system for fissile materials [127] studied using high energy neutrons. Fast neutrons imaging has also been used as an inspection tool for investigating two-phase flows in nuclear fuel bundles [75, 128] with reactor as a fast neutron source. Though there are important applications of FNR, it is yet to be a widely used technique and most of these studies have been demonstrated at laboratory scale. This is because of various unresolved issues related to the fast neutron imaging. The major or critical components of FNR such as source intensity requirement, optimum collimator design, sensitive imaging system and reduction in fast neutron scattering from surrounding materials or from thick object itself to improve image quality are still under development and need optimization [129–131].

This chapter describes the simulation study of FNR carried out for understanding of its potential and limitations for various objects and the feasibility experiments performed for imaging of low Z sample masked with high Z material. Different samples ranging from low Z, metallic and high Z materials were simulated for their radiographic images. The quality of constructed neutron radiography images in terms of relative contrast and the contrast-to-noise ratio (CNR) were calculated for their dependence on parameters such as thickness, voids inside high/low Z material and for low Z material hidden behind

high Z material. Contrast is defined as the magnitude of the ratio of the maximum signal (pixel intensity) to the minimum signal in an image. The relative contrast in general can be explained as $\Delta I/I$, where I is the average background intensity (in the vicinity of the region of interest) and ΔI is the relative change in intensity at the region of interest with respect to the background. The details of the experimental set-up with D-T neutron generator and feasibility experimental results are reported in second part of chapter. The experimental FNR system consist of a D-T neutron generator, collimator assembly of mild steel with inlet aperture (D) of 10 mm, L/D 43 (L=length of the collimator) and a neutron imaging system (NIS). The NIS consists of a thick plastic scintillator in combination with a front coated mirror and an Electron Multiplying Charge Coupled Device (EMCCD) camera. Various imaging experiments have been performed on different test objects of low to high Z materials to demonstrate the imaging capability of the D-T based FNR system. Test samples of step wedge, hole features in step wedge [polyethylene, mild steel (MS) and lead (Pb)] and a sample of low Z masked with high Z were imaged and reported here.

3.2 Neutron radiography principle

Neutron radiography [132] is based on projection imaging of an object under investigation upon transmission of neutrons through it. Depending upon the attenuation of neutrons along the path of neutrons a shadow image of the object is cast on the detector. This two-dimensional shadow image of sample provides first-hand information about the objects internal details in macroscopic scale (see Figure 3.2). If we consider a sample having a linear attenuation coefficient, say μ (cm $^{-1}$), the transmitted intensity (I) of radiation passing through a sample can be written as

$$I = I_0 e^{-ut} \tag{3.1}$$

Where I_0 is the intensity recorded by the detector with neutron beam without the sample and t is the thickness of the sample. As a simplistic case we consider that in this sample there is an inhomogeneity or some structure hav-

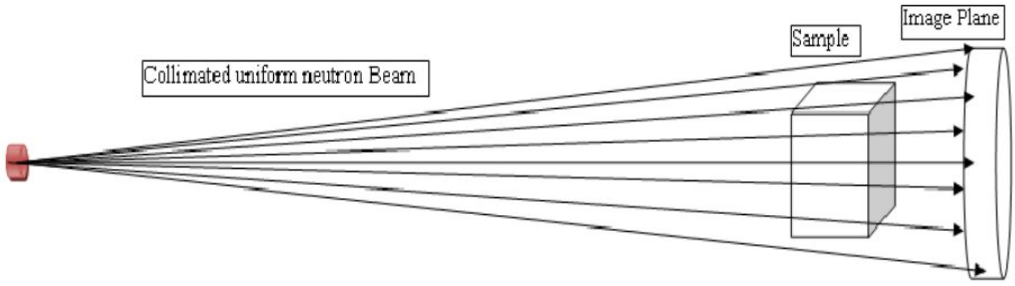

Figure 3.2: Schematic of FNR.

ing thickness t_1 with linear attenuation coefficient μ' the transmitted intensity recorded by the detector will be (3.2).

$$I = I_0 e^{-\mu(t-t_1)+\mu' t_1} \tag{3.2}$$

The intensity pattern recorded by the detector will show a different pattern at a position in-line with the location of inhomogeneity inside the sample with respect to the rest of the image. This is the basic essence followed for the simulations carried out for FNR. In more simple way an image can be defined as a two-dimensional function f(x,y), where x and y are spatial (plane) coordinates and its amplitude at any point (x,y) is called the intensity. The intensity is transformed into gray level for digitization purpose. The elements of the image are referred to as image elements or pixels.

3.3 Design for FNR simulation

A typical FNR consists of a source of neutrons, a collimator to shape the emitted neutrons into a fairly directional beam with minimized scattering, the object for investigation and a neutron sensitive detector assembly for recording the image. The simulations have been carried out using GEANT4 (version 9.5) simulation kit [133]. GEANT4 provides an efficient virtual environment to model the interactions between particles and matter over a wide range of energies. It provides several powerful tools for configuring radiation sources, detectors and a variety of complex shaped objects. The main components of the GEANT4 code used for the present study consists of i) the primary gener-

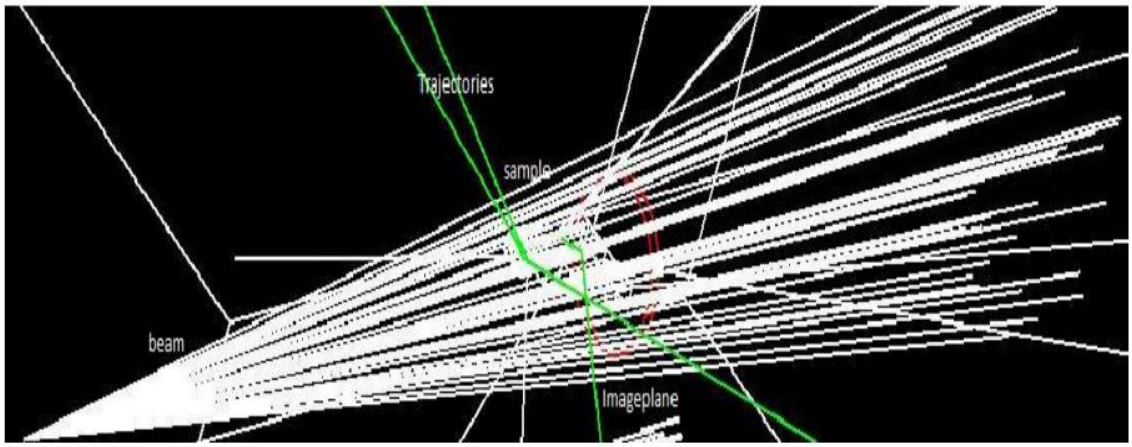

Figure 3.3: FNR system modelled using GEANT4.

ator class which generates the 14 MeV neutrons, ii) the detector construction class which constructs the geometry of setup including material type, sample geometry and the detection system iii) the physics list which activates the appropriate physical processes and iv) analysis class which stores the event by event data as histograms. The physics list $QGSP\_BIC\_HP$ is used for the simulation. This high-precision package uses the ENDF/B–VII data library and describes the neutron interactions very well for energies below 20 MeV . The X, Y position of each neutron track is recorded for each event as two dimensional histograms using ROOT package [134] coupled to GEANT4. Figure (3.2) and (3.3) show the schematic and simulated FNR model. FNR simulation design comprises of three parts viz neutron source, sample and image construction. Each of these components is described below.

Neutron source

14 MeV neutron source was modeled in GEANT4 as a point source placed at a distance of 65 cm from the object, emitted within a limited angle such that a collimated uniform cone beam falls directly on the object. The neutron emission in small cone reduces simulation time. To image the object of size $\sim$ 8-10 cm, cone beam of solid angle 1.32×10^{-2} was modelled. This was also to approximate the experimental conditions (sample size, sample position, collimator aperture etc) of fast neutron radiography as described in the section

Table 3.1: Elemental composition of different samples used in FNR simulation study

Sample	Composition	Fraction (%)	Density (g/cc)
Pb	Pb	100	11.35
Cd	Cd	100	8.65
Fe	Fe	100	7.86
Al	Al	100	2.7
Graphite	C	100	2.2
HDPe	C	85.57	0.92
	H	14.28	2.7
Air	N	70	1.29(mg/cc)
	O	30	

(3.7). The simulation was executed with 10^8 neutron histories emitting in the solid angle. Hence the total source strength of neutron generator (in 4π) was expected to be 9.5×10^{10}n/s and the neutron flux at the sample position was approximately 1.8×10^6 n/cm^2. An identical number of neutron histories were generated for each time for various sample configurations.

Sample configuration

We have examined five cases with different configurations as given below.
Sample 1: Effect of Pb thickness on image: Step wedge sample
Sample 2: detection sensitivity of various sized defects/voids inside a thick Pb slab.
Sample 3: detection sensitivity for a certain void size inside varying Pb thickness.
Sample 4: imaging of Low Z material (HDPE) inside Pb.
Sample 5: imaging of nested cylindrical shells material(low to high Z).
These are detailed in the section (3.4). The elemental composition of different materials used in the simulation is listed in table 3.1.

Plotting

Root based plot programme was written and density plot was used for plotting transmitted neutron intensity distribution at the image plane. The images reconstructed were grayscale images of 8 bit. Grayscale images have many shades of gray in between. For example, 8 bit image have 256 different intensities (i.e., shades of gray) means total 2^8 levels form black to white (where 0 = black and 255 is white). Image processing and qualitative analysis was carried out using ImageJ [135]. The length corresponding to one pixel of the reconstructed images was 260 micron.

3.4 Sample description and analysis

3.4.1 Sample 1: effect of Pb thickness on image

A step wedge of Pb was constructed having dimension of 1cm x 1cm -(width) x (height), and thickness varying from 2 to 28 cm in steps of 2 cm. The thickness variation was along the beam path. The transmitted neutron distribution was collected and 2-D image was constructed. The object configuration and its constructed images are shown in Figure 3.4 and Figure 3.5 respectively. The image of the step wedge shows the high transmission capability of 14 MeV neutrons for Pb. Figure 3.5 shows that 14 MeV neutrons are able to penetrate through and can distinguish the variable thicknesses ranging from 2 cm to 20 cm but could not at higher thickness above 20 cm. The relative contrast values were evaluated [(I_{max}-I_{min})/I_{min}], where I_{max} and I_{min} represents maximum and minimum intensity respectively] across the edges of different steps as shown in Figure 3.6. It shows (Figure 3.6) that maximum contrast (5.3%) exists between 8 cm and 10 cm lead and decreases at either sides. This is due to increase in attenuation at higher thickness and decrease in attenuation at lower thickness as well as increased scattering effect with sample thickness. The simulated transmission values for thicknesses of 2 cm, 10 cm and 20 cm were found out to be 94%, 73% and 41% respectively.

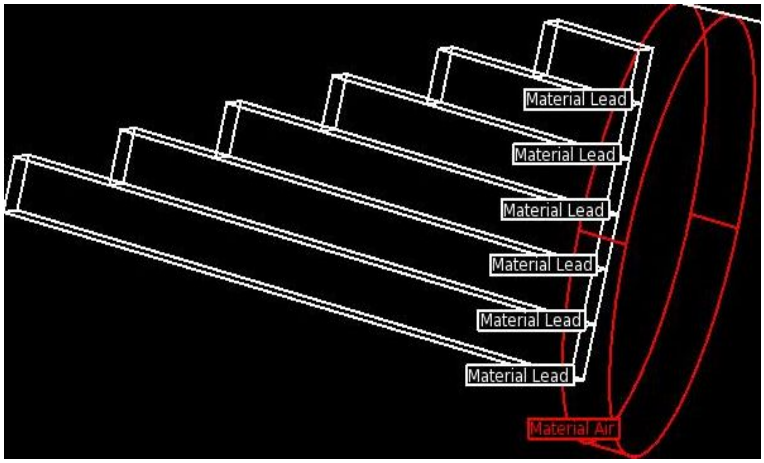

Figure 3.4: Schematic image of lead step wedge sample as per configuration 1.

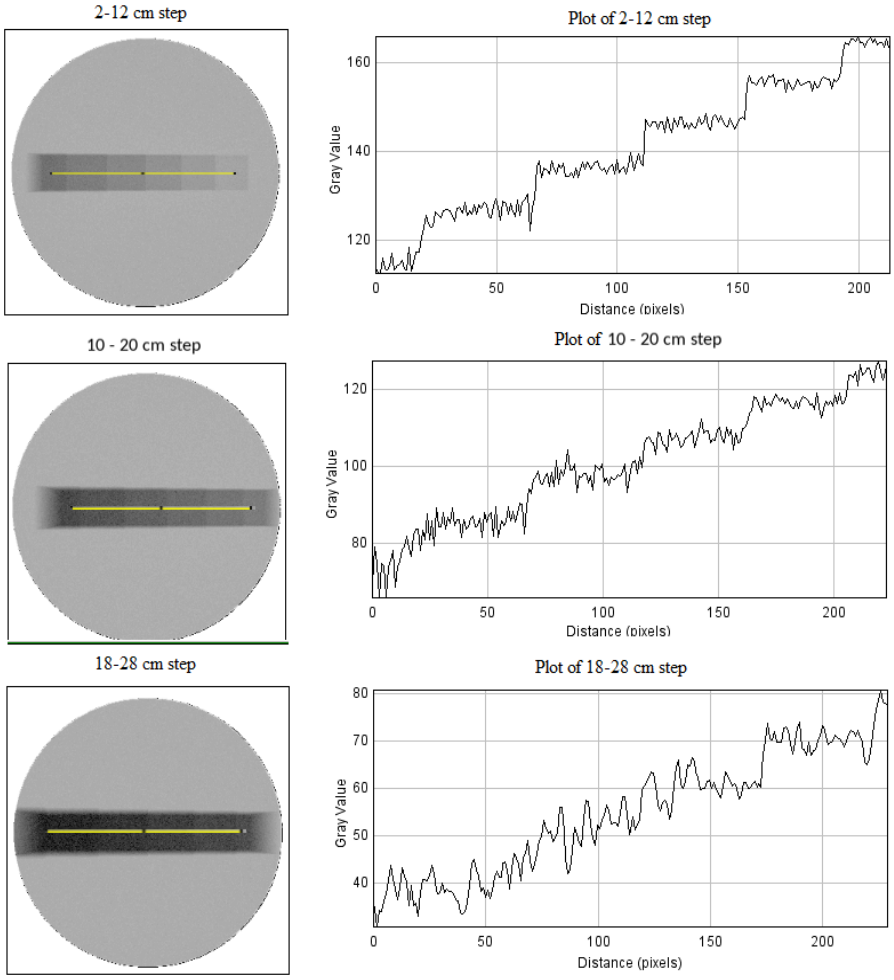

Figure 3.5: (Left) The constructed images for various step wedge ranges ((top) 2-12 cm, (middle) 10-20 cm and (bottom) 18-28 cm) and (right) their corresponding intensity line profiles at the central plane (yellow line).

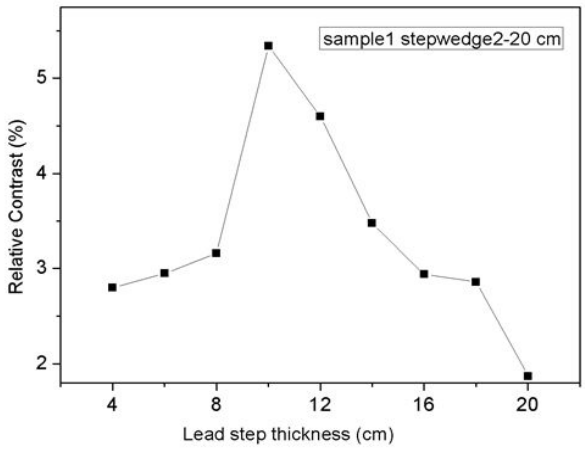

Figure 3.6: Plot of relative contrast at the interfaces for 2-20 cm steps of sample1.

3.4.2 Sample 2: detection sensitivity for various sized holes inside a thick Pb slab

This sample consists of a rectangular solid block of Pb (width = 1 cm, height = 7 cm, thickness = 10 cm) with number of holes drilled inside the block. The holes were of 10 cm length having varying diameters such as 0.5 mm, 1 mm, 2 mm, 3 mm and 4 mm. The object configuration as per GEANT input file is shown in Figure 3.7. All the holes baring 0.5 mm are clearly distinguished in the constructed image as shown in Figure 3.8 along with intensity line profile across the object centre. The hole contrast was calculated with [(I_{max}-I_{bg})/(I_{bg}), where I_{max} is the intensity inside the hole and I_{bg} is the intensity values on the Pb step other than hole region.] and obtained result is shown in Figure 3.9. It is seen that the contrast is maximum for 2 mm hole and decreases for smaller or larger hole sizes. For the evaluation of hole sizes in the image, FWHM of the intensity profile at the holes of different sizes was calculated and the deviation (normalized) from actual hole size is shown in Figure 3.9. From this plot it is evident that the deviation in the constructed image is minimized while approaching larger holes.

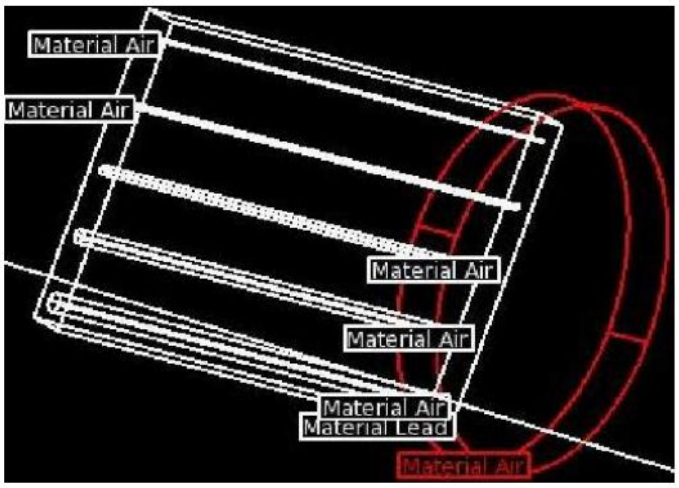

Figure 3.7: Schematic of sample2 configuration having holes of varying diameter (0.5 mm to 4 mm) in 10 cm thick Pb slab.

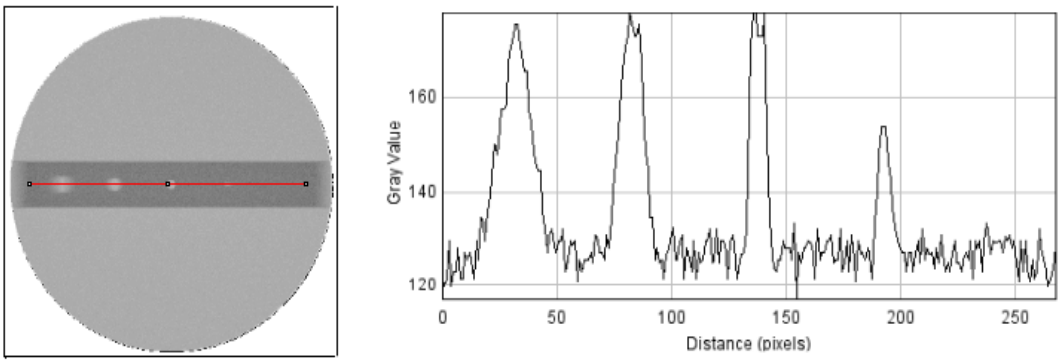

Figure 3.8: (Left) Constructed image and (right) intensity line profile across center (red marked line) of sample 2.

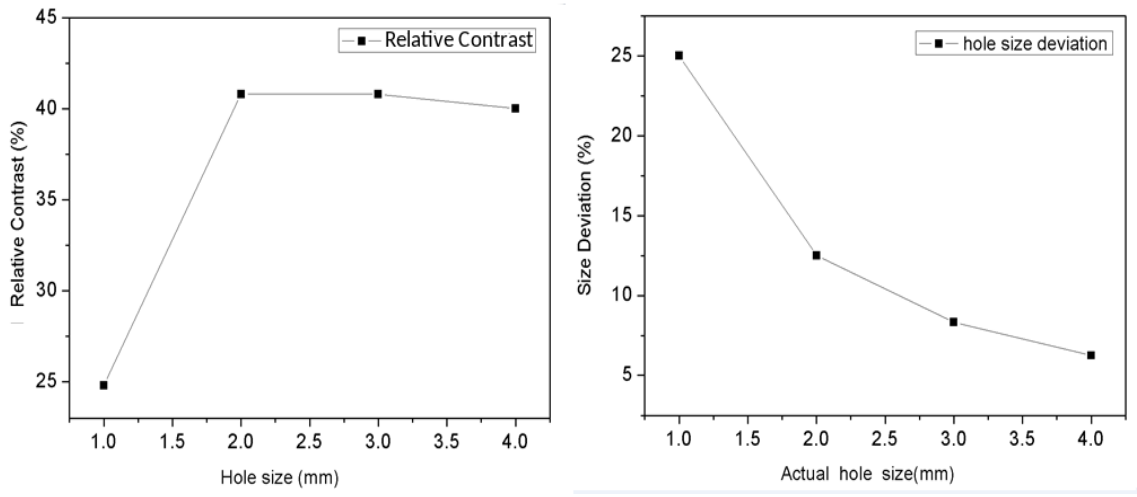

Figure 3.9: (Left) Hole Contrast (1-4 mm) and (right) deviation of calculated hole size from actual with respect to actual hole diameter.

3.4.3 Sample 3: detection sensitivity for a certain void size inside varying Pb thickness

As per analysis of sample 2 we could not resolve 0.5 mm hole inside 10 cm thick Pb slab. Investigating further we have constructed a Pb step wedge having thickness varying from 2 cm to 12 cm in steps of 2 cm with drilled holes of 0.5 mm for each thickness along its depth as shown in Figure 3.10. It has been observed from the constructed image (Figure 3.11) that 0.5 mm size hole is visible in Pb sample for depths ranging from 2 cm to 10 cm but not at depth of higher then 10 cm. For Pb thickness of more than 10 cm scattering effect is high and 0.5 mm hole is not visible. The line profile across the centre of the sample encompassing all the holes is shown in Figure 3.11. The hole contrast calculated for 0.5 mm hole in different lead step was found out to be maximum for 8 cm thick portion as shown in Figure 3.12. The hole size in the constructed image were evaluated as per their FWHM and is also shown in Figure 3.12 with respect to Pb thickness. Such sample images are in practical use for determining overall resolution of neutron imaging systems and how efficiently it can detect small cracks inside a thick Pb sample. It can be inferred that 0.5 mm hole can be seen at a good contrast (11%) in 8 cm Pb compared to other step sizes. For comparatively smaller thickness, the attenuation is lower and hence the contrast is poor. For more thicknesses there is blurring effect in the image due to scattering. Similarly the calculated (FWHM) hole size deviation is minimum at 6-8 cm.

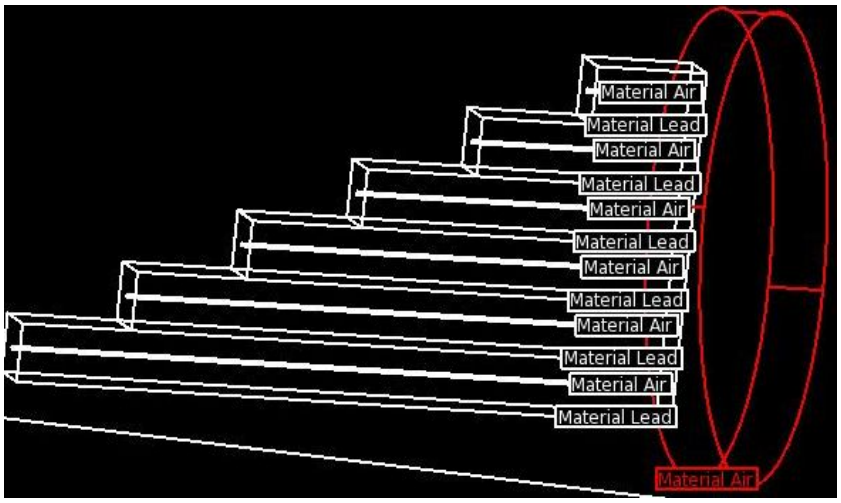

Figure 3.10: Schematic image of sample 3.

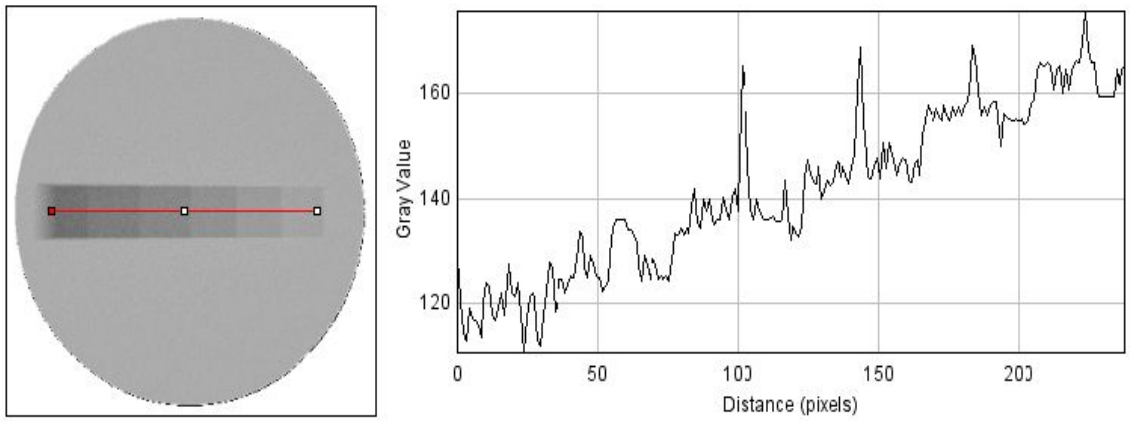

Figure 3.11: (Left) Constructed image of sample 3 and (right) line profile across the centre of the object.

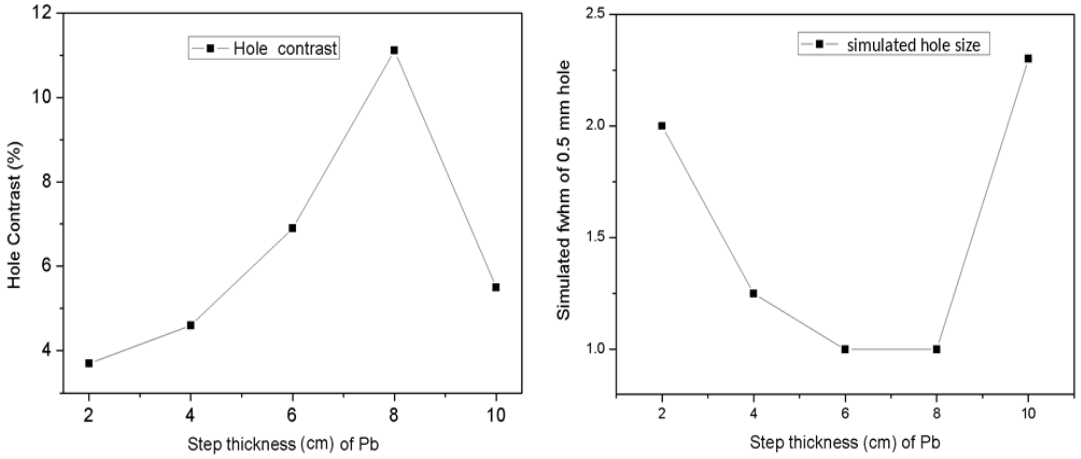

Figure 3.12: (Left) Plot of hole contrast versus Pb step thickness and (right) plot of simulated FWHM of 0.5 mm hole with respect to varying Pb thickness.

3.4.4 Sample 4: imaging of Low Z material (HDPe) inside Pb

One of the preferred applications of FNR is to image low Z material hidden inside high Z material such as Fe, Cd and Pb. For such cases we have configured a sample of HDPe cylinder (diameter = 4 cm and thickness = 5 cm) with holes of various sizes, enclosed inside concentric Pb cylinder (diameter = 6 cm and thickness = 8 cm) as shown in Figure 3.13. Holes inside HDPe were of size 1-5 mm in steps of 1 mm. Projection image was constructed with this configuration and is shown in Figure 3.14. All the holes in HDPe along with the contrast between HDPe and Pb were seen with good contrast. In the next step, the depth of Pb cylinder was increased step by step such that effective thickness of Pb over HDPe varies from 3 cm to 15 cm and the constructed images are shown in Figure 3.14. Figure 3.14 also shows the intensity profile across the centre of the sample image revealing the polythene-lead interface contrast and across the 5 mm hole. Hole (5 mm) contrast and HDPe-Pb interface contrast are plotted in Figure 3.15. The HDPe-Pb interface contrast is maximum for Pb slab thickness of 7 cm and the hole contrast is maximum at 11 cm Pb thickness. The CNR (Eq 3.3) has also been evaluated for 5mm hole and its values with Pb thickness is shown in Figure 3.15.

$$CNR = |\frac{2(\mu_h - \mu_b)}{(\sigma_h + \sigma_b)}|, \mu = \frac{1}{N}\sum_{i=1}^{N} x_i, \sigma = \sqrt{\frac{1}{N}\sum_{i=1}^{N}(x_i - \mu)^2} \tag{3.3}$$

Here μ_h is defined as the mean gray value of the region of interest inside the feature (which is 5 mm hole inside HDPe), μ_b is mean value of the same size region just outside the feature in the HDPe sample region, σ stands for standard deviation, x_i is pixel data value of i^{th} pixel and N is the total number of pixels in the region of interest.

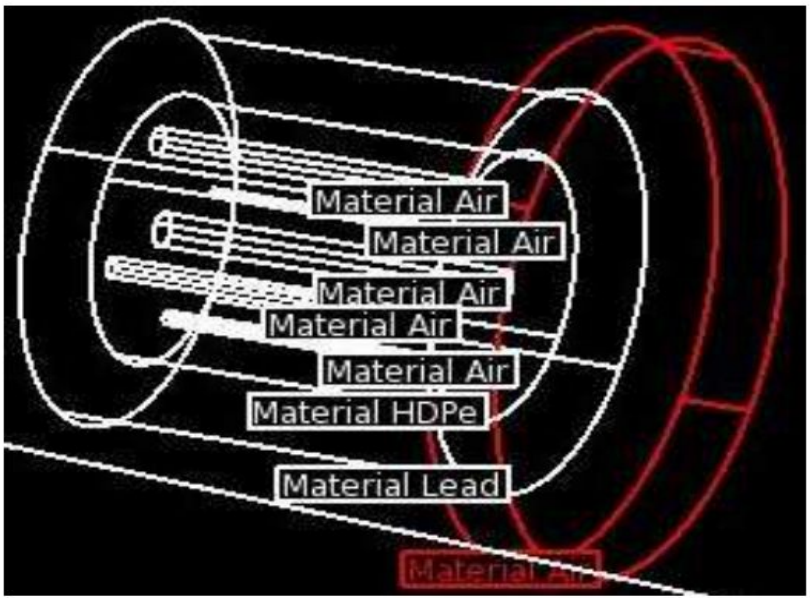

Figure 3.13: Schematic of sample configuration 4.

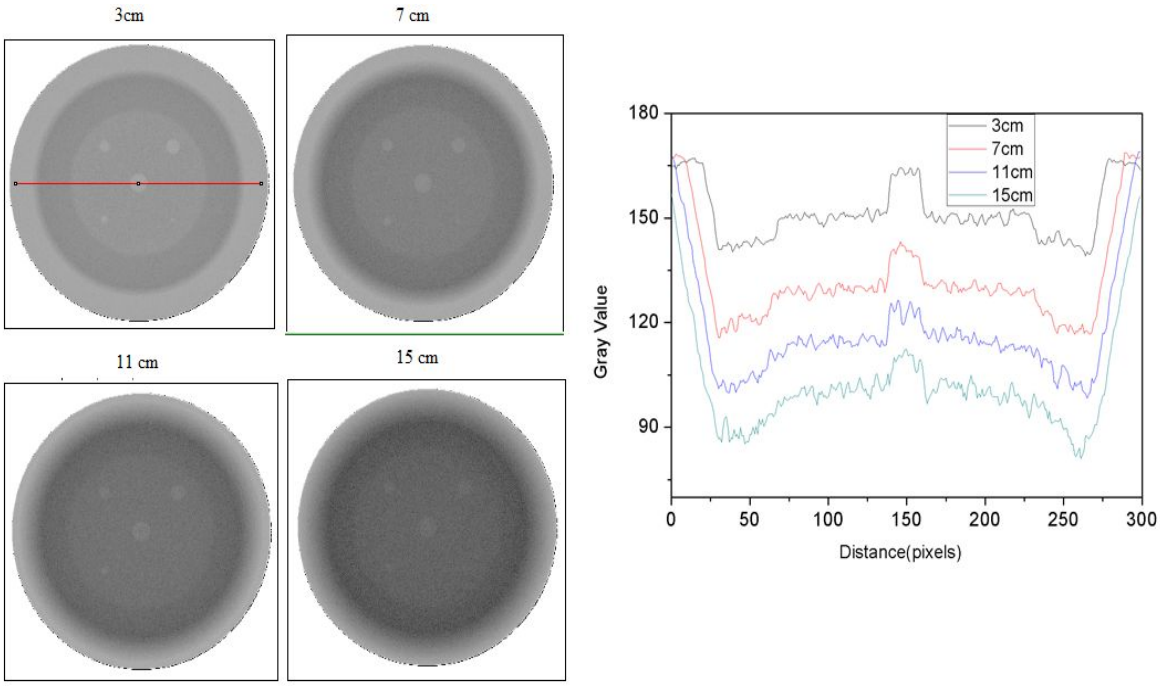

Figure 3.14: (Left) The constructed projection images at increasing Pb thicknesses (clockwise from top left image: 3 cm, 7 cm, 15 cm and 11 cm) and corresponding intensity value plots across the centre of sample4.

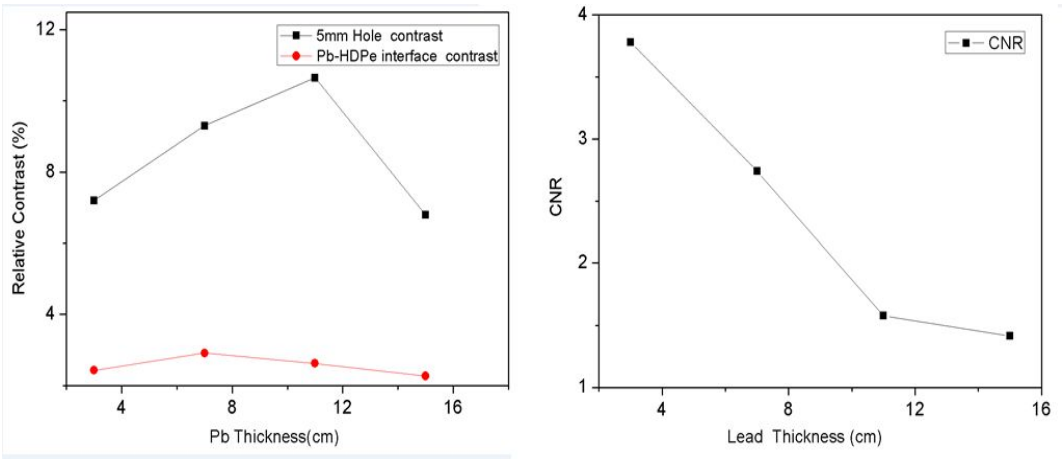

Figure 3.15: (Left) Plot of HDPe-Pb interface contrast and 5 mm hole contrast with respect to Pb thickness. (Right) Plot of CNR of 5 mm hole with respect to Pb thickness.

3.4.5 Sample 5: imaging of nested cylindrical shells material (low to high Z)

Another configuration was simulated with cylindrical objects composed of nested shells having low to high Z materials in the radial direction. Materials used were HDPe, Graphite (C), Al, Fe, Cd and Pb of thickness 10 cm each and of width 5 mm (as shown in Figure 3.16). In the constructed image (Figure 3.17) HDPe, Graphite, Al were clearly distinguishable as per their interfaces but as we move towards higher Z like Fe, Cd and Pb the contrast reduces. Cd and Fe could not be distinguished between them but they are visualized with good contrast with respect to Pb as has been shown in the line profile Figure 3.17. In that case both Fe and Cd can be clearly distinguished if Pb is kept between these two. This simulation provides us with possible combinations of materials which could be used for imaging with 14 MeV neutrons. For example we can be sure of achieving good contrast image of HDPe/C/Al (low-Z) material in combinations with Fe/Pb (high-Z) material. Table 3.2 tabulates the contrast at different interfaces in the sample.

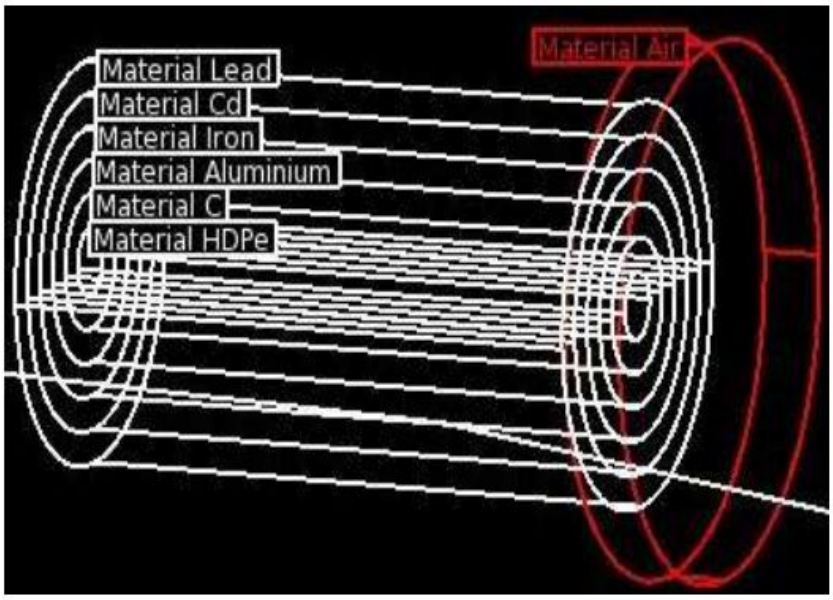

Figure 3.16: Schematic of sample configuration 5.

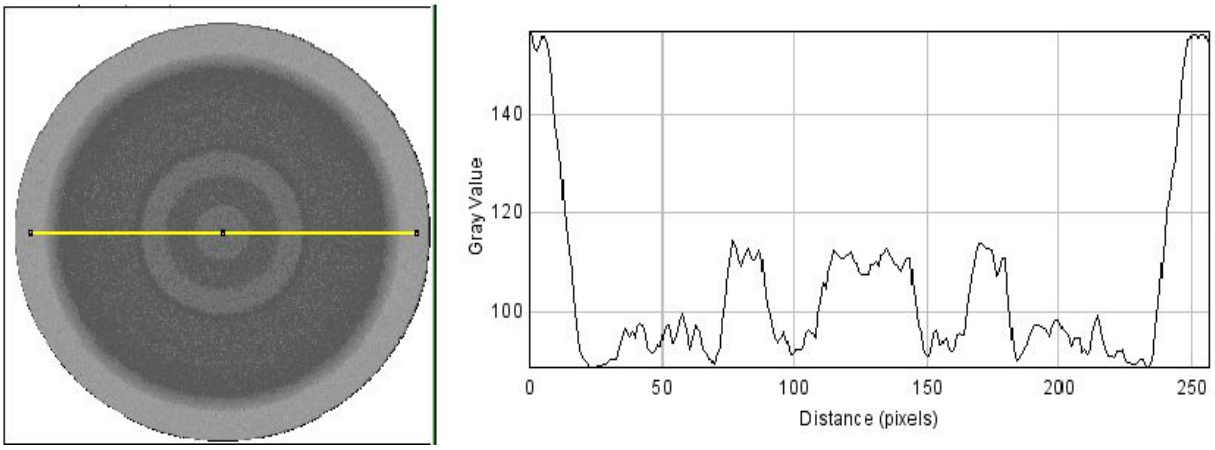

Figure 3.17: (Left) Constructed image of the sample 5 and (right) the intensity line profile across the marked portion showing the individual interfaces

Table 3.2: Relative contrast at interfaces between different materials as per configuration 5

Interfaces between Sample	Relative Contrast ($(I_{max} - I_{min})/I_{min}$)
HDPE-Graphite	20.2
Graphite-Aluminum	21.2
Aluminum-Iron	26.4
Iron-Cadmium	Nil
Cadmium-Lead	5.4

3.5 Conclusion

Simulation study of FNR with 14 MeV for wide range of samples including low Z, metallic and high Z materials has been carried out. Results have shown the high transmission (73%) capability of 14 MeV neutron in thick high Z material (10cm lead) and in this holes of size 1 mm or larger can be imaged with FNR. Thus it can be concluded that FNR could provide spatial resolution of mm order in such configuration. The results also reveal that the presence of low Z (HDPe) material encapsulated inside thick and high Z could be imaged with FNR, if the thickness of the masked material (lead) is not more then 10 cm. The simulation study of the sample where number of materials present from low to high Z (such as HDPE, Graphite, Al, Fe, Cd and Pb) placed in increasing order of their atomic number, has provided the possible combinations of low (HDPE/C/Al) and high Z (Fe/Pb) materials which could be used for imaging with 14 MeV neutrons.

3.6 Experimental Studies

The simulation study has provided insight of FNR method and its capabilities and limitations with respect to different sample configurations ranging from low Z to high Z. Based on simulated results the HDPe and lead were chosen for experimental study. In addition to that an iron sample was also taken under consideration for response of FNR towards structural material.

To implement the FNR and to image the large sample (containing mixed low-Z/high-Z materials) with reasonable contrast various practical factors like fast neutron source intensity, source spot size, scattered neutron background and efficient fast neutron detection system play important roles.

We have designed an experimental set-up of FNR with D-T neutron generator and initial experimental results are reported. Most of the reported experimental studies on FNR using D-T/D-D neutron generator were carried out at laboratory scale with intensity of neutron sources of 10^{10} or higher otherwise with long exposure duration of about 30-60 minutes [136–138]. This work has

been aimed towards development of a small FNR system with a D-T neutron generator of moderate intensity $\backsim 2\times10^9$ n/s for imaging of thick samples containing mixed low-Z/high-Z materials in encapsulated manner. As neutrons from the D-T generator have higher energy and almost two orders high neutron yield with respect to D-D generator, the former is always preferred.

3.7 FNR Experimental set-up

Neutron source

The D-T neutron emitting area on the tritium target was about 20 mm in diameter. The DT NG yield was about $\backsim 2\times10^9$ n/s in 4 pi directions. The NG is located in a laboratory with approximate dimensions of 7m x 7m x 7m (WxHxL), with thick concrete walls. These walls are typically at a distance of 1.5 m, 1.8 m and 2 m from the target and hence relatively high level of scattered neutrons can be expected at the imaging detector position.

Collimator

It is well known that the source size, flux and source-to-detector distance play an important role in image quality. Though the resolution improves with a reduction in the source size it suffers from a low signal-to-noise ratio on account of probe flux reduction. Hence there is trade-off between these three above-mentioned parameters for optimum image quality. Moreover scattering flux results in lowering of contrast in the image. A suitably designed collimator along with a proper detector shielding can take care of the issues related to source size and scattering. Various types of FNR collimator configurations have been reported by different research groups depending upon the type of neutron source used [139, 140].

The collimator material is an important factor in determining the beam quality as it should prevent stray and scattered neutrons from reaching the image plane or object. We have used mild steel to construct the collimator since it is found to be more suitable (though tungsten is also suitable but of

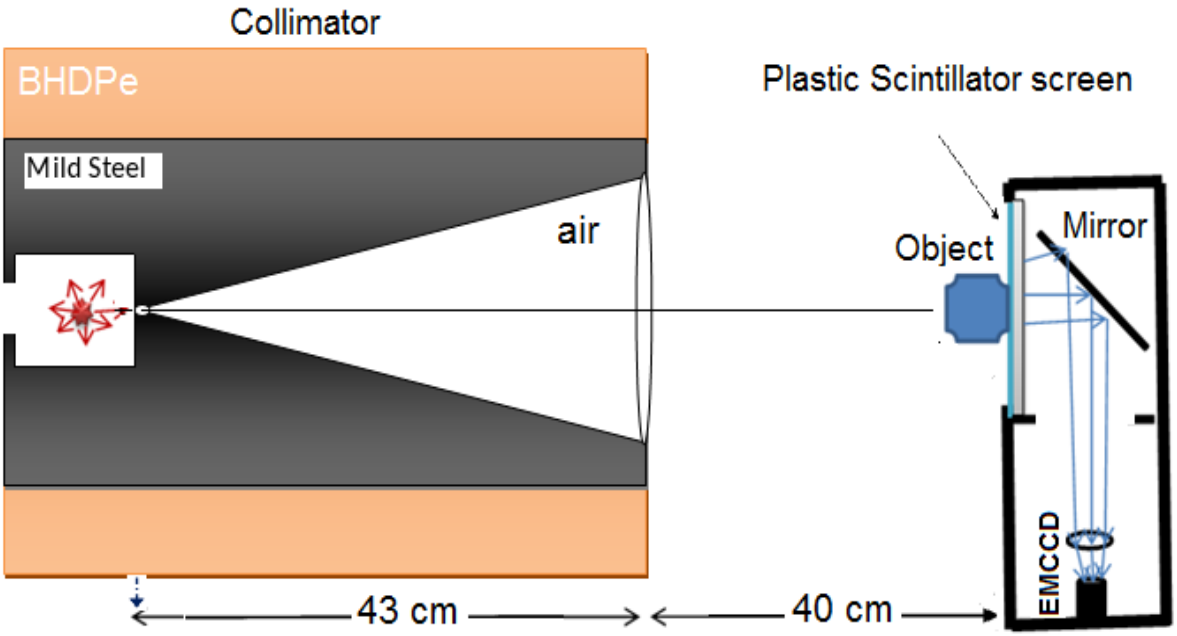

Figure 3.18: Schematic diagram of the neutron imaging system.

high cost) for fast neutrons compared to the traditionally used neutron moderating materials. In metallic collimator the neutrons would get scattered away from the interior walls of the collimator following very few collisions, with an insignificant loss in energy. The collimator consists of two parts. The first part consists of a MS block of dimension 200 mm (width) x 200 mm (height) x 100 mm (depth) with a cut-out of 100 mm x 100 mm x 100 mm at the centre for coupling the neutron generator target flange. The second part of the collimator consists of a MS block of dimension 200 mm (W) x 200 mm (H) x 430 mm (L) with a centrally cut cone along its full length having an inlet aperture of 10 mm (D) and an output aperture of 135 mm. These two parts are coupled together as a single unit of length 530 mm. Other than the inlet and outlet sides, all four sides of the collimator are covered with a 100 mm high density polyethylene (HDPe) (5% boron) layer to absorb the transmitted neutrons from the metal collimator layer and the scattered neutrons from walls. This way it reduces the scattered neutron contribution at the image plane. As per the design this collimator provides an L/D ratio of about 43. The schematic of the imaging system is shown in Figure 3.18.

For this collimator geometry, the total neutron flux and source neutron frac-

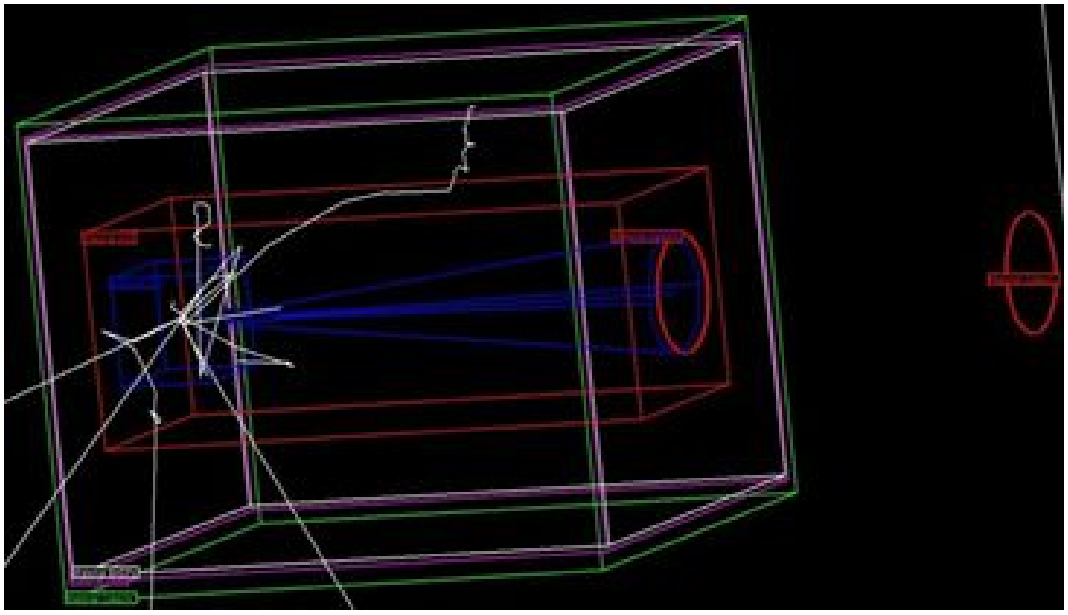

Figure 3.19: The simulated geometry of FNR collimator

tion (ratio of unscattered neutron flux to total neutron flux) unscattered neutron flux at collimator end and at image plane (400 mm from the collimator end) were calculated via simulation. In this simulation the neutron (14MeV) source was of same size as of target size of neutron generator and neutrons were generated isotropically. Figure 3.19 shows the simulated geometry in GEANT and the results of neutron flux at the collimator exit as well as at the image plane with varying collimator lengths of 300 mm, 400 mm, 430 mm and 500 mm are provided in Table3.3. The results are discussed below.

Simulations have shown that source neutron fraction at the collimator exit improved from 48.76% to 61.92% and the total neutron flux ($ncm^{-2}sec^{-1}$) decreased from 2.2x10^5 to 6.42x10^4 with increasing L/D (30-50). Similarly at the image plane (400 mm from the collimator exit) the source neutron fraction increases from 74.0% to 82.47% and total neutron flux ($ncm^{-2}sec^{-1}$) reduces from 4.06x10^5 to 1.92x10^4 with increasing L/D (30 - 50). Hence by increasing the L/D ratio or locating the imaging system far from the collimator resulted in an improvement of the beam quality and less contribution of scattered neutrons from collimator material at the expense of reduction in the neutron flux. Fandtis et al [140] have reported similar simulation work with a high source neutron fraction of 97% - 98% at an L/D ratio of 100-300. Such a high L/D

Table 3.3: Results of simulation for neutron (14 MeV) source strength of 2×10^9 n/s

L/D	Collimator exit		Image plane	
D= 10 mm	Total neutron flux ($ncm^{-2}sec^{-1}$)	unscattered neutron(14MeV) flux(%)	Total neutron flux ($ncm^{-2}sec^{-1}$)	unscattered neutron (14MeV) flux(%)
30	2.20*10^5	48.76	4.06 *10^4	74.0
40	1.12*10^5	52.06	2.64*10^4	76.35
43	9.34*10^4	55.18	2.4*10^4	79.34
50	6.42*10^4	61.92	1.92*10^4	82.47

Table 3.4: Comparison of measured and simulated flux for L/D=43(for detail see the text).

L/D =43	Collimator exit	Image plane
Simulated	7.34*10^4 (78.5%)	2.01*10^4 (84.14%)
Measured	1.8x10^5	4.6 x10^4

ratio will definitely yield good quality images but practically difficult to be realized with a source of neutron yield 2x10^9 $nsec^{-1}$. In this context to achieve a good S/N ratio the image acquisition period would increase. Considering our NG source strength we have used a collimator assembly with an L/D ratio of 43 providing neutron ($\geq$11MeV) flux of 1.8x10^5 ($ncm^{-2}sec^{-1}$) and 4.6 x10^4 ($ncm^{-2}sec^{-1}$) at the collimator exit and at image plane respectively. The fast neutron flux was experimentally measured using the standard copper foil activation technique [15] with ^{63}Cu(n,2n)^{62}Cu reaction, which has threshold of 11MeV [141]. To compare the measured flux with simulation, the flux of neutron $\geq$11MeV was evaluated in simulation for L/D=43 as given in the Table 3.4 On comparison it was found that the measured values are higher then that of simulated by a factor of 2.46 and 2.28 at collimator exit and image plane respectively. This can be attributed to the additional contribution of scattered neutrons from surrounding materials mainly from nearby room walls, floor, experimental iron tables and different components of NG system (for example vacuum system, HV system etc), which were not addressed in the simulation study.

Fast neutron imaging system

One of the most effective way of fast neutron detection is via recoil proton method and we have used a large plastic scintillator screen (BC400) of size 300 mm (width) x 300 mm (height) [142] for neutron to optical conversion and image is acquired using a sensitive EMCCD (Andor make: Luc247-Mono) [143] camera. Fast neutrons are scattered by hydrogen nuclei, the energetic recoil proton ionizes and excites the molecule or crystal of the scintillator, causing emission of light. The small interaction cross section of D-T neutrons necessitates the need of thick scintillator for sufficient light output for optimum imaging. Though a higher converter thickness increases the neutron conversion efficiency it also adversely affects the spatial resolution. For efficient image acquisition, individual scintillations need to be collected and hence a sensitive, light tight as well as background radiation shielded (neutron and gamma) imaging unit has been designed. The imaging system consists of 40 mm thick plastic scintillator (polyvinyl toluene base having density of 1.03 gm cm^{-3} and refractive index 1.58, H/C = 1.103), a front coated aluminium mirror (placed at 45 degree with respect to the scintillator to avoid possible damage to the camera from a direct beam) and an EMCCD camera system, all incorporated into a light-tight box. EMCCD has 658 (h) x 496 (w) pixels with pixel size of 8 μm x 8 μm, 14 bit and it was operated at gain of 50. The image was acquired with EMCCD coupled to a 25 mm f/0.95 lens. The scintillator to lens distance was 570 mm and in this condition the field of view was 130 mm (H) x 150 mm (V). This can be translated to 200 microns of the screen for each pixel of the CCD. The schematic of the imaging system is shown in Figure 3.18. The whole imaging box is made light tight and is also shielded with 100 mm thick lead blocks from all sides and an additional 50 mm of borated HDPe on the nearest wall side. The actual FNR experimental setup is shown in Figure 3.20.

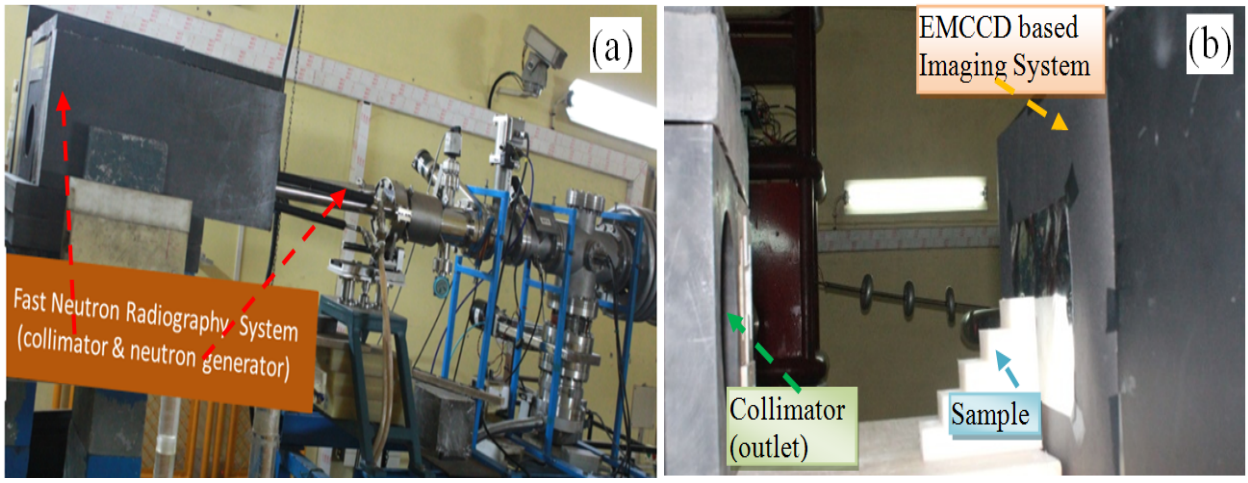

Figure 3.20: Experimental system (left) Collimator and neutron generator (right) close up view of the collimator and part of the EMCCD based imaging system.

3.8 Experiments, results and analysis

3.8.1 Test Samples

The samples selected for FNR imaging study were of HDPe, MS and Pb in the range from low Z to high Z. We have examined the three cases with HDPe, MS and Pb materials in different geometrical configuration similar to simulated one but of different diamenson as given below.

Configuration I: Study of thickness effect on image for HDPe, MS and Pb.

The first configuration was of step wedge samples of size 50 mm x 100 mm x 20-100 mm [width (w) x height (h) x depth (d)] and each step of 20 mm height.

Configuration II: Detection sensitivity for a certain hole size inside HDPe, MS and Pb of varying thickness.

Second configuration had the same sized step wedges as configuration I, with holes of sizes 5 mm, 10 mm and 15 mm drilled in each of the steps. *Configuration III: Imaging of low Z material (high density polyethylene HDPE) masked with high Z (Pb) material.*

Third configuration was to study of the hole-features in HDPe block of [50mm (w) x 30mm (h) x100mm(depth)] having a 5 mm hole and shielded by lead block having thickness of 50 mm and 100 mm.

The geometries of these samples are shown in Figure 3.21. Experimentally

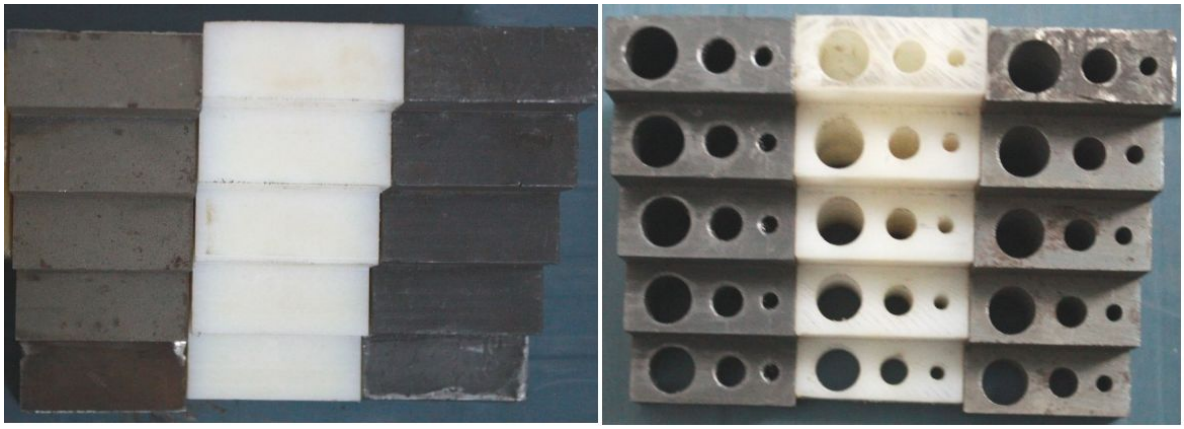

Figure 3.21: The step wedge test samples of MS, HDPE and Pb without and with holes.

acquired images generally suffer from various noises which limits image quality. It may arise from beam inhomogeneity, gain variations of the detector response and dark noise of detector. The experimental images were flat field corrected via normalizing sample image with an image acquired at same parameter without sample with neutron beam ON. The imges were processed with ImageJ and relative contrast, hole contrast and CNR were evaluated for demonstration of image quality.

3.8.2 Configuration I : Imaging of step wedge samples

The step wedge sample was placed in contact with scintillator screen and varying step thickness (20-100 mm) along the beam direction. The images were acquired for exposure time of 10 minutes and images (flat field corrected) are shown in Figure (3.22) along with the intensity profile across the sample. All the three samples (HDPe,MS and Pb) were imaged individually. Intensity profile drawn across the steps shows that all the steps are visible in HDPe sample clearly. The relative contrast calculated for the step wedge sample is plotted in Figure (3.24). We have observed that the contrast value increases (5.4% to 7.8%) first for a thickness of 2 - 6 cm and then it is reduced to the value of 4.5% for the thickness of 10 cm. It was obvious since at a lower thickness the attenuation is small and at higher thickness side the attenuation is more. As a result there is maximum contrast at a certain thickness and it is less value at lower and higher thicknesses. A similar behaviour was also observed in case of MS

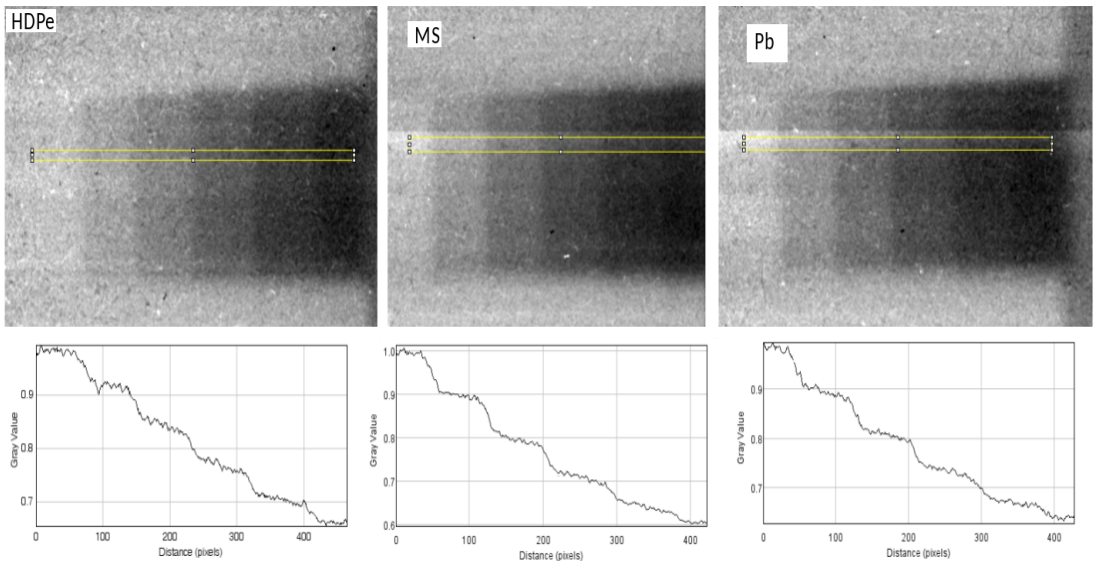

Figure 3.22: Images of step wedge sample of (left) HDPe, (middle) MS and (right) Pb with their intensity profile across the steps (marked yellow line).

and Pb step-wedges and the maximum contrast is 10.3% and 7.9% at thickness of 6 cm and 4 cm for MS and Pb, respectively. The maximum contrast (7.8% at 6 cm) value of HDPe is found to be lesser than that of the MS (10.3% at 6cm) and for Pb (8% at 4 cm). This is due to the fact that, being a low Z material, the HDPe is a highly scattering medium compared to MS and Pb.

3.8.3 Configuration II :Imaging of hole features in step wedge samples

Sample of configurationII with holes of diameter 5 mm, 10 mm and 15 mm was fabricated to study features of holes. Since these experiments were carried out for the first time using our D-T neutron generator with designed FNR system, relatively bigger sized holes were chosen. This study is important from the point of view of determining the detection limit of FNR as per the experimental configuration for understanding sensitivity condition for small size defects such as holes or cracks in thick samples. The images were acquired in a manner detailed in section (3.8.2) and flat field corrected images are shown in Figure (3.23) with intensity profiles across the 5 mm hole. The images clearly show that larger size holes (15 mm and 10 mm) are visible in all steps of HDPe, MS

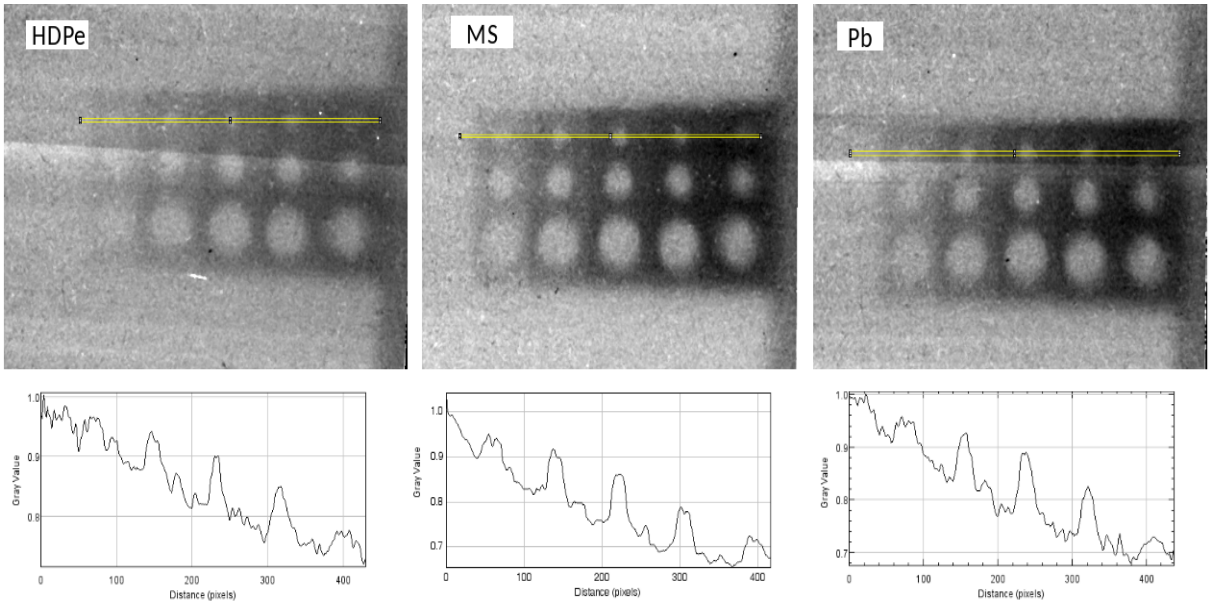

Figure 3.23: Images of holes in step wedge sample of(left) HDPe, (middle) MS and (right) Pb with intensity profiles across the 5 mm hole

and Pb. The 5 mm hole has shown variable and limited visibility in lower thickness (20 mm) steps as well in steps of higher thickness (100 mm). The hole contrast of 5mm hole for HDPe, MS and Pb sample was evaluated and and plotted against step thickness as shown in Figure(3.24). The 5 mm hole in 2 cm thick step of HDPe is barely visible with a hole contrast of 3% and with increasing thickness the hole contrast increases to a maximum of 12.7% at 8 cm thick step and again it reduces to 4.8% for further increase in the step thickness. We can infer from this that, with the present imaging setup, it is difficult to detect holes of sizes less than 5 mm for 2 cm thick HDPe and the same for higher thickness of 10 cm or more using FNR. For MS and Pb samples holes of 5 mm have a better contrast even at lesser thickness (2 cm) in comparison to that of HDPe, but at steps of high thickness (8 and 10 cm) the HDPe shows hole with comparatively higher contrast.

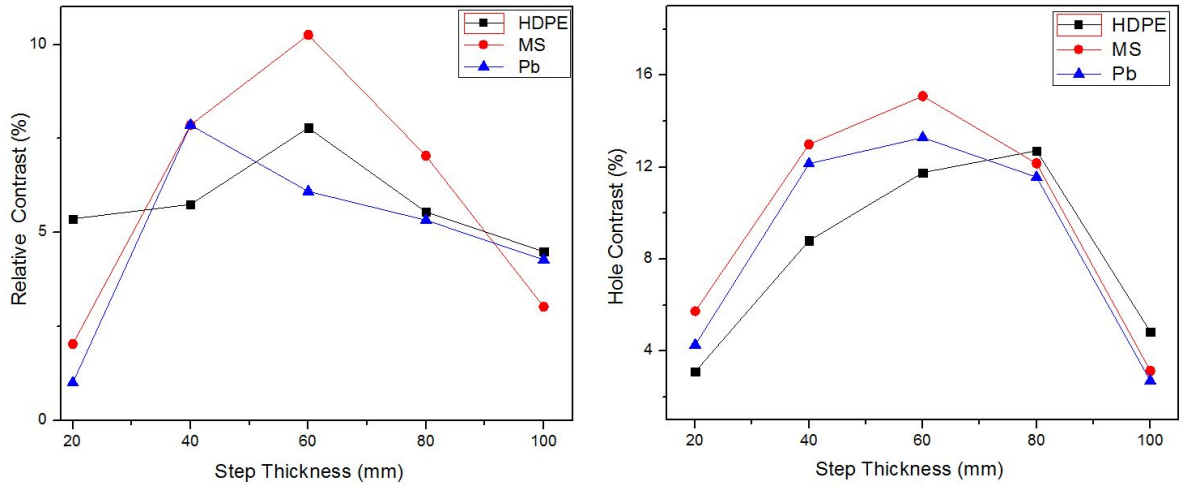

Figure 3.24: (left) Relative contrast for step wedge sample of configuration I and (right) hole contrast (5 mm) in step wedge sample of configuration II for material of HDPe, MS and lead.

3.8.4 Configuration III : Imaging of low Z material in presence of high Z material

The capability of FNR for imaging of low-Z materials encapsulated in thick high-Z shielding materials as demonstrated in simulation study with DT neutron . This makes fast neutron imaging a promising inspection modality for many practical problems and its superiority in comparison to the conventional high-energy X-ray/gamma ray imaging techniques. Such a configuration is important for imaging of low Z explosives shielded behind thick layers of high Z materials and have practical applications in nuclear security [144, 145].

The aim of this study was imaging of 5 mm hole in a HDPe block [50 mm (w) x 30 mm (h) x 100 mm (d)] placed behind a Pb block of dimension 100 mm (w) x 150 (h) mm and thickness of 50 mm and 100 mm.The images were acquired for 15 minutes. For comparison, an image was also acquired without the Pb block. The images (flat field corrected) with and without lead are shown in Figure (3.25). It can be observed from the images that 5 mm hole and HDPE-lead interface are clearly visible with good contrast in both the cases with and without the 50 mm thick Pb block. With 100 mm thick Pb the hole is not visible but the presence of HDPE could still be observed. The hole contrast and the HDPE-Pb interface relative contrast were evaluated and listed in Table 3.4. The hole contrast reduces from 13.7% to 0.8% and the HDPE-Pb interface relative

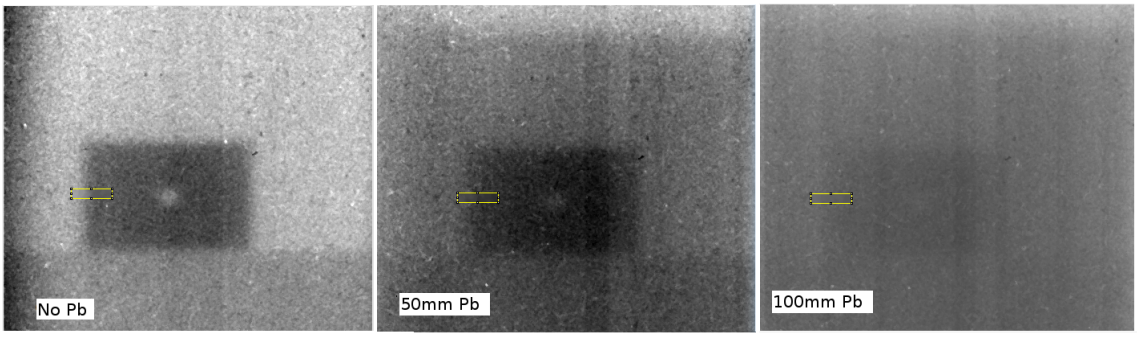

Figure 3.25: Images of 5 mm hole in HDPe in presence of lead of thickness (left) no lead (middle) 50 mm (right) 100 mm.

Table 3.5: Hole contrast, HDPe-Pb interface contrast and CNR for the HDPe block having 5mm hole

Lead thickness (mm)	hole contrast (%)	Relative contrast at HDPe-Pb interface (%)	CNR
0	13.7	21.8	5.33
50	6.2	9.7	2.32
100	0.8	5.8	0.29

contrast from 21% to 6% for a change in the Pb thickness from 0 (no Pb block) to 100 mm. The CNR of the hole was also evaluated and it was observed to be less than 1% for lead thickness of 100 mm. The CNR results are summarized in Table 3.5 with increasing Pb thickness. The CNR decreases (from 5.3 to 0.3) with the increasing Pb thickness (from 0 to 100 mm).

3.9 Conclusion

Experimental study of fast neutron radiography with indigenous designed DTNG of neutron yield of 2x10^{9}n/sec has been demonstrated and images of reasonable contrast were acquired for low/high Z materials with in 10-15 minutes exposure time. The experiments were performed using an metallic collimator assembly of mild steel, 40 mm thick plastic scintillator and EMCCD camera. Design of the collimator for an optimum flux at the image plane with varying L/D ratios was arrived through simulations using GEANT4. The designed collimator assembly of L/D =43 provided fast neutron flux of $\sim 4.6\times10^4$ ncm^{-2}s^{-1} at image plane. The images of test specimens of steps wedge and

hole features in step wedge configuration of HDPe, MS and Pb materials have shown the high transmission capability of FNR at a large thickness (100 mm) of these materials and sensitivity of system to image minimum of 5 mm size hole in such configurations. The reasonable contrast images of 5 mm hole in HDPe masked with lead of thickness 0-100 mm demonstrated the capability of the FNR system for imaging of low Z material masked inside a large sample of complex and composite structure made up of both low and high Z materials.

Two major factors affecting the image quality in such FNR systems were presence of a significant scattered neutron background and low source strength. This can be minimized with increasing sample-to- detector distance that would however decrease the flux at image plane which in turn increase the acquisition time. Alternative would be the use of neutron source of higher strength. Overall, though, despite a non-optimal setup the results were promising and demonstrated the potential for applied fast neutron imaging of robust samples containing mixed low-Z/high-Z materials at DTNG with moderate neutron yield.

Eventhough FNR based system was able to image the composite structure containing mixed low-Z/high-Z materials, but it lack the information of elemental constitutes of the interrogated object. Elemental composition can be acessed either with advanced version of FNR known as ”Fast Neutron Resonace Radiography” (FNRR) or Prompt Gamma based Neutron Activation Analysis. We have adopted PGNAA over FNRR due to its feasibility with monoenergetic neutrons (D-D or D-T) of NG , rather then a variable energy neutron source which is a pre-requisite for FNRR.

CHAPTER 4

Elemental detections in bulk with PGNAA using D-D/D-T NG

PGNAA was performed to detect the wide range of light elements (C, H, N, O, Cl, Fe) in bulk, which are key elements of the illicit materials. The study was performed with PGNAA based TNA and FNA neutron interrogation techniques using D-D/D-T NG. Neutron induced gamma signatures of various elements C, H, N, O, Cl were detected in benign samples (urea, salt, graphite)of bulk amount.

4.1 Introduction

PGNAA is widely used technique for in-situ and online elemental analysis of bulk samples in several scientific disciplines [146, 147]. Its area of application ranges from quality-control tasks in mining, environmental [148] and building construction industries [149] to contraband detection for national security in concealed containers [51]. In PGNAA, an unknown object is exposed to a neutron flux, neutron interacts with the target nuclei and compound nucleus is formed in excited state. The excited compound nucleus then de-excites quickly (less than 10^{-14} s) to the ground level by emitting gamma rays that are unique for each element [146]. These characteristic gamma rays are detected using specific gamma detectors [9]. The energy values of the gamma rays identify the nuclide and their intensities are proportional to the number of atoms.

In principle, PGNAA can detect the presence of nearly all elements and hence characterization of material composition. The relative intensity of the gamma ray peaks in the energy spectrum can be used to measure the relative fractions of elements inside the unknown target and thus can proceed to

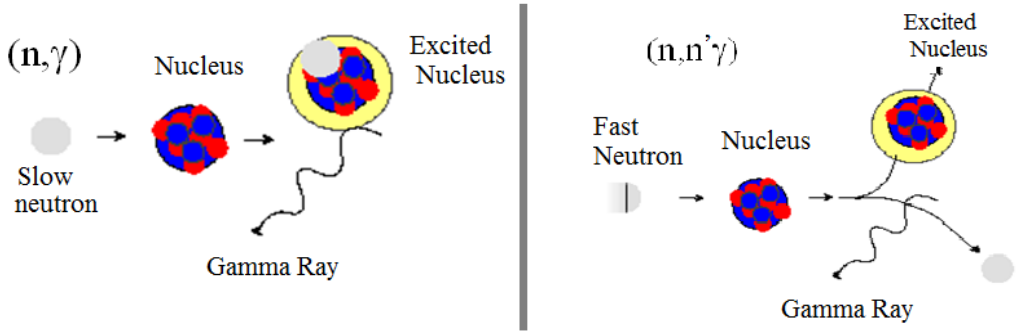

Figure 4.1: Mechanism of prompt gamma emission on neutron interaction with nucleus.

material identification. The prompt gamma-ray emissions can occur either on thermal neutron capture (n,γ) or via fast neutron inelastic scattering (n,n'γ) reactions as shown in figure(4.1). Former reaction is used for elements with appreciable thermal neutrons capture cross-sections, while later reaction is used for elements with negligible thermal neutron capture cross-section, see the Table (4.1). For an inelastic scattering event to result in gamma-ray emission, the interacting neutron must be a fast neutron with a kinetic energy larger than the energy of the gamma emission of the target isotope, see the Table (4.2). For instance, prompt gamma rays produced via 14 MeV neutron inelastic scattering from elements can be used to measure C, N and O concentrations in bulk samples [150]. However, detection of nitrogen in FNA is quite difficult task. This is because of interference of nitrogen prompt gamma peaks with oxygen peaks as well as the nitrogen peaks are of weak intensity due to their small cross section. For example, 5.12 MeV ($\sim$45 mb) [151] nitrogen peak get interfere with 2nd escape peak of 6.13 MeV (134 mb) gamma. Similarly, 6.91 MeV (60 mb) oxygen peak interfere with nearby nitrogen peak at 7.03 MeV (32 mb) [151]. On the other hand, inspite of small thermal neutron capture cross-section, nitrogen can be easily detected via prompt gamma ray (10.83 MeV) in thermal neutron capture reaction due to low background of high energy gamma.

Applications of the PGNAA technique exist in many contexts and specialized systems are designed based on the materials, elements and isotopes that must be identified in each application. Some luggage handling and buried mine detection systems rely specifically on the use of thermal neutrons [152] [153], known as TNA systems, while some cargo handling systems focus on

Table 4.1: Characteristic gamma-ray of few elements induced by thermal neutron, interest for the identification of illicit (explosives or narcotics)(taken from [158]).

Element	Reactions	Energy (MeV)	Sigma (b)
H	^{1}H (n, γ) ^{2}H	2.22	0.3326
C	^{12}C (n, γ) ^{13}C	4.945	0.026
		0.1261	0.0012
N	^{14}N (n, γ) ^{15}N	1.884	0.014
		5.267	0.03
		10.83	0.075
O	^{16}O (n, γ) ^{17}O	0.87	0.0001
Cl	^{35}Cl (n, γ)^{36}Cl	1.951	6.51
		6.11	4.3
Fe	^{56}Fe (n, γ)^{57}Fe	7.631	0.68

the use of fast neutrons [154], named FNA system. The use of PGNAA for threat detection applications is an emerging area and continuous efforts are being carried out in this field [155–157].

As described in chapter1, Thermal Neutron Analysis is primarily based on the detection of nitrogen which is found in relatively high concentrations in military explosives. On thermal neutron capture nitrogen generates a unique gamma ray energy of 10.8 MeV, highest among (almost) all elements. The intensity of the detected 10.8 MeV gamma-rays is an indication of the presence of nitrogen rich material. Although a certain concentration level of nitrogen is a good indicator of explosives, the combinations of oxygen, hydrogen and carbon should be considered since some common compounds such as melamine and silk contain high concentrations of nitrogen similar to explosives and might produce false alarms. A measurement of the C/O and N /O ratio provides good separation of explosives from benign [3] and FNA is a suitable technique for CNO element detection via inelastic scattering. Major elemental signatures with reaction type, cross-section and threshold are mentioned in the Table (4.2) for CNO. Total inelastic scattering cross section of neutron populating various states of C, N, O and Gamma Ray decay scheme from inelastic scattering of neutrons from C, N, O are shown in figure (4.2-4.3) respectively.

Table 4.2: Selected elements and relevant major neutron induced prompt gamma signature (taken from[40]), measured at En=14MeV

Element	Reaction	E_n^{thresh} (MeV)	Sigma (mb)	E_γ (MeV)
C	^{12}C(n, n'γ)^{12}C	4.8	200	4.44
N	^{14}N(n, n'γ) ^{14}N	4.7	70	2.31
O	^{16}O(n, n'γ)^{16}O	6.4	96	6.13
O	^{16}O(n, pγ)^{16}N (β^-)	10.3	38	6.13

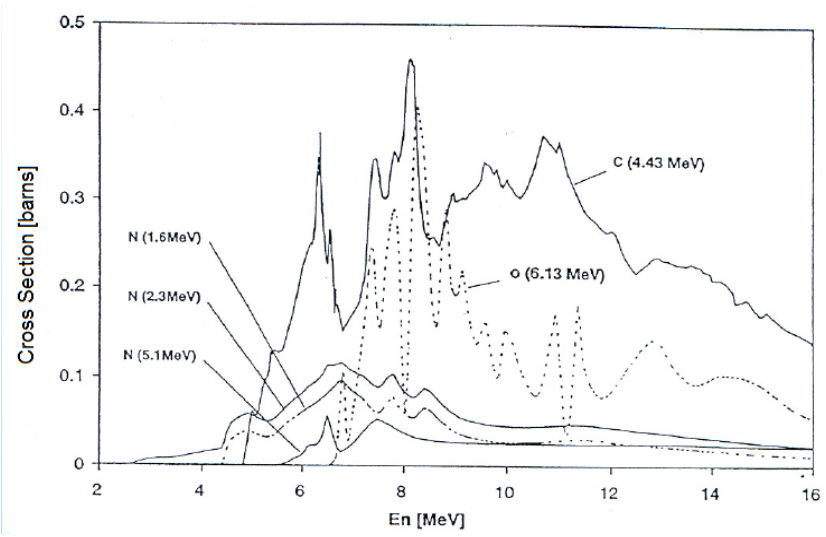

Figure 4.2: Total inelastic scattering cross section of neutron populating various states of C,N,O (taken from [150]).

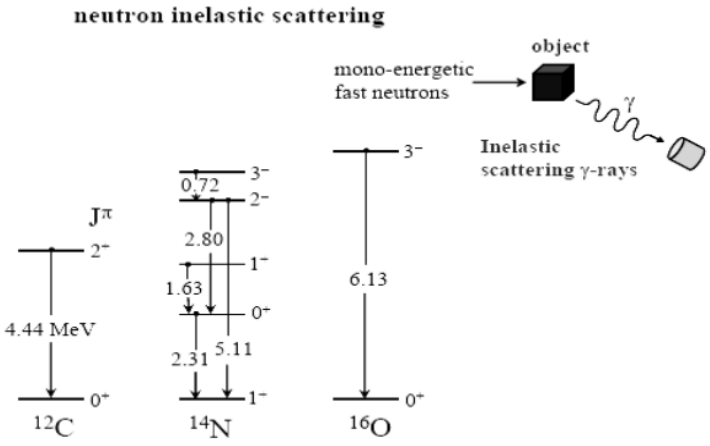

Figure 4.3: Gamma Ray decay scheme from inelastic scattering of neutrons from C,N,O [159].

4.2 Methodology

In this chapter, methodology of PGNAA via neutron interrogation TNA and FNA methods were studied for feasibility of light elements (H, C, O, N and Cl) detection in bulk using D-D/D-T NG. The representative set of elements (H, C, N, O, Cl) were selected as an example of isotopes found in most of the explosive, illicit drugs, chemical threats, coal and other benign materials. Based on neutron interaction cross section the PGNAA requires both a thermal neutron and a high energy neutron for detection of elemental signature of wide range elements. The elements H, N and Cl has high thermal neutron capture cross-section and hence their detection can be realized with D-D/D-T neutron if their energy can be moderated to thermal and then detecting the capture (n, γ) prompt gammas. Conventionally, N, H and Cl detection in bulk sample via thermal neutron capture is carried out using a ^{252}Cf neutron source [160]. In present study these elements were detected in bulk samples using thermal neutrons via D-D NG using a suitable moderator. Since the D-D/D-T NG is a clean source of neutrons with energy of 2.45/14.1 MeV respectively. In this line D-T neutrons of 14.1 MeV from DTNG can also be utilized but the moderator medium to thermalize it and shielding becomes huge, also the high energy neutrons produce excessive background.

In compare to that, it is quite easy to thermalize the D-D neutrons and the shielding requirements become less stringent. So DDNG can be labeled as a suitable test bed for thermal neutron capture reaction studies. Polyethylene and graphite are good moderators and are suitably used depending upon the requirements. On the other hand D-T based neutrons can be utilized for threshold inelastic (n, n$'$ γ) reactions of elements C,N,O having threshold and their element signature can be recorded. Since the neutron inelastic reaction threshold of the elements CNO is higher than 2.45 MeV, hence detection of these elements using D-D fast neutrons is not possible.

In the first step, we have investigated the presence of H and N in urea, Cl in salt and Fe lines in iron sample using thermalised/moderated D-D neutrons and C in graphite, C, O and N in Urea with DT neutrons. Bulk amount

of benign samples were chosen to mimic the detection of these elements in bulk explosive kind material having elemental compositions of N, H, Cl, C, O etc present in various proportions. Special approaches have been adopted for the detection of the gamma lines. Firstly, graphite moderator has been used in place of polythene (though polythene being a better candidate for moderation of neutrons) to reduce signal contamination of hydrogen line from investigated sample with the same line coming from the polythene itself. Secondly, BGO detector has been preferred in place of NaI(Tl) though the later one has comparatively better resolution and high light yield[161]. The reason can be emphasized by the higher density (7.13 gm/cc) of BGO compared to NaI (3.67 gm/cc) and hence more interaction with higher energy gammas and their detection efficiency. Care has been taken into account to shield the BGO detector from direct neutrons to avoid damage and also the production of neutron induced gamma in the BGO elements itself.

This chapter, presents the experimental study performed for detection of hydrogen, nitrogen, chlorine, carbon and oxygen elements present in bulk material using a 3"x3" BGO detector and signal-to-background ratio evaluated for each element. The chapter is organized as follows: Experimental set-Up and experiments are described in section 4.3, results are discussed in the section 4.4 and chapter is concluded in section 4.5.

4.3 Experimental Setup and Experiments

The PGNAA experiments were performed at neutron yield (n sec^{-1}) $\sim 10^7$ of D-D and $\sim 10^9$ of D-T. First experiments were carried out with DDNG. Layers of graphite moderator ((150-200 mm) were stacked in between the neutron source (D-D) and sample, to moderate/thermalise the D-D neutrons. A 75 mm x 75 mm BGO detector was placed at 100 mm below the sample, the experimental arrangement is shown in figure (4.4). The BGO was shielded all around except the sample side using 50 mm lead (Pb) blocks. The output of the BGO was fed into the input of the spectroscopy amplifier of a NIM bin (ECIL make No. PA572B) and pulse height spectra were recorded with multi-channel analyzer

Figure 4.4: (Left) Photograph of D-D based neutron generator facility and (right) close view of the experimental arrangement for the detection of capture gamma lines from urea using BGO detector.

(MCA -4K, Oxford make). MCA was calibrated with BGO detector using 1.17 MeV line of ^{60}Co and the 4.44 MeV gamma line emitted from Am-Be source [162]. The data were collected separately for background (neutron ON without sample) and signal (neutron ON with sample) for the same duration. In order to detect the characteristic 2.22 MeV hydrogen line and nitrogen 10.83 MeV line urea sample was irradiated. The chlorine prompt gamma was acquired with sample of Salt (NaCl) and one more sample irradiated was iron for spectrum of structural material. In these experiments the data for different samples were acquired for a period of 1800-3600 sec.

For inelastic prompt gamma signal detection, deuterium target was replaced with tritium, graphite moderator was removed and samples were directly irradiated with bare D-T neutrons. BGO detector was masked with polyethylene (250-300 mm) and lead block to protect it from direct D-T neutrons to reduce radiation damage as shown in Figure (4.5). The samples of graphite and urea were irradiated and data were collected with and without sample for acquisition time of nearly 1800 sec. The elemental compositions of the samples used in the experiment are listed in table (4.3).

Efficiency Curve of BGO

The photopeak efficiency of the gamma detector is an important parameter particularly for the high energy gamma detection. To estimate the photo-

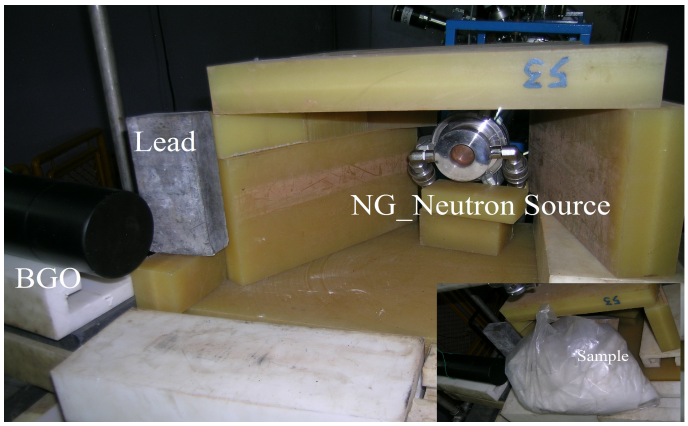

Figure 4.5: Experimental Setup for the detection of D-T Neutron induced inelastic prompt Gamma with BGO. Inset is photograph of setup with Urea Sample

Table 4.3: Samples (with their elemental compositions) used in the present study.

Sample	Formula	density (gm cm^{-3})	Composition (wt%)			
Urea	CH_4N_2O	1.33	H-6.7	C-20.0	N-46.7	O-26.7
Salt	NaCl	2.16	Na-39.35	Cl-60.66		
Iron	Fe	7.8	Fe-100			
Graphite	C	2.2	C-100			

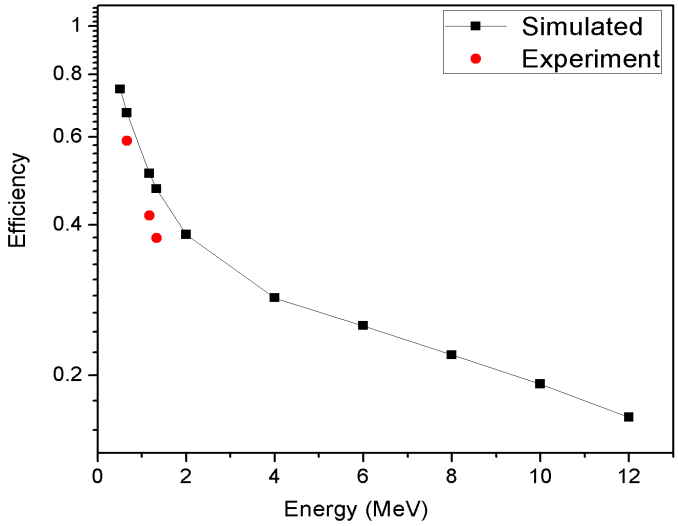

Figure 4.6: Photopeak efficiency curve for BGO (76 mm diameter, 76 mm high).

peak efficiencies at several energies GEANT4 simulation was performed as described in Chapter 5. Photopeak efficiency is defined as ratio of the total counts under photopeak to the number of the incident gamma counts on the detector. Figure 4.6 shows the photopeak efficiency curve evaluated via GEANT4 simulation. The experimental values of the efficiency at 662 KeV, 1173 $\&$ 1330 KeV were measured using ^{137} Cs and ^{60}Co gamma sources as plotted in Figure 4.6. The experimental efficiencies were found to be 12-17 $\%$ less then the simulated one. This difference can be due to variation in parameters of simulation and experimental such as accuracy of the source activity, source size and the material property of the detector (impurity etc).

4.4 Result and Discussion

4.4.1 Urea($CO(NH_2)_2$): (n,γ)

Initial experiments were performed on 2 Kgs of urea packed in a thin polythene bag. But to get an appreciable signature of the gamma lines of nitrogen and hydrogen the data collection time was large 3600 secs. So a trade-off was made between the data acquisition time and amount of sample. Finally we collected data with 4 kgs of urea and acquisition time of 1800 secs, though the respective signatures were registered within 240 secs only, as shown in Figure(4.7) with background. Major peaks at 10.83 MeV – nitrogen capture photopeak, its single escape (SE) peak -10.32 MeV and 2.22 MeV - hydrogen capture line were observed above background. Though the presence of 2.22 MeV gamma line in the background merges with the hydrogen capture line, it can be distinguished clearly. The nitrogen prompt gamma ray photo peak was located at the higher energy end of the pulse height spectrum. The inset graph (Figure(4.7)) depicts the nitrogen photopeak as a clean signal with no background contamination. The apparent slight drift in the peak position can be attributed to the drift in BGO response, due to temperature variation of electronics for the said acquisition time. Further higher energies 10.83 MeV gamma rays had poor statistics because photo absorption cross-section of gamma rays

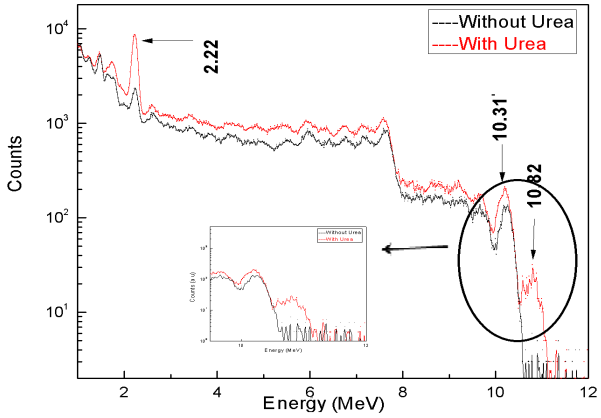

Figure 4.7: Capture prompt gamma pulse height spectra of urea sample(red) and background (black). The nitrogen photopeak(10.83 MeV),SE peak(10.31 MeV) and Hydrogen peak at 2.22 MeV are labelled.

above approximately 3 MeV energy decreases drastically due to competing compton scattering and pair production reactions. The photoelectric cross-section drops by a factor of nearly 300 from 2 to 10 MeV gamma rays. This reduces detection probability of high energy gamma rays at 10.83 MeV.

Nitrogen single escape peak does not possess the same quality as its photo-peak because of the presence of the neutron induced 10.2 MeV line of germanium ^{73}Ge (n,γ) present in BGO [6]. Shielding the BGO detector with thermal neutron absorbing material can further reduced the interference of ^{73}Ge with the nitrogen SE lines. The signal(S)-to-background(B) ratios (or say SNR) evaluated for respective photopeaks of hydrogen and nitrogen are tabulated in Table 4.4. For data analysis purpose, the signal was peak integration counts after subtraction of background and background was the integrated counts under the same region from the background spectrum. The SNR for nitrogen peak (10.83 MeV) was 7.6 much higher than that obtained for hydrogen line 1.8.

4.4.2 Salt (NaCl): (n,γ)

The emphasis to carry out the detection chlorine (Cl) capture lines in salt as feasibility is attributed to detect the same in chlorine based explosives. Since Cl has high thermal neutron capture cross section (43b) than that of sodium (0.53b) the capture gammas of Cl are much more detectable than Na [158]. In a data collection time of 1200 seconds we could detect four Chlorine photo-

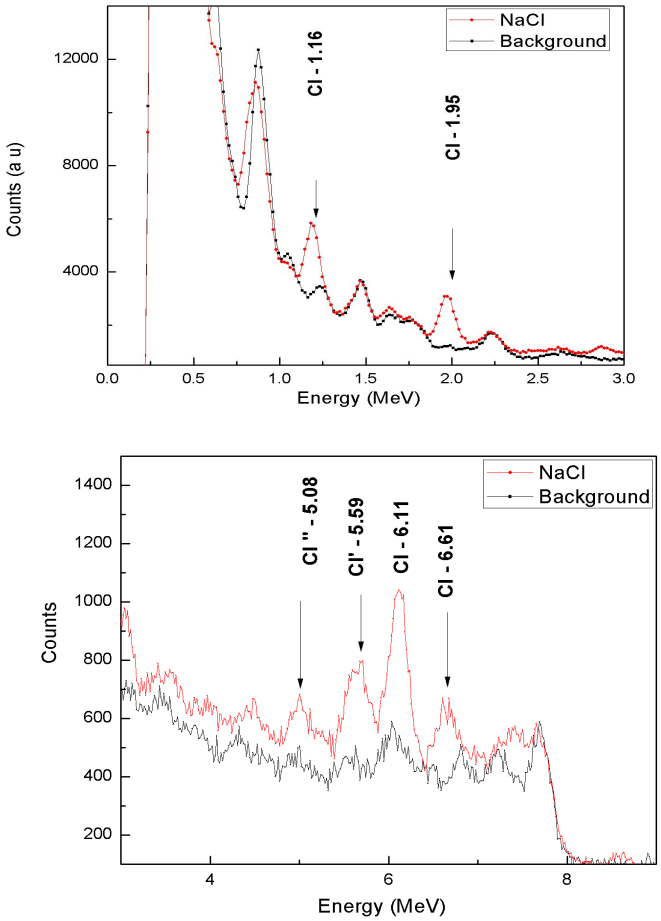

Figure 4.8: Prompt gamma pulse height spectra of NaCl sample (red) and background (black). Top graph (enlarged spectra over the range 0-3 MeV) shows the chlorine lines at 1.16 MeV and 1.95 MeV. The bottom graph (Enlarged spectra over the range 3-8 MeV) shows the Chlorine peaks Cl–6.11 MeV and Cl-6.619 MeV along with its single escape peak (5.599 MeV) and double escape peak (5.08 MeV).

peaks and one of their escape peaks with good intensity over the background as shown in Figure(4.8).

Spectra over the energy range 0-8 MeV presented with two energy regions (0-3 MeV and above 3 MeV) to have enlarged view of energy peaks in respective region. Top spectrum of Figure(4.8) shows two prominent peaks at 1.16 MeV and 1.95 MeV. Above the 3 MeV the major peaks observed were 6.11 MeV, 6.62 MeV photopeaks and their escape peaks 5.59 MeV and 5.08 MeV. The first escape peak of 6.62 MeV overlaps with 6.11 MeV photopeak. The SNR ratio evaluated for 1.95 MeV was 1 and for remaining peaks it was much less than 1.

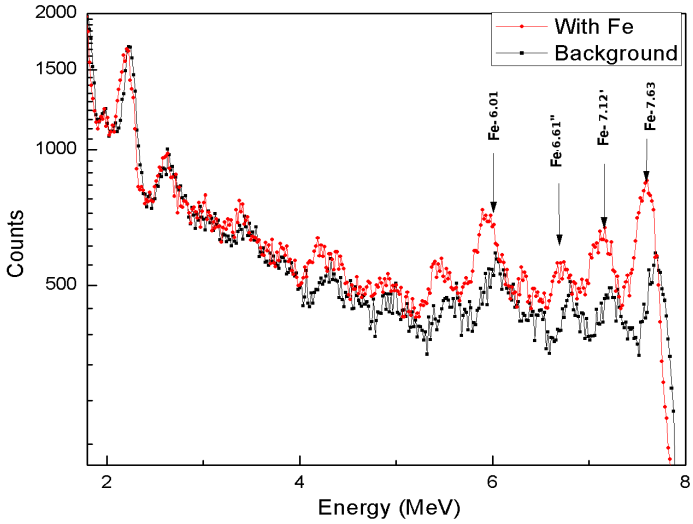

Figure 4.9: Measured prompt gamma pulse height spectra of iron sample (red) and background (black) without sample

4.4.3 Iron (Fe):(n,γ)

We have also detected a couple of iron capture lines by taking iron sheets as sample. Particularly the lines corresponding to photopeak 7.63 MeV, its escape peaks and the 6.01 MeV are clearly distinguished from the background as shown in Figure(4.9). The iron being a part of structural material the knowledge of neutron induced gamma capture lines are of importance as it contributes to background spectra. In this case, the signal-to-noise ratio obtained was also less than 1.

4.4.4 Graphite(C):(n, n'γ)

Considering carbon as a promising elemental constituent of explosives and good candidate of PGNAA because of the strong 4.44 MeV line from the ^{12}C(n, n$\prime$ γ) reaction a pure carbon sample (graphite) was chosen for investigation. Graphite block was irradiated for 1200 seconds with DT neutron. The prompt gamma-ray spectrum of a 7.6 cm thick rectangular graphite target with background is shown in Figure (4.10). The carbon gamma line at 4.43 MeV and its first escape at 3.91 MeV (SE) can be observed in sample spectrum above the background. Such lines were not observed with earlier case of urea irradiation with thermal neutrons. It can also be noted down that the strong peak at 4.44

MeV and 2.22 MeV recorded in background spectrum , the source of background 4.44 MeV gamma line arised from the fast neutron interaction with polyethelne $(CH_2)_n$ used as shielding material for BGO detector. The hydrogen capture line 2.2 MeV was due to some of the fast neutrons moderated in the bulk shielding or target material and get captured in polythene. However the SNR ratio for 4.44 MeV obtained was again less than one.

4.4.5 Urea:(n, n'γ)

Urea sample spectrum acquired with D-T neutron is shown in Figure (4.11). The various gamma lines corresponds to different elements observed were Carbon (^{12}C) – 4.44 MeV, its first escape(SE) –3.92 MeV, Nitrogen (^{14}N) – 5.12 MeV and Oxygen (^{16}O) – 6.13 MeV, its first escape (SE) – 5.62 MeV and 6.91 MeV above the background. Carbon line intensity is not as strong as observed in case of graphite that is because of small amount of carbon (800 gm) in urea in compare to that in graphite. Thus, the SNR this case is still poor. The nitrogen line at 5.12 MeV peak intensity is very small even though the content of nitrogen is nearly 47% in urea that means nitrogen of 1.8 kg amount present in $\sim$4kg urea. That is due to small cross-section ($\sim$45 mb) of fast neutron of (n, n $\prime\,\gamma$) reaction [163]. It can be noted that oxygen peak at 6.13 (5.62 (SE)) and 6.91 MeV were also observed in the background, that is possibly due to interaction of fast neutrons with oxygen composition of BGO.

The C, O and N are significant component elements of urea and the relative intensity of characteristic gamma-ray energies (C,O,N) present in the sample can be used to determine the quantity of elements in sample. Since the knowledge of the ratio of these elements and analysis the peak of energy is considered to be key factor to distinguish the benign and illicit material [5]. However, in this experiment the background intensity is very high and the element's intensity above the background is quite small. Therefore it is quite difficult to calculate the quantitative value of these elements with required accuracy.

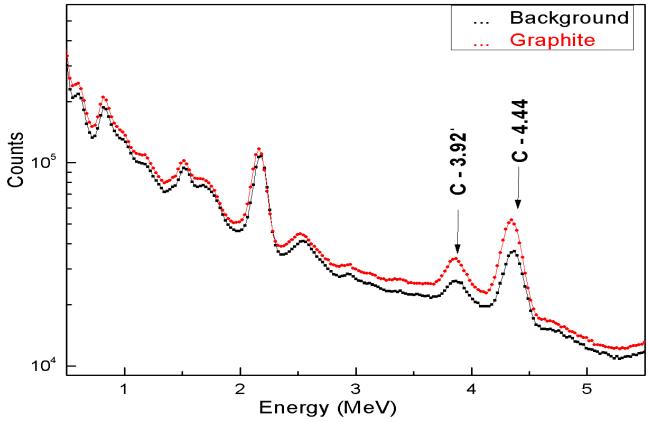

Figure 4.10: DT neutron induced prompt gamma spectrum of graphite sample (red) with background (black)

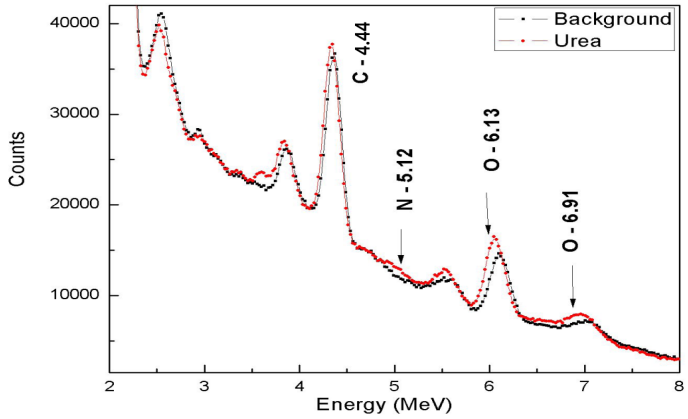

Figure 4.11: DT neutorn induced Prompt Gamma Spectrum of Urea sample (red) with background (black)

Table 4.4: Signal (S) to Background (B) of different photopeaks.

PGNAA Method	Sample	elements	Peak Energy (MeV)	S/B
TNA	Urea	H	2.22	1.77±0.01
		N	10.83	7.6±0.98
	Salt	Cl	1.16	0.64 ±0.01
			1.95	1.01±0.01
			6.11	0.58±0.01
			6.62	0.31±0.004
	Iron	Fe	6.018	0.09±0.01
			7.631	0.69 ±0.01
FNA	Graphite	C	4.44	0.36 ±0.006
	Urea	C	4.44	0.16 ±0.003
		N	5.12	0.15 ± 0.004
		O	6.13	0.28±0.006
			6.91	0.023±0.003

4.5 Summary

The present work has demonstrated the detection of elemental signature of hydrogen, nitrogen, chlorine and iron elements with TNA via (n, γ) reaction using D-D NG and inelastic signatures (n, n$\prime$ γ) of Carbon, Nitrogen and Oxygen elements could detected using FNA with D-T neutron . The most challenging task however, has been the detection of high energy gamma rays 10.83 MeV from small amounts of nitrogen (1.8 kg) in urea using 3″ x 3″ BGO gamma detector. This is important in view of threat material detection which are rich in nitrogen. Inspite of low neutron yield of D-D NG and small amounts of nitrogen, the nitrogen signal detected in urea is of reasonable intensity with good SNR of 7.6. The prominent chlorine lines detected from NaCl sample indicate the possibility of TNA with DDNG for application of chlorine based narcotics detection. However in this case the SNR was not as good as of nitrogen. Also the capture lines of Fe detected could provide useful information's about the surrounding or structural materials.

Inelastic signatures of C, O and N in urea observed with FNA, which could not be detected with TNA, due to their threshold reaction. However, the intensities of C, O and N element lines recorded were not high above the background and have shown poor SNR, much less than one.

In the present experiment the main difficulty faced was high background gamma rays emitted from the surrounding materials or structural materials of system during neutron irradiation. A method for improvement of SNR has been discussed in next chapters 5-6.

CHAPTER 5

Modelling of Associated Particle Imaging

5.1 Introduction

As discussed in chapter 4 the PGNAA based conventional neutron interrogation methods TNA and FNA have shown one of the enabling technology for elemental detection in bulk. FNA is an improvement over TNA in respect to multi-element detection such as C and O elements having threshold reaction, which are important for explosive detection. However, study of FNA has showed two major drawbacks (1) poor imaging capability and (2) high background due to DT neutron's interaction with surroundings, since DTNG emits neutron in all direction. One way to reduce huge effect of high background is to reduce the volume that is irradiated by DT neutron source, that means collimating the DT neutron source as well as shield the gamma detectors. To collimate DT neutron source, one require a large shielding and it will make system bulky. The equivalent to a tightly collimated beam of neutrons can be obtained by tagging the neutron with the associated alpha particle created by the D-T reaction. The method, known as associated particle imaging.

API is a three-dimensional, imaging technique for determining the location and chemical composition of hidden materials such as drugs or explosives. The technique is based on the use of fast neutrons produced by accelerating deuterium ions and bombarded onto a tritium target. This reaction produces neutrons and alpha particles of 14.1 and 3.5 MeV energies, respectively. The two particles are correlated in space and time relative to the production site in the tritium target and this correlation is used to tag a specific fraction of the neutrons that are used for imaging. The neutrons within this "beam" defined by the detection of correlated alpha particles (known "Tagged neutrons"), interact with the nuclei of the object under interrogation and can produce gamma

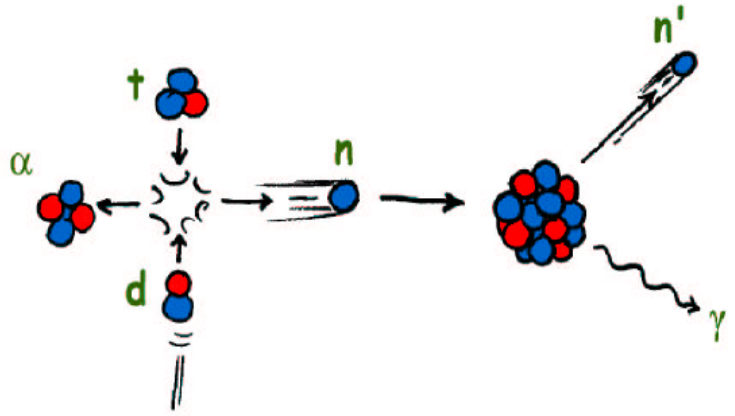

Figure 5.1: Schematic view of the DT tagged neutron production and nuclear reaction initiated by tagged neutrons.

radiation (Figure 5.1). The measurement of the time difference between the detection of the alpha particle and the detection of the gamma radiation provides a measurement of the distance traveled by the neutron before it scattered from a nucleus in the interrogated object. The energy spectrum of the gamma rays provides a method of identifying the nuclear species that the neutron scattered from, thus the type of material within the object. A schematic representation of the technique is shown in Fig (5.2). Hence, in contrast to traditional neutron interrogation techniques, API is a self-collimating method where the alpha particles are used to determine the position and direction of the neutrons emitted [45]. Since neutrons are emitted isotropically from the source, the alpha particles limit the background noise by selecting events that are caused by tagged neutrons only.

The implementation and to develop a complete API system with maximum true positives, various parameters needs to be studied thoroughly. These include detector response, detector geometry arrangement, data set generation of pure elemental spectra, algorithm development for spectral analysis and 3D image construction of the inspected object. As a first step towards development of API System, a computer simulation can provide fast and effective estimation of different parameters and theirs dependencies for a configuration of experimental device. To facilitate the design and construction of a prototype lab based API system, a simulation model was developed using the Geant4

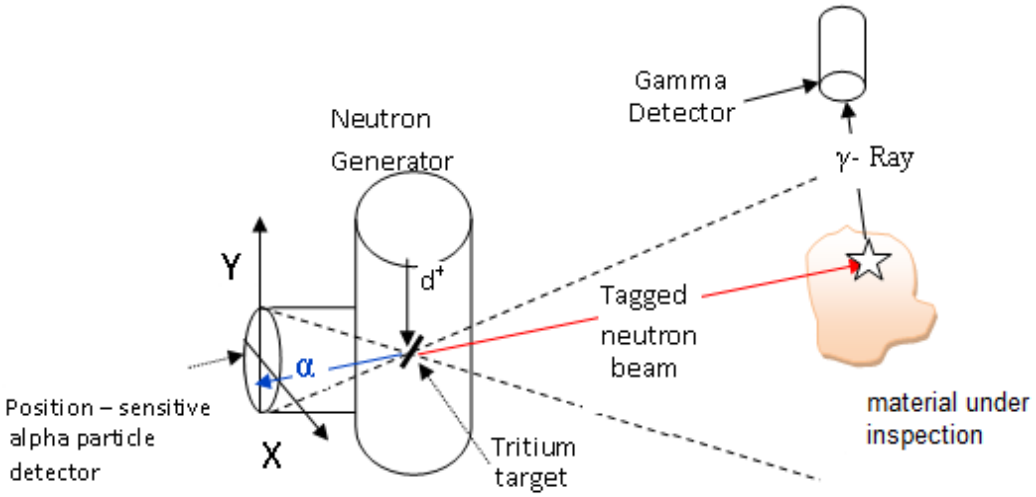

Figure 5.2: Schematic representation of Associated Particle Imaging Technique.

[107]. Tagged neutron beam was modeled and neutron induced gamma was measured with an array of BGO gamma detectors. To incorporate the physical response of the BGO in simulation, the energy deposited in BGO detector was smeared and matched with experimentally measured (FWHM) resolution. Simulations were implemented in different stages. In the first step detectors' elemental response was simulated for different elements (C, N, O, Al and Fe). These elemental responses take the realistic spectral features of 14.1 MeV neutron interaction into account and their individual intensity from a measured gamma ray spectrum of a sample containing mixture of them can be correctly determined. In the next step various benign and explosives samples were irradiated and their spectra were decomposed/unfolded with linear combination of reference data set of pure elements to extract the individual element's C, N and O contribution. Finally an explosive (1 kg RDX) placed inside a container filled with metallic / organic matrix was simulated to study the effects of matrix material on detection capability of the system.

This chapter present the modeling of API technique with BGO detectors in Geant4 environment for (a) generating tagged neutrons, their transport and interactions within a bulk to induce characteristic gamma emission and their detection, (b) quantitative analysis of different sample spectra with pure elemental spectra, (c) effect of matrices on sample spectra and (c) 2D- 3D image

reconstruction of the interrogated object using the neutron and gamma-ray time of flight information.

5.2 Simulation

Simulation studies were carried out with Geant. The version G4.10.01p.02 was used in this work. It provides a Monte Carlo based programming environment for simulating problems of production and transport of radiation through different materials [133],[Appendix C].

5.2.1 Gamma response of BGO detector

Response of gamma detector play significant role in spectrum analysis as well as in quantitative analysis of complex spectra. To incorporate the detector response in the simulation, BGO detector was modelled as a 3"x 3 " cylindrical vessel filled with BGO material, encapsulated in an aluminium casing of 1 mm thickness. A monoenergetic point source of gamma-rays was positioned at 10 cm distance (same distance as in experiments) from detector face and gamma-rays were directed onto the cell along its symmetry axis. The amplitude of the signal was provided by a sensitive-detector class which recorded the total energy deposited in BGO volume. The simulations were performed with different energies 0.511 MeV, 0.662 MeV, 1.170 MeV & 1.330 MeV and 4.44 MeV. While performing the simulation it is essential to apply some corrections to match the simulated spectrum to that of experimental spectrum. The major correction is for the effect of energy resolution observed in the experimental spectrum which depends on the energy of the photon. The experimentally measured energy resolution was taken into account as (FWHM/E_γ) = 0.095 $(E_\gamma)^{-1/2}$, where E_γ is gamma energy in MeV. It was obtained by adjusting the width of the 0.662 MeV peak in the simulated spectra to match this peak width in the experimental spectra of ^{137}Cs. It was further used for other energies of 0.511 MeV, 1.170 MeV & 1.330 MeV and 4.44 MeV and compared with their experimental spectra. Experimental spectra of different energies were acquired with a BGO detector of size 3″×3″ using different gamma sources of ^{22}Na

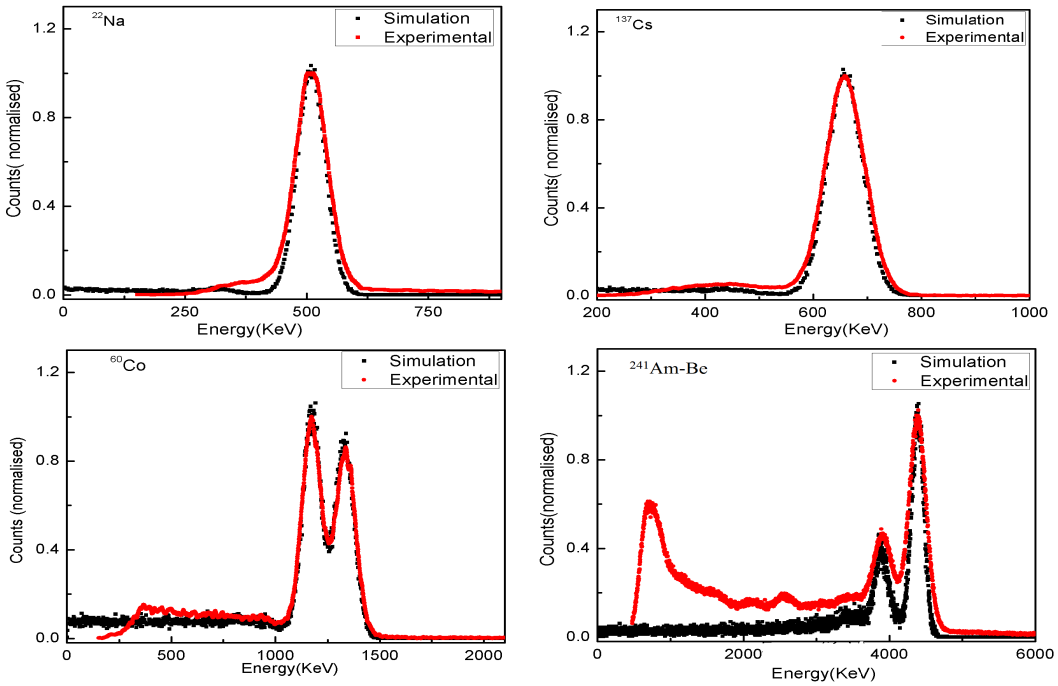

Figure 5.3: Comparison of Simulated and Experimental Gamma response of BGO detector at different energies.

(0.511 MeV), ^{137}Cs (0.662 MeV), ^{6}Co (1.170 MeV & 1.330 MeV)) and an isotopic neutron source of ^{241}Am-^{9}Be for 4.44 MeV. The details of these gamma sources have been provided in the Appendix A and the experimental setup has been described in next chapter 6.

Figure (5.3) presents simulated and measured energy spectra of different gamma energies 0.511 MeV, 0.662 MeV, 1.173 MeV, 1.330 MeV and 4.44 MeV. It shows that simulated spectra are in close match with experimental result except at 4.44 MeV energy. The full width at half maximum (in %) obtained from simulated spectra at different energies are listed in Table (5.1). The experimentally measured energy resolution ($\sim$ 5.8 %) at 4.44 MeV is slightly higher than that of simulated spectra 4.6 %. This is because Am-Be source emits neutrons with typical neutron spectrum including photons of energy 4.44 MeV. In simulation only 4.44 MeV gamma was simulated and the neutron part was not taken into account. Also the presence of neutron spectrum as well as gamma background due to interaction of neutrons with surrounding material makes experimental spectrum quite different from that of simulated one particularly at lower energy region.

Table 5.1: Energy Resolution of BGO detector at different energies

Source	Energy (MeV)	FWHM (%)
^{22} Na	0.511	13.31±0.05
^{137}Cs	0.662	11.68±0.08
^{60}Co	1.173	8.77±0.07
	1.330	8.23±0.07
^{241}Am-Be	4.44	4.56±0.09

5.2.2 Modelling of Tagged Neutron with BGO

Tagged neutron beam in API was modeled with an isotropic point source using Primary Generator Action class invoking two particle guns, one producing a 14.1 MeV neutron and the other producing a 3.5 MeV alpha particle at same time and in opposite directions. The size of the tagged neutron beam is defined by an alpha detector's dimension (5×5 cm^2) and its position (13 cm) from the tritium target. In this simulation, X-Y plane is determined by the alpha detector and the z axis is determined by its perpendicular plane in the direction of neutron towards the experimental volume. 14.1 MeV neutron source particles were tracked towards sample (cube having side length of 25 cm) placed at 65 cm (center of object) with respect to source position. An array of 16 numbers of BGO detectors were arranged in a square geometry around the sample placed at 30 cm distance from the object center and is vertically aligned as shown in Figure (5.4). These detectors were defined to be sensitive to record the necessary hit informations. The energy and time of the particle hitting at any of the detector were recorded to build the energy and time spectrum respectively. To be specific, the time here refers the total flight time of neutron from the start of neutron emission, its interaction with the sample and generation of a gamma-ray (or scattered neutron) to its hitting in the gamma detector. In similar way (x,y) position of the associated alpha particle emitted with tagged neutron were recorded from position sensitive alpha detector. The simulated geometry (Figure 5.4) was designed to approximate the geometry of experimental API set up at laboratory.

In the first step, different samples viz. graphite (for C), liquid nitrogen (for N), water (for O), Aluminum (Al) and Iron (Fe) were simulated and a data set

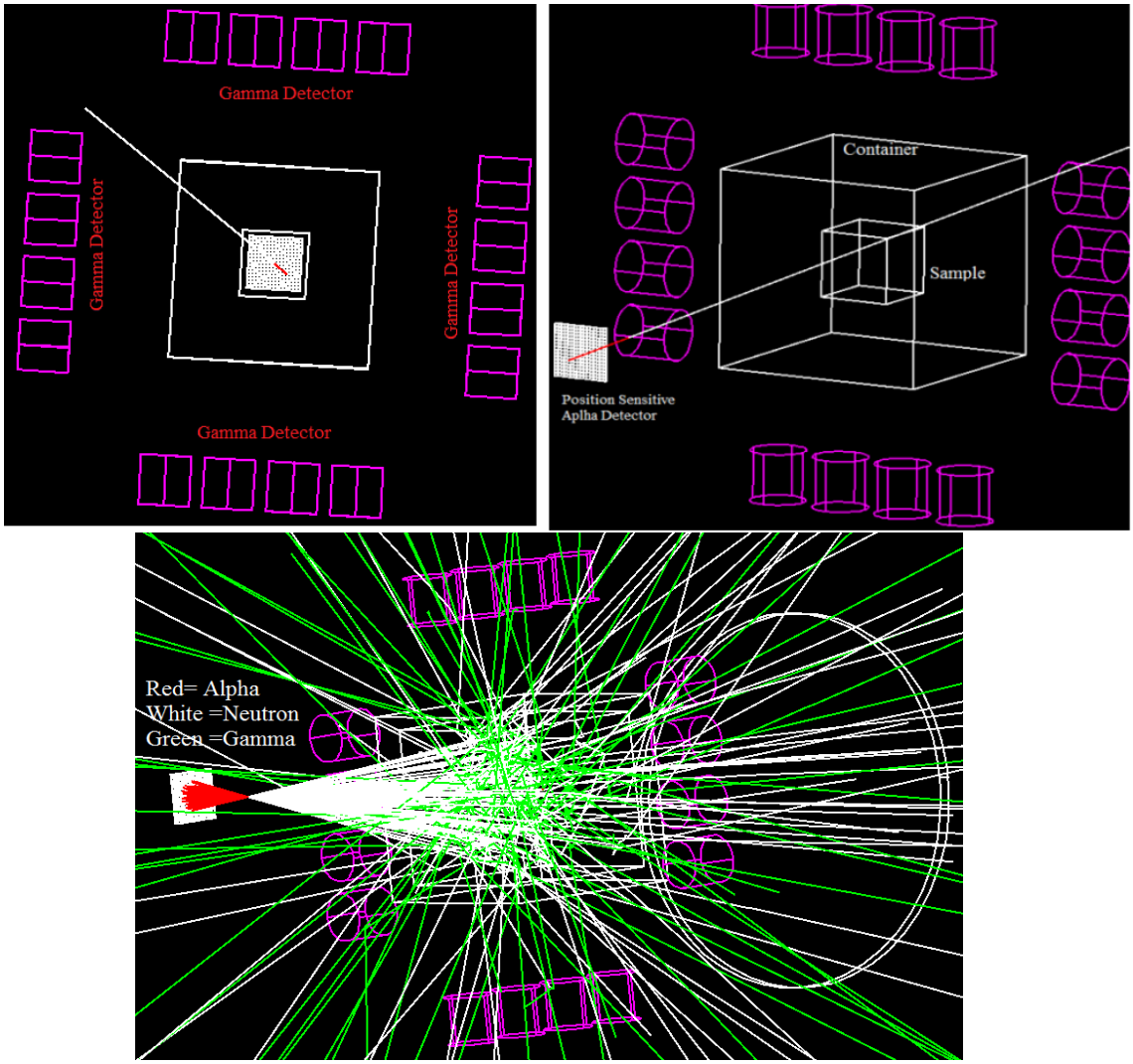

Figure 5.4: GEANT4 simulated Geometry with BGO's (top left) front View (top right) side View and (bottom) Full geometry with neutron beam ON.

of neutron induced gamma spectra of pure elements were generated. In the second step the various benign (urea, melamine) and explosives (RDX, TNT and Ammonium nitrate) samples were simulated and spectra were acquired. Table 5.2 details the list of materials of the simulated objects. Further to study the matrix effect and to detect hidden explosive, a container of size 30 cm $\times$30 cm $\times$ 50 cm (W $\times$ H $\times$ L) was simulated with an explosive target of 1 kg RDX (cube of 8.2 cm) placed at its center (65 cm from neutron source). The explosive was surrounded with matrix material that fills all the remaining container volume. Wood and iron were used as filler material with an average density of 0.1 and 0.2 gm/cc.

Table 5.2: List of the samples used in the study.

Samplel	Element	Density (g cm^{-3})
Graphite	C	2.23
Water	H_2O	1.0
Liq. Nitrogen	N	0.806
Aluminum	Al	2.7
Iron	Fe	7.86
Liq. Oxygen	O	1.141
TNT	$C_7H_5N_3O_6$	1.654
RDX	$C_3H_6N_6$ O_6	1.82
Urea	CH_4N_2O	1.32
Ammonium Nitrate	$H_4N_2O_3$	1.72
Melamine	$C_3H_6N_6$	1.574
Wood matrix	$C_{2.59}H_{5.05}N_{0.55}O_{1.6}$	0.1-0.2

Table 5.3: Main characteristics gamma signature of different elements on interaction with 14.1 MeV neutron (taken from [163][151]).

Elements	E(MeV) (σ[mb])	Reaction
C	4.439 (187)	^{12}C(n, n$'\gamma$) ^{12}C
O	2.74 (38)	^{16}O(n, n$'\gamma$) ^{16}O
	3.10 (22)	^{16}O(n, $\alpha\gamma$)^{13}C
	3.68 (58)	^{16}O(n, $\alpha\gamma$)^{13}C
	3.85 (34)	^{16}O(n, $\alpha\gamma$)^{13}C
	4.44 (40)	^{16}O(n, n$'\alpha\gamma$)^{12}C
	6.13 (148)	^{16}O(n, n$'\gamma$)^{16}O
	6.91(47)	^{16}O(n, n$'\gamma$)^{16}O
N	1.63 (21)	^{14}N(n, n$'\gamma$)^{14}N
	2.30 (41)	^{14}N(n, n$'\gamma$)^{14}N
	4.44 (54)	^{14}N(n, tγ)^{12}C
	5.12 (45)	^{14}N(n, n$'\gamma$)^{14}N
	7.03 (32)	^{14}N(n, n$'\gamma$)^{14}N
Al	1.81 (184)	^{27}Al(n, dγ)
	2.21 (145)	^{27}Al(n, n$'\gamma$)^{27}Al
	3.00 (111)	^{27}Al(n, n$'\gamma$)^{27}Al
	3.20 (32)	^{27}Al(n, n$'\gamma$)^{27}Al
Fe	0.85 (620)	^{56}Fe(n, n$'\gamma$)^{56}Fe
	1.24 (290)	^{576}Fe (n, n$'\gamma$)^{56}Fe
	1.69(54)	^{56}Fe(n, n$'\gamma$)^{56}Fe

5.3 Results, Analysis and Discussion

5.3.1 Energy and Time Spectra of water sample

Before proceeding for actual simulation, a test sample of water was simulated and its energy and time spectra were recorded as shown in Figure 5.5. Time spectrum shows one prominent peak (T1) around followed by a broad and smaller peak (T2). The first dominant peak (T1) corresponds to the neutron induced gammas from sample and second broad peak (T2) is the result of neutrons scattered from sample and the reaching at gamma detector. Hence the energy spectrum have contributions from sample as well as of scattered neutrons. To get neutron induced gamma spectrum of sample as well a scattered neutrons, one needs to put suitable gate on time spectrum accordingly. We have put a 5 ns time window around T1 (11-16 ns) peak and respective time correlated energy spectrum (E_T1) obtained as shown in Figure 5.5b. In the same figure, energy spectrum (E_T2) corresponds to the time T2 ($>$ 16 ns) and energy spectrum (E_Total) when no time window was applied has also been shown for sake of comparison. It can be observed that scattered neutrons have significant contribution in energy region below 2 MeV and minimal contribution in the higher region. On the other hand sample spectrum (E_T1) has several gamma peaks (discussed in next section) in the region of 2-8 MeV. Hence via appropriate time window sample gamma spectrum can be extracted from total energy spectrum without contribution of scattered neutron.

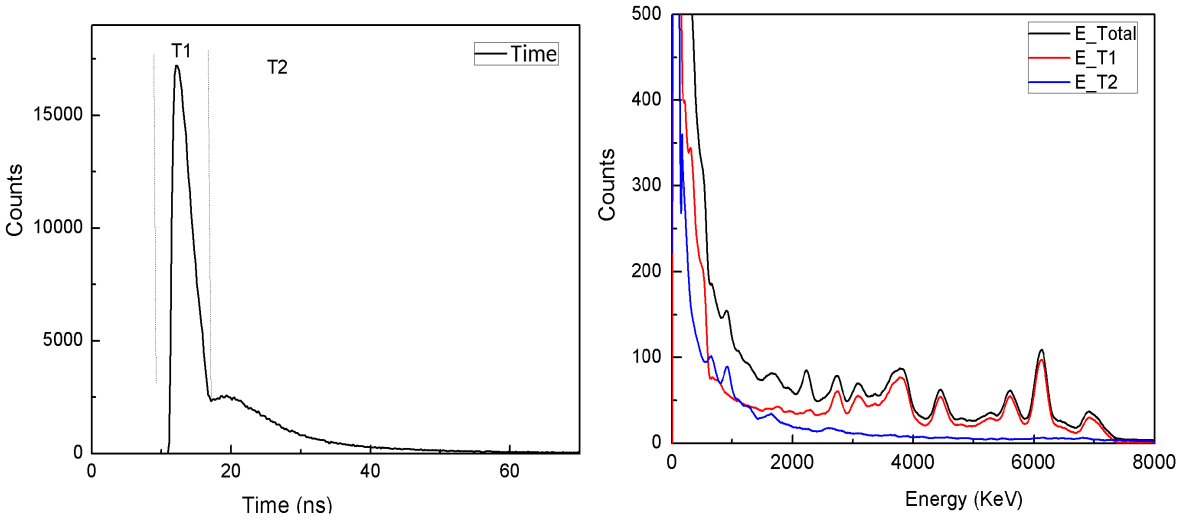

Figure 5.5: Simulated water sample spectra (left) Time Spectrum and (right) Energy spectra obtained when, (E_Total) - no time window applied, (E_T1) - with 5 ns (11-16 ns) time window and (E_T2) with a time window above 16 ns.

5.3.2 Elemental Spectra

This section deals with study of 14.1 MeV neutrons induced inelastic gamma rays on C, N, O, Al and Fe elements. List of the main characteristic gamma lines of these elements with 14.1 MeV neutrons are presented in Table 5.3 with their cross section and type of reaction. The C,O and N elements are of importance in material identification and their unique ratios C/O, N/O decide the nature (explosive or benign) of the investigated material. The elements Al and Fe were studied as they are structural materials and their contributions cannot be ignored.

In the simulation geometry water sample was replaced with choice of material (graphite (C), liquid oxygen (O), liquid Nitrogen (N), Aluminum (Al) and iron (Fe) (Table 5.2). The time correlated energy spectra (obtained with a time window selection, as explained in the previous section 5.3.1) of different samples are shown in Figure(5.6). The major peaks observed in different spectra were labeled to highlight the characteristic gamma signatures of the respective element. These are 4.44 MeV from carbon, 1.63 MeV, 2.30 MeV, 4.44 MeV, 5.12 MeV, 7.03 MeV from nitrogen, 2.74 MeV, 3.08 MeV, 3.68 MeV, 3.85 MeV, 4.44 MeV, 6.13 MeV, 6.91 MeV from oxygen 1.81 MeV, 2.21 MeV, 3.0 MeV from aluminum and 0.84 MeV, 1.24 MeV, 1.69 MeV from iron.

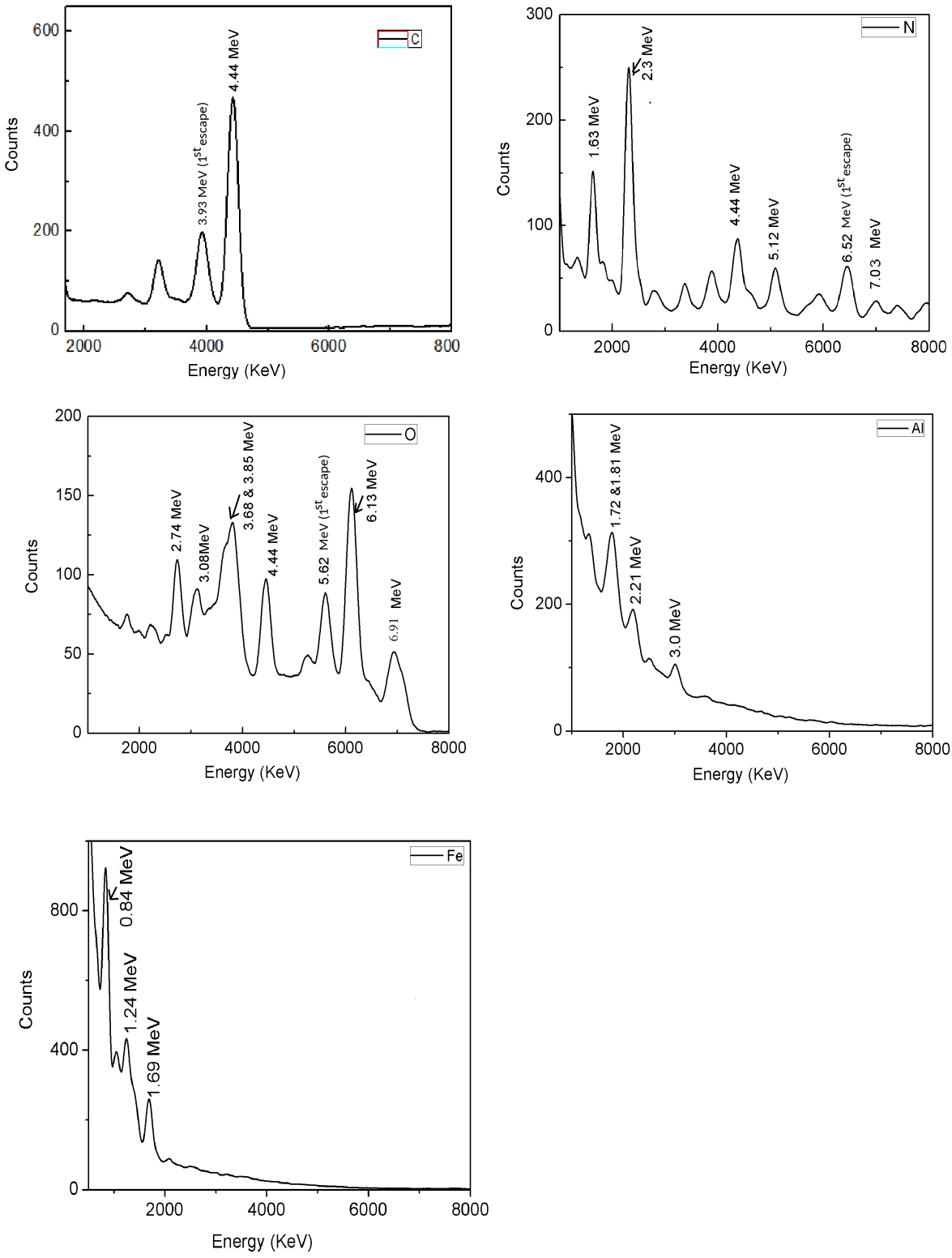

Figure 5.6: Simulated elemental gamma ray spectra of C, O, N, Al and Fe as reference spectra for analysis of complex spectra .

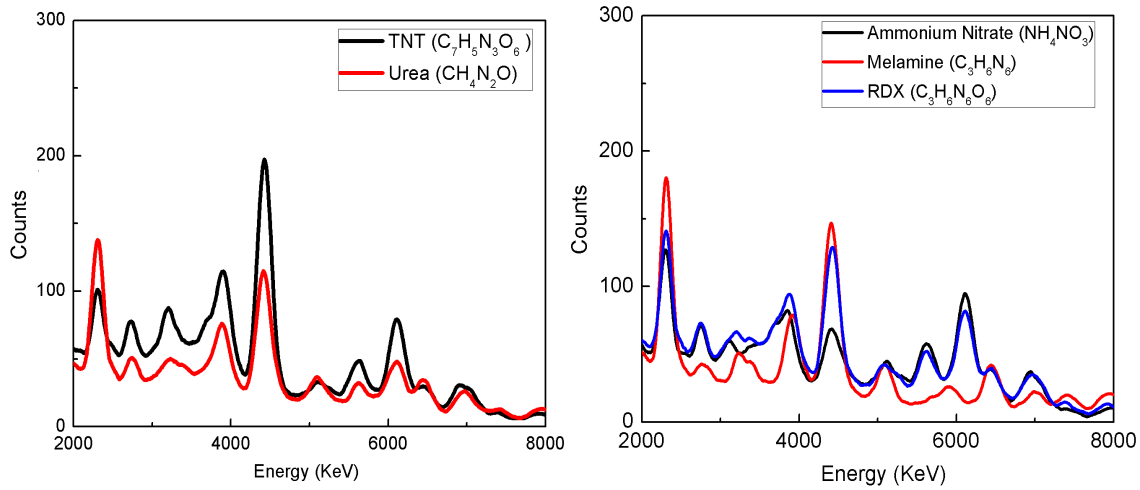

Figure 5.7: Simulated time correlated energy spectra of investigated samples (Left) TNT, Urea sample and (Right) Ammonium Nitrate (AN), Melamine and RDX.

5.3.3 Complex Sample Spectra

After successful generation of reference data set of pure elements, the sample spectra of benign and explosives were analyzed. Sample studied were Urea, Melamine, RDX, TNT and Ammonium nitrate. Simulated spectra of these materials are shown in Figure (5.7). The simulated spectra of TNT, Urea and RDX has shown the elemental signatures of all three elements C, N, O. while Melamine spectrum shows no oxygen peak (6.13 MeV) due to absence of oxygen element. Similarly in Ammonium nitrate, carbon is absent, hence no carbon peak - 4.44 MeV should be observed. But in the spectrum a low intensity peak at 4.44 MeV has been observed that is due to from contribution of oxygen (^{16}O(n, n' $\alpha\gamma$)^{12}C) and nitrogen ^{14}N(n,tγ)^{12}C elements of Ammonium nitrate.

5.3.4 Analysis of sample spectra and CNO element's contribution

To identify the sample from gamma spectrum, the contribution of carbon, oxygen and nitrogen elements have to be extracted from the spectrum. To deduce these individual element's contribution, the sample spectrum (S^{sim}) was fitted with a spectrum (I^{fit}). The I^{fit} fit is obtained by linear combination of simu-

lated pure elemental spectra or say responses (R).

$$I^{sim} = \sum_{i=0}^{i=n} a_i R \;\; = \;\; a_1 C^{sim} + a_2 N^{sim} + a_3 O^{sim} + ... \tag{5.1}$$

Where, C^{sim}, O^{sim} and N^{sim} are the simulated pure elemental spectra of C, O and N, respectively. The a_i's are the corresponding coefficient of fitting. The three coefficient parameters (or more depending on the number of elements chosen) are set as unknown and were obtained by minimizing the chi square of fitting χ^2. The coefficients (a_i's) corresponding to the smallest χ^2 were taken as the optimized fitting parameters and least squares algorithm was used for χ^2 minimization. The ratio of a_3/a_1 and a_2/a_1 gives O/C and N/C chemical ratios, respectively. As an example of the fitted sample spectrum and its decomposed C, N and O element spectra are shown in Figure 5.8. The ratio of integral counts of element spectrum (decomposed) to the integral counts of the fitted spectrum gives elemental fraction of that particular element in the investigated sample. The calculated fraction of C, O and N in different samples is given at Table 5.4 and their actual values used in the simulation provided at Table 5.5. Based on these values (C, O, N), Figure 5.9 presents the positions of the investigated samples using triangle diagram [164]. The triangle diagram corresponds to a barycentrical representation of the C, N and O fraction, where each sample is a point based on C,N,O values [165]. Since triangle diagram occupies two dimensional (2D) space, it simplify the analysis by transforming the 3D coordinates (C,N,O) into 2D coordinates (X,Y) using following (5.2) relations [166].

$$X = \frac{\sqrt{2}(N + 0.5O)}{C + N + O}, Y = \frac{\sqrt{6}(0.5O)}{C + N + O} \tag{5.2}$$

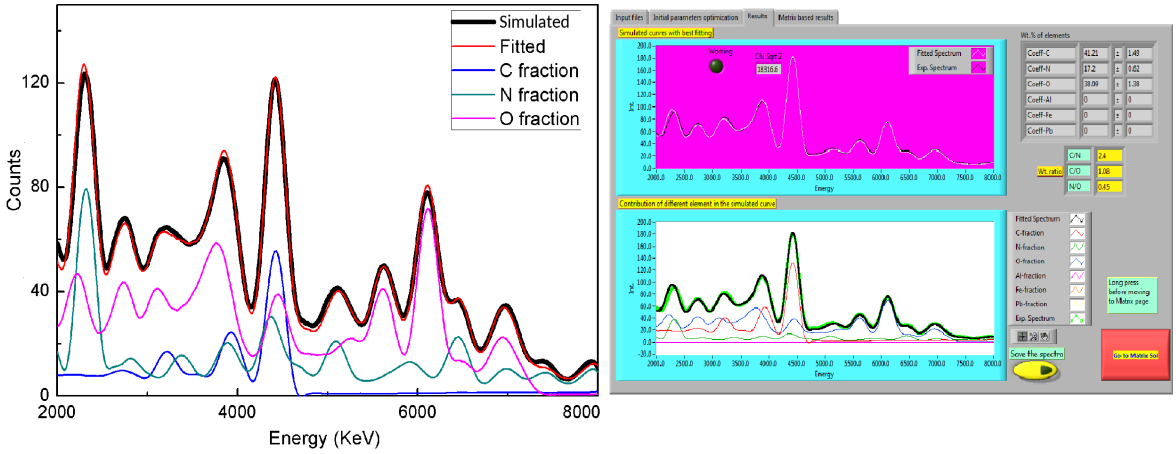

Figure 5.8: (Left) Fitted spectra of Urea with decomposed portion of carbon, nitrogen and oxygen element (right) Snap shot of the GUI developed for spectrum fitting with a linear combination of pure elements.

Table 5.4: Calculated composition of C, N, and O elements via fitting the simulated spectra of different investigated samples

sample	C(%)	N (%)	O (%)
RDX	18.92	39.62	41.46
TNT	43.45	17.55	39
Urea	21.75	54.12	24.13
Melamine	29.23	70.77	-
Ammonium Nitrate	-	40.26	59.74

Table 5.5: Chemical composition (weight%) of explosives and benign materials used in the simulation

Material	C (%)	H (%)	N (%)	O (%)
RDX	16.22	2.72	37.84	43.22
TNT	37.02	2.22	18.50	42.26
Urea	19.98	6.7	46.64	26.65
Melamine	28.56	4.8	66.64	–
Ammonium nitrate	–	5.0	35.01	60

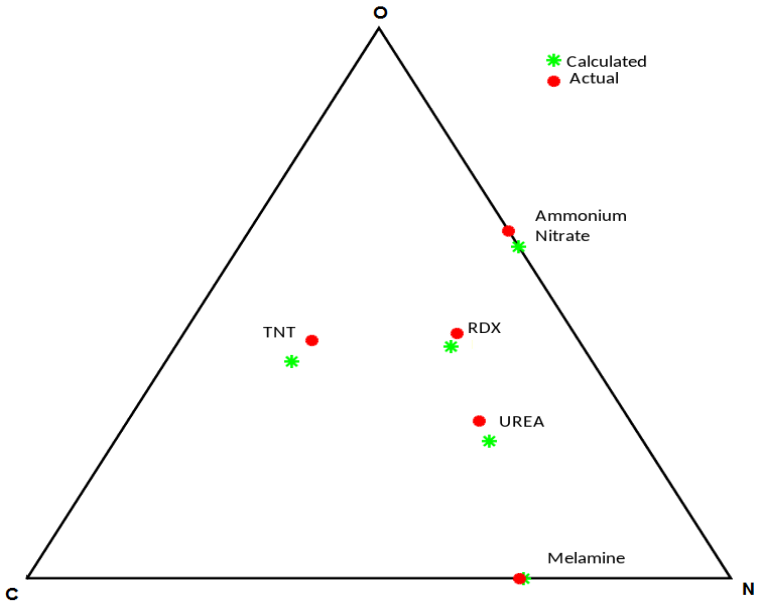

Figure 5.9: Triangle diagram of the carbon, nitrogen and oxygen proportions, showing elemental composition of C, O and N extracted (green dot) from simulated spectra with actual values (red dot) used in the simulation for different investigated samples.

5.3.5 Effect of Matrix Material

Surrounding materials in the threat material detection is of utmost importance, it generates the background against which the threat material signal has to be identified. Threat materials are usually contained within small volume inside large volume (truck, car etc) of variable matrices. We have studied the influence of organic and metallic matrix material on the hidden threat material's spectrum and its effects on API method to identify hidden threat material. To study the matrix effects, simulations were carried out for 1 kg RDX hidden inside container with remaining volume filled with of a matrix (iron or wood). The sample (RDX) was placed at the center of the container and simulation was run for case of average matrix density of 0.1 and 0.2 gm cm^{-3} and without matrix material. The results (Time and time correlate energy spectra of RDX) are reported in Figure 5.10). Time spectrum shows an intense peak around 13.5 ns that is corresponds to the sample position hidden in container.

The time correlated (obtained with time window selection of 12.8 -14.4 ns on time spectrum) energy spectra of RDX in presence of wood matrix (Figure 5.11), shows the carbon (4.44 MeV) and Oxygen (6.13 MeV) gamma peak

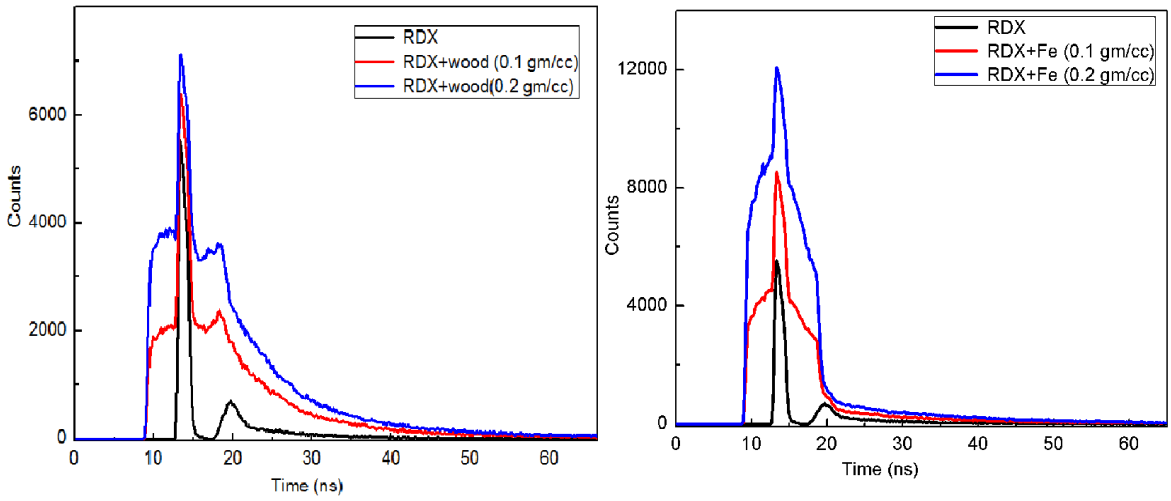

Figure 5.10: Time spectrum of hidden RDX inside a container filled with and without matrix of (left) wood and (right) iron .

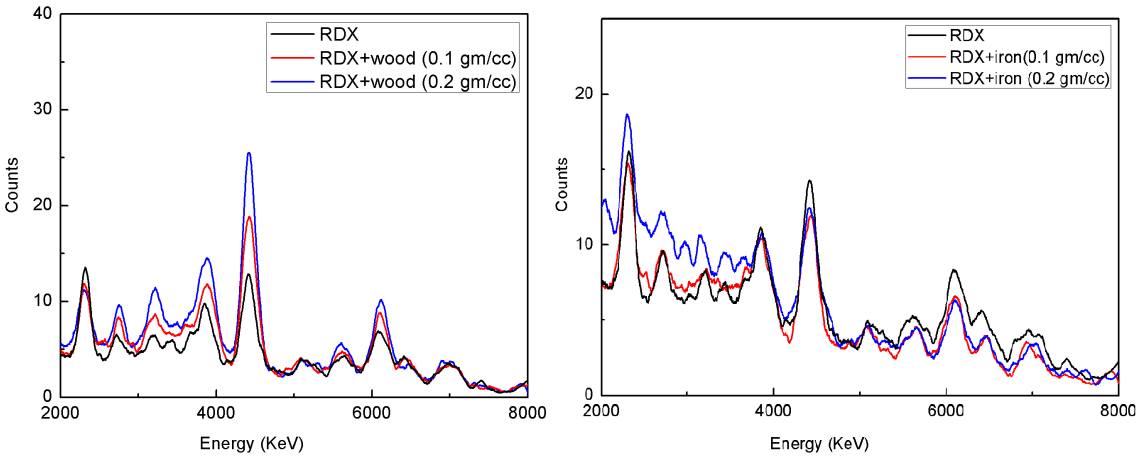

Figure 5.11: Time correlated energy spectra of 1kg RDX in presence of matrix (left) wood (right) iron.

intensity high, in compare to the case when RDX sample spectra was taken without wood matrix. This additional contribution is the result from wood (having similar element composition) that surrounds the RDX and its complete removal is difficult. This contribution has increased with increase of matrix density (0.1 to 0.2 gm cm^{-3}). In case of iron matrix there is no such effect at carbon (4.44 MeV) and oxygen (6.13 MeV) energy line, in RDX energy spectra was observed that is because the 14.1 MeV neutron induced iron lines are mostly lies in lower energy region Figure(5.6) followed by a continuum. The C, N, O element's contribution (in %) of RDX obtained for the case of iron and wood matrix are provided in Table 5.6.

Table 5.6: Calculated C, N and O element's contribution from simulated spectra of 1kg RDX hidden inside a matrix

Matrix Type	Matrix density (gm/cc)	C (%)	N (%)	O (%)
Iron	0.1	16.8	41.87	41.33
Iron	0.2	14.28	45.7	40.03
wood	0.1	38.28	22.37	39.34
wood	0.2	47.3	12.89	39.8

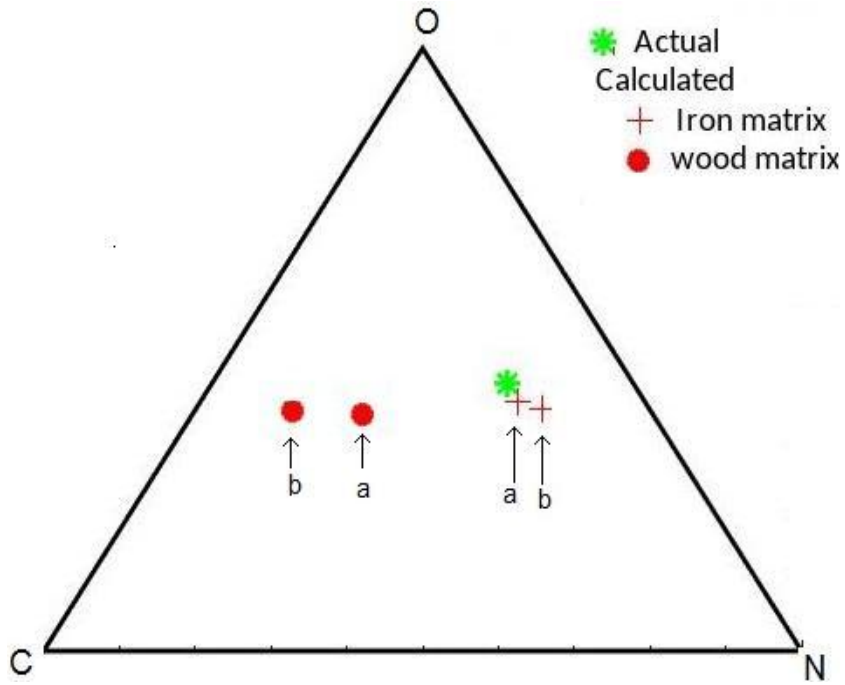

Figure 5.12: Triangle diagram of the carbon, nitrogen and oxygen proportions, showing elemental composition of C, O, and N extracted from simulated spectra of RDX placed inside a container filled with iron (plus "+") or wood(red dot) matrix with actual values(green dot) used in the simulation. Here a=0.1gm/cc and b=0.2 gm/cc are matrix density.

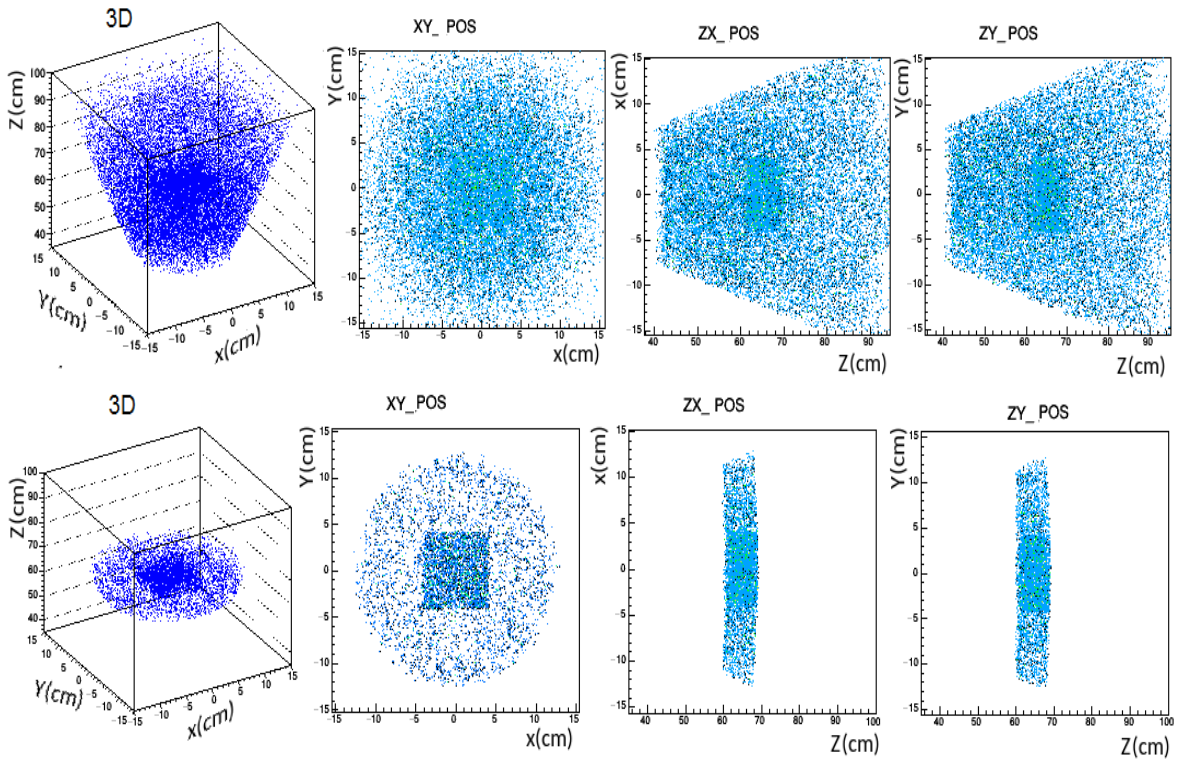

Figure 5.13: Reconstructed images (3D, 2D) of neutron interactions for the case of RDX (1kg) hidden inside container filled with iron matrix of density 0.1 gm/cc. (Top) when no time window selected (Bottom) with a condition of 1.6 ns time window (12.78 -14.4).

Extracted element contribution of C, N and O for RDX energy spectra in presence of matrix material is shown in Figure 5.12. The CNO point in case of iron matrix (”+”) lies close to actual point (green dot) of RDX in plot while for wood (red dot) matrix (even for 0.1 gm cm^{-3}) the point (CNO) lies far the from actual values. It indicates the high detection possibility of hidden RDX (1kg) in metallic matrix while for organic matrix it would be quite difficult.

5.4 2D and 3D imaging of interrogated object

Position sensitive alpha detector measures the x-y coordinates of the alpha particle which allows determining time and direction of neutron escape. ROOT [134] based algorithm was developed to reconstruct 2D-3D images of the interrogated object. It utilizes the principles of euclidean geometry and the geometrical correlations between an alpha and the tagged neutron to track the neutron direction. In addition to that time stamping of gamma-rays as reg-

istered by Geant4 and the known velocities of the 14.1MeV neutron (5.12 cm ns^{-1}) and gamma-rays (30 cm ns^{-1}) were used to reconstruct the exact location of neutron interaction point in 3D space. The constructed images (3D, 2D) of hidden RDX (1 kg) inside iron matrix (0.1 gm/cc) container are shown in Figure 5.13 with and without time window.

The reconstructed 2D and 3D images correctly reveal the location of the interrogated object placed 65 cm away from the neutron production site along with its length of 8.2 cm.

5.5 Conclusions

API based neutron interrogation was modelled successfully in Geant4 with an array of BGO (3"X3") for explosive detection and image reconstruction to locate the position of the interrogated object. The methodology and different aspects of API technique were studied. Data set of response spectra of pure elements (C, O, N, Al and Fe) were generated and used for complex sample spectra analysis using linear combination of these reference data. The simulated spectra of benign (urea, melamine) as well as explosive (RDX, TNT, AN) samples were analyzed for determination of their C, N, O elemental compositions. The calculated values found to be close to the actual values in respective samples and it has shown the novel and reliable approach of API for identification of different samples. The results of matrix study have indicated that API system in the given configuration, would be able to detect hidden explosive (1 kg RDX) inside a container filled with an iron matrix of density 0.1- 0.2 gm cm^{-3}, while in organic matrix the detection of hidden explosive would be difficult even at density of 0.1 gm cm $^{-3}$.

In conclusion, this studies has provided the groundwork for analysis of gamma-ray spectra utilizing detector's elemental responses measured with tagged (14.1 MeV) neutron in the actual geometry of API and image reconstruction of object's location under inspection. Future work will be focus on implementation of API technique with inhouse developed D-T NG.

CHAPTER 6

Implementation of Associated Particle Imaging

The work on API was further extended by implementing it and system development. The API, technique was realised with a laboratory based inhouse developed D-T NG and a system was designed, assembled and tested within the course of this doctoral work.

6.1 Introduction

As discussed in the Chapter 5, in contrast to traditional neutron interrogation techniques, API is a self-collimating 3-D imaging method where the alpha particles are used to determine the position and direction of the neutrons emitted [45, 104]. Since neutrons are emitted isotropically from the source, the alpha particles limit the background noise by selecting events that are caused by neutrons emitted in the direction of the interrogated object. This can be termed as electronic collimation. This method provides effective suppression of background by spatial and time discrimination of events.

The major components required for implementaion of API technique and to produce the complete system are

1. A D-T Neutron Generator
2. Position sensitive alpha particle detector
2. Gamma-ray detector or array of gamma-ray detectors
3. Data acquisition system
4. Hardware and Software for data acquisition, processing and analysis.

Under the programme of Tagged Neutron based API System developement, a laboratory based D-T neutron generator of neutron yield 10^8 n/sec has been developed at BARC. D-T neutrons were tagged with a position sensitive

alpha detector (8 X 8 matrix of YAP:Ce crystals) and the tagged neutron induced gamma rays were detected with a BGO gamma detector in coincidence with alpha particle. The system's performance was evaluated with benign and explosive simulants.

This chapter presents important attributes of implementation of API technique and system development using inhouse developed DTNG followed by detail description of its major components including DTNG, tagging detectors, gamma detectors, Front-End-Electronics to perform coincidence and spectroscopic measurements and software development to manage data acquisition, processing and analysis. After that various experiments of system characterization and experimental results for C, O, N elemental signature detection in benign and explosive simulants performed using one gamma detector have been presented.

6.2 Experimental Set-Up

At the initial stage, to demonstrate the tagging of D-D/D-T neutron, we have installed a system for the production of tagged neutron beams at PURNIMA D-D/D-T neutron generator facility, BARC. This study was performed in collaboration with Prof. Giuseppe Viesti, University of Padova, Italy and his co-workers [167]. On the basis of their past experience on the production of tagged neutron beams of DT neutron through the associated particle technique [96], there was an interest to extend the study of such technique with D-D neutrons produced in the ^{2}H (^{2}H, n) ^{3}He reaction. The energy of about 800 keV of the ^{3}He recoiling nucleus associated with D-D neutron makes detection more critical. On the other hand, lower energy of D-D neutron beam will induce a much lower background rate. NIM based Front-End-Electronics and YAP:Ce crystal(14 pixels) as tagging detector brought from Padova University were installed and tested with both the reactions (D-D and D-T) of NG for tagging of D-T and D-D neutron [168]. The photograph of the system is given in Figure 6.1. The detail of the experiments and results are reported in the reference [168].

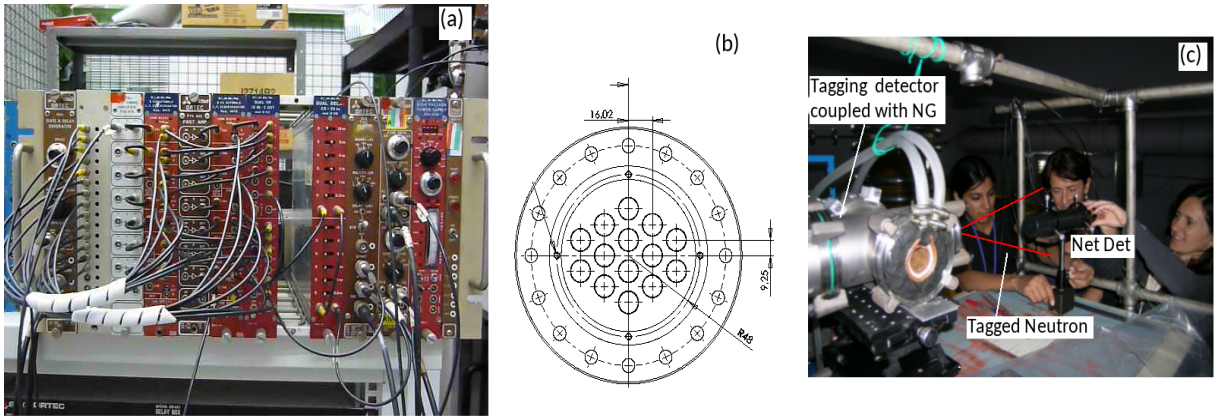

Figure 6.1: NIM based Front-End-Electronis (b) Schematic of Tagging detector and (c) Photograph of the experimental setup showing coupled tagging detector with DT NG

Table 6.1: Important specifications of Neutron Generator

Neutron Energy	14.1 MeV
Maximum neutron Yield(in 4pi)	10^8 ns^{-1}
Alpha Detector	YAP(Ce)
Maximum Beam current	200 μA
Maximum high voltage	150 kV

Later on we have developed our own Tagged Neutron based API system. A dedicated DTNG was developed for this, since the PURNIMA DD/DT neutron generator was a common facility for various applications at BARC.

6.2.1 Neutron Generator

A neutron generator with a built-in position sensitive alpha-detector is a key component of the API system. In this work we have used a laboratory based DTNG inhouse developed at BARC. The design and major components of this DTNG is similar to that of Purnima Neutron Generator as detailed in chapter1, except that it is a 150 kV deuteron accelerator with maximum neutron yield of 10^8 n/sec of DT neutron with the tritium target. The photograph of NG is shown in Figure6.2 and major specifications of NG are given at Table 6.1.

To improve the signal to background ratio, API which is a timing technique uses coincidence between alpha and gamma and reduces the contribution of the random coincidences arising from background. The technique tracks an

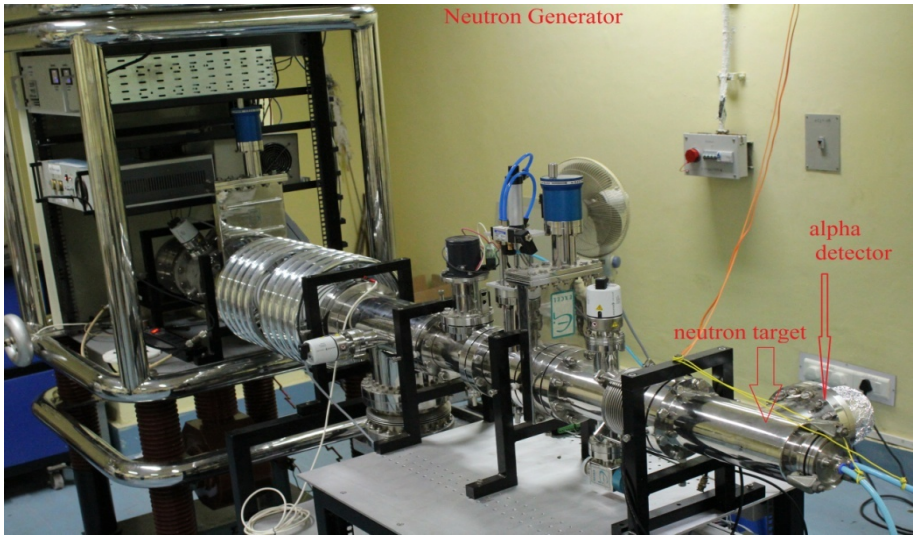

Figure 6.2: Neutron Generator with Alpha Detector

individual neutron to an interaction site and then a gamma-ray from the interaction site to a gamma detector. If two neutrons are produced in a coincidence window, the system has no way to know which neutron produced the gamma ray. In this technique, the time from neutron production to gamma detection is less than $\sim$ 100 ns. The production of neutrons which go in the direction of the target (object) must then be kept below about 10^6 n sec^{-1}. Therefore, the total neutron production (in 4 pi) must be kept in the 10^7 -10^8 n sec^{-1} range.

The operation of the NG was optimized at 60 - 80 kV High Voltage and 50 - 90 μA beam current setting to have neutron output $\approx$ 1-3 x 10^7 n sec^{-1} for experiments.

6.2.2 Alpha Detector (YAP:Ce)

As a tagging detectors we have used 64 YAP:Ce crystals (Table 6.2) arranged in an array of 8 $\times$ 8 matrix coupled to a multianode PMT. Each crystal has square shape with size of 5.8 mm x 5.8 mm, thickness 0.5 mm and crystals are held on a stainless steel grid made by electro-erosion. It was manufactured by CRYTUR [169]. The crystals are read by Hamamatsu H8500 multianode PMT (Table 6.3) with an effective area of 49$\times$49 mm^2, which provides 64 independent anodes matching the crystals geometry [170]. The crystals and the PMT are mounted on opposite sides of a vacuum flange equipped with a sapphire window of 4

Table 6.2: Proprties of YAP:Ce detector

Density	5.37 g/cm3
Refractive index	1.93
Light output (percentage NaI)	40
Decay time (fast)	25/30 ns
Wavelength of maximum emission	370 nm

Table 6.3: Hamamatsu H8500 PMT characteristics.

Type	8×8 Multianode
Anode Size	5.8 mm $\times$ 5.8 mm
Effective Area	49 mm $\times$ 49 mm
Spectral response	300 to 650
Wavelength maximum response	400
Photocathode Material	Bialkali
Window Material	Borosilicate glass
Structure	Metal channel, 12 dynode
Max. Applied Voltage	-1000 V
Gain	1.5 x 10^6
Transit Time Typ.	6ns

mm thickness. The crystal's surface is coated with a layer of 1mg/cm^2 to protect the YAP:Ce detectors from light and scattered deuterons and additional thin SiO_2 layer to prevent oxidation. The photograph of position senstive alpha detector assembly and the schematic of the reaction chamber is shown in Figure 6.3.

A chamber was designed to couple the alpha detector with NG. It holds tritium target at 45 degree with respect to the d^+ beam direction (axis) and a 90 degree port for alpha detector as shown in Figure 6.3. With this provision the alpha crystals are at a distance of about 12 cm from the tritium target and each crystal subtends a solid angle of about 0.019% of 4 π. Based on the position and dimension of the alpha detector, the tagged neutron beam cone at 1 meter distance from the tritium target will be approximate to 42 cm (lateral position, x- and y-axis)) that means an object of size 42 cm diameter can be scanned at a time in x-y plane.

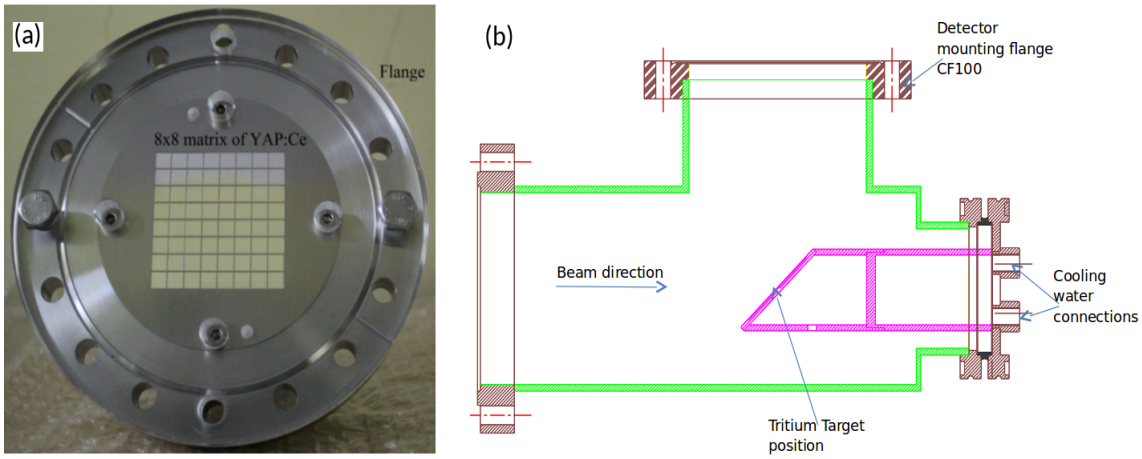

Figure 6.3: (a) Multi pixel YAP:Ce detector and (b)Reaction Chamber for alpha detector to couple with NG .

6.2.3 Gamma detector:BGO

A right-circular cylinder (BGO γ-detector) of size 3 inch $\times$ 3 inch used for gamma spectra measurements. It was the same BGO detector used for PGNAA experiments (ch 4) and modelled in API simulation (ch5). As described earlier the BGO detector was chosen because of its high efficiency for high energy gamma-rays detection and the fact that it is less sensitive to neutron radiation damage as compared to other detectors such as NaI, HPGe etc [knoll2010]. The details of comparison for different gamma detectors is provided in the chapter1. The detector was shielded from direct source neutrons by using a neutron shield of 65 cm, made of iron, boron-loaded polyethylene and lead material combination. The gamma-ray detector was placed inside a lead cave, 10 cm thick on each side. The front and rear of the detector were usually unshielded. Figure 6.4 shows the gamma-ray detector inside lead cave.

The energy and time resolution are important parameters for any gamma detector considered for use with the associated particle technique. The time resolution directly affects the spatial resolution of the system that can be obtained by the technique. The energy resolution is important for interpretation of complicated gamma energy spectra and for improving SNR for weak gamma-ray peaks on a significant continuum background. The experimental

measurements of energy and time resolution of BGO is provided at section 6.4.

6.3 Front-End Electronics

The read-out of system (alpha and scintillator) in time and energy measurements are usually performed using standard Nuclear Instrument Module (NIM) electronics. However, the number of channels (64YAP:Ce + gamma detectors) and the count rate expected in this system demanded a solution based on high density cards, as those built in VME standard. VME bus is a computer architecture. The term VME stands for "VERSA Module Eurocard" and was first defined in 1980 by a group of manufacturers. Unlike NIM standard, the use of VME bus allows direct communication between different boards hosted in the same crate: each board is identified by a logical 32 bit address (base address) defined by a switch on the board itself. The first board of the crate acts as controller of data flow. In each board, a set of readable memory registers contains the data. Another set of writeable registers is available for committing instructions or writing down configuration parameters. The possibility to operate all the boards from the controller is of great advantage because it results in various levels of automation of an experiment. In our configuration, the controller board is connected to a PC and driven by a dedicated software interface developed especially for this configuration including different n-number of boards.

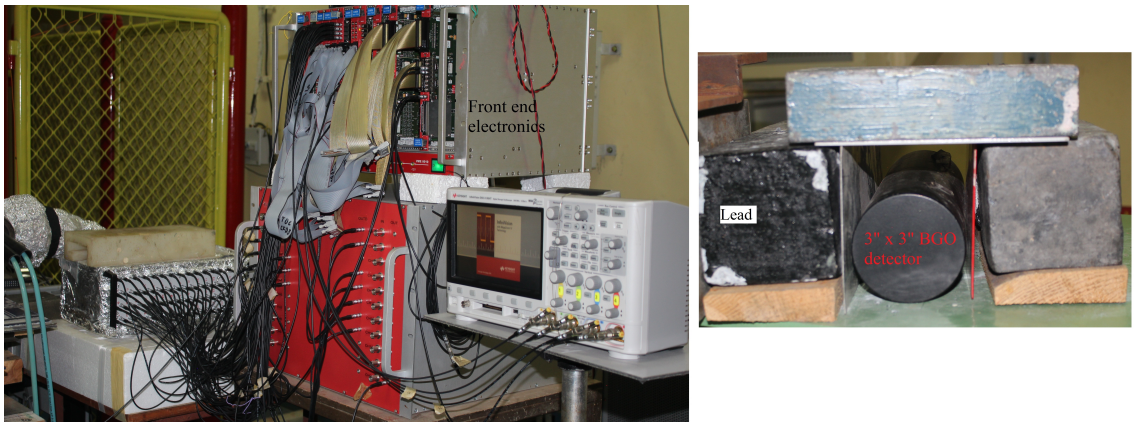

Figure 6.4: Electronics and BGO detector

The VME based electronics modules [171] of electronic set-up are listed below:
1. One 21 slot VME crate
2. Six 16 channel Constant Fraction Discriminators **(CFD Mod. V812)**
3. Two 16 channel Charge ADCs **(QDC Mod. V792)**
4. One 128 channel 100ps Time to Digital Converter (TDC Mod. V1190)
5. One Programmable Trigger Unit **(TRG V1495)** with custom firmware for FPGA (Field Programmable Gate Arrays)
6. One VME to PCIe Optical Link Bridge **(Mod. V2718 + Mod. A3818)**
7. One 22 channel splitter and delay box **(custom design)**
8. Cable adapters and optical fiber
The first four CFDs (0-63 ch) were used for alpha (marked as CFD0-CFD3) and last two (CFD4,CFD5) for gamma (see the Figure6.5). Effectively the system with these modules can accomodate at the maximum 64 alpha channels and 32 gamma channels. However in this present study we have demonstrated the system's performance with 64 pixels of YAP:Ce and only one gamma detector.

6.3.1 Principle of operation

The neutron from DTNG hits the sample and induces prompt gammas. For each neutron, an alpha particle is emitted in opposite direction,this particle is detected by the embedded 64 pixel alpha tracker whose outputs are connected to first four CFDs. The ECL digital output of the CFDs (2x fan-out) feed channels 0-63 of the TDC and 64 inputs of the Trigger Logic implemented in the FPGA of V1495. One or more adjacent pixels can be fired by the alpha particle, event data from TDC allow for reconstruction of the neutron direction (X-Y coordinates) and for the calculation of the Start Time (T0) of time spectrum. The neutron induced gammas are detected by a BGO detector whose output is splitted into two branches. One branch goes into another CFDs (CFD4 or CFD5) that feed the TDC and the trigger logic as for the alpha signals. The other branch of gamma signal goes into a 150 ns delay line (inside delay box) and then into the QDCs for the energy measurement. The delay line is necessary in order to fit the pulses into the integration gate that arrives from the trigger logic with some latency. The diagram of the electronic Set-Up is shown

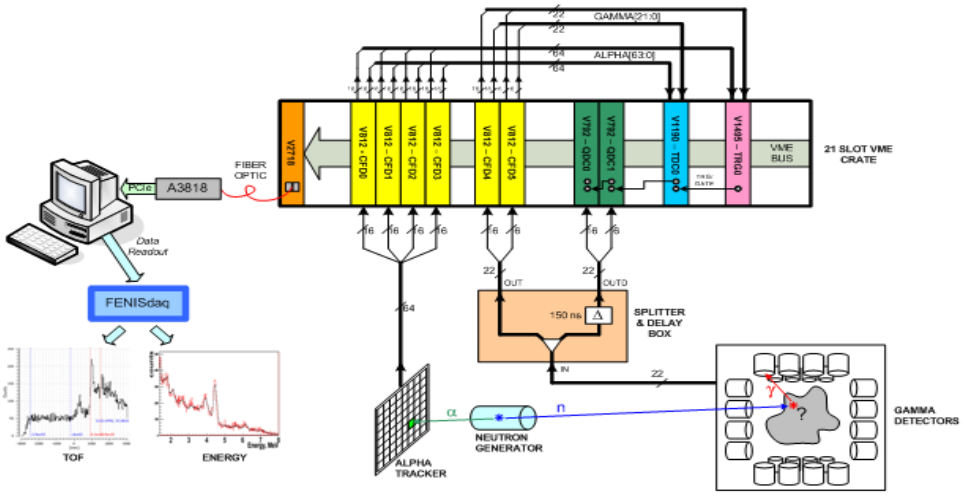

Figure 6.5: Block Diagram of Electronic SetUp

in Figure6.5.

Trigger Logic (V1495): The trigger logic implemented in the FPGA of the V1495 (custom firmware developed by CAEN [171]) looks for the coincidence between alphas and gammas in a programmable time window and generates the integration gate signal for the QDCs and the trigger for the TDC. Figure 6.6 shows the block diagram of the trigger logic. Alpha and gamma signals coming from the CFDs (ECL) enter inputs A, B and D of the V1495 module, it is possible to mask (in other words disable) each channel individually. For testing purposes, it is possible to emulate alpha and gamma signals by means of the test inputs E[1] and E[0] respectively. After the mask, the OR of the alphas is used to start the coincidence gate, if any gamma arrives within the coincidence gate, then the integration gate for the QDCs (which corresponds also to the trigger for the TDC) is activated. In order to keep the event acquisition synchronized in different boards (2 QDCs and 1 TDC), the trigger logic uses the busy signals from those boards as a veto for the trigger/gate generation, so that it never happens that one trigger is accepted by one board and not by another one. Besides the trigger logic that generates the gate signal, the FPGA provides also some utilities such as a certain number of rate meters that counts the number of pulses of a given signal in a programmable time slot ($\sim$ 1 sec), so that the DAQ software can read the value of the counters and calculate the relevant frequency of the signals. The rate meters are reported in the block

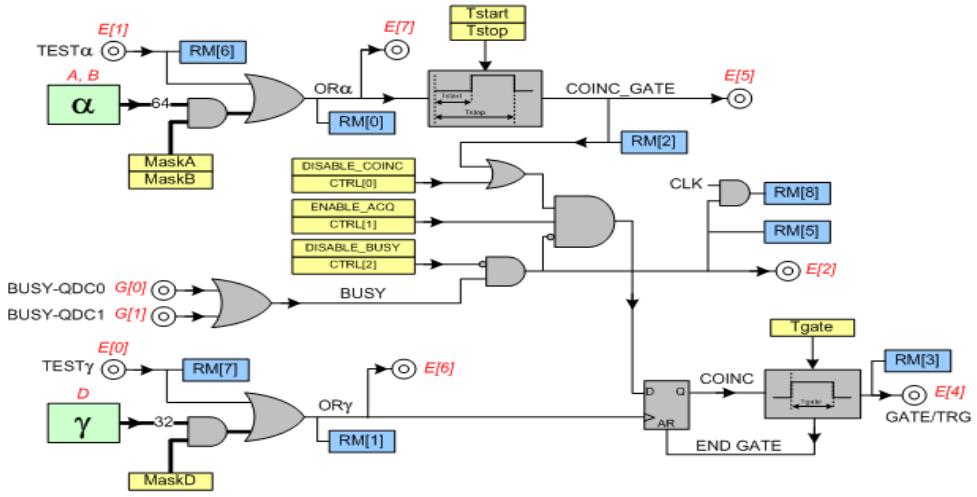

Figure 6.6: Trigger Logic (V1495) block diagram

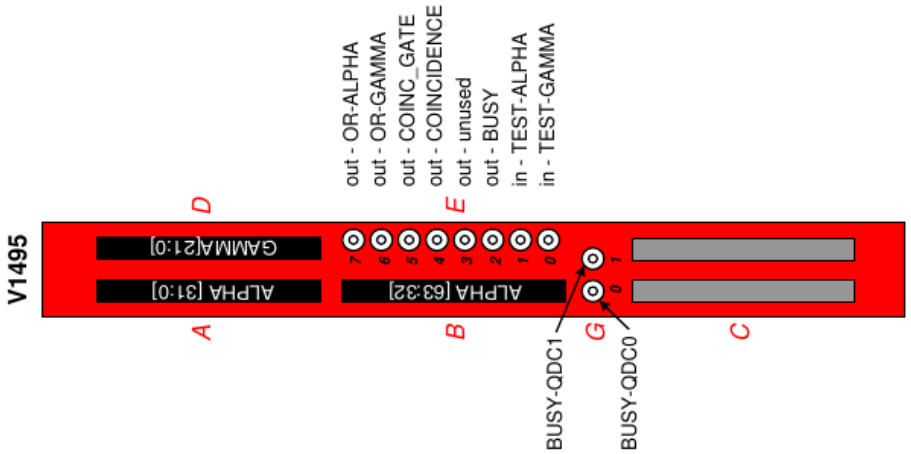

Figure 6.7: V1495 Front Panel I/Os [171].

diagram as RM[i] in a cyan box. The V1495 mounts a 8 channel NIM/TTL I/O expansion (A395D) that is used to generate the gate/trigger and other monitor signals as reported in the next Figure(6.7). The Trigger Logic implemented in the FPGA of the V1495 is controlled by a set of registers that can be accessed.

Another most important module is **USB bridge**. A USB bridge model CAEN V2718 provides standard connection with the computer, with a maximum transfer rate of **30 MB/s** . This module placed in the first position on VME-crate provides interface between computers and the VME, it takes care of the conversion from software commands to the VMEbus hardware language.

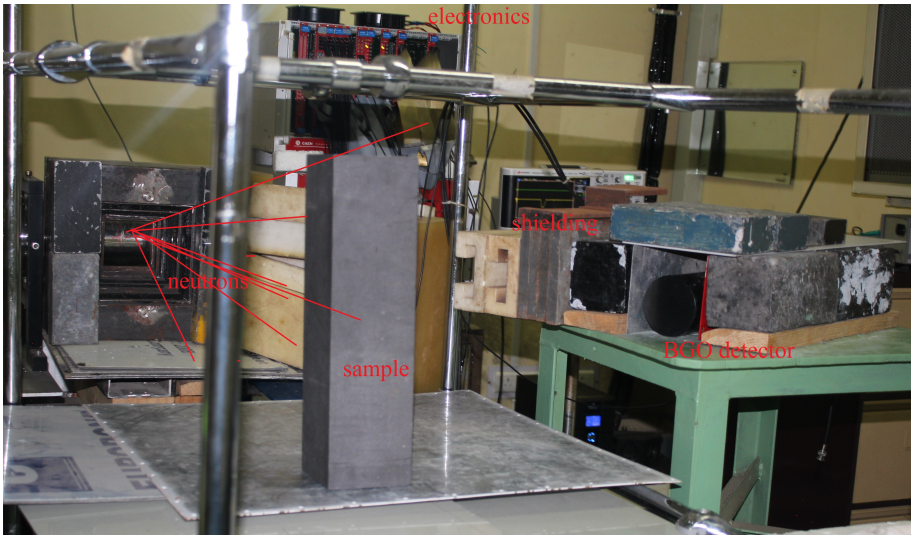

Figure 6.8: Experimental Set Up

6.3.2 Data Aquisition Software

Data Aquisition Software is a C based program that performs the following operations: It opens one or more configuration files (text files) that contain all the parameters for the acquisition and perform the following operations

1. Open the connection from the PC to the VME crate through CAEN VME bridges (V2718).
2. Open the VME boards (CFDs, QDCs, TDCs and Trigger Unit).
3. Configure the boards writing the relevant registers with the parameters read from the Config file.
4. Start the acquisition (enable Gate/Trigger generation in the trigger unit).
5. Read events from the boards in synchronized manner.
6. Cumulate the energy and time correlation histograms of all the channels with the value calculated for each event.
7. Manage the energy and time calibration.
8. Print few statistics (trigger rate, data throughput, rate meters, etc.) to console (Figure 6.9).
9. Plot histograms using gnuplot/ROOT as a plotter engine.
10. Save histograms and events to output files.

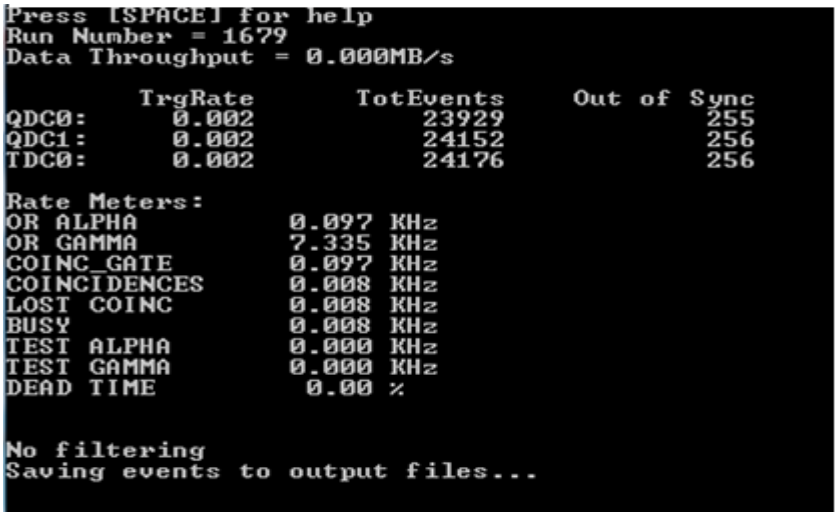

Figure 6.9: Rate meter output.

6.4 Experimental Measurements

Before performing actual experiments, various measurements necessary to characterised the system were performed as described in this section.

6.4.1 TDC Calibration

At first test pulse signals were used and time spectra were acquired to verify proper operation of electronic modules. A pulse of amplitude 1 volt and width of 40 ns generated from a pulse generator, splitted into two pulses corresponds to alpha and gamma signal. The alpha signal is connected to Alpha-Channel no.30 (input 14ch of the CFD1) and the gamma signal connected to Gamma-Channel no 4 (channel 4 of the splitter and delay box, whose outputs goes into the input 4 of the CFD5 and the input 4 of the QDC0). The typical signals observed from V1495 are shown at Figure (6.10). In this test, the delays of 0, 25, 50 and 75 ns were added/set in the gamma line and data were acquired in coincidence mode as shown in Figure (6.11-6.12). The alpha distribution shows that the only one alpha ch30 has been fired out of 64 pixels, as expected. The channel to time conversion for TDC is obtained $\Delta t = \Delta c \times 0.098$ ns/channel, where Δc is the number of channels considered. The time spectrum found to have a spread (FWHM) of 0.16 ± 0.01 ns (Figure 6.12) for pulse signal from a pulser.

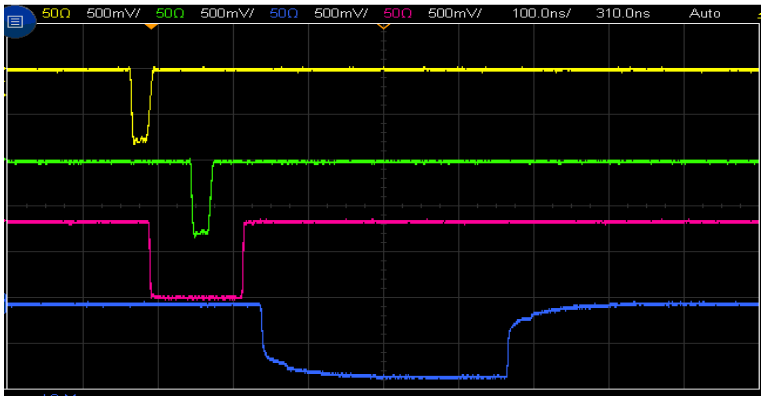

Figure 6.10: Typical Signals from V1495: Yellow=alpha, Green=gamma, Pink=CoincWindow, Blue=Gate/Trigger.

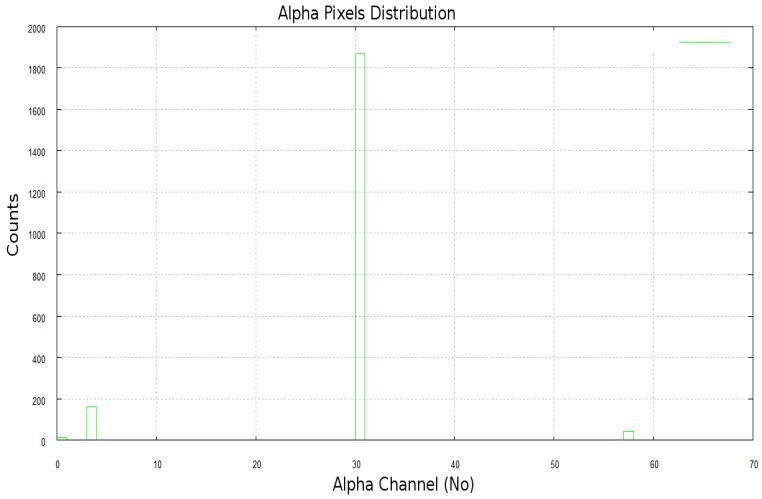

Figure 6.11: Alpha Pixels Distribution

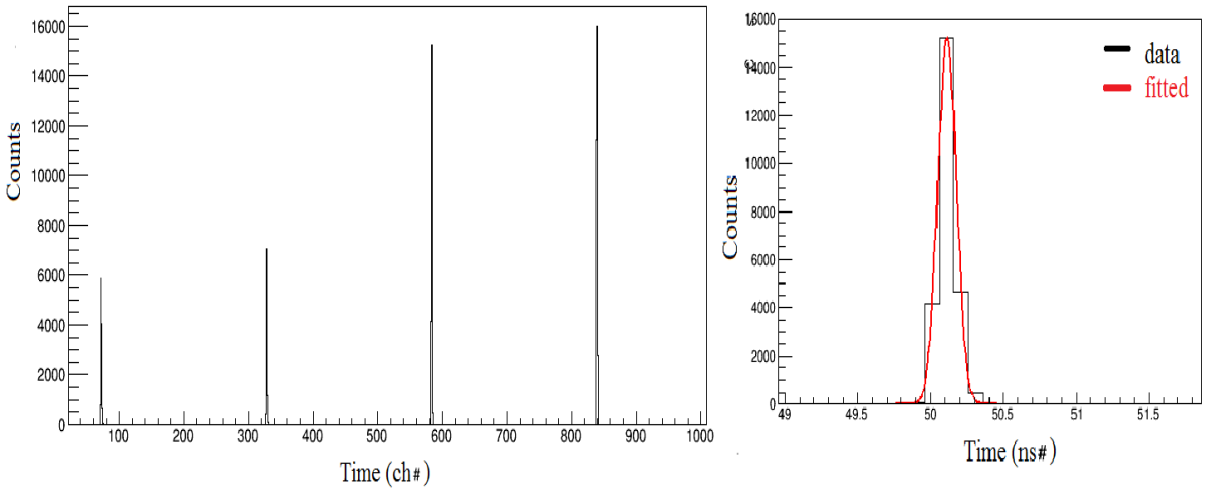

Figure 6.12: (left)Time spectra obtained with pulse generator and (right) FWHM of Time spectrum at 50 ns.

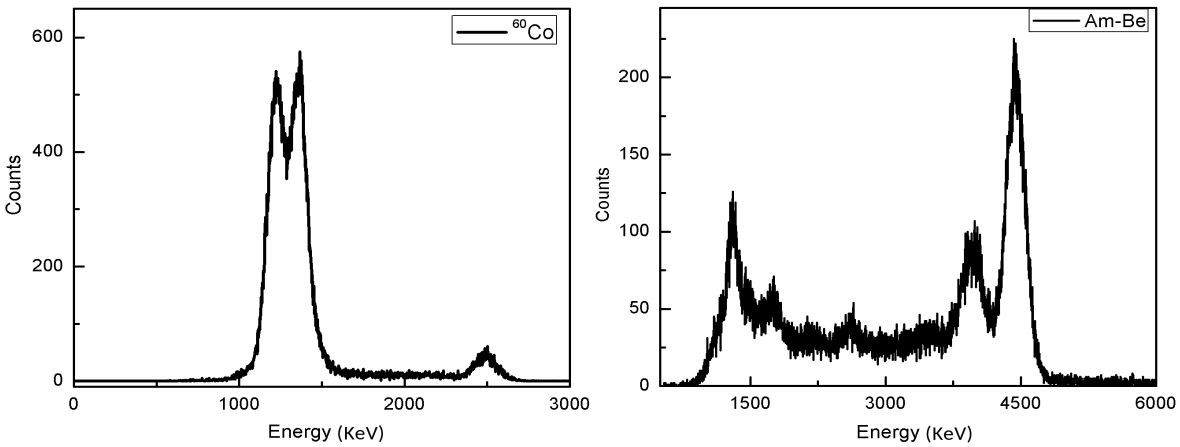

Figure 6.13: Energy spectra of ^{60}Co and Am-Be.

6.4.2 Energy Resolution of BGO

The energy resolution of the system is almost entirely determined by the resolution of the BGO detector. Energy spectra of BGO for various gamma energies at 0.511 MeV (^{22}Na), 0.662 MeV (^{137}Cs), 1.17 MeV-1.33 MeV (^{60}Co) and 4.44 MeV (Am-Be) were acquired in direct spectroscopy mode (no coincidence mode) with the VME electronics as described above. The 4.44 MeV is the energy of the 2^+–0^+ γ transition in ^{12}C, an isotope produced in the reaction of α-particles with Be in a AmBe neutron source [172].

$^{241}{}_{95}\text{Am} \rightarrow {}^{237}{}_{93}\text{Np} + \alpha$

$^{9}{}_{4}\text{Be} + \alpha \rightarrow {}^{12}\text{C} + \text{n} + \gamma$

The measured energy resolution (FWHM) was less then δE = 5.8% (FWHM) at E_γ = 4.44 MeV as described in the chapter 5. Finally the detector was calibrated with the 1.17 MeV, 1.30 MeV of ^{60}Co and 4.44 MeV from Am-Be source [172]. Typical energy spectrum of ^{60}Co and Am-Be are shown in figure (6.13).

6.4.3 Time resolution of BGO

The time resolution of BGO detector was studied by measuring γ-γ coincidences with a ^{60}Co and neutron-γ coincidences from Am-Be source. A plastic scintillator of 2 inch x 2 inch coulped with 2 inch PMT used as a reference detector. Two detectors were 21 cm apart and time spectra of γ-γ coincidences in ^{60}Co as well as n-γ coincidences in Am-Be source were measured. Because

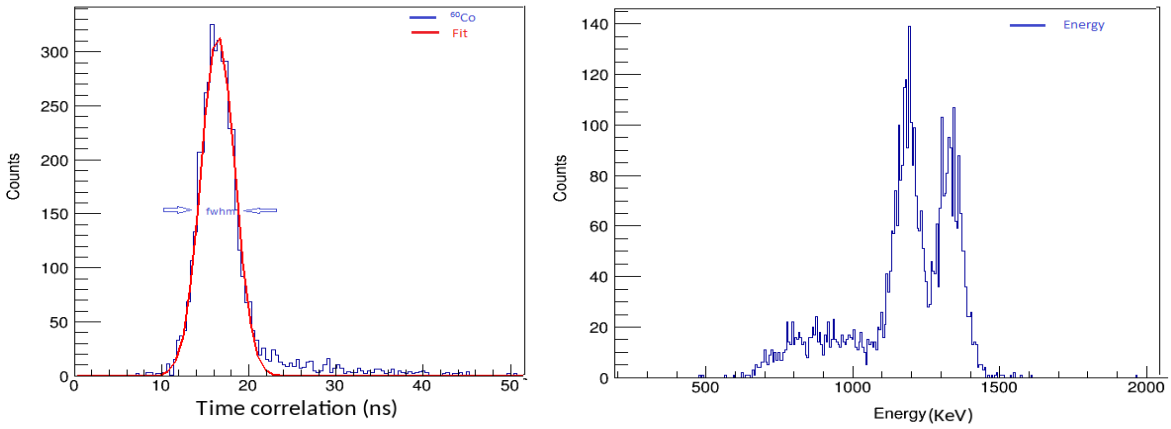

Figure 6.14: (Left) Time correlation spectrum of γ-γ coincidences of 1.17 MeV and 1.33 MeV gamma rays of ^{60}Co and (right) energy spectrum of ^{60}Co acquired in this coincidence mode.

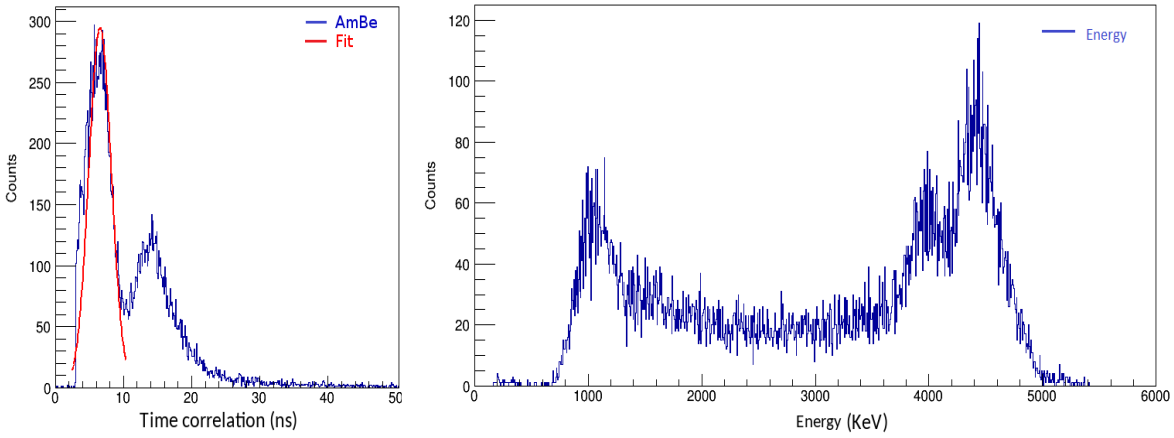

Figure 6.15: (Left) Time correlation spectrum of n-γ and γ-n coincidences using AmBe source and (right) the energy spectrum of AmBe acquired in this coincidence mode.

of the considerably low γ efficiency of the small plastic scintillator the ^{60}Co source was placed as close to the reference detector. The measured time spectra are presented in Figure (6.14-6.15). A sharp peak of coincidences of 1.17 keV and 1.33 keV transitions of ^{60}Co observed and time resolution (FWHM) obtained close to 4.2 $\pm$ 0.05 ns. The Figure 6.15, depict the time spectra of the coincidences measured with AmBe source and its respective energy spectra. There two peaks in time spectrum are mainly n-γ and γ-n coincidences resulting, first peak from the detection of a neutron in plastic and gamma in BGO and the accompanying, broader right peak is the result of the opposite situation when neutrons triggered a stop signal in the gamma detector. The FWHM of first peak was around 3.8 $\pm$ 0.05 ns.

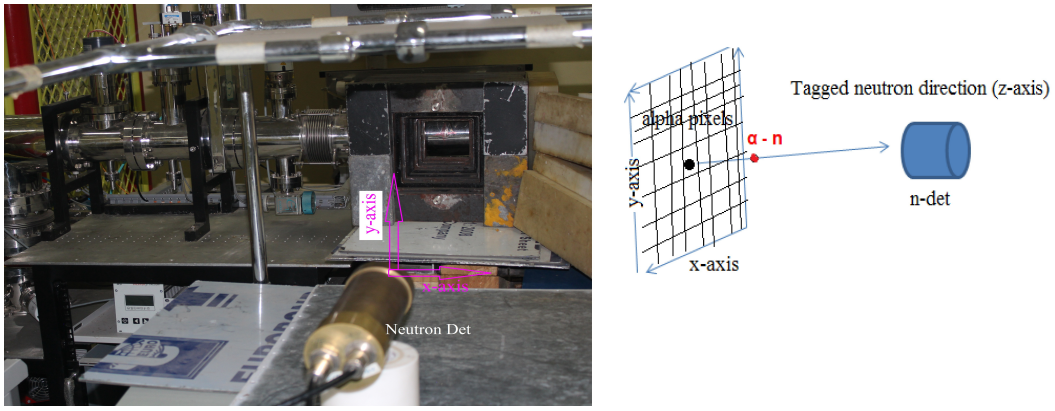

Figure 6.16: (left) Experimental arrangement for beam profile measurement and (right) its schematic representation.

6.4.4 Tagged Beam Profile Measurement

In order to map the tagged neutron beam geometry, a beam profile measurement was performed using a neutron detector (plastic) in coincidence with alpha particle detector (alpha detected in any of the 64 pixels). The plastic scintillator of 2 inch $\times$ 2 inch placed at about 107 cm from the tritium target as shown in Figure 6.16. A scan along the x and y axes (horizontal and vertical directions) was performed in step of 5 cm. The parameters recorded were total alpha count rate (per second) detected by alpha detector (all 64 pixels) in single mode (no coincidence required) and alpha - neutron coincidence event rate. The total alpha count rate was 150 kHz and kept constant for the experiment. The measured α-neutron coincidence rate was plotted as function of neutron detector's position as shown in Figure6.17 and Figure6.19 for horizontal and vertical scan respectively. The Full Width at Half Maximum (FWHM) of the tagged beam profile found to be of the order of Δx $\simeq$ 45$\pm$ 2 cm and Δy $\simeq$ 46$\pm$ 2 cm at about 107 cm.

The distribution of the alpha pixels fired/detected in coincidence with neutron at different positions of neutron detector has shown in the figure (6.18-6.20) at few positions ($\pm$ x or y). This distribution indicate that different alpha pixels got fired (in coincidence) with respect to different position of the neutron detector. Also, the number of fired alpha pixels (color intensity) increases as position of the neutron detector moves towards the center of tagged neutron beam.

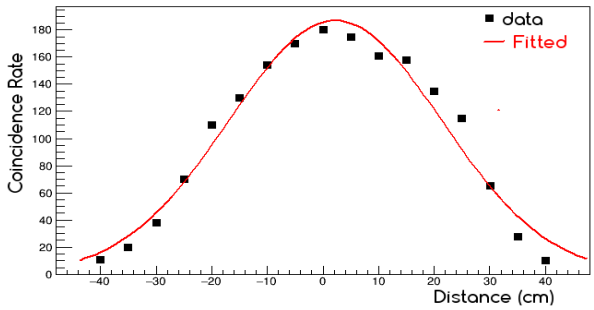

Figure 6.17: α-neutron coincidence rate as a function of the horizontal positions($\pm$x) of neutron detector.

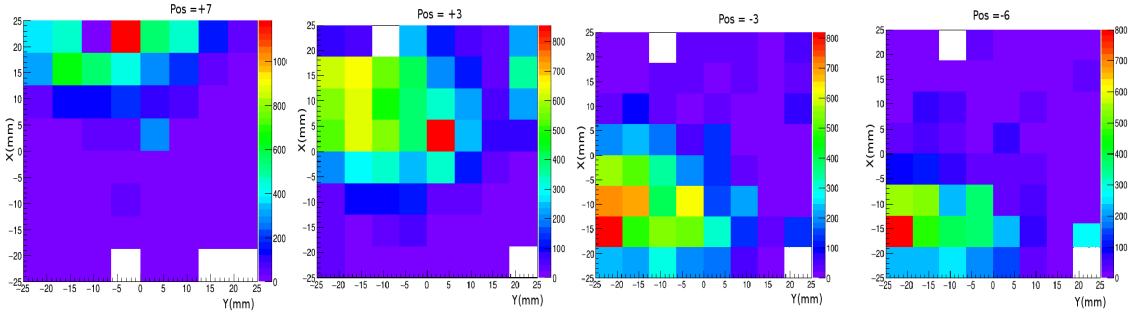

Figure 6.18: Distribution of alpha pixels detected/fired in coincidence with neutron at different positions of neutron detector in horizontal scan. The color represents the number of times a pixel fired.

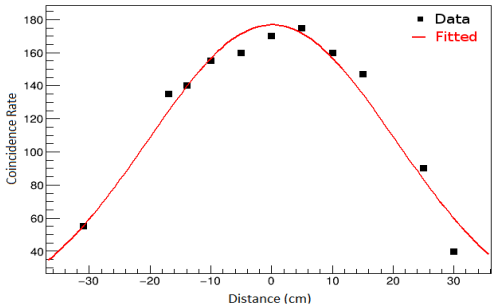

Figure 6.19: α-neutron coincidences rate as a function of the vertical position of neutron detector.

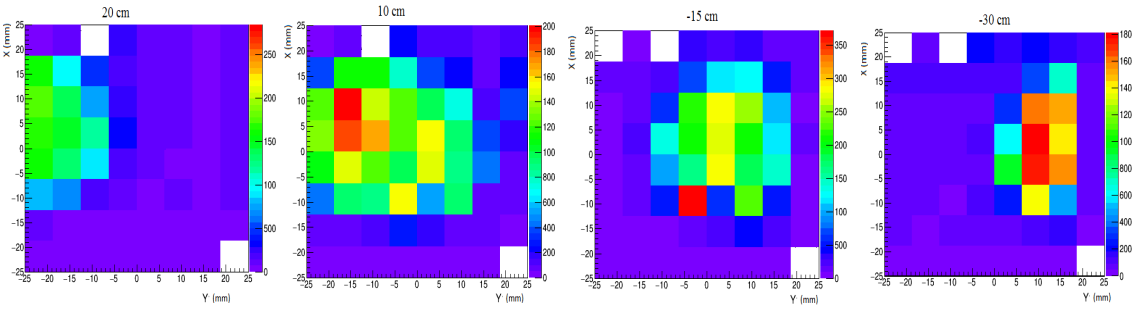

Figure 6.20: Distribution of 64 alpha pixels detected/fired in coincidence with neutron at different positions of neutron detector in vertical direction. The color represents the intensity of the fired alpha pixels in coincidence with neutron.

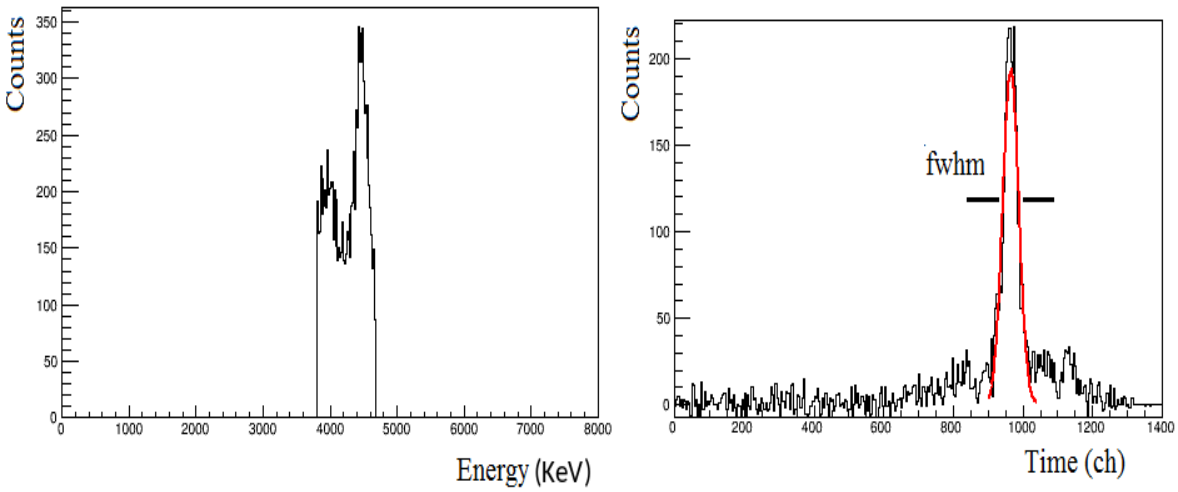

Figure 6.21: Energy and time distribution of graphite block obtained setting a gate on the E_γ = 4.44 MeV (including its first escape).

For example at $\pm$3 position the number of alpha pixels fired were more then that of at $\pm$7 position. Similar behaviour has also been observed in vertical direction as neutron detector moves from top (+Y) to bottom (-Y) Figure(6.20).

6.4.5 Time Resolution of System

An important point in characterization of the system is the determination of its timing properties and such characteristic depends upon the depth resolution (z-axis) along the neutron flight path direction. The achievable overall time resolution of the system was determined by detecting characteristic γ-rays from a graphite block ($15\times15\times15 cm^3$) bombarded with tagged neutron. In this experiment, the BGO detector was used in coincidence with the 64 alpha pixels. The α-γ coincidence time distribution obtained via setting a gate on 4.44MeV γ-rays (including its first escape at 3.92 MeV) energy peak as shown in Figure 6.21 (no background subtraction).

The FWHM of time spectrum peak corresponds to δt =4.8 $\pm$ 0.1 ns, which translates into a position resolution of $\approx$ 25 cm. This, in turn is a combination of the timing resolutions of both the alpha and gamma detectors, and the contribution of sample geometry.

6.5 Experiments with Samples

In order to evaluate performance of the system, measurements have been done with real benign material following simulants of explosives (containing C,N,O elements). Different objects investigated were Graphite (C), Water (H_2O), melamine ($C_3H_6N_6$) and explosive simulants (C4, RDX) using one BGO gamma detector.

The sample is centred in the middle of the tagged-neutron beam and the BGO gamma detector was placed close to the sample but outside the tagged-neutron cone.Note that with one BGO detector, several-hour acquisitions required to have sufficient counting statistics. However, we have to perform the experiments with data acquisition time of 10-25 minutes for each sample, due to constraint of limited allowed tritium target utilization at NG. Hence, within this short period to have reasonable counting statistics and to demonstrate the system's capability for elemental signature detection in the investigated material, we have chosen sample (3-10 kg) size and the experimental geometry (distance and size of the sample) was such that all 64 alpha tagged neutrons intercept the sample so as to improve counting statistics.

The low-energy threshold was fixed to 1 MeV during the measurements with actual samples in the laboratory, because the gamma rays of the main elements of interest (C, N, O) are located mostly above this energy.

6.5.1 Case1: Pure Element Spectra

Graphite (C)

A graphite block of 10 $\times$10$\times$37 cm^{-3} placed at 118 cm from tritium target in tagged neutron beam, irradiated for 10 minutes. The $\alpha - \gamma$ coincidence time and gamma energy spectra were recorded in coincidence of all 64 alphas. The count rate of total alpha was $\sim$270 kHz, gamma rate $\sim$ 1.2 kHz at BGO and alpha-gamma coincidence event rate $\sim$ 65 Hz observed from rate meter of trigger logic (V1495). The background data was also collected for the same time without sample. Figure 6.22 (a) presents a α-γ coincidence time spectrum for graphite and background. Figure 6.22 (c) shows plot of time versus energy of graphite sample. The two-peaks structure of the time spectrum su-

perimposed on the flat background is clearly visible in Figure 6.22 (a). The flat part of the spectrum corresponds to the random α-γ coincidences. The main prominent coincidence peak (around 960 ch) corresponds to the detection of prompt gamma rays produced in the reaction ^{12}C(n,n'γ)^{12}C for interaction of the tagged neutrons with the sample. The second peak following the main peak is due to tagged neutrons scattered inside the sample and detected by the detector.

Figure 6.23(left) reports measured energy spectra of sample which includes all these contribution. To minimize the random and the scattered-neutron contribution in the energy spectrum of the sample a window on time (900-1025 ch) spectrum has been chosen.

To demonstrate this fact, Figure 6.22(b,d) present a selected time window (ch= 900 -1025 ch) around sample peak and the associated time corelated energy spectra is shown in Figure 6.23(middle). The difference spectrum (Figure 6.23(right)) was obtained subtracting the background spectrum from the sample one.

From the background subtracted spectrum (Figure 6.23) one can see a clear twin peak feature from the carbon line of 4.44 MeV with its single escape (SE).

The Figure 6.24 shows the energy spectrum for the time gate on random background and the gate on scattered neutron regions separately. These spectra are moreover smooth, without any trace of carbon line at 4.44 MeV. Thus this analysis illustrate the principal advantages of the API method for identification of material via elemental signature detection with enhanced SNR and locating the position of investigated object by slicing the time spectrum.

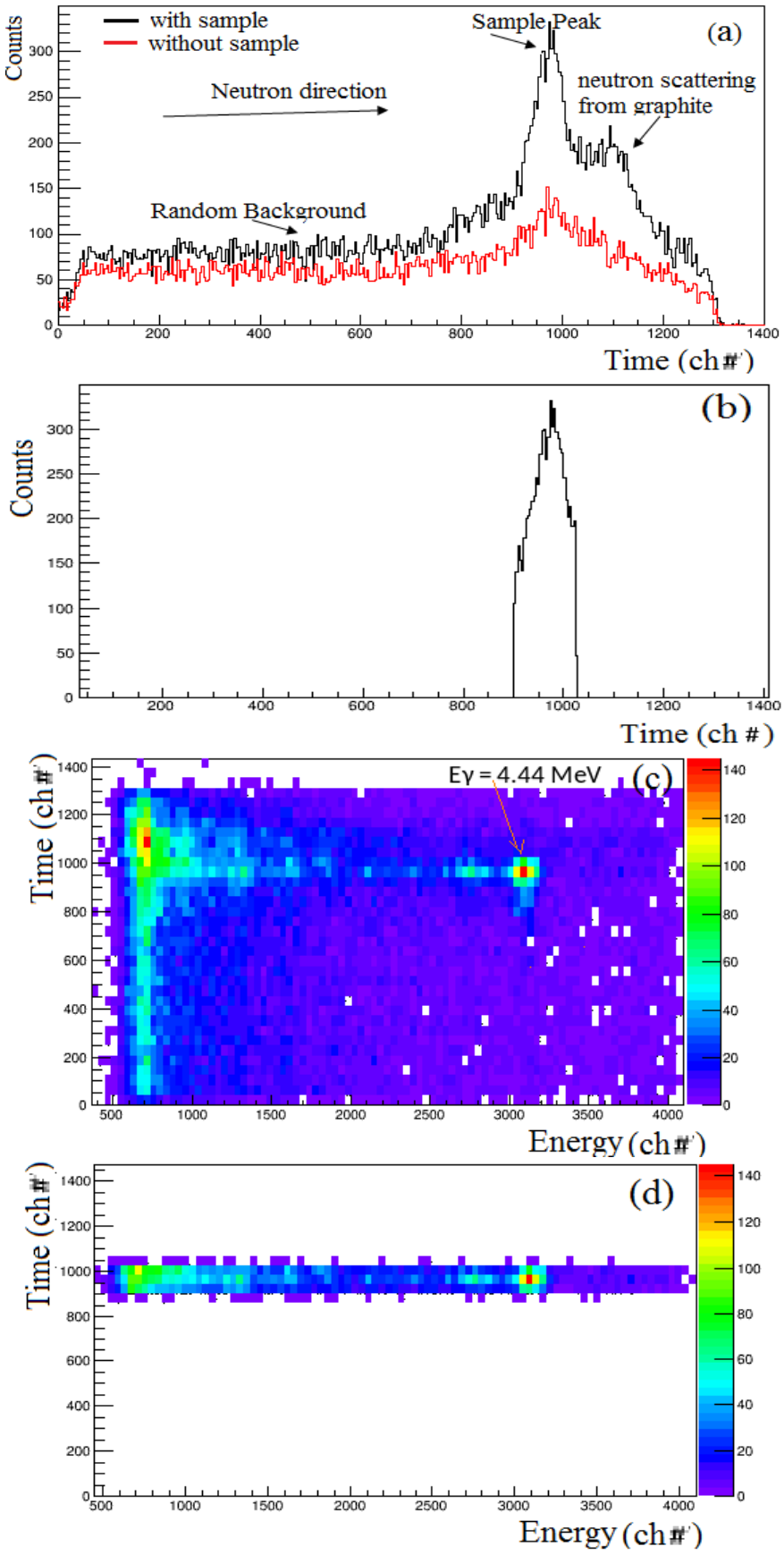

Figure 6.22: (a) α-γ coincidence time distribution measured with (black) and without (red) graphite sample (b) selected time window (925 -1020 ch) around sample peak (c) 2D plot of α-γ coincidence time versus gamma energy (E_γ) and (d) selected time window on 2D plot.

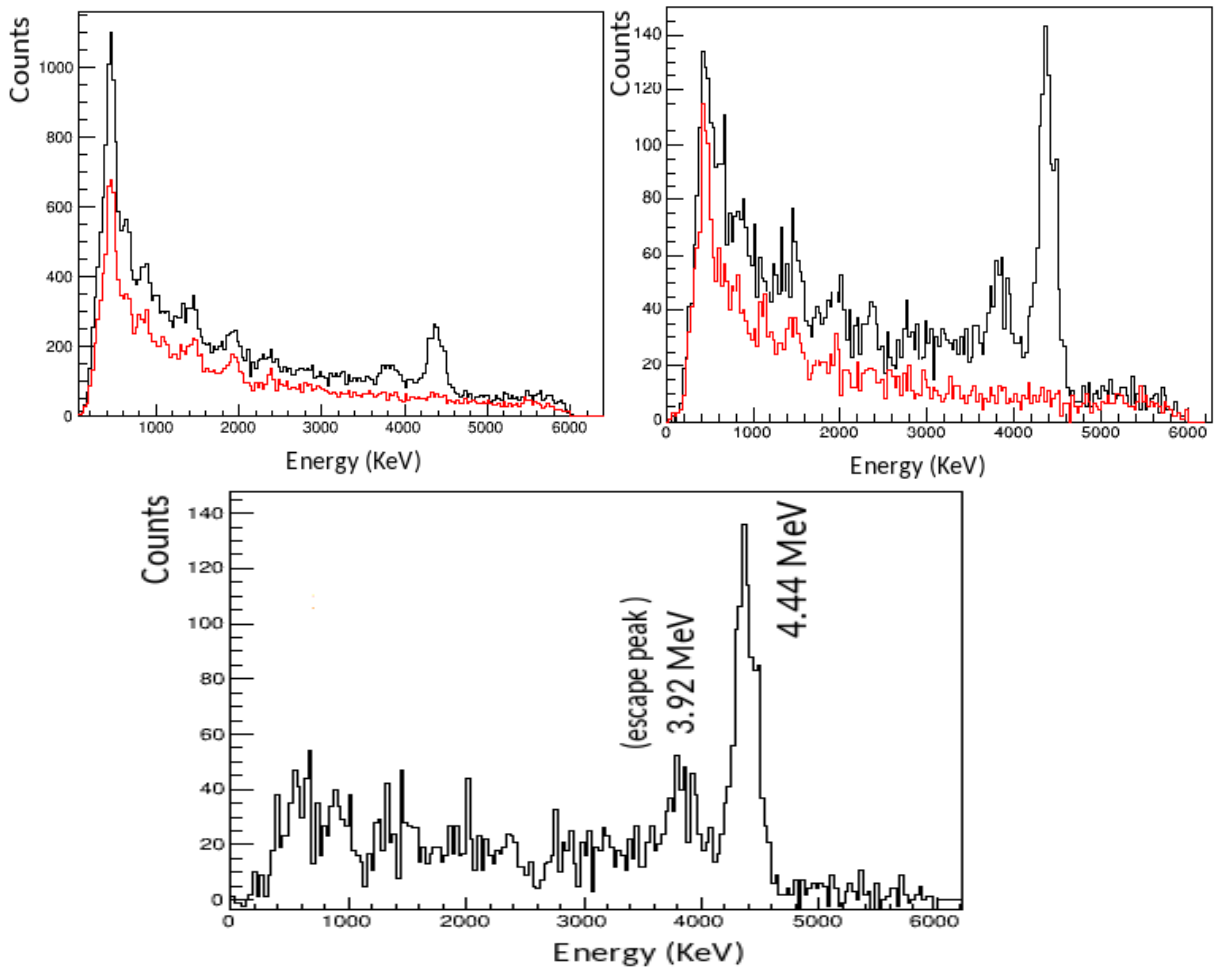

Figure 6.23: Time correlated energy spectra with (black) and without (red) graphite sample when (left) no window selected on time (middle) with time window (925 -1020 ch) selected around sample peak (right) difference spectrum obtained subtracting the background spectrum from the sample one.

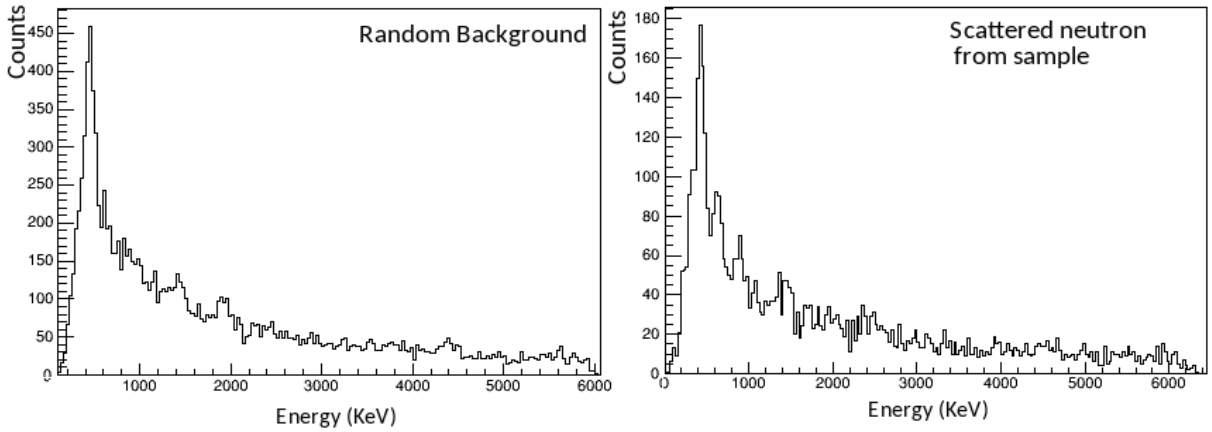

Figure 6.24: Time correlated energy spectra obtained with (left) time gate of 0-700 ch on random background and (right) time gate 1050-1170 ch on scattered neutron contribution for graphite sample

Note that in the next step graphite was replaced with different sample (water, melamine and explosive simulants) and time and energy spectra for each were measured. Time spectra of these samples were similar in nature having random background, sample peak and scattered neutron region, hence only energy spectra of these sample were reported here and discussed .

Water (H_2O)

Next to obtain pure element spectra of oxygen, Water (H_2O) sample was investigated. Following the similar approach (as in case of graphite) the measured energy spectra of water sample are presented in the Figure(6.25). The oxygen spectrum is quite complex in compare to graphite, because a number of states can be excited via 14.1 MeV neutron-induced reactions, as reported in[95, 151] [173]. Major gamma lines observed in the spectrum are 2.74, 3.10, 3.68, 3.85, 6.13 and 6.91 MeV. Effectively, these prompt gamma-rays are produced via different nuclear reactions: the E_γ = 2.74, 6.130 and 6.91 MeV gamma rays are produced in the ^{16}O(n, n'γ)^{16}O reaction. The other gamma rays at 3.10, 3.68 and 3.85 MeV are produced in the ^{16}O(n,$\alpha\gamma$)^{13}C reaction. Similarly, the E_γ= 4.44 MeV gamma ray is emitted following the ^{16}O(n, n'$\alpha\gamma$)^{12}C reaction.

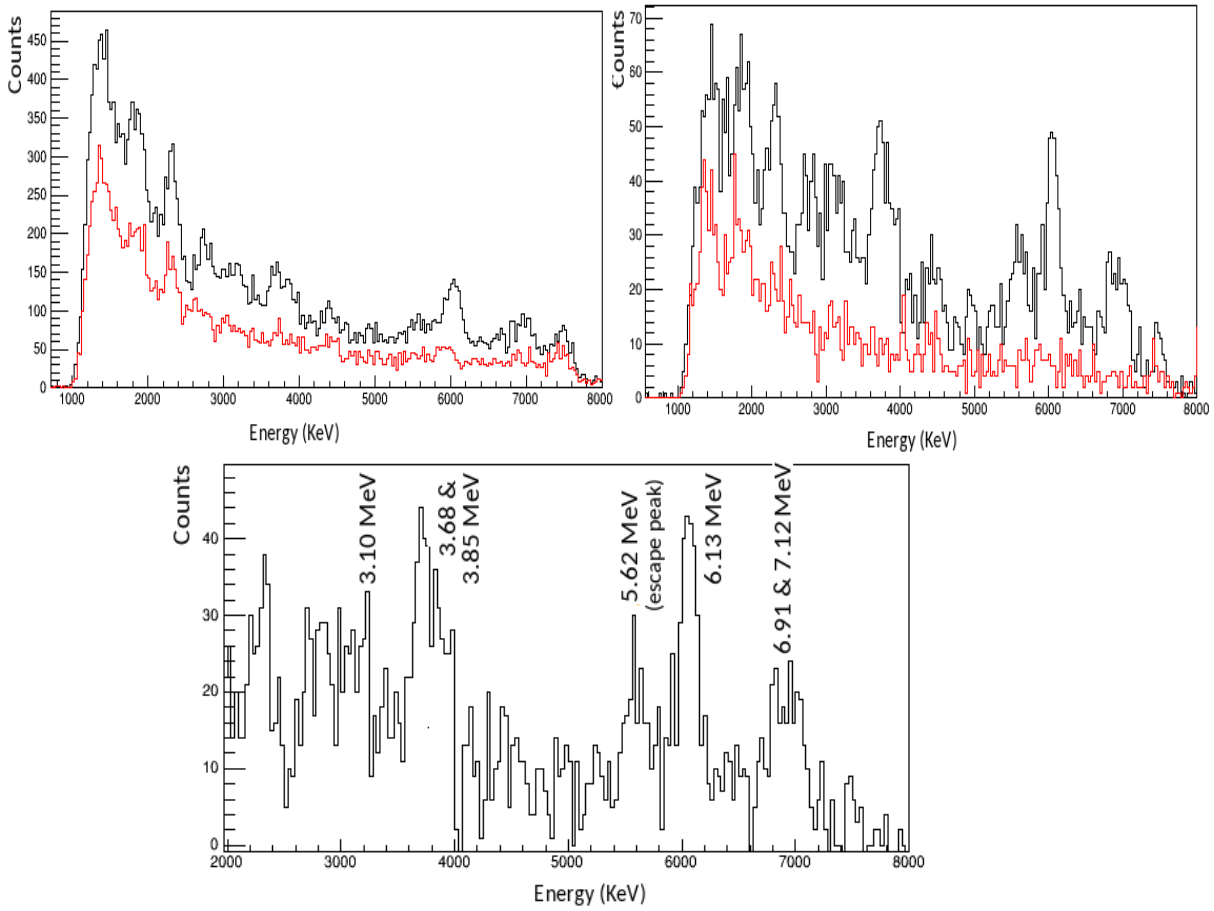

Figure 6.25: Energy energy spectra with (black) and without (red) water sample when (left) no time selection (middle) with a time window on sample peak and (right)difference spectrum obtained subtracting the background spectrum from the sample one.

Table 6.4: SNR for C,O and N evaluated from graphite, water and melamine spectra.

Peak Energy (MeV)	SNR
4.44 (^{12}C)	6.5±0.56
5.12 (^{14}N)	2.2±0.15
6.13 (^{16}O)	3.2±0.35
6.91 (^{16}O)	3.3±0.42

6.5.2 Case2: Complex Sample Spectra

Melamine ($C_3H_6N_6$)

In practical the sample spectra are more complex then having only one element as discussed above and in this case Melamine sample was studied. It contains a high percentage (66.6 %) of N and can be used as explosive simulants. The 4 kg melamine powder sample was irradiated for 20 minutes and the measured energy spectra are presented in the Figure (6.26). The spectra have the characteristic gamma-rays equal to Eγ = 4.44 MeV with its single escape (SE) for C and $_\gamma$ = 2.30 MeV and 5.12 MeV for N that constitute the melamine sample. The gamma rays of energy 2.30 MeV and 5.12 MeV are produced from the reaction ^{14}N(n,n'γ)^{14}N of tagged neutrons with nitrogen elements of melamine. It proves the capability of the system to detect multielements present in complex sample.

The signal-to-noise ratios were evaluated for the elements C (4.44 MeV from graphite), O (6.13 and 6.91 MeV of water) and nitrogen (5.12 MeV from melamine). Where signal was integrated counts under peak area subtracted from the integrated background counts under the same area. The ratio of signal to background is provided in the Table 6.4.

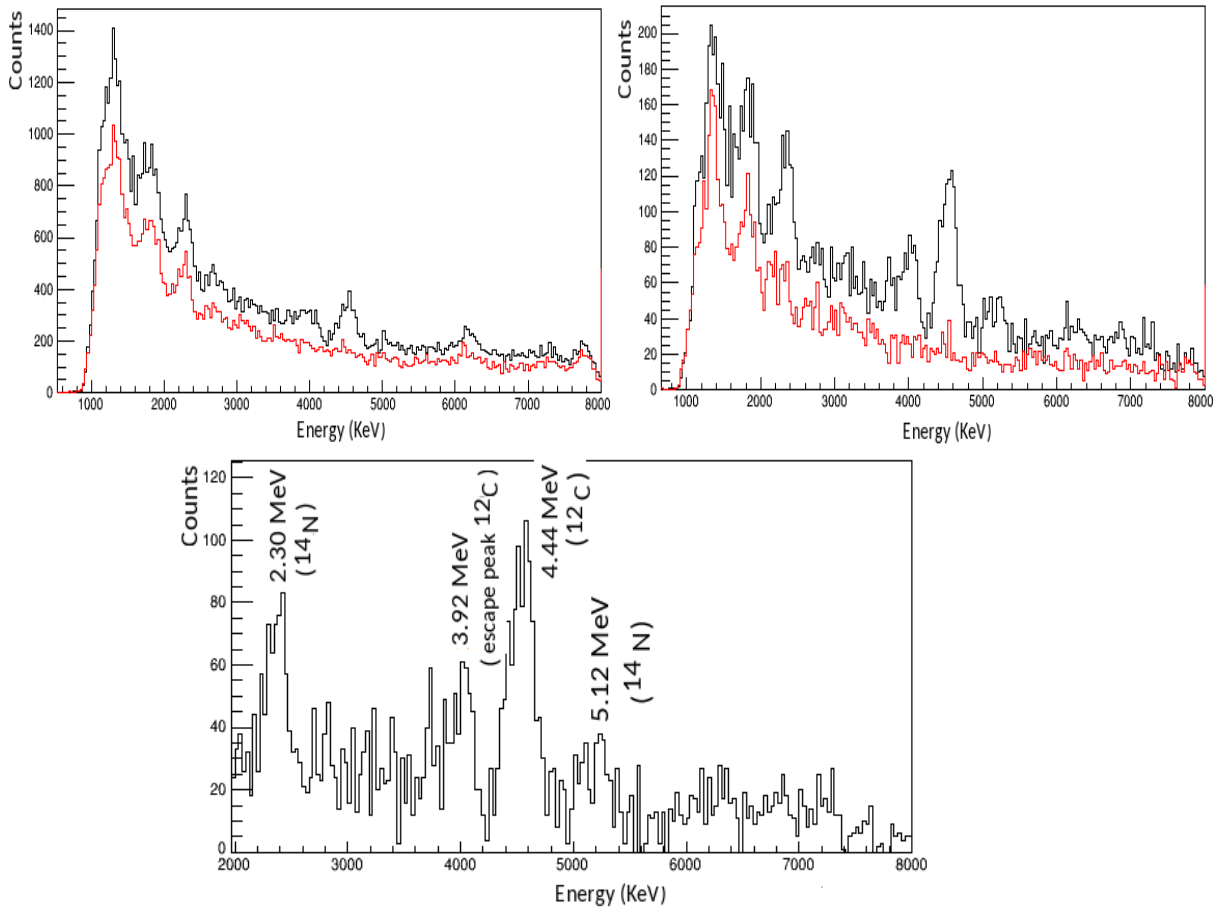

Figure 6.26: Energy energy spectra with (black) and without (red) Melamine ($C_3H_6N_6$) sample when (left) no time selection (middle) with a time window on sample peak and (right) difference spectrum obtained subtracting the background spectrum from the sample one.

Figure 6.27: Water and graphite sample placed together one behind another inline at a distance.

6.5.3 Case3: Locating two objects placed in combination

Water and Graphite Sample

In order to test the capability of the system to identify the hidden materials with different elemental compositions, a water can (5 Liter) was positioned in front of the graphite block (10(depth) x 20(width) x 35 (height)) cm^{-3} as shown in Figure 6.27.

The water sample was placed at 107 cm from target and graphite at 45 cm far away from water sample. Based on system's spatial resolution (in z-axis $\sim$ 24cm), minimum distance of $\sim$ 24 cm required between two samples and being the samples of larger dimension, we kept them apart at a distance of 45 cm (center-to-center distance). The time and energy spectra, acquired with the "water + graphite" samples, are presented in Figure 6.28. The two peaks with centroid at 956 ch and 1045 ch were observed. Difference between the centroids of the two time peaks (Δch = 90 ch) translates to the neutron fight path difference (Δch x 0.098 ns per ch x 5.12 cm $nsec^{-1}$) of 45 cm from the center of the water sample to the center of the graphite sample.

The data were further processed offline via putting a suitable time window (from 925-1025 ch) on first peak as well as on second peak (from 1007-1070 ch) one by one and respective time corelated energy spectra were obtained as shown in Figure 6.29. Background subtracted these spectra were shown in next Figure 6.30. It was observed that with time window on first peak the time co-

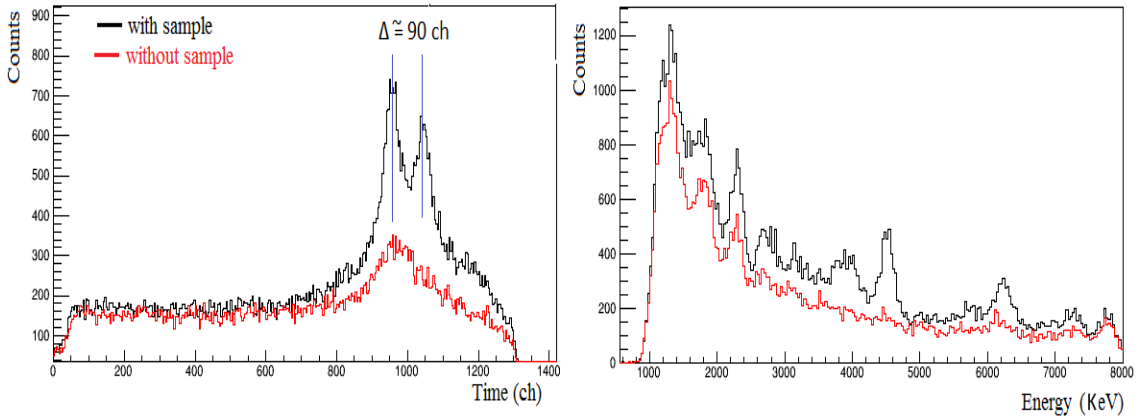

Figure 6.28: (left) $\alpha - \gamma$ time spectrum and (right) energy spectrum of "water+graphite" sample with background (red).

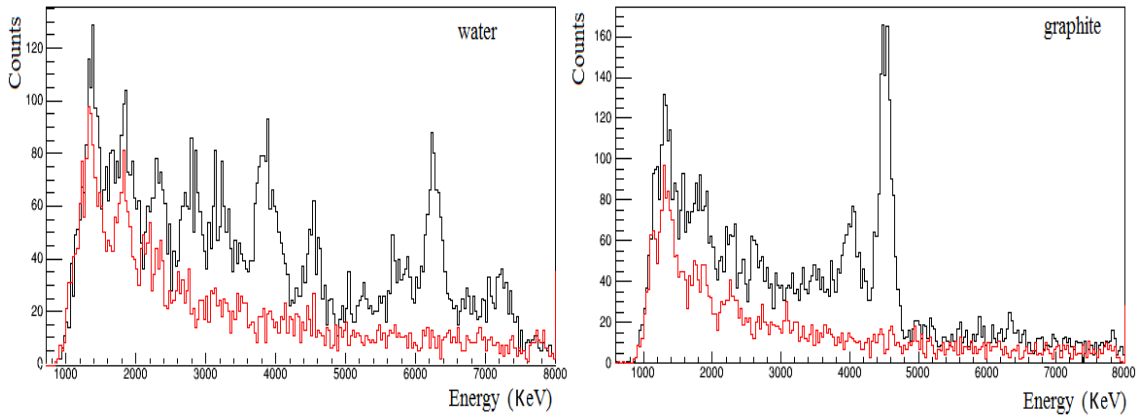

Figure 6.29: Time corelated energy spectra for selected time window (left) T1 (925 -987) ch and (right) T2 (1007-1070 ch) with background (red).

related energy spectrum contain major gamma lines at 2.74 MeV, 3.10 MeV, 3.85 MeV and 6.13 MeV, which are from neutron interaction with oxygen element present in water. On the other hand the energy spectrum obtained with time gate on second peak, shows only one major energy line at 4.44 MeV (with its first escape 3.92 MeV), are neutron induced gammas from carbon element of graphite sample.

Hence it confirms presence of water and graphite sample at different locations corresponds to first and second time peak respectively.

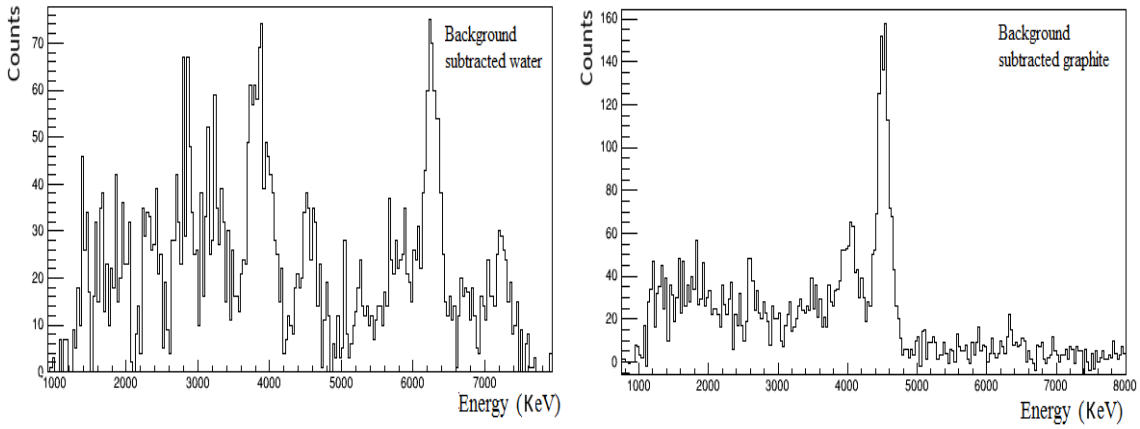

Figure 6.30: Background subtracted energy spectra of (left) water and (right) graphite .

Table 6.5: Simulant of C4(or Plastic military explosive [174].)

simulant	Simulant material	Mass (g)	Element	Mass(g)
	Melamine	51.6	H	2.5
			C	14.7
			N	34.4
	Sand	75.4	Si	35.2
			O	40.2
	Polyethylene	7.3	C	6.3
			H	1.0
	Graphite	0.9	C	0.9
	Total	135.2		

6.5.4 Case4: Simulants of Explosive

In order to perform test with explosive, a mixture of Sand (silicone oxide), Melamine, Polyethylene and Graphite materials were used to prepare simulants of C4 (or Composition C-4 a plastic explosive) as described in Table 6.5. The simulants have similar elemental (C,N,O) composition but not chemically bonded as in actual explosive material. To represent the 100 gm of C4 explosive, 135.2 g of this simulant to be prepared. We have used 5.4 kg of this simulant to represents 4 kg of C4 . Similarly we have prepared simulant of RDX (3.6 kg) using Sand and Melamine. The simulants were irradiated for 25 minutes, the recorded energy spectra with one BGO are reported in the Figure (6.31-6.32). From the background subtracted spectrum we have observed the characteristics gamma at E_γ = 4.44 MeV of carbon, E_γ = 6.13 MeV of oxygen and E_γ = 2.3 MeV and 5.12 MeV of nitrogen elements constitute of C4 as

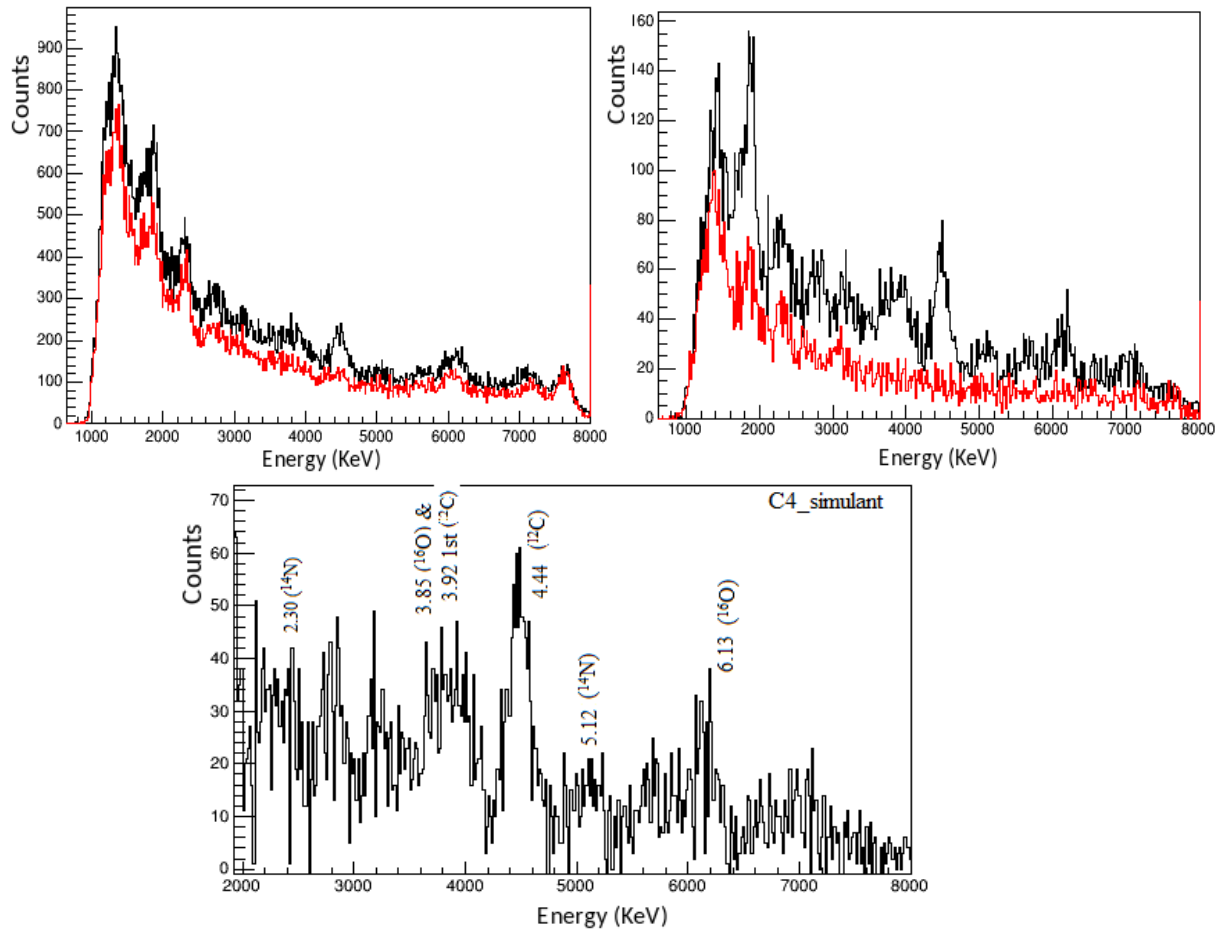

Figure 6.31: Energy energy spectra of C-4 simulant (black) and background (red) (left) no time selection (middle) with a time window on sample peak and (right)difference spectrum obtained subtracting the background spectrum from the sample one.

well as in RDX spectra Figure 6.32. The spectra illustrate the sensitivity of the tagged neutron method to the elemental content of the explosive.

Eventhough, the counting statistics are not as good as required but it is sufficient to indicate the presence of C, O, N element's fingerprints in the sample spectra. These results provides a confidence of the system's ability to provide the C, O, N elemental signature in explosive like samples and thus its suitability towards application of chemical explosive detection.

Further a comparison study was performed and experimental energy spectra of melamine and RDX simulant were compared with GEANT4 simulated (Chapter 5) as shown in Figure 6.33. The simulated spectra were scaled to experimental 4.44 MeV peak intensity for comparison. The general shape of the melamine spectrum, in particular the possible photo peaks and their relative

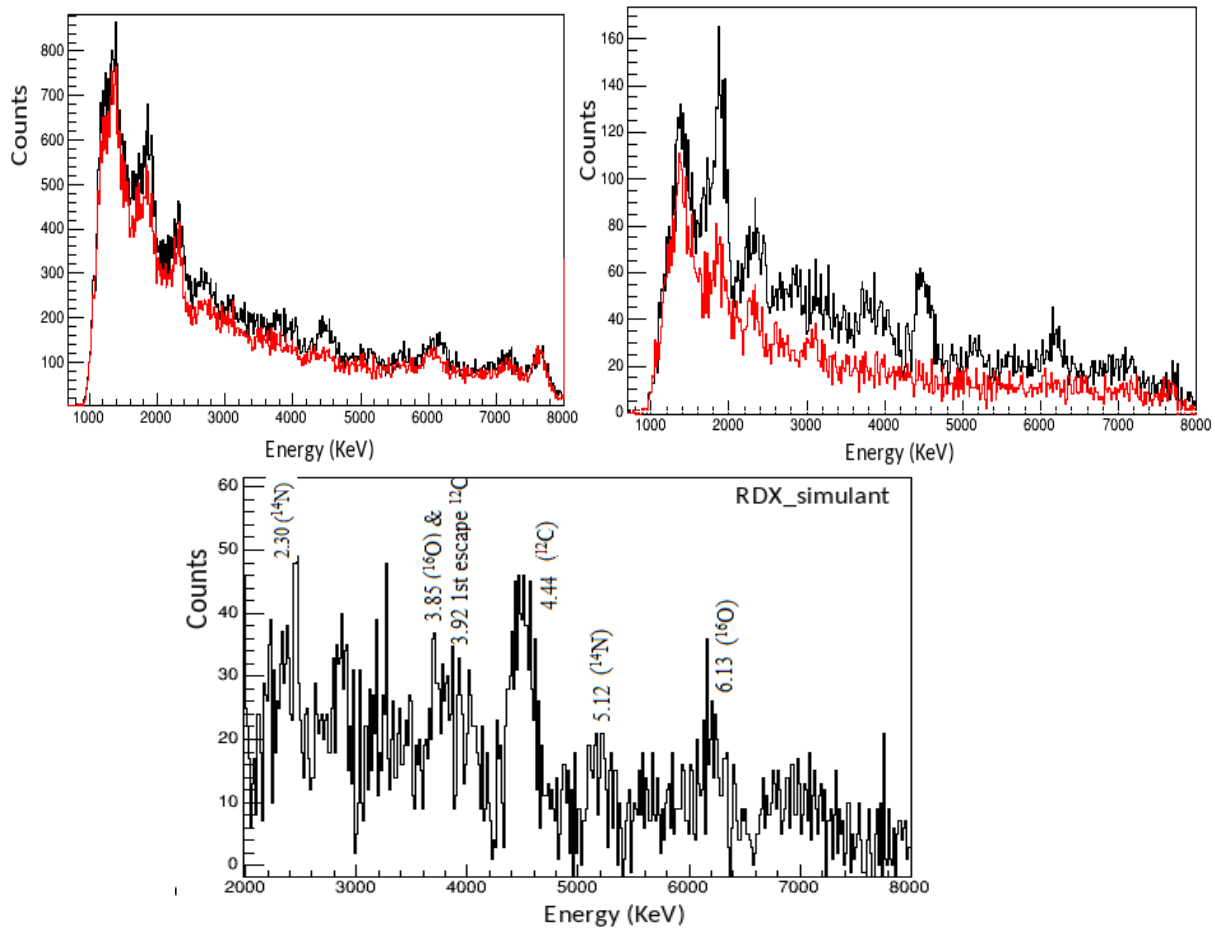

Figure 6.32: Energy energy spectra of RDX simulant (black) and background (red) (left) no time selection (middle) with a time window on sample peak and (right)difference spectrum obtained subtracting the background spectrum from the sample one.

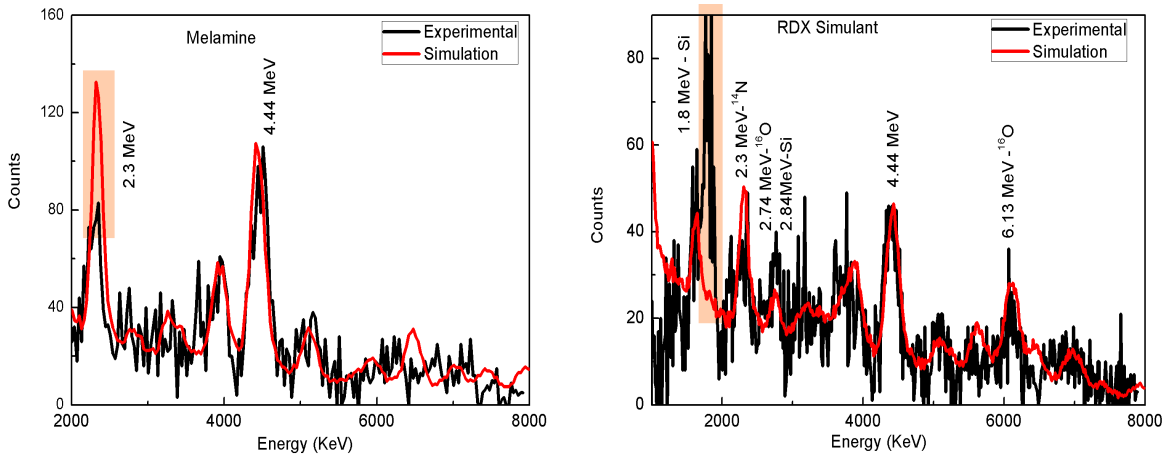

Figure 6.33: Comparison of simulated and experimental energy spectra of (left) Melamine and (right) RDX simulant.

intensity w.r.t to carbon peak (4.44 MeV) is quite satisfactory with simulation except at 2.3 MeV. The significant discrepancy at 2.3 MeV gamma line of nitrogen has also been observed from other researchers [95, 175] and that is attributed to the lack of precision in the evaluated cross section data of nitrogen. In the case of RDX, overall simulated and experimental spectra are in close agreement except at energy 1.8 MeV and 2.8 MeV, that is due to Si present in the RDX simulant sample prepared from benign materials including sand (SiO_2). From the litrature [151, 173] it can be found that the Si element has the prominent prompt gamma line at 1.78 MeV and 2.84 MeV on interaction with 14.1 MeV neutron.

6.6 Conclusion

API based neutron interrogation system has been developed and characterized using an array of 8x8 matrix of YAP:Ce crystals coupled to a laboratory D-T NG. The system was integrated with VME based Front-End-Electronics for data acquisition and processing. The experiments were performed with the system at laboratory conditions for benign and explosive simulants using one BGO detector. The overall time resolution of the system achieved was 4.8 ns, which corresponds to spatial resolution of 25 cm in the flight path of tagged neutron direction (z-axis). This could be further improved using γ-detector of

better time resolution, since present BGO has shown quite poor time resolution. The dimension of the tagged neutron beam measured at 107 cm was around 46 cm that defines the maximum x-y dimension (perpendicular to the tagged neutron beam direction) of an object that can be scanned at a time.

Proof-of-concept laboratory experiments have been successfully performed to demonstrate the efficacy of the API system for C,O,N elemental analysis of pure and complex sample spectra with high SNR. Using the information of alpha-gamma coincidence time distribution, an object of interest was located by means of its characteristic prompt gamma-ray emission signals. The characteristics gamma lines of C (4.44 MeV) and O (6.13 MeV etc) element were obtained from graphite and water sample in 10 minutes acquisition and the SNR obtained for C (4.44 MeV and O(6.13 MeV) were 6.5 and and 3.3 respectively. We could locate and identify the two samples (water and graphite), when placed together inline at a distance using time information and characteristics prompt gamma spectra. In the next step melamine and explosive simulants of C4 (and RDX) were investigated. Despite the poor statistics , it is possible to discern these signatures above the background in the 25-minutes acquired energy spectrum. The recorded characteristic gamma lines at 4.44 MeV (^{12}C), 6.13 MeV (^{16}O) and 2.3 and 5.12 MeV (^{12}N) in their complex energy spectra have proven the system's capability towards application of explosive detection. The close agreement of the general shape of experimental and simulated energy spectra (of melamine and RDX) in particular the possible photo peaks and their relative intensity w.r.t to carbon peak (4.44 MeV) validates the simulated model developed for tagged neutron method. Based on these results and conclusions, it can be directed to proceed towards development of the field deployable system.

Under the future plan, the present proof-of-concept work need to extend further with an array of gamma detectors to increase the sensitivity of the system and adequate data representation within 10 minutes and further validation of simulated results. Apart from the hardware part, the development of analysis and decision making software tools are equally important and necessary for identification of threat from benign material.

CHAPTER 7

Summary and future scope

7.1 Summary of thesis

Neutron interrogation techniques offer unique capabilities towards non-intrusive and non-destructive inspection in comparison to X-ray/gamma based techniques. These techniques span the range from being few single specific element to multiple element and direct imaging with time of flight technique or transmission based imaging. A broad range of applications are possible with these techniques. This thesis work has focused on neutron interrogation techniques of Fast Neutron Radiography and Associated Particle Imaging for imaging and detection of materials composed of light element, in bulk. Particulary for the materials with elemental composition of C, N, O which are the key elements of high explosives. The fast ($\sim$ MeV) neutrons are suitable for interrogation of medium (luggage) and large (cargo containers) scale objects. A detail simulation study on these techniques were performed to thoroughly understand the methodology, their potentials and limitations. These techniques were then implemented using in-house developed Neutron Generator. Apart from these developments, D-D/D-T Neutron Generator was characterized and detection tools were developed for real time D-D/D-T neutron monitoring. It includes associated particle based neutron detector and optical fiber based miniature neutron detectors.

The following is a summary of the work done in the thesis:

1. **Characterization of D-D/D-T Neutron Generator**

   The thesis work commences with characterization of in-house developed D-D/D-T NG. It operates either in D-D or D-T mode producing monoenergetic neutron of energy 2.45 MeV or 14.1 MeV. Neutron emission rate

of the NG is an important parameter for their characterization and experimental data analysis. The neutron yield of NG measured with foil activation technique was 1×10^{10} for D-T neutron and 3×10^{7} n/sec of D-D neutron. Foil activation technique being an offline method, it provides no information about any variation in neutron flux over the exposure duration. Real time monitoring of neutron emission rate is necessary to maintain a stable neutron output during the experiments. For this purpose an Associated Particle based Neutron Detector was developed using passivated ion implanted planar silicon detector, it is based on charged particle detection associated with D-D/D-T neutron emission. It was calibrated with foil activation method and has been successfully used for PGNAA experiments.

Performance of the Associated Particle based Neutron Detector degrades with usage time due to radiation damage particularly with regular exposure of high energy DT neutrons. To overcome this, a fiber based miniature ($\sim$ mm), fast neutron detector was developed for DT neutron monitoring with ThO_2+ZnS (Ag) scintillator. However, at first a thermal neutron detector with ^{6}LiF+ZnS (Ag) was developed, as ^{6}Li has high cross section ^{6}Li (n,α) for thermal neutron in comparison to (n,f) of DT neutron with ^{232}Th, ensuring high probability of successful development of such miniature detectors. The sensitivity of thermal and fast neutron detector was 3×10^{-4}cps and 3.6×10^{-6}cps per unit neuron flux of thermal and D-T neutrons respectively. The performance of thermal neutron detector was investigated with thermal neutron flux profile measurements across the experimental channels in a sub-critical reactor system. The fast neutron detector was tested for neutron emission profile measurement of a D-T neutron generator and was used as neutron monitor for the Fast Neutron Radiography experiments

2. **Fast Neutron Radiography: FNR**

   Simulation study of FNR with 14 MeV for wide range of samples including polythelene, graphite, metallic (Al, Fe) and lead (high Z) material has been carried out. Results of step wedge configuration have shown high

transmission (73%) capability of 14 MeV neutron in thick (100 mm) lead and holes of size 1 mm or larger in such slabs can be imaged. The results also reveal that the presence of hydrogenous material HDPe, which is a low Z material encapsulated by thick lead could be imaged with FNR, if the thickness of the masked material (lead) is not more then 100 mm. The case of configuration where number of materials HDPe, Graphite, Al, Fe, Cd and Pb (from low to high Z), placed concentrically in increasing order of their atomic number was investigated. The simulation results have provided the possible combinations of low (HDPe/C/Al) and high Z (Fe/Pb) materials which could be used for imaging with 14 MeV neutrons. Effectively, the study has provided insight towards understanding of the potentials and limitations of the FNR with respect to different sample configurations. Based on simulated results, the experiments were carried out for experimental imaging of composite structure made up of HDPE-Lead. To implement the FNR, we have designed an experimental setup with D-T NG having yield $\sim 2\times 10^{9}$ nsec^{-1}. Imaging with such moderate source intensity and source spot of 20 mm, was a challenge. In this regards an iron collimator with inlet aperture (D) of 10 mm, L/D 43 (L=length of the collimator) and Electron Multiplying CCD camera used in combination with thick plastic scintillator. The experimentally obtained images of test specimens (step wedge, holes in step wedge) have shown the high transmission (70% in 100 mm lead) of DT neutrons through thick and high density objects. The reasonable contrast images of 5 mm hole in HDPe masked with lead block of thickness 0-100 mm demonstrated the capability of the FNR system for imaging of low Z material masked with a thick layer of high Z material.

Eventhough FNR has shown a promising method for imaging of thick objects especially for shielded complex samples containing mixed low-Z/high-Z materials but elemental informations could not be obtained. For elemental detection, a study of PGNAA was performed with conventional techniques.

3. **Elemental detection in bulk with PGNAA**

The starting point of our study was demonstration of PGNAA with D-D/D-T NG, based on neutron induced element (C, O, N, H, Cl and Fe) specific gamma signature detection in investigated objects. The fingerprint of these elements were exploited using traditional TNA and FNA nuclear techniques, which are based on prompt gamma emitted via thermal neutron capture (n,γ) and inelastic scattering reaction respectively. TNA method was executed using D-D NG. The detection of 10.8 MeV high energy gamma rays from small amounts of nitrogen present in urea was a difficult and challenging task, however, inspite of low neutron yield ($\sim 3 \times 10^7$ nsec^{-1}) of the D-D neutron generator, the nitrogen signal could be detected with good SNR $\approx$7. Since most of the explosives are nitrogen rich containing compounds, therefore, this technique can be used to identify such materials that contain nitrogen. On the other hand the detection of prominent chlorine lines in NaCl with SNR =0.6, indicate the capability of TNA method for application of chlorine based narcotics detection. Although the concentration of nitrogen is a good indicator of explosives, the combinations of oxygen and carbon should be considered as well. The additional information about the concentration of oxygen and carbon can be used to discriminate among different materials using relative elemental ratios such as O/C and N/C. However, TNA method has shown no signature of C and O elements due to their threshold reactions. In this context, FNA was studied as a limiting case of TNA and experiments were performed using D-T NG. The energy spectra of urea has provided signatures of C (4.44 MeV), O (6.13 MeV)and N (5.12 MeV) elements but with poor SNR $\leq$ 0.3. In the present experiment,, the main difficulty faced was the high background due to neutron interactions with surrounding materials. To improve the signal to noise ratio it is possible to shield these neutrons, which makes system bulkier and as a result system footprint is large. To overcome this we have adopted alternative approach of Tagged Neutron based API technique.

4. **Associated Particle Imaging: API**

To facilitate the design and construction of a prototype laboratory system, a simulation model has been developed, using the Geant4 toolkit. This simulation work has established the toolkit environment for (a) generating tagged neutrons (b) their transport and interactions within a sample to induce emission and detection of characteristic gamma rays and (c) 2D - 3D image reconstruction of the interrogated object using the known velocities of 14.1 MeV neutron (5.1 cm ns^{-1}) and gamma-rays (30 cm ns^{-1}). The techniques was modelled using an array of BGO gamma detector and it's physical response was incorporated in simulation to have realistic spectral features in API. Different aspects of API were studied : a data set of pure elements (C, O , N, Al and Fe) spectra was generated, simulated spectra of various benign (urea, melamine) and explosive (RDX, TNT, Ammonium Nitrate) samples were studied and analyzed. The elemental contributions (weight fraction) of C, N, O from sample spectra were determined using linear combination of reference set of pure elements spectra generated via simulation in same configuration. The result of matrix study indicated that tagged neutron based API system, could detect hidden explosive (1 kg RDX) inside a container filled with an iron matrix of density 0.1- 0.2 gm cm^{-3}, while in organic matrix it is quite difficult even at average matrix density of 0.1 gm cm $^{-3}$. The reconstructed 2D and 3D images correctly reveals the location of the interrogated object. To summarize, these studies have provided the groundwork for analysis of gamma-ray spectra utilizing detector/s elemental responses measured with tagged (14.1 MeV) neutron in the particular geometry of API.

Further, API technique was implemented and realized using in-housed developed D-T NG at BARC. The API system was developed using a 8x8 matrix of YAP:Ce crystals coupled to the NG in a designated manner and integrated with VME based Front-End-Electronics for data acquisition cum processing and a BGO detector. The overall time resolution of the system achieved was 4.8 ns, which corresponds to spatial resolution

of 25 cm in the direction of flight path of tagged neutron (z-axis). This could be improved using gamma detector of better time resolution, since the time resolution of the present BGO gamma detector was quite poor. The tagged neutron beam dimension measured at 107 cm was $\sim$46 cm that defines the maximum x-y dimension (perpendicular to the tagged neutron beam direction) of an object that can be scanned at a time. The performance of the system was investigated with benign and explosive simulants using a $3'' \times 3''$ BGO detector. Proof-of-concept laboratory experiments have been successfully performed to demonstrate the efficacy of the API system for detection of key elements -Carbon, Nitrogen and Oxygen (necessary for identifying explosives) with high SNR. The characteristics gamma lines of C (4.44 MeV) and O (6.13 MeV etc) element could obtained with signal to noise ratio of 6.5 and 3.3 respectively, from pure sample (graphite and water) spectra acquired in 10-15 minutes. The system has shown the ability to locate and identify the two samples (water and graphite), placed together inline at different distances using α-γ coincidence time information and characteristics prompt gamma spectra. In case of complex sample spectra of melamine and explosive simulants of C4 (and RDX) despite the poor statistics, it was possible to discern signatures of C(4.44 MeV), O(6.13 MeV) and N(2.3 and 5.12 MeV) clearly above the background. It emphasizes the system$'$s capability towards application of explosive detection based on signatures of prime C,O,N elements. The comparison of experimental and simulated energy spectra (of melamine and RDX) has shown the close agreement in their general shape in particular, the possible photo peaks and their relative intensity w.r.t to carbon peak (4.44 MeV) and this way it validates the simulated model developed for API technique.

Based on these results, the work can be proceed further towards development of the field deployable system.

7.2 Future work

The directions on which further research will be focused on the following:

1 Improvement of sensitivity and time resolution of the API system using an array of gamma detectors with better time resolution $\leq$ 2 ns. The present study has been demonstrated at laboratory scale, it will be extended into a fully engineered scanning system for field deployment. Benchmark experiments for validation of simulated results and software tools will also be developed.

2 The FNR system developed is at initial stage, mainly dealing with physics concepts and demonstration of feasibility experimental results. From the perspective of future potential applications of fast neutron imaging, the performance of the whole setup could be further optimized with an improved design of collimator geometry, imaging detector setup using ZnS(Ag) loaded thin plastic screen in place of thick plastic scintillator. Other approach could be the use of high intensity NG with smaller source spot which will enable to have large L/D and hence there is improvement in the image quality.

3 Alternative applications of API and FNR techniques based system could be explored. For instance Tagged Neutron Method could be applied to search for narcotics, landmines (in addition to find conventional explosives), which are also comprised of light nuclides and have unique elemental ratios. There are other fields that may benefit from FNR such as imaging of nuclear stockpile stewardship and fissile materials imaging using high energy neutrons.

Bibliography

[1] L.GRODZINS. *Nucl. Inst. Meth. Phys. Res. B*, **255**, 1531 (1992).

[2] FAINBERG A. *Science,DOI: 10.1126/science.255.5051.1531*, **255**, 1531 (1992).

[3] FURTON K.G., MYERS L.J. *Talanta*, **54 (3)**, 487 (2001).

[4] BERMBACH, R., VEY S. *Proc. Int. Soc. Opt. Eng.*, **1824**, 199 (1992).

[5] GOZANI T., STRELLIS D. *Nucl. Instrum. Meth. B.*, **261(1-2)**, 311 (2007).

[6] C. BRUSCHINI. *Commercial Systems for the Direct Detection of Explosives (for Explosive Ordnance Disposal Tasks)* (ExploStudy, Final Report, 2001).

[7] YINON J. *Forensic and Environmental Detection of Explosive* (John Wiley and Sons,Chichester,UK, 1999).

[8] LISA THIESAN ET AL,. *Survey of Commercially Available Explosives Detection Technologies and Equipment* (2004).

[9] HUSSEIN EMA. *Detection of explosive materials using nuclear radiation: a critical review.Proc SPIE .*, **1736:130137** (1992).

[10] R. LANZA. *Nucl. tech. for explosive detection: Current prospects and requirements for future development, Proc. of an IAEA Technical Meeting.*, **1736:130137**, 13–17 (2006).

[11] EMA HUSSEIN AND EDWARD J. WALLER. *Radiation Measurements*, **29 (6)**, 581–591 (1998).

[12] P.BACH ET AL. *Nucl. Instr. and Meth. B*, **79**, 605 (1993).

[13] A. BUFFLER. *Radiation Physics and Chemistry*, **71**, 853 (2004).

[14] J. C. OVERLEY. *Int. J. Appl. Radiat. Isot.*, **36(3)**, 185 (1985).

[15] G.F.KNOLL. *Radiation detection and measurement* (3rd Edition ,John Wiley and Sons Inc. New York, 1999).

[16] G J CSIKAI. *CRC handbook of fast neutron generator, Volume I* (CRC Press,Inc., 1987).

[17] RADIATION PROTECTION AND MEASUREMENT FOR LOW-VOLTAGE NEUTRON GENERATORS. *NCRP Report No. 72* (1990).

[18] ALEKSANDROV, V.D. ET AL. *Appl. Radiat. Isotopes*, **63 (5-6)**, 537 (2005).

[19] DAVID L. CHICHESTER. *Production and Applications of Neutrons Using Particle Accelerators ,INL/EXT-09-17312* (2009).

[20] S. BISHNOI ET AL. *Proc. DAE Symp. On Nucl. Phys*, **56**, 1102 (2011).

[21] TARUN PATEL. *www.barc.gov.in/publications/nl/2013/spl2013/web/newsletter*, p. 146 (2013).

[22] J. M. VERBEKE ET. AL. *Appl. Radiat. Isot.5*, **53**, 801809 (2000).

[23] . *http://www.ortec-online.com/detectors/chargedparticle*.

[24] J. S. NEAL ET AL. *Nucl. Instr. and Meth. A*, **568**, 803 (2006).

[25] J. C. COOPER ET AL. *Nucl. Instr. and Meth. A*, **505**, 498 (2003).

[26] L. E. USSERY AND C. L. HOLLAS. *Design and Development of the Associated-Particle Three-Dimensional Imaging Technique, Report LA -12847-MS (UC-706 and UC-700)* (1994).

[27] J. C. COOPER ET AL. *Associated Particle Imaging, DOE/NV11718 -223* (1998).

[28] S.BACCARO ET AL. *Nucl. Instr. and Meth. A*, **361**, 209–215 (1995).

[29] J. C. COOPER ET AL. *Associated Particle Imaging, DOE/NV11718 -223* (1998).

[30] E. V. D. VAN LOEF ET AL. *Appl. Phys. Lett.*, **79**, 1573 (2001).

[31] E. V. D. VAN LOEF ET AL. *Appl. Phys. Lett.*, **77**, 1467 (2000).

[32] MENGE, P.R ET AL. *Nuclear Instruments and Methods*, **A579**, 6–10 (2007).

[33] GIERLIK ET AL. *IEEE Trans. on Nucl. Sci.*, **53(3)**, 1508 (2006).

[34] GOZANI T. *Proc. SPIE 2936*, pp. 9–20 (1996).

[35] G. NEBBIA ET AL. *Nuclear Physics A*, **752**, 649c658c (2005).

[36] IAEA PUBLICATION IAEA/PS/AG-1093: IAEA. *A Remotely Controlled Multi-Sensor Platform for Humanitarian Demining* (2000).

[37] CLAUDIO BRUSCHINI. *A Remotely Controlled Multi-Sensor Platform for Humanitarian Demining,ExploStudy, Final Report 17/2/2001* (2001).

[38] GOZANI T ET AL. *Nucl. Inst. Meth. Phys. Res. A*, **505**, 482–485 (2003).

[39] LEE W.C ET AL. *Nucl. Instrum. Methods A*, **353**, 641 (1994).

[40] G. VOURVOPOULOS. *Nucl. Inst. Meth. Phys. Res. B*, **89**, 388 (1994).

[41] KOLTICK D, KIM Y ET AL. *Nucl. Instrum. Methods A*, **261(1-2)**, 277 (2007).

[42] S. SINGH AND M. SINGH. *Signal Processing*, **83(1)**, 31 (2003).

[43] T. GOZANI. *Nucl. Instr. and Meth. in Phys. Res. B*, **99**, 743 (1995).

[44] D.R. BROWN, A. COATES ET AL. *Proc. of the SPIE*, **2396**, 743 (1997).

[45] V. VALKOVI ET AL. *Nucl. Instr. and Meth*, **76**, 29 (1969).

[46] BEYERLE A, HURLEY JP, TUNNEL L. *Nucl Instrum Meth A*, **299(1-3)**, 458 (1990).

[47] GOKHALE P., HUSSEIN E. *Appl. Radiat. Isotopes*, **48 (7)**, 973–979 (1997).

[48] EBERHARDT J.E., RAINEY S. ET AL. *Appl. Radiat. Isotopes*, **63 (2)**, 179 188 (2005).

[49] J HALL, F DIETRICH ET AL. *Development of High-Energy Neutron Imaging for Use in NDE Applications,UCRL-JC-134562*, **63 (2)**, 179 188 (2005).

[50] G CHEN AND R C LANZAL. *Proc. Sixteenth Int. Conf. Appl. of Accel. in Res. and Indus.* (2000).

[51] A. BUFFLER, J. TICKNER. *Radiation Measurements.*, **45**, 1186–1192 (2010).

[52] SOWERBY B.C., TICKNER J.R ET AL. *Nucl. Instrum. Meth. A*, **580 (1)**, 799–802 (2007).

[53] W.L.RAAS, B. BLACKBURN ET AL. *Neutron Resonance Radiography for Explosives Detection:Technical Challenges ,UCRL-CONF-217017* (2005).

[54] IAEA-TECDOC-1604. *eutron Imaging:A Non-Destructive Tool for Materials Testing* (2003-2006).

[55] H. BERGER. *Neutron Radiography* (Elsevier Publishing Company, New York, 1965).

[56] H. RAPP. *Materials Evalua-tion*, **27**, 245 (1969).

[57] E. BAGGEET AL. *Nucl. Instr. and Meth*, **147**, 109 (1977).

[58] Y.P. BOGOLUBOV ET AL. *Adelphi Technology Inc., http://www.adelphitech.com/*.

[59] HIGH YIELD NEUTRON GENERATORPHOENIX NUCLEAR LABS. *http://phoenixnuclearlabs.com/product/high-yield-neutron-generator*.

[60] J. REIJONEN. *Proc. Particle Accelerator Conf.*, p. 49 (2005).

[61] Y.P. BOGOLUBOV ET AL. *Nucl. Inst. and Meth. in Phys. Res. A*, **605**, 62 (2009).

[62] WU YANG ET. AL. *Physics Procedia*, **43**, 205 (2013).

[63] J.J. RANT. *Proc. Sixth World Conf. on Neutron Radiography*, p. 23 (1999).

[64] HALL J., RUSNAK B., FITSOS P.J. *High-energy neutron imaging development at llnl. Tech. Rep. UCRL-CONF-230835* (2007).

[65] MOR ET AL. *Phys. Procedia*, **69**, 304 (2015).

[66] Y. SEKI ET AL. *Nucl. Inst. Meth. Phys. Res. A*, **870**, 148 (2017).

[67] OTAKE Y ET AL. *Journal of Disaster Research*, **12-3**, 585 (2017).

[68] OSTERLOH ET AL. *Phys. Procedia*, **69**, 472 (2015).

[69] OSTERLOH ET AL. *Proc. Int. Symp. on Digital Industrial Radiology and Computed Tomography*, **69**, 472 (2011).

[70] T. BUCHERL ET AL. *Appl. Radiat. Isot.*, **61**, 537 (2004).

[71] IKEDA ET AL. *Nucl. Inst. Meth. Phys. Res. A*, **276**, 183 (1989).

[72] ZBORAY ET AL. *Appl. Radiat. Isot.*, **119**, 43 (2017).

[73] R. ADAMS ET AL. *Appl. Radiat. Isot.*, **107**, 1 (2016).

[74] N. TAKENAKA ET AL. *Nucl. Instrum. Methods Phys. Res. A*, **424**, 73 (1999).

[75] ROBERT ZBORAY ET AL. *Nuc. Eng. and Design*, **273**, 10–23 (2014).

[76] R. ZBORAY ET AL. *Rev. Sci. Instrum.*, **86**, 075103 (2015).

[77] RANT J. ET AL. *Proc. 7th European Conf. on NDT.*, p. 2763 (1998).

[78] MIKEROV V.I. ET AL. *J. Asppl. Rad. Isotopes.*, **61**, 519 (2004).

[79] MATSUBAYASHI M. ET AL. *Nucl. Instr. Meth. A*, **463**, 324 (2001).

[80] Y. IKEDA ET AL. *Nucl. Inst. Meth in Phys. Res. A*, **833**, 61 (2016).

[81] MAKOWSKA ET. AL. *J. Imaging*, **3**, 60 (2017).

[82] TRITEC. *http://www.rctritec.com/en/scintillators.htm* (2017).

[83] M.S. JOHNSON ET AL. *Physics Procedia*, **90**, 47 (2017).

[84] E RHODES ET AL. *IEEE Trans. Nucl. Science*, **39**, 1041 (1992).

[85] E RHODES ET AL. *Report ANL/ACTV-95/1* (1995).

[86] HOLLAS ET AL. *Report LA-11876-MS* (1990).

[87] D.L.CHICHESTER ET AL. *Nucl. Instr. Meth. Phys. Res. B*, **241**, 753 (2005).

[88] GORDON C. M. ET AL. *App. Rad. Iso.*, **41**, 1111 (1990).

[89] G. NEBBIA ET AL. *Nucl. Instr. Meth. Phys. Res. A*, **533**, 475 (2004).

[90] SUDEEP MITRA ET AL. *IEEE Nucl. Sci. Symp. Conf. Record*, pp. 285–289 (2011).

[91] D.N. VAKHTINI,Y. U GORSHKOV ET AL. *SENNA Portable Sensor for Explosive Detection Based on Nanosecond Neutron Analysis. In:Detection and Disposal of Improvised Explosives* (Springer, Dordrech, 2006).

[92] PERRET G., PEROT B., ET AL. *EURITRACK Tagged Neutron Inspection System,Journal of Physics: Conference Series,ISSN 1742-6596*, **4**, 375 (2006).

[93] ELEON C., PEROT B., ET AL. *Nucl. Instr. and Meth. in Phys. Res. A*, **629**, 220 (2011).

[94] M. LUNARDON ET AL. *Applied Radiation and Isotopes*, **61**, 43–49 (2004).

[95] B. PEROT ET AL. *Nucl.Inst. Meth. Phys. Res. B*, **261**, 295–298 (2007).

[96] S. PESENTE, G. NEBBIA, G. VIESTI ET AL,. *Nucl. Instr. and Meth. B*, **261**, 268 (2007).

[97] M. LUNARDON ET AL. *Nucl. Instr. and Meth. in Phys. Res. B*, **261**, 391 (2007).

[98] UNDERWATER COASTAL SEA SURVEYOR 'UNCOSS' . *Project Final Report-218148, http://www.uncoss-project.org*.

[99] V.VALKOVIC ET AL. *Nucl. Instr. and Meth. in Phys. Res. A*, **703**, 133 (2013).

[100] D.SUDAC ET AL. *AIP Conf. Proc.*, **1099**, 574 (2009).

[101] C. CARASCO ET AL. *IEEE Trans. Nucl. Sci.*, **59**, 1438 (2012).

[102] V.YU.ALEAKHIN ET AL. *Nucl. Instr.Meth. Phys. Res. A*, **785**, 9 (2015).

[103] I.N. RUSKOV ET AL. *Physics Procedia*, **64**, 163 (2015).

[104] GARRETT R, MITRA S. *Med Phys*, **18**, 916 (1991).

[105] S. MITRA ET AL. *Asia Pac. J. Clin. Nutr.*, **4**, 187 (1995).

[106] S. MITRA ET AL. *Phys. Med. Biol.*, **40**, 1045 (1995).

[107] S.AGOSTINELLI. "Geant4a simulation toolkit".

[108] ALLISON ET AL. "Geant4 Developments and Applications".

[109] JINCHOON KIM. *Nucl. Inst.Meth. in Phys. Res. A*, **274**, 425–430 (1989).

[110] M. J. LOUGHLIN ET AL. *Fusion Engineering and Design*, **58-59**, 967–971 (2001).

[111] . *www.nndc.bnl.gov*, **53 (1)**, 270–278 ((2006)).

[112] . *http://physics.nist.gov*.

[113] RADIATION MONITOR. *http://atomtex.com*.

[114] KIM ET AL. *Nucl.Eng.Tech.*, **40**, 299 (2008).

[115] AMAR SINHA. *Nucl. Inst. Methods B*, **350**, 66 (2015).

[116] AMAR SINHA. *Annals of Nuclear Energy*, **75**, 590 (2015).

[117] MAYANK SHUKLA. *Nucl. Inst. Methods A*, **772**, 118 (2015).

[118] J.M. HALL, B. RUSNAK AND P.J. FITSOS. *Proc. 8th World Conf. Neutron Radiography.* (2006).

[119] I.SABO NAPADENSKY. *Proc. 2nd Int. Workshop on Fast Neutron Det. and App.*, pp. 6–11 (2011).

[120] B.TANG. *Sci. China.*, **52**, 1330 (2009).

[121] J.S. BRZOSKO ET AL. *Nucl. Instrum. Meth. B*, **72**, 119 (2007).

[122] ERZSEBET SVAB, MARTON BALASKO,. *Phys. Meth. Inst. Meas. ,1V-Non-destructive Testing; Neutron Radiography*.

[123] E.H. LEHMANN ET AL. *Nucl. Inst. Meth. in Phys. Res. A*, **531**, 228237 (2004).

[124] B.D. SOWERBY. *Proc. of Int. Topical Meeting on Nucl. Res. App. Utilization of Accelerators* (2009).

[125] F.P. DOTY, H.B. BARBER, H. ROEHRIG AND E.J. MORTON. *Nucl. Instrum. Meth. A* (2010).

[126] W. L. RAAS ET AL. *IEEE Nucl. Sci. Symp. and Medical Imaging Conf;UCRL-CONF-217017* (2005).

[127] A. HAUSLADEN ET AL. *Nucl. Inst. Meth. in Phys. Res. B*, **261**, 387–390 (2007).

[128] TAKENAKA ET AL. *Nucl. Inst. Meth. in Phys. Res. B*, **424**, 73–76 (1999).

[129] V. POPOVET AL. *12th Int. Workshop on Rad. Img. Detectors* (2010).

[130] V. MIKEROV ET AL. *Nucl. Inst. Meth. in Phys. Res. A*, **424**, 48–52 (1999).

[131] E. BOGOLUBOVA ET AL. *Nucl. Inst. Meth. in Phys. Res. A*, **542**, 187–191 (2005).

[132] HAWKESWORTH M.R. AND WALKER J. *In: Barton J.P., von der Hardt P. (eds) Neutron Radiography. Springer, Dordrecht* (1983).

[133] . *http://cern.ch/geant4*.

[134] . *http://root.cern.ch/*.

[135] HTTP://IMAGEJ.NIH.GOV/IJ/.

[136] ROBERT ADAMS ET AL. *Applied Radiation and Isotopes*, **107**, 1–7 (2016).

[137] E. LEHMANN ET AL. *IEEE Transactions on nuclear science*, **52**, 1–7 (2005).

[138] BERGAOUI ET AL. *J Radioanal Nucl Chem*, **299**, 4151 (2014).

[139] I. SABO-NAPADENSKY ET AL. *JINST*, **7** (2012).

[140] J.G. FANTIDIS ET AL. *Nucl. Inst. Meth.Phys. Res. A*, **618**, 331335 (2010).

[141] HTTPS://WWW.NNDC.BNL.GOV.

[142] HTTP://WWW.DETECTORS.SAINT-GOBAIN.COM.

[143] HTTP://WWW.ANDOR.COM/SCIENTIFIC-CAMERAS.

[144] T.A. WELLINGTON ET AL,. *Physics Procedi*, **66**, 432–438 (2015).

[145] JESSICA HARTMANA ET AL,. *Physics Procedia*, **66**, 85 (2015).

[146] N.M. SPYROU. *J. Radioanal. Nucl. Chem.*, **239(1)**, 59 (1999).

[147] R. L. PAUL, R. M. LINDSTROM. *J. of Radioanal. Nucl. Chem.*, **243,1**, 181 (2000).

[148] H. KURTH ET AL.,. *Proc. Mettal. Plant. Design Op. Strategies.*, p. 493 (2008).

[149] L.G. EVANS. *Nucl. Inst. Meth. Phys. Res. A*, **242,2**, 346 (1986).

[150] T.GOZANI. *NucL Instr. and Meth. in Phys. Res. A.*, **353**, 635 (1994).

[151] W. EL KANAWATI ET AL. *Appl.Radiat. Isot.*, **69**, 732 (2011).

[152] W. C. LEE ET AL.,. *Nucl Inst Meth B*, **99(1)**, 739 (1995).

[153] P.M. SHEA, T. GOZANI, M. BOZORGMANESH. *Nucl. Inst. Methods A*, **299**, 444 (1990).

[154] D.R BROWN AND T. GOZANI. *Nucl.Inst. Meth. Phys. Res. A*, **99**, 753 (1995).

[155] A. J. CAFFREY, J. D. COLE ET AL. *IEEE Trans Nucl Sci.*, **39**, 1422 (1992).

[156] J. YINON. *Forensic and Environmental Detection of Explosives.*, **Wiley, New York** (1999).

[157] T.R. TWOMEY ET AL.,. *Idaho National Laboratory report*, **INL/CON07-12304** (2007).

[158] H. D. CHOI ET AL. *IAEA, http://www-pub.iaea.org/MTCD/publications/PDF/Pub1263 web.pdf* (2007).

[159] A. BARZILOV,P. C. WOMBLE,. *J Radioanal Nucl Chem*, **301**, 811–819 (2014).

[160] W.C. LEE ET AL. *Nucl.Instr.and Meth. in Phys. Res. B*, **99**, 739 (1995).

[161] J. K. JOSEPH. *Nucl. Inst. Meth. A*, **353**, 444 (1994).

[162] D.M.DRAKE ET AL.,. *Nucl. Inst. Meth.*, **62**, 349 (1968).

[163] B. PEROT. *Appl. Rad. Isot.*, **66**, 421 (2008).

[164] WO 99/49311,PCT/US99/03491. *Method and Apparatus for Detecting, Locating and Analyzing Chemical Compounds using subatomic particle activation (Atomatry)*.

[165] V. F. BATYAEV ET AL. *WIT Transactions on Modeling and Simulation,ISSN 1743-355X doi:10.2495/CMEM150151*, **59**, 171 (2015).

[166] V. F. BATYAEV ET AL. *International Journal of Modern Physics: Conference Series*, **27**, 1460131–1 (2014).

[167] . *https://www.unipd.it/en/*.

[168] SAROJ BISHNOI ET AL. *Proc. of the DAE Symp. on Nucl. Phys*, **55**, 670–671 (2010).

[169] . *https://www.crytur.cz*.

[170] . *https://www.hamamatsu.com*.

[171] . *https://www.caen.it*.

[172] S CROFT. *Nucl. Instr. and Meth. A*, **281**, 103 (1989).

[173] . *https://www-nds.iaea.org*.

[174] . *ANSI N42.41-2007, American National Standard Minimum Performance Criteria*.

[175] W. EL KANAWATI ET AL. *IEEE Trans. Nucl. Sci.*, **57(5)**, 2879 (2010).

[176] R. A. CECIL ET AL. *Nucl. Inst. Meth.*, **161**, 439 (1979).

[177] J. SCHERZINGER ET AL. *Nucl. Inst. Meth. Phys. Res. A*, **840**, 121 (2016).

[178] N.V. KORNILOV ET AL. *Nucl. Inst. Meth.*, **599**, 70 (2009).

[179] SMITH D L ET AL. *Nucl. Inst. Meth.*, **64**, 157 (1968).

[180] DIETZE G. *IEEE Trans. Nucl. Sci*, **26(1)**, 398 (1979).

[181] . *https://www.mesytec.com/products/nuclear-physics/MPD-4.html*.

[182] ANDREAS RUBEN ET AL. *IEEE Nucl. Sci. Symp. Conf.* (2007).

[183] DIETZE G. ET AL. *Nucl. Inst. Meth.*, **193**, 549 (1982).

[184] R.E. PYWELL ET AL. *Nucl. Inst. Meth. Phys. Res A*, **565**, 725 (2006).

[185] R. BATCHELOR ET AL. *Nucl. Inst. Meth.*, **13**, 70 (1961).

[186] C. HAGMANN ET AL. *Trans. Nucl. Sci.*, **60**, 545 (2013).

[187] JEROME M. VERBEKE ET AL. *LLNL Fission Library 2.0.2., UCRL-AR-228518-REV-1.* (2016).

[188] GEANT4 PHYSICS REFERENCE MANUAL. *http://geant4.web.cern.ch/geant4/G4UsersDocument /UsersGuides/PhysicsReferenceManual/html/PhysicsReferenceManual.htm*.

APPENDIX A

Foil Activation and HPGe Gamma Spectrometry

A.1 Foil Activation Technique

Foil Activation technique has been used to measure neutron yield of DD/DT NG [109].

Principle

Consider a target isotope X of mass m and nuclear density N being irradiated in a neutron flux (ϕ) to yield another isotope Y with nuclear density n(t). Isotope Y undergoes gamma decay with decay constant (λ) during and after irradiation. Activation foils are irradiated for time t_1 followed by a cooling period of t_2 and counting time duration of t_3. Let σ be the activation cross-section for reaction X $\rightarrow$ Y. Then the density of Y isotope n(t), is governed by the following equations:

$$\begin{aligned} \frac{du}{dt} &= N\sigma\phi - \lambda n(t) \; for \; 0 \leqslant t \leqslant t_1 \\ &= -\lambda n(t) \; for \; t_1 \leqslant t \end{aligned} \tag{A.1}$$

The soultion of these equations are given as;

$$n(t) = \frac{N\sigma\phi}{\lambda}(1 - e^{-\lambda t}) \; for \; 0 \leqslant t \leqslant t_1 \tag{A.2}$$

$$n(t) = n(t_1)e^{-\lambda(t-t_1)} \; for \; t_1 \leqslant t \tag{A.3}$$

Let A be the atomic mass number of X, a_i the isotopic abundance, N_A the Avogadro's constant, P_k the number of photo-peak counts, η the photo-peak efficiency, I_γ the γ-ray intensity of photo-peak of interest, and Ω the solid angle. Then the neutron flux Φ is given by Eq A.4:

Table A.1: Parameter values used for the neutron flux calculation using Aluminum Activation

Parameter	Value	Relative Error (%)
A(gm)	26.98	na
λ(sec^{-1})	1.221x10^{-3}	0.13
N_A	6.02x10^{23}	5x10^{-6}
m(gm)	0.22	-
σ(cm^2)	7.16$\times$10^{-26}	3.07
a_i	1	na
I_γ	0.7184	na
η(843.76 KeV)	0.038	0.3

Table A.2: Parameter values used for the neutron flux calculation using Copper Activation

Parameter	Value	Relative Error (%)
A(gm)	62.93	na
λ(sec^{-1}	1.185x10^{-3}	0.021
N_A	6.02x10^{23}	5x10^{-6}
m(gm)	0.28	-
σ(cm^2)	4.603$\times$10^{-25}	4.25
a_i	0.692	na
I_γ	1.956	na
η(511 KeV)	0.02	0.35

$$\Phi = \frac{P_k A \lambda}{N_A m \sigma a_i I_\gamma \eta \Omega (1 - e^{-\lambda t_1}) e^{-\lambda t_2} (1 - e^{-\lambda t_3})} \tag{A.4}$$

The neutron flux has been calculated using equation A.4. The different parameter values used for the neutron flux calculation with Al,Cu and F foil are listed in table A.1,A.2 and A.3.

The reaction cross-section data for the above reactions were taken from ENDF/B-VII.O library [111] and physical constants from [112].

Table A.3: Parameter values used for the neutron flux calculation using Fluorine Activation

Parameter	Value	Relative Error (%)
A(gm)	18.99	na
N_A	6.02x10^{23}	5x10^{-6}
m(gm)	0.23	-
σ(mb)	55.8	4.84
a_i	1	na
I_γ	1.934	na
η(511 KeV)	0.02	0.35

A.2 γ-ray spectrometry

The neutron induced γ-ray activity was measured with High Purity Germanium (HPGe). HPGe detector used in the experiment was a p-type vertical coaxial. The relative efficiency of the HPGe detector is 30% (compared with a 3″ × 3″ NaI crystal) and energy resolution at 1332 keV of ^{60}Co is 1.90 keV. Detector was operated at 2.8 kV (negative) High voltage and the signal from the detector was processed with a charge-sensitive pre-amplifier. The output signal of pre-amplifier was shaped and amplified by a spectroscopy amplifier. The pulse height spectrum was recorded with 4k MCA (MCA -4K, Oxford make). The HPGe detector was covered with a 10 cm thick layer of lead having 1cm inner layer of SS, to shield HPGe from background gamma.

The energy calibration and photo-peak efficiency curve of HPGe detector was performed using ^{252}Eu gamma point source within energy range of 121-1408 keV. Eu is widely used in efficiency calibration because of its multi-gamma peaks and good branching ratio of each peak as listed in Table (A.4). Pulse height spectrum of Eu-152 acquired with HPGe is shown in figure (A.1). The photo-peak efficiency as a function of energy was measured for different detector-to-source distance. The measured photo-peak efficiencies were least square fitted with the following function.

$$ln\eta = \sum_{i=0}^{i=2} a_i (lnE)^i \tag{A.5}$$

Where, E is the photon energy. a_i's are the unknown coefficients.

The least square fitted photo-peak efficiencies (solid line) at distance 1.5 cm, 4.5 cm and 7.5 cm are shown in the Figure(A.2).

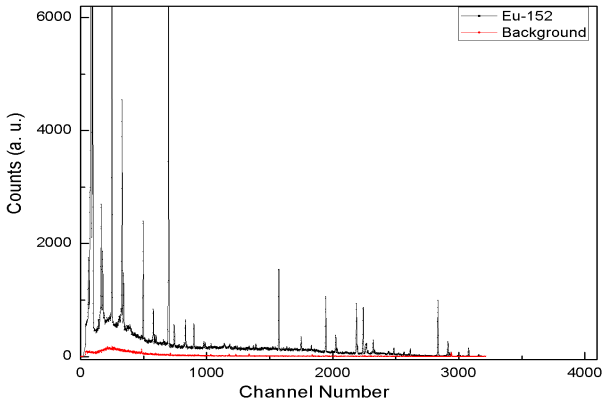

Figure A.1: Pulse height spectrum of Eu-152

Table A.4: Eu-152 gamma source

Energy (KeV)	Abundance (%)
121.79	28.37
244.72	7.53
344.27	26.57
410.97	2.23
443.91	3.13
778.89	12.97
964.01	14.63
1112.11	13.55
1408.54	20.85

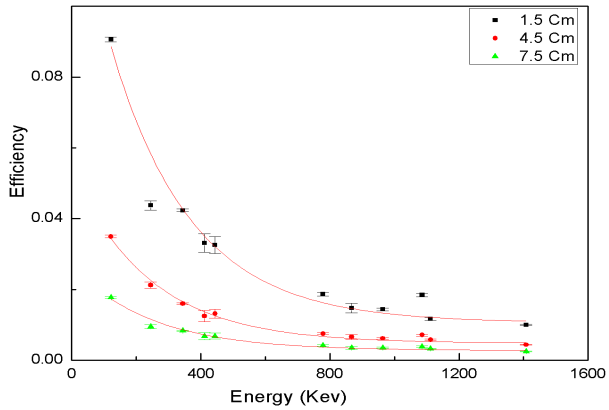

Figure A.2: Photo-peak Efficiency of HPGe detector for detector-source distance of 1.5 cm, 4.5 cm and 7.5 cm.

Table A.5: List of isotopic Neutron Sources used in the thesis.

Sources	Reaction Type	Average Alpha Energy(MeV)	Average Neutron Energy(MeV)
^{238}PuBe	(α,n)	5.49	4.5
^{241}AmBe	(α,n)	5.48	5.0
^{252}Cf	Spontaneous fission	NA	2.1

Table A.6: List of Gamma Source used in the thesis work

Nucleide	Gamma Energy (MeV))	Half Life	Activities μCi(KBq)
^{137}Cs	0.662	30.17	1.8(66.6)
^{60}Co	1.17,1.33	5.27	1.0(37)
^{22}Na	1.275	2.6	2.0(74)

APPENDIX B

Characterisation of 5" Liquid Scintillator Detector

Organic Liquid Scintillators are widely used for the detection of fast neutrons in a mixed field of neutron and gamma-ray because of their fast time response, high detection efficiency and excellent neutron-gamma discrimination. The organic Liquid Scintillator detectors are sensitive to neutrons as well as to gamma radiation, where the neutrons interact mainly through recoil protons while γ-rays interact via Compton electrons. If the light output response function of a detector and the exact reaction cross-sections are precisely known, the efficiency of a detector can be determined reasonably well by a Monte-Carlo simulation. The efficiency which is a function of the incident neutron energy and threshold is essential for obtaining the accurate neutron spectrum. The response function for the Liquid Scintillator detector using different type or make of scintillators have been reported [176–178] in the past and it has been observed that the response function depends on the scintillator type and size of the detector. The response of liquid scintillators is a complex function of not only the particle's energy, but also the type of particle along with its unique ionization mechanism [179]. The response of the organic liquid scintillator to particle energies is nonlinear except for electrons [180]. The gamma or electron energy response of a LS detector with standard gamma sources is important for 1) energy calibration, 2) estimation of effective neutron detection thresholds and 3) determining the accurate neutron detection efficiency. In the present study, characterization of a 5″ x 5″ size LS detector in terms of response function and efficiency was performed. The electron light output response of LS detector was investigated with standard ^{137}Cs and ^{22}Na gamma sources and compared with the simulated results. The neutron response of the detector was measured with mono-energetic neutrons (neutron energy (En) =

2.45 MeV and 14.1MeV) from D-D/D-T NG. To compare the experimental data of electron and neutron response, the geometry of the detector was modeled with GEANT4. The paper is organized as follows: In section two the details of experimental set- up consisting of sources, detector, data acquisition and methodology. The third section describes the experimental results along with the simulated n-γ response while the fourth section summarizes the findings.

Experimental methodology and Set-Up

Gamma and Neutron Sources

We have used standard gamma sources ^{22}Na and ^{137}Cs for gamma response study while the neutron response study was carried out with mono-energetic neutrons of 2.45 MeV and 14.1 MeV produced from D-D/D-T neutron generator.For the D-D experiment the d+ ions (current 120μA) were accelerated up to 70 kV and in case of the D-T, these parameters were 15μA and 50 kV. During the experiment the detector was placed at distance 100 cm from the neutron emitting target at the 90 degree angle with respect to D+ ion beam. The study was extended further for Time-of-Flight and efficiency calculation using continuous neutron spectrum of energies (1-10 MeV) from a ^{252}Cf spontaneous fission neutron source of strength 2000 neutrons/s.

Experimental setup

The cylindrical liquid scintillation detector was coupled to a 5 inch photo-multiplier tube (ETEL-9390KB), and a negative bias of 1000 Volt was applied to the photo-multiplier tube (PMT.) The anode signal of the PMT was fed to the input of a 4-channel pulse shape discriminator(PSD) module (Mesytec MPD4) [181, 182]. This module provides pulse-height, pulse-shape and trigger signals for neutron and gamma-rays. The walk, threshold and gain of each channel were optimally adjusted through the control software through an usb interface. The pulse-height and pulse-shape signals from MPD4 were fed to Analog-to-Digital Convertor (ADC). The data were collected on event-by-event basis us-

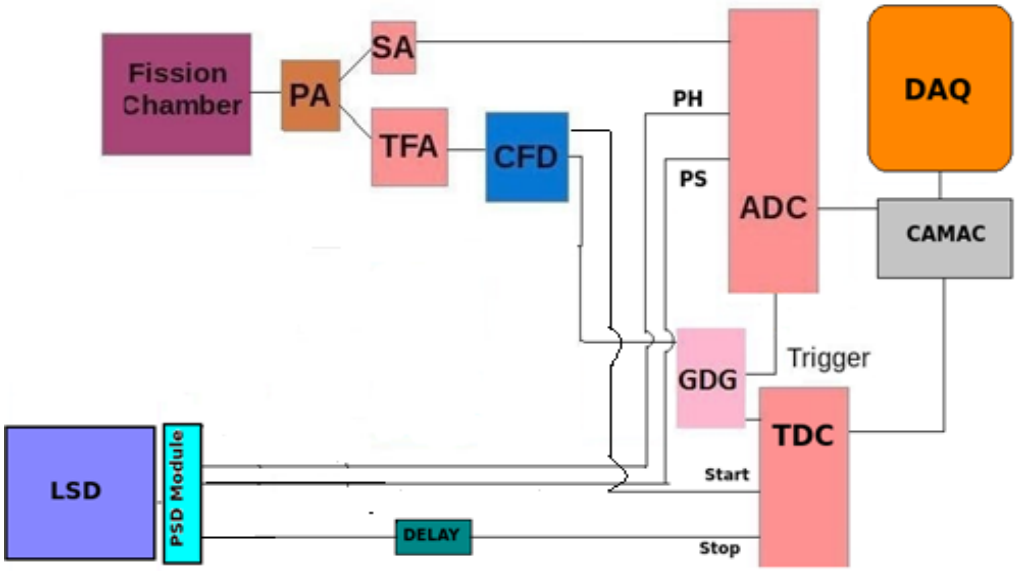

Figure B.1: Block-diagram of the TOF experimental setup

ing a CAMAC-based DAQ system. In the first set, the experiment was carried out with gamma sources for electron response and in the second set the neutron response was measured with D-D/D-T neutrons.

Next, a T-O-F experiment was set up for the measurement of prompt fission neutron spectra of^{252}Cf, via coincidence with fission fragment. In the T-O-F experiment, an ionization chamber with ^{252}Cf source embedded inside was used as a reference detector and ionization chamber was placed at a distance of 75 cm from the neutron detector. The ionization chamber, which acts as a trigger detector for fission fragments consists of an anode and cathode each having 4.5 cm diameter separated by a distance of 3 mm using a Teflon insulator ring. A positive voltage of 500 V was applied to the anode. The fission fragment deposits its energy in the active region of the fission chamber. The resultant ion-electron pair drifts towards the respective electrodes and constitute an electronic signal for further processing to obtain the deposited energy and timing information. The time output of ionization chamber was fed to timing filter amplifier (TFA) and output of TFA to Constant Fraction Discriminator (CFD), which provides a logic output when the input signal exceeds a preset threshold value. Logic output of the CFD was used as the start of a time to digital converter (TDC) unit in the CAMAC. Hence, the start signal for the T-

O-F measurement was generated from the ionization chamber. The stop signal was provided by neutron detector via trigger output of PSD. The energy signal from ionization chamber was given to the ADC after processing through a spectroscopy amplifier for the fission fragment energy loss pulse-height. A gate and delay generator (GDG), triggered by the CFD output of the ionization chamber provided the master gate for the ADC as well the TDC for data acquisition. The block-diagram of the T-O-F experimental setup with detector is shown in Figure B.1.

Experimental results and simulation

B.0.1 Gamma Response

In the gamma response measurement, the sources were placed approximately 15 cm from the face of the cylindrical scintillator and were aligned with the cylinder's axis of symmetry and the detector was exposed to 0.662 MeV gammas from ^{137}Cs and 0.511, 1.274 MeV gammas from ^{22}Na. The background was measured for the same acquisition time and subtracted in the offline data analysis. Since there is no distinct photo-peak in organic low-Z scintillators, in order to calibrate the measured light output with the actual energy of the recoiling electron, the channel numbers of the Compton edges of different gamma sources were recorded. The energy calibration of neutron detector is obtained with relating the position of the measured Compton edge to the maximum energy of the Compton recoil electron. The position of the Compton edge (in channel) was determined from the measured light output spectrum at half height of maximum peak position [183]. Thus, the energy calibration of the scintillator in terms of the equivalent Compton electron energy (in energy units denoted by keVee) was obtained. The measured pulse-height spectra for ^{22}Na and ^{137}Cs gamma source are shown in Figure B.2. The experimentally measured light output response of detector for gamma sources were compared with simulated one. The simulations were carried out using GEANT4. The gamma and neutron responses were simulated using the

standard electromagnetic-interaction package and hadronic physics list QGSP-BIC-HP which provided high-precision data-driven models for neutron interactions below 20 MeV. Material components of the scintillator were H and C (ratio of atoms is 1.23, density of the scintillator is 0.874 gcm^{-3}. The scintillator is modelled as a 5″ x 5″ cylindrical vessel having a wall of 0.5 mm thick aluminum. The amplitude of the signal was provided by a sensitive-detector class which recorded the total energy deposited in the liquid scintillator volume. The data were analyzed using the ROOT analysis software. For the purpose of the gamma response simulation, a point source of gamma-rays was positioned along the cylindrical symmetry axis of the detector cell at a distance of 15 cm from the face. The gamma-rays were directed onto the cell along its symmetry axis. The energy deposit was then converted to the light output based on the following equation (1) [184]. The light output (L) is proportional to the electron energy (Ee) and can be written as

L(Ee) = Lee = k*Ee——————(1)

To match it with the experimental resolution the electron light output (Lee), was smeared by the following function Eq.(2),

Lsm = Lee + R(σ1) + R(σ2) Lee ——————— (2)

Where, Lsm =smearing function, R (σ) is random number sampled from a normal distribution that has centroid at zero and having a standard deviation . The values of σ1 and σ2 were fixed as 0.01 MeV and 0.077 $MeV^{0.5}$ respectively to match the experimental data.

The measured and simulated detector response functions for 0.662 MeV, 0.511 MeV and 1.274 MeV gammas are shown in Figure B.2. Small variations at the lower energy region could be attributed to the ambient background in the experiment that was not modeled in the simulation.

B.0.2 Neutron Response

For the neutron response measurement the detector was exposed to mono-energetic neutrons of energy 2.45 MeV and 14.1 MeV from neutron generator. The detector was placed at 100 -150 cm from the target at a height of target center and data were collected. The 2D plots of pulse-height vs pulse shape

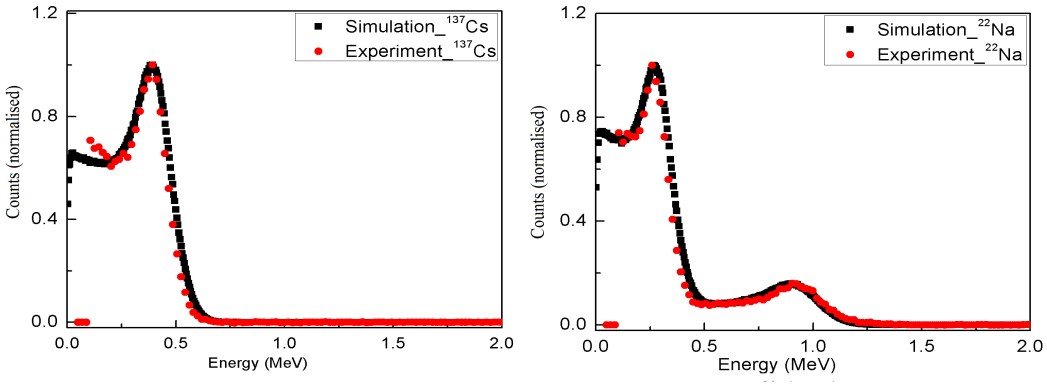

Figure B.2: Comparison of measured and simulated gamma responses of LSD for (left) ^{137}Cs (0.662 MeV), and (right) ^{22}Na (0.511, 1.274 MeV)

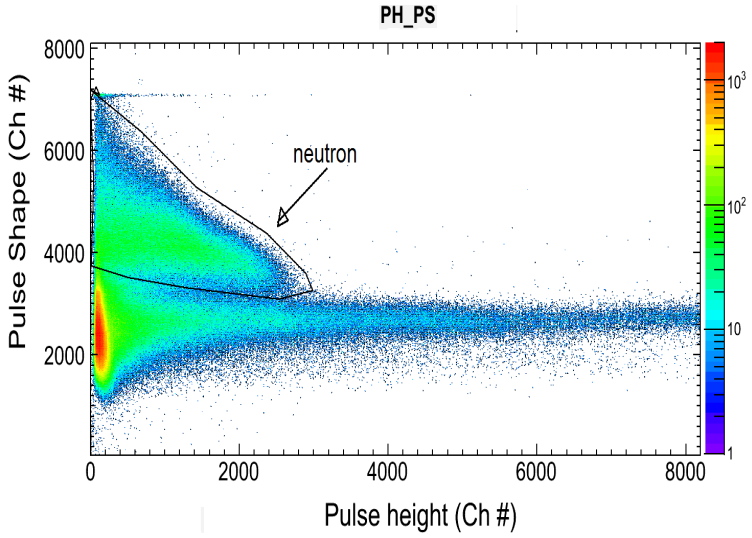

Figure B.3: (left) 2D plot of pulse-shape vs. pulse-height of 2.45 MeV neutron.

acquired via PSD were obtained for all the three cases. One of the 2D plots is shown in Figure B.3 for D-D case. The neutron events were selected from the 2D plot of pulse-shape parameter versus the pulse-height (energy light output) and projected it on an axis. The neutron pulse-height of the PSD-selected neutron events for D-D and D-T are shown in Figure B.4. The neutron response of the detector was reproduced from simulation and the response function was determined. As described in the subsection 3.1, for simulation the cylindrical detector cell was exposed to a neutron point source (2.45MeV/14.1MeV) from a distance (100 cm for 2.45 MeV and 150 cm for 14.1 MeV, the same as used in the experiments) and deposited neutron energy in the sensitive detector medium was converted to the light output. The relation used for the

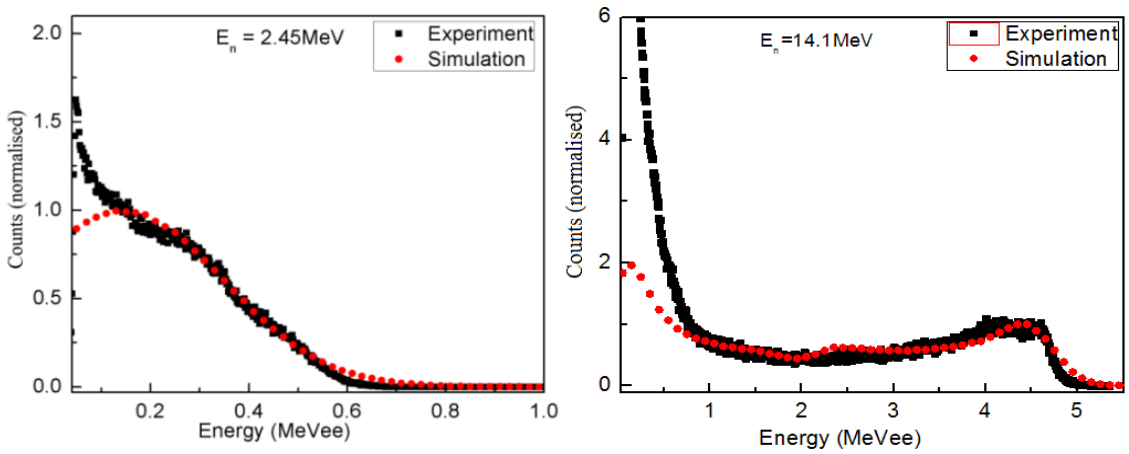

Figure B.4: Experimental (black) and simulated (red) neutron response of LS detector for neutron energy (left) 2.45 MeV and (right) 14.1MeV.

conversion of deposited energy to the light output (electron energy equivalent) over a wide energy (0-14.1MeV) range is given by,

L = 0.025Ep + 0.030Ep2 (0<Ep $\leq$ 8 MeV) ... (3)

= 0.4Ep - 1.04 (8 < Ep $\leq$ 14.1 MeV)

Where, Ep is the energy of the recoil nucleus. To match with the experimental resolution the simulated light output (L), was smeared by the function of equation2. The simulated response functions for 2.45 MeV and 14.1 MeV neutrons are shown in Figure B.4 with the experimental response. It was found that the neutron response function for 5″ x 5″ LS can be described well with the prescription of Batchelor et al [185]. On comparison, the shape of the simulated spectra (expressed in electron energy equivalent) at neutron energies of 2.45 MeV and 14.1 MeV, match well with the experimental one except at lower pulse-height regions, as shown in Figure B.4. The variations at the lower energy region could be attributed to a poor separation of neutron and gamma pulse-shape signals and therefore some contamination due to gamma at these low energies would be expected.

B.1 Evaluation of Detector Efficiency

We have simulated the detector efficiency over an energy range from 1 to 10 MeV. The knowledge of intrinsic efficiency, which is a function of the incident

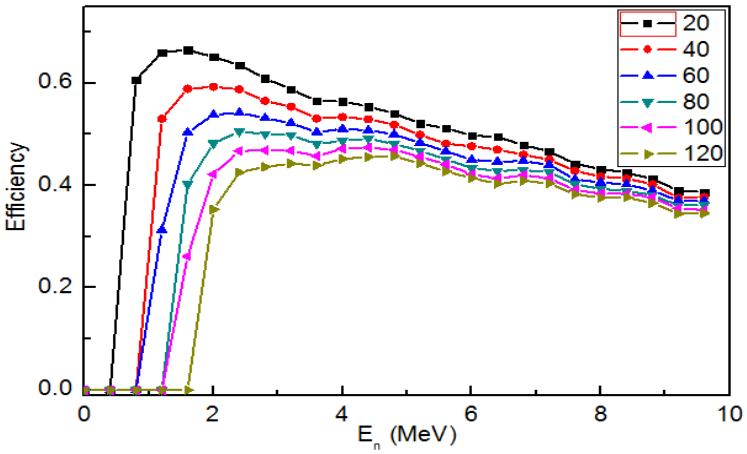

Figure B.5: Geant4 simulated efficiency curve at different energy threshold (keVee- electron energy equivalent).

neutron energy and threshold, is essential for obtaining the neutron spectrum. The neutron detection efficiency is sensitive to the detection bias which is set in terms of electron equivalent energy. Hence the efficiency was simulated at different threshold energies of 20, 40, 60, 80, 100,120 keVee, as shown in the Figure B.5. The evaluated efficiency curve was further verified and implemented to the measured neutron spectra of ^{252}Cf via T-O-F. Experimental results of the T-O-F experiment, the 2D plot of pulse-shape vs pulse-height, 2D plot of Pulse-shape vs T-O-F, fission energy spectrum and T-O-F are presented in Figures (B.6, B.7). The efficiency corrected neutron energy spectra were compared with the FREYA [186, 187] generated theoretical neutron spectra of ^{252}Cf as shown in Figure B.8.

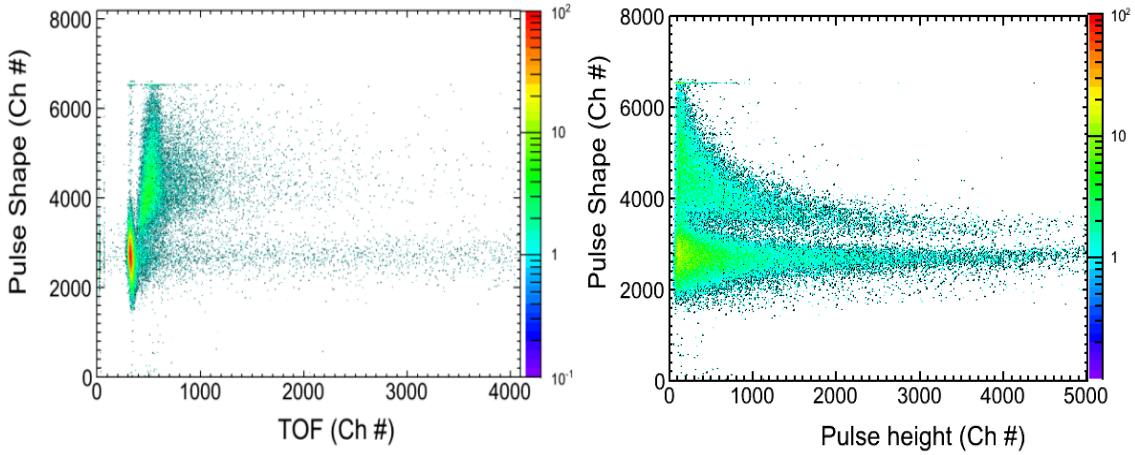

Figure B.6: 2D plot of (left) pulse shape vs. the pulse-height and (right) Pulse-shape vs T-O-F for ^{252}Cf

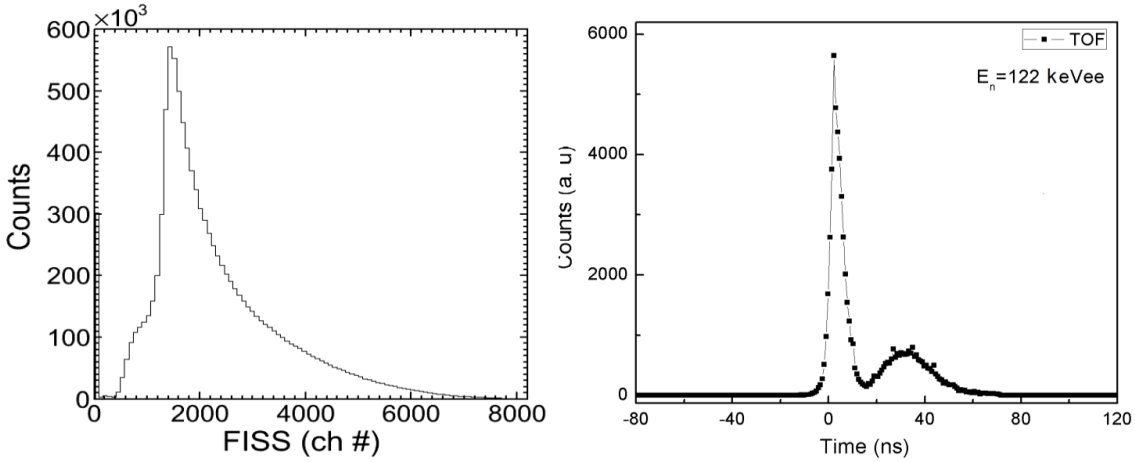

Figure B.7: (Left) Pulse-height spectra of fission fragment of ^{252}Cf and (right) Typical Time-of-Flight spectrum.

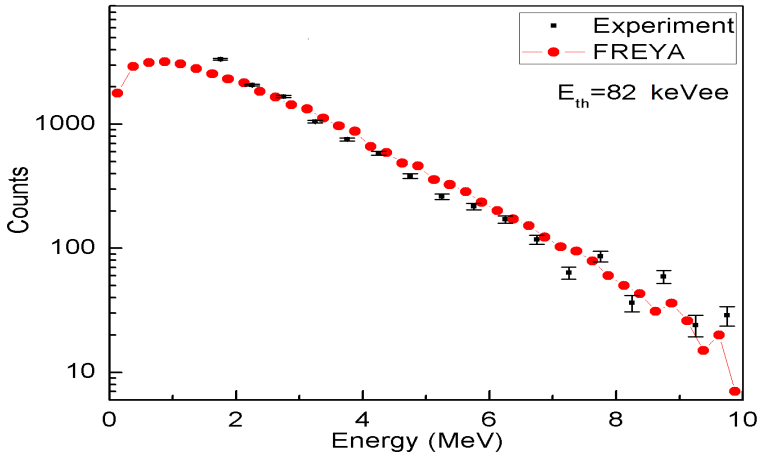

Figure B.8: Comparison of efficiency corrected experimental (black) and theoretical (red) neutron energy spectra of ^{252}Cf.

Conclusions

A detailed study of n-γ response and efficiency measurement has been carried to characterize a 5x 5 size liquid scintillator detector. The gamma response study performed using standard gamma sources of ^{22}Na and ^{137}Cs was found in good agreement with simulated light output response for the gamma energies 511, 662 and 1275 keV. The measured neutron response at mono-energetic neutrons of 2.45 MeV and 14.1 MeV showed good agreement with the GEANT4 simulations and the response function was evaluated. Overall it was found that the light output function for the detection of neutrons by the liquid scintillator over an energy range from 1 to 14 MeV could be described successfully with the analysis proposed by Batchelor et al. The study was further extended for efficiency calculation that predicted the efficiency over a wide energy range of neutrons via Monte Carlo simulation at threshold bias of 20 - 120 keVee. The efficiency corrected measured neutron energy spectrum of ^{252}Cf agrees well with the theoretical spectrum and reasonably explains the validity of the predicted efficiency.

APPENDIX C

Monte Carlo Simulation Code : GEANT

A detailed simulation study of the API and FNR imaging techniques is necessary to get first hand information and apparatus performance. Similarly the evaluation of response matrix of liquid scintillator, detector modeling is required. The simulations were performed using GEANT4 toolkit [107] and each system was modelled with approximate geometry of real experimental set up as explained in respective chapters. Detail description of Geant4 simulation code and ROOT analysis software has been provided at the websites https://geant4.web.cern.ch/ and https://root.cern.ch/ respectively. However, a brief introduction of the Geant4 simulation code [133] and ROOT analysis software [134] used in the thesis is discussed here.

C.1 GEANT4 : History and introduction

GEANT4 (GEometry ANd Tracking) is a toolkit for simulating the passage / transportation of particles through matter using Monte Carlo methods. The toolkit is developed at CERN under a worldwide collaboration of physicists and software engineers. The first version was released in December 1998. Initially designed for applications in the field of high energy particle physics, it has spread to many other fields, including particle physics, nuclear physics, accelerator design, space engineering and medical physics. It is based on object-oriented technology and implemented in the C++ programming language [133]. A certain number of versions have been released since, and the one used in this thesis research work was version 9.6 (2011) and geant4.10.01.p02 (2014) [108]. Geant4 simulates the transportation of particles through the matter. Therefore it provides all the tools needed to build an experimental set up such as geometry, tracking, detector response. The GEANT4 system allows to:

- Describe an experimental setup by a structure of geometrical volumes.
- Generate fundamental particles of interest with their properties such as position, energy etc.
- Transport particles through the various regions of the setup, taking into account geometrical volume boundaries and physical effects according to the nature of the particles themselves and their interactions with matter.
- Record particle trajectories and the response of the sensitive detectors.
- Visualize the detectors and the particle trajectories.

Geant4 is not an executable but a collection of C++ based libraries organized in classes. Major features the Geant4 includes are handling geometry, tracking, detector response, run management, visualization and user interface. Geometry is an analysis of the physical layout of the experiment, including detectors, absorbers, etc. and considering how this layout will affect the path of particles in the experiment. Tracking is simulating the passage of a particle through matter. This involves considering possible interactions and decay processes. Detector response is recording when a particle passes through the volume of a detector and approximating how a real detector would respond. Run management is recording the details of each run (a set of events), as well as setting up the experiment in different configurations between runs.

C.2 Program Description

The main program consists of several steps, most of them performed through calls to GEANT subroutines. Setting up a Geant4 simulation, there are three mandatory classes to be implemented and derived from the base classes of Geant4: G4VUserDetectorConstruction, G4VUserPhysicsList and G4VUser PrimaryGeneratorAction. GEANT4 classes used in the program are:

DetectorConstruction: it defines the spatial configuration or geometry of the setup i.e. materials and their properties, geometry and volumes of interest to be studied by GEANT4. It has number of volumes. Each volume represents

an object with its shape and its physical characteristics, except the largest volume Called World volume, which in fact is a virtual volume and contains all other volumes in the detector geometry. A small volume can be placed in a big volume; we call this big one mother volume and the small one "daughter" volume. A coordinate system of the mother volume is used to specify where the daughter volume is place.

PhysicsList is the class defining particles and physical processes to be taken into account.

PrimaryGeneratorAction is used to generate primary particles. The ParticleGun class is designed to create a beam of particles by defining their type, position, direction of motion and kinetic energy. At present it was used to shoot particle from one point in a defined direction and then modified to achieve more complex situations (different energy distributions, directions etc.).

EventAction divides the simulation by primary event. It allows getting all the data subsequent to a single primary neutron. Event is the main unit of simulation. An event represents the whole process of an incident particle from its emission from the particle gun through interactions with the target particles if applicable to coming to rest in or leaving the detector system. The number of events is set before each run.

RunAction is dealing with the entire simulation. It is therefore very similar to EventAction but on a broader basis. Run is the largest unit of simulation in GEANT4. One Run represents performing the simulation once. It consists of a sequence of events. Conceptually, a run is a collection of events which share the same detector conditions.

SDetector Sensitive detector is a user-defined class derived from G4VSensitive Detector, for extracting information from the physics simulation. It gives the user a handle to collect simulated quantities for example: energy deposited, position, time information etc.

Analysis: storage of all the useful data in n-tuple using root (see the section C.3).

Modelling of the API mathod was more involved and complex, a brief description with extracts of programme is given below for understanding purpose:

Definition of Setup Geometry and Materials

The layout of geometry set up, material composition, sample and detector position were already defined in the Chapter 5. Here the sensitive elements defined were the 16 BGO detectors. Extract of the code for material definition, sensitive detector (BGO) placed in world volume:
Code snippet:

```
*****************************************************************************
G4Material BGO=new G4Material("BGO",density=7.13*g/cm3,ncomponents=3);
BGO->AddElement(Bi, natoms=4);
BGO-> AddElement(Ge, natoms=3);
BGO->AddElement(O, natoms=12);
.....
G4ThreeVector positionTarget = G4ThreeVector(0,0,(dis+10.+20.+dz)*cm);
solidTarget = new G4Tubs("Target",rin*cm,rout*cm,dz*cm,0.*deg,360.*deg);
logicTarget = new G4LogicalVolume(solidTarget,BGO,"Target",0,0,0);
.....
logicTarget->SetSensitiveDetector(targetSD);

    G4VisAttributes* VisAtt1 = new G4VisAttributes(G4Colour(1.0,0.0,1.0));
physiTarget = new G4PVPlacement(0, positionTarget, logicTarget, "Target",
logicWorld, false, 0);
*************************
```

Production of Neutrons and Particles

In order to simulate the alpha and neutron in primary generator a point source emitting neutron of En = 14.1 MeV and α= 3.5 MeV paticles, placed at origin of (0,0,0) in world volume. The three components of the momentum (p_n) of neutron are: p_x, p_y, p_z. For each neutron, the program generates an α-particle with momentum (p_a) components of -p_x, -p_y and -p_z. z-axis is chosen as the the emission direction of tagged neutron beam towards object and the emission angle of the emitted neutrons has been set in order to hit and cover the

whole sample volume.

Code snippet:

```
*************************************************************************
void PrimaryGeneratorAction::SetDefaultKinematic()
G4ParticleTable* particleTable = G4ParticleTable::GetParticleTable();
G4String particleName;
G4ParticleDefinition* particle
= particleTable->FindParticle(particleName="neutron");
particleGun->SetParticleDefinition(particle);
particleGun->SetParticleEnergy(14.1*MeV);
particleGun->SetParticlePosition(G4ThreeVector(0,0.*cm,0.*cm));
.....
void PrimaryGeneratorAction::SetDefaultKinematic2()
G4ParticleTable* particleTable = G4ParticleTable::GetParticleTable();
G4String particleName;
G4ParticleDefinition* particle
= particleTable->FindParticle(particleName="alpha");
particleGun2->SetParticleDefinition(particle);
particleGun2->SetParticleEnergy(3.5*MeV);
particleGun2->SetParticlePosition(G4ThreeVector(0.*cm,0.*cm,-60.*cm));
.....
particleGun->SetParticleMomentumDirection(G4ThreeVector(ux,uy,uz));
particleGun2->SetParticleMomentumDirection(G4ThreeVector(-ux,-uy,-uz));
.....
G4double cosTheta = 1.0-(1.0-rbyl)*G4UniformRand(), phi = CLHEP::twopi*G4UniformRan
G4double sinTheta = std::sqrt(1. - cosTheta*cosTheta);
G4double ux = sinTheta*std::cos(phi),
uy = sinTheta*std::sin(phi),
uz = cosTheta;
*************************************************************
```

Physics List

The gamma and neutron interactions were simulated using the standard electromagnetic interaction package and hadronic physics list QGSP_BIC_HP which provided high-precision data-driven models for neutron interactions below 20 MeV. A complete description of the Geant4 physics models can be found at [188].

Storage and Analysis of Data

The information about the arrival time of gamma and neutrons at any of the BGO detectors and the energy deposited have been stored in a n-tuple with 20 parameters. All the n-tuple have been converted into root files and analyzed with the ROOT package [134], C.3. By using the information stored in the n-tuple the conditions on γ-ray energy spectra and on time spectra can also be set for data anlysis. Also location of the gamma ray origin can be reconstructed using known velocities of 14.1 MeV (5.12 cm ns^{-1}) and γ-ray (30 cm ns^{-1}).

C.3 ROOT

ROOT is an object-oriented analysis framework for data processing developed at CERN [134]. It provides all the functionalities needed to deal with big data processing, statistical analysis, visualisation and storage. It is mainly written in C++. It save data (and any C++ object) in a compressed binary form in a ROOT file, the ROOT files are self-descriptive. ROOT provides a data structure, the tree, that is extremely powerful for fast access of huge amounts of data - orders of magnitude faster than accessing a normal file. Powerful mathematical and statistical tools are provided to operate on your data. The full power of a C++ application and of parallel processing is available for any kind of data manipulation. Data can also be generated following any statistical distribution and modeled, making it possible to simulate complex systems. Results can be displayed with histograms, scatter plots, fitting functions. It has provision of build your own application and compile it. ROOT provides different ways to

create a graphical user interface (GUI).

In summary, the GEANT4 is a powerful and suitable tool for imaging applications and image reconstruction using ROOT. FNR and API imaging techniques were successfully modelled in GEANT4 toolkit and the simulated results were used as a platform for implementation of these techniques. Geant4 is also an important tool for study of detector response with various options and to estimate characteristic observables such as energy resolution. The gamma response of the BGO gamma detector and n-γ response of liquid scintillator were successfully modelled.